MONASH University

Analysis of Exciton-Plasmon Nanohybrids

Harini Pranami Hapuarachchi
BSc Eng (Hons)

A thesis submitted for the degree of Doctor of Philosophy at
Monash University in year 2019
Department of Electrical and Computer Systems Engineering

Summary

Metamaterials formed by combining different types of nanoparticles are gaining increasing research attention due to their unprecedented capabilities to manipulate light at the nanoscale. Metal nanoparticles (MNPs) and quantum dots (QDs) are two categories of widely studied nanoparticles whose exceptional photophysical properties synergize when combined. Metal nanoparticles much smaller than the wavelength of the incident light (λ) exhibit strong dipolar excitations in the form of localized surface plasmon resonances, which give them a remarkable ability to concentrate optical energy in the nanoscale. This enables the use of individual MNPs as nanoscale optical cavities that can focus electromagnetic energy to spots much smaller than λ, overcoming the half-wavelength size limitation of the conventional optical cavities. This strong electric field localization can significantly enhance the interactions of metal nanoparticles with excitonic gain media such as QDs. Semiconductor quantum dots have strong luminescent capabilities widely used in a plethora of applications such as bio-sensing. QDs possess unique optical properties which make them quite appealing as *in-vivo* and *in-vitro* fluorophores in a variety of diagnoses, and as the optical gain medium of spasers (the nanoscale counterparts of lasers). When a quantum dot is kept in the vicinity of a metal nanoparticle, a dipole-dipole coupling occurs between the two nanoparticles giving rise to fascinating optical signatures in the absorbed and scattered spectra. This coupling makes the two nanoparticles behave like a single hybrid molecule possessing novel and interesting optical signatures which are tunable using a multitude of system proper-

ties such as the particle sizes, composition, inter-particle distance and the optical properties of the submerging medium. When an exciton-plasmon nanohybrid is optically excited, an additional electric field superposed on the external driving field is experienced by the MNP due to the dipole moment of the optical transitions in the QD. The resulting electric field induces a dipole moment in the MNP which in turn alters the field experienced by the QD, leading to a self-feedback. Due to this interaction, artificial hybrids formed by MNPs placed in nanoscale proximity to QDs exhibit a variety of optical phenomena that can be exploited in a wide array of applications such as spasing, optoelectronics, photovoltaics and bio-sensing. This thesis entails improved and computationally efficient analytical and numerical studies of such exciton-plasmon nanohybrids formed by illuminating a metal nanoparticle-quantum dot pair, placed in nanoscale vicinity, followed by a numerical demonstration of their prospects in bio-sensing.

General Declaration

This thesis is an original work of my research and contains no material which has been accepted for the award of any other degree or diploma at any university or equivalent institution and that, to the best of my knowledge and belief, this thesis contains no material previously published or written by another person, except where due reference is made in the text of the thesis.

Harini Pranami Hapuarachchi
March 2019

Publications During Enrollment

- Harini Hapuarachchi, Malin Premaratne, Qiaoliang Bao, Wenlong Cheng, Sarath D Gunapala and Govind P Agrawal. **Cavity QED analysis of an exciton-plasmon hybrid molecule via the generalized nonlocal optical response method.** Phys. Rev. B 95 (24), 245419, June 2017.

- Harini Hapuarachchi, Sudaraka Mallawaarachchi, Haroldo Hattori, Weiren Zhu and Malin Premaratne. **Optoelectronic figure of merit of a metal nanoparticle-quantum dot (MNP-QD) hybrid molecule for assessing its suitability for sensing applications**. J. Phys. Condens. Matter 30 054006, Jan. 2018.

- Yiyi Liu, Xiaohui Dai, Sudaraka Mallawaarachchi, Harini Hapuarachchi, Qianqian Shi, Dashen Dong, San H Thang, Malin Premaratne and Wenlong Cheng. **Poly (N-isopropylacrylamide) capped plasmonic nanoparticles as resonance intensity-based temperature sensors with linear correlation**. J. Mater. Chem. C,5, 10926-10932, Oct. 2017.

- Harini Hapuarachchi, Sarath D Gunapala, Qiaoliang Bao, Mark I Stockman and Malin Premaratne. **Exciton behavior under the influence of metal nanoparticle near fields: Significance of nonlocal effects**. Phys. Rev. B 98 (11), 115430, Sept. 2018.

- Viraj Senevirathne, Harini Hapuarachchi, Sudaraka Mallawaarachchi, Sarath D Gunapala, Mark I Stockman and Malin Premaratne **Scattering characteristics of an exciton-plasmon nanohybrid made by coupling a monolayer graphene nano flake to a carbon nanotube**. J. Phys. Condens. Matter 31 (8) 085302, Jan. 2019.

- Harini Hapuarachchi and Malin Premaratne **Thermoresponsive Nanohybrids for Tumor Imaging**. IEEEXplore Digital Library, proceedings of the 12th IEEE Conference on Nano/Molecular medicine and Engineering, Dec. 2018

- Harini Hapuarachchi, Sarath D Gunapala and Malin Premaratne **Plasmonic metaresonances: harnessing nonlocal effects for prospective biomedical applications**. (Accepted and in press for J. Phys. Condens. Matter)

Acknowledgements

Firstly, I would like to express my wholehearted gratitude to my Ph.D. supervisor and mentor, Prof. Malin Premaratne for all his support, kindness, encouragement and for believing in me throughout this journey, without whose timely guidance this thesis would not have been possible. I sincerely could not have asked for a better supervisor.

I am extremely grateful to my colleague and co-author Sudaraka, and the former Ph.D. students of my research group, Dilusha, Chathurangi, and Charith, following whose footsteps, I believe, has immensely contributed to make me the researcher I am today. I extend my heartfelt gratitude to all my colleagues at the Advanced Computing and Simulation Laboratory, Lakshitha, Tharindu, Ashan, Dasuni, Champi, Viraj, Kamani, Asha, Nisal, Ravi, Tharaka and Sachinthana for their encouragement, support, insightful discussions and for all the good times we shared together as a team. I thank my housemates Dinesha, Puwasala, Dilini, Chathurika, and all my friends in Melbourne for making my stay pleasant and memorable.

I sincerely acknowledge Monash University for providing me with all the support, facilities and financial assistance needed throughout my candidature. I would also like to thank all staff members at the Department of Electrical and Computer Systems Engineering for their support throughout my Ph.D.

Last, but certainly not least, I'm much indebted to my beloved parents Vijitha and Preethi Hapuarachchi, brother Harin and my fiancé Dinuka for their unconditional love, understanding, and support.

Contents

List of Figures

Chapter 1
Introduction

1.1 Background and Motivation

A metal nanoparticle (MNP) placed in the nanoscale proximity to a semiconductor quantum dot (QD) forms a tunable hybrid system which exhibits remarkable optical phenomena upon coherent illumination. Small MNPs exhibit nanocavity-like optical concentration capabilities due to the presence of strong dipolar excitation modes in the form of localized surface plasmons. QDs possess strong luminescent capabilities widely used in many applications such as biosensing. When a quantum dot is kept in the vicinity of a metal nanoparticle, a dipole-dipole coupling occurs between the two nanoparticles which gives rise to various optical signatures in the absorbed and scattered spectra. This coupling makes the two nanoparticles behave as an exciton-plasmon hybrid molecule [2].

Due to the synergizing impact excitons and plasmons placed in nanoscale vicinity exhibit on each other, nanohybrids formed by optically coupling MNPs to QDs possess a potential of emerging as strong candidates for a plethora of applications [4]. Such applications include bio-sensing, optoelectronics, photovoltaics and transmission of quantum information [4–7]. The exciton-plasmon nanohybrid can also be interpreted as the basic building block of a spaser, which is the nanoscale counterpart of a laser, proposed by Bergman and Stockman in 2003 [8]. A number of leading laboratories around the globe are currently inves-

tigating spasers, as its successful realization holds the potential to revolutionize the field of nano-optics by providing a coherent, intense, ultrafast (with pulse durations down to a few femtoseconds), source of optical energy concentrated to nanoscale [8]. A thorough understanding of the physical properties of the basic building block would definitely be useful in the context of design and realization of spasers.

In this thesis we theoretically study exciton-plasmon nanohybrids formed by coupling semiconductor quantum dots to metal nanoparticles placed in nanoscale proximity, with the aid of external coherent illumination. We aim at devising improved analytical models that account for the non-classical plasmonic effects observable at nanoscale, and their impact on the optical properties of the nanohybrid. Our improved analytical treatments offer the luxury of simulating exciton-plasmon nanohybrids at much lesser levels of computational complexity compared to the conventional, local response approximation based, numerical Bloch equation solving approaches widely followed in the literature, and the *ab initio* methods such as the density functional theory. Following our theoretical study, we numerically demonstrate the vivid prospects of exciton-plasmon nanohybrids in minimally-invasive bio-sensing applications, namely, *in-vitro* and *in-vivo* early cancer screening.

1.2 Research Aims

Development of a generalized nonlocal optical response method assisted cavity quantum electrodynamical model of an MNP-QD hybrid molecule

Hybrid molecules made of metal nanoparticles (MNPs) coupled to semiconductor quantum dots (QDs), under the influence of an external driving field, have been extensively studied in literature, using the local response approximation (LRA) based numerical models. However, such previous work in this area were

not adequate to explain some experimental observations such as the size dependent resonance shifts of metal nanoparticles which become quite significant with decreasing diameter.

The nonlocal response of metallic nanostructures which is hitherto disregarded by many studies currently available in the literature is a main reason for such nonclassical effects. The generalized nonlocal optical response (GNOR) model provides a computationally less demanding path to incorporate such properties into the theoretical models. It allows unified theoretical explanation of observed experimental phenomena which previously seemed to require *ab initio* microscopic theory. In this stage, we aim to analytically model an MNP-QD hybrid molecule incident by a coherent external driving field, as an open quantum system, using a GNOR assisted cavity-QED approach.

Analysis and comparison of different resonator based exciton-plasmon nanohybrids

In this stage, we aim to propose a simple, elegant relative figure of merit (RFoM), which focuses on maximizing the scattered intensity and the refractive index sensitivity of nanohybrids, to rank them in the order of their scattering prowess for sensing applications. The proposed RFoM will be used to analyse the optical spectra of noble, transition, post transition and alkali metal based MNP-QD nanohybrids using the representative metals Au, Ag, Cu, Al and Na, adopting the generalized nonlocal optical response (GNOR) method based cavity QED approach developed in the earlier stage.

This stage also aims to assess the suitability of MNP-QD nanohybrids for scattered intensity based sensing applications, in comparison to the individual constituents.

Investigating the effects of nonlocal plasmonic response on coherent dynamics of vicinal excitons

In this stage, we aim to analytically characterize the influence of a neighboring metal nanoparticle on the behavioral trends of a quantum dot using a GNOR based approach, taking the MNP distance dependent modifications to the QD population relaxation and dephasing rates into account. Attempts to incorporate MNP nonlocal effects in the analytical characterization of vicinal excitons found in literature utilize the phenomenological hydrodynamic model and assume the absence of MNP interband effects. Moreover, they are only applicable to narrow parameter regions. In this stage, we will present an analytical characterization which overcomes these drawbacks and lends to the perusal of the system over wide continua of various parameters. This enables us to get an elevated view at a much lesser level of complexity compared to the conventional LRA based numerical methods or the *ab initio* approaches of accounting for the nonlocal effects.

Improved modeling of plasmonic metaresonances

Plasmonic metaresonances (PMRs) form a class of optical events gaining increasing popularity due to their promising prospects in sensing and switching applications. Unlike the basic excitonic and plasmonic resonances in MNP-QD nanohybrids, PMRs occur in the space/time domain. A nanohybrid experiences PMR when system parameters such as the QD dipole moment, MNP-QD centre separation or the submerging medium permittivity reach critical values, resulting in the plasmonically induced time delay of the effective Rabi frequency experienced by the QD asymptotically tending to infinity. Theoretical analyses of PMRs available in the literature utilize the local response approximation (LRA) which does not account for the nonlocal effects of the MNP, and neglect the MNP dependence of the QD decay and dephasing rates which hinder their applicability to QDs in the close vicinity of small MNPs. In this stage, we aim to address these limita-

tions using an approach based on the GNOR formalism. We also aim to suggest prospective applications of PMR based nanoswitches, and mimic an example of the *in vivo* operation of PMR based nanoswitches using a two-dimensional skin tumour model.

Further investigation of the bio-sensing prospects

In the final stage, we aim to theoretically demonstrate the prospect of using thermoresponsive polymer capped MNP-QD nanohybrids for minimally invasive detection of skin cancer tissue and for feedback control of tumor temperature in localized hyperthermia therapy conducted using gold nanorods, to minimize damage to the surrounding healthy tissue, using the GNOR based cavity QED model developed in stage 1.

1.3 Thesis Outline

This thesis comprises twelve chapters which are organized as follows:

Chapter 1 introduces the topic of this thesis by outlining the background and motivation, which are followed by the research objectives. A detailed literature review is then presented in the chapters 2, 3 and 4, to equip the reader with the analytical tools utilized in the chapters that follow. In chapter 2, we present a detailed and rigorous overview of three different approaches of modeling localized surface plasmons in metal nanoparticles, namely, the local response approximation, the hydrodynamic and the generalized nonlocal optical response models. Chapter 3 presents the quantum mechanical formalism used to treat quantum dots as artificial atoms with discrete levels of energy that interact with incoming radiation followed by chapter 4, where the density matrix formalism and methodologies of accounting for the environmental interaction of a quantum mechanical system are discussed.

Chapter 5 presents a generalized nonlocal optical response method based fully analytical approach to model the behaviour of an exciton in a semiconductor quantum dot, placed in nanoscale proximity to a metal nanoparticle. Chapter 6 utilizes the analytical model developed in chapter 5 to peruse the system over wide continua of parameters while comparing the results to those obtained using the conventional local response approximation, followed by chapter 7 which presents a detailed numerical analysis of the plasmonic metaresonances in exciton-plasmon nanohybrids. The astute reader will notice that the thesis chapters do not follow the exact order of the research aims to enhance the readability and flow.

In chapter 8, we devise a quantum mechanical model for the entire exciton-plasmon nanohybrid utilizing a GNOR assisted cavity QED formalism. In chapter 9 that follows, we numerically analyse the Rayleigh scattering spectra of different nanoresonator based nanohybrids using the cavity QED formalism introduced in the earlier chapter. In chapter 10, we demonstrate the superior and versatile scattering prowess of exciton-plasmon nanohybrids compared to the individual constituents and introduce a relative figure of merit (RFoM) that can be utilized to arrange a set of nanohybrid configurations in the order of their scattering prowess. In chapter 11 we numerically demonstrate the prospects of exploiting the interaction of exciton-plasmon nanohybrids with incoming radiation for minimally invasive *in-vivo* and *in-vitro* cancer diagnoses and monitoring procedures. Finally in chapter 12, we summarize the research contributions of the thesis and outline the prospective future research stemming from the presented contributions.

Chapter 2
Localized Surface Plasmons

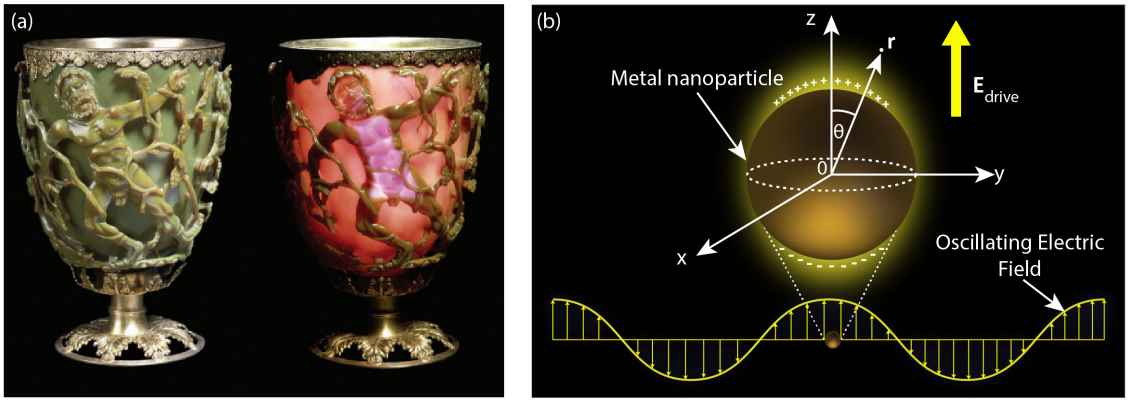

Figure 2.1: (a) The Lycurgus cup [1] made of ruby glass by the ancient Romans. In daylight, when light is reflected off the cup, it appears in green, whereas when light is shone within the cup and transmitted through the ruby glass, it appears in red. (b) Formation of surface plasmons in a small metal nanoparticle embedded in an oscillating electric field.

Localized surface plasmons (LSPs) are non-propagating modes of excitation of conduction electrons in metallic nanostructures which form due to their coupling with an externally incident oscillating electromagnetic field [2]. An effective restoring force is exerted on the electrons (driven by externally incident field) due to the curved surface of the particle which leads to an amplification of the electric field both inside and in the near-field of the outside. The resonant condition of the above phenomenon is termed the localized surface plasmon resonance (LSPR) [9].

For noble metal nanoparticles such as silver and gold, LSPR resides in the visi-

ble region of the electromagnetic spectrum resulting in the exquisite bright colors exhibited by such nanoparticles both in reflected and transmitted light, owing to the resonant enhancement in absorption and scattering [9]. Such nanoparticles own a rich history which dates back to the times of ancient Romans where they were used in the staining of glass for windows and ornamental cups [10]. A classic example would be the Lycurgus cup made of ruby glass by the ancient Romans in the fourth century, depicted in Fig. 2.1(a).

When the particle dimensions are much smaller than the wavelength of the incident light as depicted in Fig. 2.1(b), the interaction can be analyzed using the simple *quasi-static* approximation. For such particles, the phase of the electromagnetic field would be apparently constant over the particle volume due to its miniature size, enabling one to assume that the spatial field experienced by the particle takes an electrostatic form [5]. Once the solutions to the scattering problem under *quasi-static* field distribution are known, the harmonic time dependence can then be added to arrive at their final form. It has been shown that this lowest-order approximation of the full scattering problem provides solutions that adequately describe the behavior of optically illuminated particles of sizes below 100 nm for a multitude of purposes [9].

2.1 The Local Response Approximation

We first analyse the interaction of a metal nanoparticle (MNP) with an applied optical field using the conventional local response approximation (LRA). We consider a homogeneous, non-magnetic, isotropic metal sphere of radius a and dielectric permittivity ϵ_m situated at the origin of the coordinate system. The MNP is driven by an electromagnetic wave with angular frequency ω which propagates in the $\hat{x}$ direction, comprising a time-varying electric field along $\hat{z}$ as indicated in Fig. 2.1(b). The submerging medium is assumed to be isotropic and

non-absorbing with a dielectric permittivity constant ϵ_b.

The common basis of theoretical modeling of plasmonic phenomena in such metallic systems is the set of Maxwell's equations. In the linear regime of our interest, the displacement field $\vec{D}$ inside the MNP at position vector $\vec{r}$ is related to the electric field $\vec{E}$ as [11],

$$\vec{D}(\vec{r}) = \epsilon_0 \int d\vec{r}' \epsilon_{\mathrm{m}}(\vec{r}, \vec{r}', \omega) \vec{E}(\vec{r}') \tag{2.1}$$

where ϵ_0 denotes the vacuum permittivity and the nonlocal permittivity of the metal is denoted by $\epsilon_{\mathrm{m}}(\vec{r}, \vec{r}', \omega)$. In the LRA, the nonlocal effects of the MNP are neglected, hence $\epsilon_{\mathrm{m}}(\vec{r}, \vec{r}', \omega) = \delta(\vec{r} - \vec{r}')\epsilon_{\mathrm{m}}(\omega)$, which enables straightforward evaluation of the integral (2.1) as, $\vec{D}(\vec{r}) = \epsilon_0 \epsilon_{\mathrm{m}}(\omega) \vec{E}(\vec{r})$, where $\epsilon_{\mathrm{m}}(\omega)$ is spatially constant and is commonly modeled using the Drude-like dielectric function,

$$\epsilon_{\mathrm{m}}(\omega) = \epsilon_{\mathrm{core}}(\omega) - \frac{\omega_p^2}{\omega(\omega + \mathrm{i}\gamma)}. \tag{2.2}$$

In the above equation, ω_p and γ denote the bulk plasma frequency and the bulk damping rate of the metal, respectively. The response from the bound ions and electrons that account for effects such as inter-band transitions is denoted by ϵ_{core}.

Since we are interested in very small MNPs in the order of 10 nm which are much smaller than the wavelength of the incident optical field ($390 - 750$ nm) [5], we can assume that the particle experiences a static field $\vec{E}_{\mathrm{drive}} = E_0 \hat{z}$, under the *quasi-static* approximation, with the aim of adding the sinusoidal time dependence later. In order to calculate the response electric field ($\vec{E}_{\mathrm{res}}$) generated by the MNP, we solve Gauss' law in the absence of charges, $\nabla . \epsilon_m \vec{E} = 0$, where $\vec{E}$ denotes the electric field experienced by an arbitrary point in space with a position vector $\vec{r}$. When substituted with the electric scalar potential $\mathcal{V}$ which abides by the relationship $\vec{E} = -\nabla \mathcal{V}$, our problem reduces to solving the *Laplace's equation* $\nabla^2 \mathcal{V} = 0$ [5,9]. In a system with azimuthal symmetry such as ours, the solution to

the *Laplace's equation* can be obtained as a sum of *Legendre polynomials* presented in terms of spherical coordinates as follows, according to the working elaborated in Appendix A.1 [9],

$$\mathcal{V}(r,\theta) = \sum_{n=0}^{\infty} \left[A_n r^n + B_n \left(\frac{1}{r}\right)^{n+1} \right] P_n\left[\cos(\theta)\right], \tag{2.3}$$

where the coefficients A_n and B_n are yet to be determined using boundary conditions and $P_n(x)$ is given by the Rodrigue's formula [12],

$$P_n(x) = \frac{1}{2^n n!} \left(\frac{d}{dx}\right)^n \left(x^2 - 1\right)^n \tag{2.4}$$

Using the substitutions of the form $A_n \to \mathcal{A}_n / a^n$ and $B_n \to \mathcal{B} a^{n+1}$ and separating out the potentials inside and outside the MNP, we can write (2.3) as,

$$\mathcal{V}(r,\theta) = \begin{cases} \sum_{n=0}^{\infty} \left[\mathcal{A}_n \left(\frac{r}{a}\right)^n + \mathcal{B}_n \left(\frac{a}{r}\right)^{n+1} \right] P_n\left[\cos(\theta)\right], & \text{for } r < a \\ \sum_{n=0}^{\infty} \left[\mathcal{A}'_n \left(\frac{r}{a}\right)^n + \mathcal{B}'_n \left(\frac{a}{r}\right)^{n+1} \right] P_n\left[\cos(\theta)\right], & \text{for } r \geq a \end{cases} \tag{2.5}$$

Using appropriate boundary conditions (see Appendix A.2), the following solution for the electric potential is obtained [5],

$$\mathcal{V}(r,\theta) = \begin{cases} -\frac{1}{\epsilon_{\text{eff}}} E_0 r \cos(\theta), & \text{for } r < a \\ \beta_{\text{LRA}} a^3 E_0 \frac{1}{r^2} \cos(\theta) - E_0 r \cos(\theta), & \text{for } r \geq a \end{cases} \tag{2.6}$$

where $\epsilon_{\text{eff}} = (2\epsilon_b + \epsilon_m)/3\epsilon_b$ and

$$\beta_{\text{LRA}} = \frac{(\epsilon_m - \epsilon_b)}{(2\epsilon_b + \epsilon_m)} \tag{2.7}$$

The term β_{LRA} is termed the *Clausius Mossotti factor* (in this case, obtained under the local response approximation) which is directly proportional to the polariz-

ability of the MNP [9,13]. Using the relation $\vec{E} = -\nabla\mathcal{V}$, the total electric field is obtained as (see Appendix A.3) [2,5],

$$\vec{E} = \begin{cases} -\frac{1}{\epsilon_{\text{eff}}}\vec{E}_{\text{drive}}, & \text{for } r < a \\ \vec{E}_{\text{res}} + \vec{E}_{\text{drive}}, & \text{for } r \geq a. \end{cases} \tag{2.8}$$

where

$$\vec{E}_{\text{res}}(r \geq a) = \frac{\beta_{\text{LRA}} a^3}{r^3}\left[3(\vec{E}_{\text{drive}}.\hat{r})\hat{r} - \vec{E}_{\text{drive}}\right]. \tag{2.9}$$

with $\hat{r}$ being the radial unit vector of our position of interest in space.

It is now evident that $1/\epsilon_{\text{eff}}$ and β_{LRA} are the two functions we need to know, in order to evaluate the response of a metal nanoparticle to an external field, in the *quasi-static* limit. The *screening-factor* $1/\epsilon_{\text{eff}}$ governs the field inside the MNP, or the absorption properties whereas the *Clausius Mossotti factor* β_{LRA} governs response outside the MNP, or the scattering properties [5].

The LRA has so far being the most prevalent and and commonly applied constitutive description to model localized surface plasmons [11]. Studies have shown that it successfully explains a multitude plasmonic phenomena and experiments based on, optical far-field measurements [14,15], electron energy loss spectroscopy (EELS) [16,17], cathodoluminescence [18,19] and near-field microscopy [20]. It has even been able to successfully explain plasmonic particles with nanometer sized separations [21] and plasmonic effects in the two-dimensional material graphene [11,22]. Our extensive literature review on exciton plasmon nanohybrids suggested that, almost all recent studies of quantum dots subjected to near fields of MNPs [23–30] utilize the LRA to model the MNP, without taking the nonlocal plasmonic effects into account.

2.2 Nonlocal Response in Metal Nanoparticles

2.2.1 Importance of Nonlocal Modeling

Despite the merits listed above, the sufficiency of modeling plasmons using the classical LRA, which overlooks the nonlocality of the MNP, has appeared questionable due to several reasons [11]. One example is its insufficiency in accounting for the MNP size-dependent surface plasmon line-width broadening experimentally observed in metal clusters and small MNPs [31–33]. Other examples include MNP size-dependent resonance shifts observed in optical [34, 35] and EELS [36,36] measurements of noble metal nanoparticles and the multipole plasmons [37] supported by metal-vacuum interfaces due to electron spill-out beyond the classical metal boundary [11]. It has also been shown that thin metal films support resonant excitations above the plasma frequency due to the existence of confined longitudinal waves [38, 39] which are not accounted for under the LRA [11]. Moreover, several recent experiments based on MNP dimers conducted with particles placed in sub-nanometer proximity have revealed that plasmonic effects certainly go beyond the LRA [11,40–43].

As a metal nanoparticle gets increasingly smaller, the ratio of the number of surface atoms to the number atoms in the bulk or core of the particle grows larger, causing the surface effects to dominate the physics of the nanoparticle [5]. Studies have shown the origin of the size dependence in nonlocal response as the smearing of surface charges, induced by an external illumination, over a finite distance (few Å) into the metal due the presence of longitudinal waves [13]. However, the classical LRA assumes that the charges induced by external illumination reside only on the geometric surface of a metal nanoparticle [11]. Due to such assumptions, nanoplasmonic experiments defy explanations with the classical LRA [11,34,36,44,45].

Experimentally observed effects such as the size dependence of the surface

plasmon resonance energy, which strengthen as the particle size decreases, are believed to be consequences of the quantum properties of the MNP free electron gas [46]. Theoretical explanations utilizing *ab initio* approaches such as density functional theory (DFT) [47–50] are capable of accurately describing the microscopic interaction effects of electrons in metals. Nevertheless, these methods put forth extensive computational demands which hinder their applicability to generic plasmonic systems beyond few nanometers in size [51] (where not a handful, but a large number of electrons contribute to the optical response), even with strong approximations such as time dependent local density approximation [49]. This is because they use extremely resource greedy approaches such as solving the Shrödinger equation for a large, but finite number of electron wave functions for all atoms considered in the system.

Surpassing the LRA using nonlocal response theories such as the nonlocal hydrodynamic model or the generalized nonlocal optical response (GNOR) model would be a simpler and computationally much less demanding alternative to the *ab initio* calculations [11, 52]. Combining these nonlocal models with fully analytical characterizations of exciton-plasmon nanohybrids enables the generation of insightful fully analytical models and the optimization of the large parameter space associated with device designing while taking the nonlocal effects into account, a functionality not fully offered by the methods currently available in literature [13].

The concept of nonlocal response in metal nanoparticles was first introduced phenomenologically, and was later based on the semi-classical hydrodynamic model (HDM) [13, 44]. This approach has been able to theoretically describe size-dependent resonance shifts of noble metal nanoparticles and gap-dependent resonance shifts in particle-film systems [53]. The hydrodynamic approach is beneficial in the theoretical studies of generic plasmonic systems with large ($> 10\,\mathrm{nm}$) feature sizes [11] which cannot be practically studied with *ab initio* approaches

due to extensive computational demands.

The generalized nonlocal optical response (GNOR) model emerged as a recent generalization and an extension of the aforementioned HDM model. It goes beyond HDM by taking into account, both the convection current and electron diffusion phenomena in the MNPs [44]. It better captures both size dependent localized surface plasmon resonance shifts and line-width broadening of the extinction cross section which strengthen with decreasing MNP dimensions. Experiments based on dimers with few nanometer sized gaps have revealed that the GNOR model yields results in plausible agreement with the experimentally-measured spectra, without the need of invoking the quantum mechanical effect of tunneling, at an extremely less level of computational complexity [11,13].

In the next two sections, we will walk through the nonlocal modeling of localized surface plasmons using the hydrodynamic and GNOR models, respectively.

2.2.2 Hydrodynamic Model

Let us now walk through the derivation of the exact nonlocal *Clausius Mossotti factor* of a spherical metal nanoparticle embedded in a non-absorbing homogeneous dielectric medium which was first presented by Raza *et al.* in [11,36], initially assuming that the free electrons in the MNP are characterized by the semi-classical hydrodynamic model. This model accounts for the nonlocal effects of the MNP while neglecting the effects of electron spill-out due to the finiteness of the confining potential [11,36]. As detailed derivations of the hydrodynamic model have been reported in earlier studies [54–56] this section will mainly focus on the essential steps of nonlocal characterization of localized surface plasmon resonances based on the HDM model.

Maxwell's equations of our interest for a non-magnetic material can be ex-

pressed as [12,57],

$$\nabla.\vec{\boldsymbol{D}} = -en, \tag{2.10a}$$

$$\nabla.\vec{\boldsymbol{H}} = 0, \tag{2.10b}$$

$$\nabla \times \vec{\boldsymbol{E}} = \mathrm{i}\omega\mu_0\vec{\boldsymbol{H}}, \tag{2.10c}$$

$$\nabla \times \vec{\boldsymbol{H}} = -\mathrm{i}\omega\vec{\boldsymbol{D}} + \vec{\boldsymbol{J}} \tag{2.10d}$$

where n denotes the free-electron density, e is the elementary charge, μ_0 is the vacuum permeability, $\vec{\boldsymbol{J}}$ denotes the free-electron current and $\vec{\boldsymbol{H}}$ is the magnetic field. The displacement field is defined in terms of the bound or core electron response of the MNP, ϵ_{core}, as $\vec{\boldsymbol{D}} = \epsilon_0\epsilon_{\text{core}}\vec{\boldsymbol{E}}$. Obtaining the divergence of the left and right hand sides of (2.10d) and using (2.10a), we can arrive at the continuity equation which relates the free-electron density to the free-electron current as follows [36],

$$\nabla.\vec{\boldsymbol{J}} = -\mathrm{i}wen \tag{2.11}$$

The fundamental assumption of the hydrodynamic model is that the many-electron energy and dynamics of a metal are characterized by the electron density (a scalar field $n(\vec{\boldsymbol{r}},t)$) and the hydrodynamic velocity (a vector field $\vec{\boldsymbol{v}}(\vec{\boldsymbol{r}},t)$), respectively [11], using which the hydrodynamic equation of motion and the continuity equation for charge conservation are expressed as [11,54],

$$\left[\frac{\partial}{\partial t} + \vec{\boldsymbol{v}}.\nabla\right]\vec{\boldsymbol{v}} = -\frac{e}{m}[\vec{\boldsymbol{E}} + \vec{\boldsymbol{v}} \times \vec{\boldsymbol{B}}] - \frac{1}{m}\nabla\frac{\delta}{\delta n}G[n] - \gamma\vec{\boldsymbol{v}}, \text{ and} \tag{2.12a}$$

$$\frac{\partial}{\partial t}n = -\nabla.(n\vec{\boldsymbol{v}}), \tag{2.12b}$$

where m denotes the mass of an electron. The first term on the right hand side of the equation of motion (2.12a) relates to the Lorentz force, whereas the second term of the same is related to the internal kinetic energy of the electron gas. The last term which accounts for the damping has been added phenomenolog-

ically [11]. The simplest and most popular approach is to obtain the functional $G[n]$ using the Thomas-Fermi model, which accounts only for the kinetic energy of the electron gas [11, 54]. By solving equations (2.12b) and (2.12a) using the detailed approach presented in the references [11, 54, 56], the following coupled electromagnetic equations of the hydrodynamic model can be obtained [11,58,59],

$$\nabla \times \nabla \times \vec{\boldsymbol{E}}(\vec{\boldsymbol{r}}, \omega) = \left(\frac{\omega}{c}\right)^2 \epsilon_{\text{core}} \vec{\boldsymbol{E}}(\vec{\boldsymbol{r}}, \omega) + \mathrm{i}\omega\mu_0 \vec{\boldsymbol{J}}(\vec{\boldsymbol{r}}, \omega), \tag{2.13a}$$

$$\sigma \vec{\boldsymbol{E}}(\vec{\boldsymbol{r}}, \omega) = \frac{\kappa^2}{\omega(\omega + \mathrm{i}\gamma)} \nabla[\nabla . \vec{\boldsymbol{J}}(\vec{\boldsymbol{r}}, \omega)] + \vec{\boldsymbol{J}}(\vec{\boldsymbol{r}}, \omega). \tag{2.13b}$$

In the high frequency limit ($\omega \gg \gamma$) of our interest, $\kappa = 3/5 v_F^2$, where v_F is the Fermi-velocity. The Drude conductivity σ is related to the Drude permittivity equation (2.2) as $\epsilon_m(\omega) = \epsilon_{\text{core}} + \mathrm{i}\sigma/(\epsilon_0\omega)$ and the response of the bound electrons can be obtained from the experimentally measured bulk permittivity $\epsilon_{\text{exp}}(\omega)$ (such as the dataset by Johnson and Christy [60] used in this thesis) using the recipe $\epsilon_{\text{core}}(\omega) = \epsilon_{\text{exp}}(\omega) + \omega_p^2/(\omega^2 + \mathrm{i}\gamma\omega)$ [11]. It is readily observable that (2.13b) reduces to the Ohm's law when $\kappa \to 0$.

Pressure of the electron gas is taken into account in the above hydrodynamic description. This gives rise to compression (longitudinal) waves, leading to spatial dispersion which is truly observable in nanoplasmonic experiments [36]. The corresponding longitudinal wave vector is characterized by [11, 52, 61],

$$k_{\text{L}}^2 = \epsilon_m(\omega)/\xi^2, \tag{2.14}$$

where the nonlocal parameter ξ is defined in the hydrodynamic model abides by the relationship,

$$\xi^2(\omega)\big|_{\text{HDM}} = \frac{\epsilon_{\text{core}}(\omega)\kappa^2}{\omega(\omega + \mathrm{i}\gamma)} \tag{2.15}$$

We are interested in metal-dielectric interfaces where an additional boundary condition should augment Maxwell's boundary conditions. This additional

boundary condition which states that the normal component of the free-electron current density must vanish, can be derived by neglecting the spill-out of electrons [36, 57, 59].

Similar to the electric scalar potential $\mathcal{V}$ defined as $\vec{\boldsymbol{E}} = -\nabla\mathcal{V}$, the current scaler potential $\mathcal{A}$ is characterized by the relation, $\vec{\boldsymbol{J}} = -\nabla\psi$ [36]. Using these relations with hydrodynamic equations (2.10), (2.11) and (2.13b), the following equations governing the scalar potentials inside the MNP can be obtained as [36, 62],

$$\left(\nabla^2 + k_{\mathrm{L}}^2\right) n = 0, \tag{2.16a}$$

$$\nabla^2\mathcal{V} = \frac{e}{\epsilon_0\epsilon_{\mathrm{core}}} n, \tag{2.16b}$$

$$\psi = \frac{1}{\mathrm{i}\omega - \gamma}\left(\epsilon_0\omega_p^2\mathcal{V} - e\kappa^2 n\right). \tag{2.16c}$$

The scalar potential $\mathcal{V}$ must satisfy the usual Laplace's equation $\nabla^2\mathcal{V} = 0$ due to the current density $\vec{\boldsymbol{J}}$ and electron density n vanishing in the surrounding dielectric, and the general solutions to the electric scalar potential and the free electron density can be obtained as [36],

$$n(r < a) = \sum_{l,m} A_l j_1(k_{\mathrm{L}} r) Y_{lm}(\theta, \phi), \tag{2.17a}$$

$$n(r \geq a) = 0, \tag{2.17b}$$

$$\mathcal{V}(r < a) = \sum_{l,m}\left[D_l r^l - A_l \frac{e}{\epsilon_0\epsilon_{\mathrm{core}} k_{\mathrm{L}}^2} j_1(k_{\mathrm{L}} r)\right] Y_{lm}(\theta, \phi), \tag{2.17c}$$

$$\mathcal{V}(r \geq a) = \sum_{l,m}\left[B_l r^l + C_l r^{-(l+1)}\right] Y_{lm}(\theta, \phi), \tag{2.17d}$$

where A_l to D_l are coefficients to be determined. The functions j_1 and Y_{lm} denote the spherical Bessel function of the first kind (of angular-momentum order 1) and spherical harmonics, respectively. Following the same *quasi-static* approach

as in section 2.1 where $\lim_{r\to\infty} \mathcal{V} = -E_0 z = -E_0 r\cos(\theta)$, all orders of l, m in the summations in equation (2.17) can be excluded except $(l, m) = (1, 0)$ [36]. Applying Maxwell's boundary conditions with the hydrodynamic additional boundary condition for the scalar potentials and following the usual approach to introducing the *Clausius-Mossotti* factor outlined in section 2.1 and reference [9], its generalized form which takes the nonlocal effects of the MNP into account can be obtained [36],

$$\beta_{\mathrm{NL}} = \frac{\epsilon_m - \epsilon_b(1+\delta_{\mathrm{NL}})}{\epsilon_m + 2\epsilon_b(1+\delta_{\mathrm{NL}})}, \text{ where,} \tag{2.18a}$$

$$\delta_{\mathrm{NL}} = \frac{\epsilon_m - \epsilon_{\mathrm{core}}}{\epsilon_{\mathrm{core}}} \frac{j_1(k_{\mathrm{L}})}{k_{\mathrm{L}} a j_1'(k_{\mathrm{L}} a)}, \tag{2.18b}$$

where prime denotes the differential with respect to the argument. It can be readily observed that when $\kappa \to 0$, $\delta_{\mathrm{NL}} \to 0$ and the classical, size-independent *Clausius-Mossotti* factor is retrieved [36].

2.2.3 Generalized Nonlocal Optical Response Model

Although the hydrodynamic model we discussed above accounts for the convective currents due to pressure, it neglects contributions of electron diffusion. The generalized nonlocal optical response (GNOR) model extends the hydrodynamic theory to account for electron diffusion using the following constitutive relation for current density (2.13b) as [11, 52],

$$\left[\frac{\kappa^2}{\omega(\omega + \mathrm{i}\gamma)} + \frac{D}{i\omega}\right] \nabla[\nabla.\vec{\boldsymbol{J}}(\vec{\boldsymbol{r}}, \omega)] + \vec{\boldsymbol{J}}(\vec{\boldsymbol{r}}, \omega) = \sigma \vec{\boldsymbol{J}}(\vec{\boldsymbol{r}}, \omega) \tag{2.19}$$

The above equation can be arrived at by setting $\kappa^2 \to \kappa^2 + D(\gamma - i\omega)$ in (2.13b), where D is the diffusion constant on the MNP. Thus, the nonlocal parameter in

the GNOR model can be found as [11,52],

$$\xi^2(\omega)\big|_{\mathrm{GNOR}} = \frac{\epsilon_{\mathrm{core}}[\kappa^2 + D(\gamma - \mathrm{i}\omega)]}{\omega(\omega + \mathrm{i}\gamma)}, \tag{2.20}$$

using which the longitudinal wave vector in the GNOR model can be obtained. Thus we can obtain the nonlocal polarizability β_{NL} in the GNOR approach bu substituting $k_{\mathrm{L}} = \epsilon_m(\omega) / \left[\xi^2(\omega)\big|_{\mathrm{GNOR}}\right]$ in (2.18).

The factor $\kappa \propto v_{\mathrm{F}}$ is associated with the pressure waves in the electron gas whereas the diffusion constant D relates to the charge carrier diffusion. While the former (κ) is prevalently known to cause blue-shifts (shifting resonances towards higher frequencies), the latter (D) causes line-width broadening in the plasmon resonances in metals. Thus, the GNOR theory unites both quantum-pressure effects and induced-charge diffusion kinetics [52], which enables it to successfully account for the main features observed in recent nanoplasmonic experiments [63–65].

It has recently been shown that nonlocal effects may manifest over distances far exceeding atomic dimensions and hence become comparable metallic structure dimensions such as the MNP radius or the gap distance of an MNP dimer, as a result, it has been proven that the generalized nonlocal optical response even dominates pure quantum mechanical effects in optical frequency regime such as the anticipated effect of quantum mechanical tunneling currents in dimers placed at sub-nanometer gaps [52].

Due to all aforementioned merits of the GNOR theory including its ability to capture the experimentally observed plasmonic phenomena at an extremely low computational cost, we utilize the GNOR model for the preceding nonlocal modeling of our exciton-plamon nanohybrids while comparing the results to those obtained using the conventional LRA as and when needed.

Chapter 3
Quantum Dots as Artificial Atoms

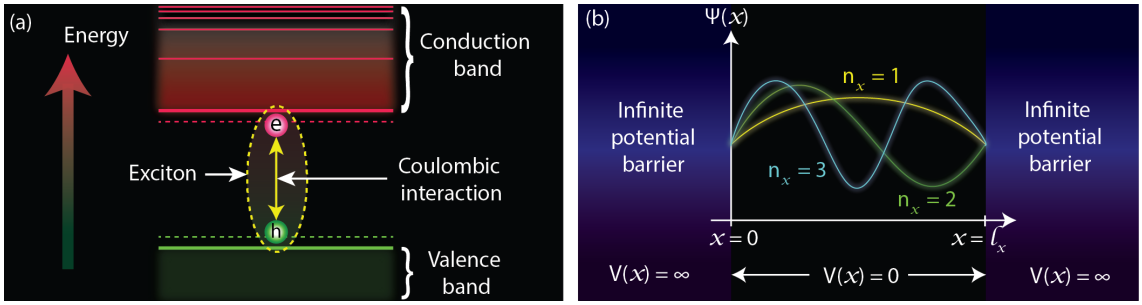

Figure 3.1: (a) Conceptual illustration of an exciton in a quantum dot which comprises an electron-hole pair coupled via Coulombic interaction. (b) Visualization of the one dimensional analogue of the infinite square well or the "particle in a box" model

.

Even though the use of surface plasmons in noble metals can be traced to antiquity as we outlined in chapter 2, the semiconductor quantum dot is a much later development [66]. Present semiconductor physics is increasingly focusing on artificially made semiconductor systems of reduced dimensionality which exhibit fascinating properties that are entirely different from those of solid-state bulk materials [67]. Semiconductor quantum dots are currently being used and considered for a wide range of applications ranging from solar-energy conversion to biological imaging [68]. They have quickly appeared as attractive alternatives to organic fluorescent dyes for bio-imaging applications because of their high resistance to photobleaching and bright, narrow emission that has enabled highly sensitive real-time observation of molecules [68].

Quantum dots form a special class of quasi zero-dimensional semiconductor structures, which can be modeled by a single electron wavefunction confined in all three spatial dimensions by the particle boundaries that serve the purpose of infinite potential energy barriers that prevent the electron from escaping [69,70]. Even though the single-electron wavefunction of a QD extends over thousands of lattice atoms, the electron-hole pair which is termed as an exciton exhibits a quantized and coherent behaviour [69]. It has been shown that the superposition of the ground and excited states of these quasi zero dimensional QDs tends to dephase at rates slower than those of higher-dimensional semiconductor structures. Moreover, QDs generally possess larger dipole moments (50-100 fold) compared to atoms. Owing to these properties, the aforementioned coherence can be detected and controlled optically, which allows scientists to manipulate the wavefunction of a single quantum dot for a multitude of diverse applications [69,71].

In non-zero dimensional semiconductor systems such as quantum wires, quantum wells and bulk semiconductors, the optical excitation raises an energy continuum due to the exciton's freedom of movement inside the crystal. However, in QDs which can be approximated as point-like objects, the exciton is completely localized and can also be strictly limited to a single state, owing to the ability to forbid unwanted states that lie outside the desired bandwidth using selection rules and optical polarization [69]. Once such states are inaccessible, we can model the QD as a two-level atom-like system where an exciton is either present (excited state) or absent (ground state) [2]. Given the existence of sufficiently long phase coherence time, a strong coherent field has the ability to rotate the Bloch vector of such systems, driving them completely to the excitonic state and back to the ground state, which is termed known as a Rabi oscillation [69,72].

3.1 The Infinite Square Well and Exciton Formation

A characteristic feature of semiconducting material is the existence of a band gap in the allowed electronic energy levels, which is usually the difference in energy between the valence and conduction band electrons. When energy is applied to such materials in form of an electric field, electrons in the valence energy band tend to absorb energy and move to the conduction band, once in which they can flow through the material. [5].

As quantum dots (QDs) are very small three-dimensional systems with dimensions less than the de Broglie wavelength of slow electrons, quantum confinement effects are quite prominent. Hence the electronic energy states constitute a discrete series similar to those of atoms [73] and the conduction band of QDs can be modelled using the "particle in a box" model or as an electron trapped in an infinite square well potential. In this model, the wave function of the trapped electron is given by [5] (see appendix B.1),

$$\Psi(n_x, n_y, n_z) = \sqrt{\frac{8}{l_x l_y l_z}} \sin\left(\frac{n_x \pi x}{l_x}\right) \sin\left(\frac{n_y \pi y}{l_y}\right) \sin\left(\frac{n_z \pi z}{l_z}\right), \tag{3.1}$$

with the associated energy,

$$E(n_x, n_y, n_z) = \frac{\pi^2 \hbar^2}{2m} \left[\left(\frac{n_x}{l_x}\right)^2 + \left(\frac{n_y}{l_y}\right)^2 + \left(\frac{n_z}{l_z}\right)^2\right] \tag{3.2}$$

where n_x, n_y, n_z are the quantum numbers of the state Ψ, l_x, l_y, l_z are potential well dimensions, (x, y, z) is the particle position, $\hbar$ is the reduced Planck constant and m is the electronic mass. For the ease of visualization, the one dimensional analogue of the above model is illustrated in Fig. 3.1(b). From (3.2) it is readily observable that, irrespective of the physical shape of the semiconducting particle, the separation between the energy levels increases as the dimensions are made smaller, enabling the creation of a quantum dot, where only the lowest conduc-

tion band energy level is effectively reachable with all higher levels being beyond reach for typical electrons. Under near resonant monochromatic optical illumination, the first electron which reaches the conduction band will further detune the valence-conduction energy gap away from the incident frequency, prohibiting another electron to reach the conduction band [5]. This creates a hole in the valence band in the void where the electron previously resided. Due to the Coulombic attraction between the electron and the hole, they will act as a quasi-particle known as the *exciton* [74] as depicted in Fig. 3.1(a). As long as energy (related to frequency) of the source of radiation is closely resonant with the excitonic bandgap, we can safely approximate the QD as an effective two-level atom with the two state ground (exciton absent) and excited (exciton present) [5].

3.2 Two-Level Atoms

Pertaining to our earlier explanations, it is clear that a judicious choice of the polarization and frequency composition of the exciting optical field can allow us to realize effective two (or if necessary three) levels atoms from QDs. In the context of this thesis, we mainly focus on the simple but extremely useful and versatile two-level model which can include the complex structure of such atom-like systems into just two parameters for effective analytical modeling. These two characteristic parameters are, the energy splitting between the two levels of the un-driven atom and the transition dipole moment that couples it to the externally incident driving field. It is evident that a detailed understanding of the related physics and spectroscopy is required for the reduction of a real system to a two-level description, and that care must be taken at the laboratory for the successful realization of a two-level atom such a system. Let us now look into the two level atomic model in detail.

3.2.1 The Unperturbed Atomic Hamiltonian

Let us define ground and excited states (the basic eigenstates) of the unperturbed atomic Hamiltonian as [5],

$$|g\rangle = \begin{pmatrix} 1 \\ 0 \end{pmatrix} \text{ and } |e\rangle = \begin{pmatrix} 0 \\ 1 \end{pmatrix}, \tag{3.3}$$

which possess the energies E_g and E_e respectively. They are orthonormal such that,

$$\langle e|g\rangle = \delta_{eg}, \tag{3.4}$$

and form a linearly independent basis set to the Hilbert space of the atomic Hamiltonian, in the absence of perturbations, where any state vector of the atom can be written as a linear combination [75]. The atomic transition frequency would then be $\omega_{\text{qd}} = (E_e - E_g)/\hbar$. The corresponding (time-dependent) two level state vector in the Schrödinger picture would be [75],

$$|\Psi(t)\rangle_{\text{s}} = c_g\,|g\rangle\,e^{-\mathrm{i}E_g t/\hbar} + c_e\,|e\rangle\,e^{-\mathrm{i}E_e t/\hbar}, \tag{3.5}$$

where $|c_g|^2$ and $|c_e|^2$ denote the probabilities of electron occupation in the ground and excited states, which also represent the probabilities of energy measurements yielding the values E_g and E_e. For the normalization of $|\Psi\rangle_{\text{s}}$ [75],

$$|c_g|^2 + |c_e|^2 = 1. \tag{3.6}$$

The eigenstates $|g\rangle$ and $|e\rangle$ relate to the atomic Hamiltonian $\mathcal{H}_a$ as [75],

$$\mathcal{H}_a\,|g\rangle = E_g\,|g\rangle \tag{3.7a}$$

$$\mathcal{H}_a\,|e\rangle = E_e\,|e\rangle\,. \tag{3.7b}$$

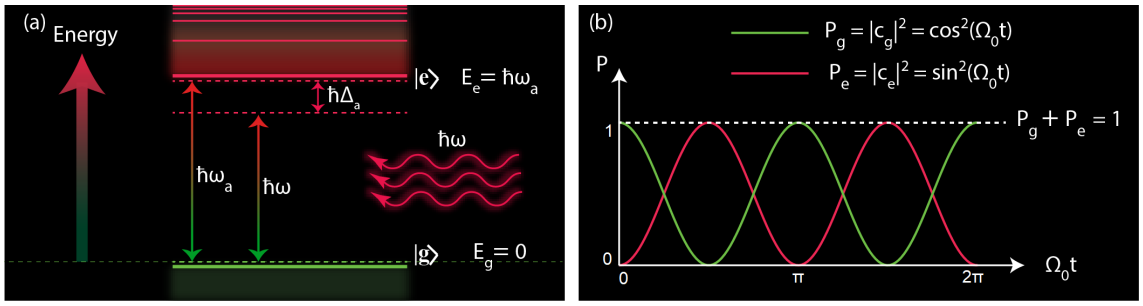

Figure 3.2: (a) Energy level illustration of a two-level atom interacting with an externally incident coherent electromagnetic field (b) Population probability oscillations of the same two level atom at Rabi frequency Ω_0

Multiplying both sides of (3.7a) and (3.7b) by $\langle g|$ and $\langle e|$ respectively, we can arrive at, $\mathcal{H}_a |g\rangle \langle g| = E_g |g\rangle \langle g|$ and $\mathcal{H}_a |e\rangle \langle e| = E_e |e\rangle \langle e|$. By adding these equations together and utilizing the completeness relation of the basis ($|g\rangle \langle g| + |e\rangle \langle e| = I$, where I is the identity matrix), we arrive at the Hamiltonian of the unperturbed two level atom,

$$\mathcal{H}_a = E_g |g\rangle \langle g| + E_e |e\rangle \langle e| , \tag{3.8}$$

which will take the following form in the matrix representation,

$$\mathcal{H}_a = \begin{pmatrix} E_g & 0 \\ 0 & E_e \end{pmatrix} . \tag{3.9}$$

Throughout this work, as we are concerned of the energy differences in the system, we choose the zero energy level of our atom to lie in the close vicinity of E_g. Hence the unperturbed atomic Hamiltonian would take the form,

$$\hat{\mathcal{H}}_a \approx \hbar\omega_{\mathrm{qd}} |e\rangle \langle e| , \tag{3.10}$$

given that the frequency separation between the ground and excited levels are defined as ω_{qd}.

3.2.2 Interaction with an Oscillating Electric Field

Let us now look at the interaction between a two level atom which is modeled quantum mechanically and an oscillating coherent electric field which is modeled classically, as depicted in Fig. 3.2(a). The system Hamiltonian for this scenario would take the form,

$$\hat{\mathcal{H}} = \hat{\mathcal{H}}_a + \hat{\mathcal{H}}_{\text{int}}, \tag{3.11}$$

where $\hat{\mathcal{H}}_a$ is the unperturbed atomic Hamiltonian we derived earlier and,

$$\hat{\mathcal{H}}_{\text{int}} = -\hat{\boldsymbol{d}}.\vec{\boldsymbol{E}} \tag{3.12}$$

is the dipole interaction energy between the atom. The externally incident field is denoted by $\vec{\boldsymbol{E}} = E_0 \cos(\omega t)\hat{z}$ and the transition dipole moment is $\hat{\boldsymbol{d}}$ [76,77]. As appropriate to transitions between states of definite parity, the diagonal elements of the dipole moment operator are obtainable as $\langle g|\,\hat{\boldsymbol{d}}\,|g\rangle = \mu_{gg}$ and $\langle e|\,\hat{\boldsymbol{d}}\,|e\rangle = \mu_{ee}$ would both be zero. The dipole moment operator would be characterized by its off diagonal matrix elements $\mu_{eg} = \langle e|\,\hat{\boldsymbol{d}}\,|g\rangle = \mu_{ge} = \langle g|\,\hat{\boldsymbol{d}}\,|e\rangle = \mu$ due to atomic symmetry [77].

Exploiting the completeness relation of the basis vectors ($|g\rangle\langle g| + |e\rangle\langle e| = I$) on (3.12), we can write,

$$\hat{\mathcal{H}}_{\text{int}} = -\{|g\rangle\langle g| + |e\rangle\langle e|\}\hat{\boldsymbol{d}}.\vec{\boldsymbol{E}}\{|g\rangle\langle g| + |e\rangle\langle e|\}, \tag{3.13}$$

the expansion of which yields,

$$\hat{\mathcal{H}}_{\text{int}} = -\{|g\rangle\langle g|\,\hat{\boldsymbol{d}}\,|g\rangle\langle g| + |e\rangle\langle e|\,\hat{\boldsymbol{d}}\,|g\rangle\langle g| + |g\rangle\langle g|\,\hat{\boldsymbol{d}}\,|e\rangle\langle e| + |e\rangle\langle e|\,\hat{\boldsymbol{d}}\,|e\rangle\langle e|\}.\vec{\boldsymbol{E}}.$$

Using $\langle g|\,\hat{\boldsymbol{d}}\,|g\rangle = \langle e|\,\hat{\boldsymbol{d}}\,|e\rangle = 0$ and $\langle e|\,\hat{\boldsymbol{d}}\,|g\rangle = \langle g|\,\hat{\boldsymbol{d}}\,|e\rangle = \mu$, we obtain,

$$\hat{\mathcal{H}} \approx \hbar\omega_{\text{qd}}\,|e\rangle\langle e| + \mu E_0\{|e\rangle\langle g| + |g\rangle\langle e|\}\cos(\omega t). \tag{3.15}$$

By adding and subtracting $\hbar\omega \left|e\right\rangle \left\langle e\right|$ to the RHS of (3.15) we can arrive at,

$$\hat{\mathcal{H}} \approx \hbar\omega \left|e\right\rangle \left\langle e\right| + \hbar\Delta_{\mathrm{qd}} \left|e\right\rangle \left\langle e\right| + \mu E_0 \{\left|e\right\rangle \left\langle g\right| + \left|g\right\rangle \left\langle e\right|\} \cos(\omega t), \tag{3.16}$$

where $\Delta_{\mathrm{qd}} = \omega_{\mathrm{qd}} - \omega$. We now perform the standard operation of moving the Schödinger picture Hamiltonian to the interaction picture in order to eliminate the non-perturbed component of the Hamiltonian. The Schrödinger picture defines states as time-dependent and operators as time-independent, whereas in the *interaction picture*, both operators and states carry a time dependence [78]. The transformation can be done as [79, 80],

$$\hat{\mathcal{H}}_I \approx e^{\mathrm{i}\hat{\mathcal{H}}_0 t/\hbar} \hat{\mathcal{V}} e^{-\mathrm{i}\hat{\mathcal{H}}_0 t/\hbar}, \tag{3.17}$$

where $\hat{\mathcal{H}}_0 = \hbar\omega \left|e\right\rangle \left\langle e\right|$ and $\hat{\mathcal{V}} = \hbar\Delta_{\mathrm{qd}} \left|e\right\rangle \left\langle e\right| + \mu E_0 \{\left|e\right\rangle \left\langle g\right| + \left|g\right\rangle \left\langle e\right|\} \cos(\omega t)$.

For an eigenstate $\left|k\right\rangle$ of $\hat{\mathcal{H}}_0$ with an eigenvalue E_k, where $\hat{\mathcal{H}}_0 \left|k\right\rangle = E_k \left|k\right\rangle$,

$$e^{\mathrm{i}\hat{\mathcal{H}}_0 t/\hbar} \left|k\right\rangle = \frac{\left(\frac{\mathrm{i}\hat{\mathcal{H}}_0 t}{\hbar}\right)^0}{0!} \left|k\right\rangle + \frac{\left(\frac{\mathrm{i}\hat{\mathcal{H}}_0 t}{\hbar}\right)^1}{1!} \left|k\right\rangle + \frac{\left(\frac{\mathrm{i}\hat{\mathcal{H}}_0 t}{\hbar}\right)^2}{2!} \left|k\right\rangle + ... = e^{\mathrm{i}E_k t/\hbar} \left|k\right\rangle \tag{3.18}$$

can be obtained by repeatedly applying the eigenvalue relations. Similarly, it is straightforward to show that,

$$e^{-\mathrm{i}\hat{\mathcal{H}}_0 t/\hbar} \left|k\right\rangle = e^{-\mathrm{i}E_k t/\hbar} \left|k\right\rangle. \tag{3.19}$$

From the adjoints [81] of (3.18) and (3.19),

$$\left\langle k\right| e^{\mathrm{i}\hat{\mathcal{H}}_0 t/\hbar} = \left\langle k\right| e^{\mathrm{i}E_k t/\hbar} \tag{3.20a}$$

$$\left\langle k\right| e^{-\mathrm{i}\hat{\mathcal{H}}_0 t/\hbar} = \left\langle k\right| e^{-\mathrm{i}E_k t/\hbar}. \tag{3.20b}$$

According to the above formulations, when $\left|e\right\rangle$ and $\left|g\right\rangle$ are eigenstates of $\hat{\mathcal{H}}_0$

with eigenvalues $E_1 \approx \hbar\omega$ and $E_2 \approx 0$ respectively, we can obtain the following eigenvalue equations for our two-level atomic model,

$$e^{\pm \mathrm{i}\hat{\mathcal{H}}_0 t/\hbar} |e\rangle = e^{\pm \mathrm{i}\omega t} |e\rangle , \tag{3.21a}$$

$$\langle e| e^{\pm i\hat{\mathcal{H}}_0 t/\hbar} = \langle e| e^{\pm \mathrm{i}\omega t}, \tag{3.21b}$$

$$e^{\pm \mathrm{i}\hat{\mathcal{H}}_0 t/\hbar} |g\rangle = |g\rangle , \tag{3.21c}$$

$$\langle g| e^{\pm \mathrm{i}\hat{\mathcal{H}}_0 t/\hbar} = \langle g| \tag{3.21d}$$

Exploiting the eigenvalue relations (3.21) to simplify (3.17) yields,

$$\hat{\mathcal{H}}_I = \hbar\Delta_{\mathrm{qd}} |e\rangle \langle e| + \frac{\mu E_0}{2}\{e^{\mathrm{i}\omega t} |e\rangle \langle g| + |g\rangle \langle e| e^{-\mathrm{i}\omega t}\} \left(e^{\mathrm{i}\omega t} + e^{-\mathrm{i}\omega t}\right) \tag{3.22}$$

Eliminating fast rotating (high frequency) terms that average to zero using the rotating wave approximation (RWA) [82], we arrive at the final interaction picture Hamiltonian of a two level atom interacting with a near-resonant classical optical field (in the absence of damping),

$$\hat{\mathcal{H}}_I = \hbar\Delta_{\mathrm{qd}} |e\rangle \langle e| + \hbar\Omega_0\{|e\rangle \langle g| + |g\rangle \langle e|\}, \tag{3.23}$$

where we have defined the Rabi frequency of the atom as $\Omega_0 = \mu E_0/(2\hbar)$ [5] (some authors like to define the same as $\Omega_0 = \mu E_0/\hbar$). Finally, the transformation of the Shrödinger picture state vector (3.5) to the interaction picture can be done as [80],

$$|\Psi(t)\rangle_I = e^{\mathrm{i}\hat{\mathcal{H}}_0 t/\hbar} |\Psi(t)\rangle_{\mathrm{s}} . \tag{3.24}$$

Due to our choice of eigen-energies where $E_g \approx 0$ and $E_e \approx \hbar\omega_{\mathrm{qd}}$, and the eigen value relations (3.21), the above equation simplifies to,

$$|\Psi(t)\rangle_I = c_g |g\rangle + c_e e^{-\mathrm{i}\Delta_{\mathrm{qd}} t} |e\rangle . \tag{3.25}$$

3.2.3 Rabi Oscillations

In the interaction picture, the states evolve as per the interaction part of the Hamiltonian such that [78],

$$i\hbar\frac{\partial}{\partial t}\left|\Psi(t)\right\rangle_I = \hat{H}_I(t)\left|\Psi(t)\right\rangle_I \tag{3.26}$$

By substituting for $\left|\Psi(t)\right\rangle_I$ and $\hat{\mathcal{H}}_I$ from (3.25) and (3.23) respectively, and assuming near-resonant conditions (vanishing detuning) we can arrive at,

$$i\frac{\partial}{\partial t}\{c_g\left|g\right\rangle + c_e\left|e\right\rangle\} = \Omega_0\left(c_g\left|e\right\rangle + c_e\left|g\right\rangle\right). \tag{3.27}$$

Equating the coefficients of $|e\rangle$ and $|g\rangle$ separately, we obtain,

$$\frac{\partial}{\partial t}c_g = -\mathrm{i}\Omega_0 c_e, \tag{3.28a}$$

$$\frac{\partial}{\partial t}c_e = -\mathrm{i}\Omega_0 c_g \tag{3.28b}$$

Differentiating (3.28) again and substituting from the same, we can obtain

$$\frac{\partial^2}{\partial^2 t}c_g = -\mathrm{i}\Omega_0^2 c_g, \tag{3.29a}$$

$$\frac{\partial^2}{\partial^2 t}c_e = -\mathrm{i}\Omega_0^2 c_e \tag{3.29b}$$

For the atom to be in the ground state, the coefficients should be of the form, $c_g = \cos(\Omega_0 t)$ and $c_e = \sin(\Omega_0 t)$. Thus, the state occupation probabilities can now be obtained as,

$$P_g = |c_g|^2 = \cos^2(\Omega_0 t), \tag{3.30a}$$

$$P_e = |c_e|^2 = \sin^2(\Omega_0 t). \tag{3.30b}$$

It is evident that the amplitude of the incident field determines the frequency of population oscillation or the Rabi frequency of the atom. This concept is graphically illustrated in Fig. 3.2(b). From this figure, we can observe that the coherent electric field incident on the two level atom causes population probability oscillations with periodic time π/Ω_0. Moreover, application of the external field for half the periodic time leads to complete population inversion.

3.3 Overview of Multi-Level Atoms

According to the theory of coherent dynamics, the level populations of N-level atoms oscillate at $N-1$ Rabi frequencies [83, 84]. In the *quasi-static* limit where temporal phase variations are neglected, the atomic transition from level $i-1$ to i is assumed to be induced by near resonant radiation of magnitude $E_i = E_{i0}\cos(\omega_i t)$. E_{i0} denotes the amplitude of the ith field whereas ω_i denotes the corresponding angular frequency. Within the electric dipole approximation, the Hamiltonian of an $N-$level atom which interacts with $N-1$ near resonant coherent electric fields can be written as [84, 85],

$$\hat{\mathcal{H}}_{\mathrm{N}} = \hat{\mathcal{H}}_0 - \sum_{i=1}^{N-1} \mu_i E_i, \tag{3.31}$$

where $\hat{\mathcal{H}}_0$ is the unperturbed atomic Hamiltonian and μ_i is the ith dipole moment.

As we are mostly concerned of coherent monochromatic electric fields nearly resonant with the plasmonic resonance, we use the two level atomic description to model the quantum dots in our exciton-plasmon nanohybrids.

Chapter 4

Density Matrix Theory and Open Quantum Systems

Before we move into our detailed analysis of exciton-plasmon nanohybrids where initially the QD, and consequently the entire MNP-QD nanohybrid, will be modeled as quantum mechanical systems, it is important to get a glimpse of a powerful tool used throughout our work. This section will outline the basics of the density matrix and its time evolution needed for the analytical models built in the chapters that follow.

4.1 Density Matrix Theory

Suppose a statistical mixture comprises an ensemble of quantum systems with independently prepared states $|\Psi_n\rangle$, where $n = 1, 2, 3...$ with corresponding statistical weights W_n. The states $|\Psi_n\rangle$ need not necessarily form an orthonormal set. The statistical operator $\hat{\rho}$, also known as the density matrix, for a mixture of this form is obtained as [86],

$$\hat{\rho} = \sum_n W_n |\Psi_n\rangle \langle\Psi_n| . \tag{4.1}$$

The selection of a convenient basis $\{|\psi_1\rangle, |\psi_2\rangle, |\psi_3\rangle ...\}$ which fulfills the su-

perposition principle such that,

$$|\Psi_n\rangle = \sum_{m'} a_{m'}^{(n)} |\psi_{m'}\rangle , \tag{4.2a}$$

$$\langle\Psi_n| = \sum_{m} \{a_m^{(n)}\}^* , \langle\psi_m| , \tag{4.2b}$$

enables recasting (4.1) as [86],

$$\hat{\rho} = \sum_{mm'} W_n a_{m'}^{(n)} \{a_m^{(n)}\}^* |\psi_{m'}\rangle \langle\psi_m| . \tag{4.3}$$

As W_n represents the probability of finding the system in the state $|\Psi_n\rangle$, and as $\left|a_m^{(n)}\right|^2$ represents the probability of finding $|\Psi_n\rangle$ in $|\psi_m\rangle$, the probability of finding the system in basis state $|\psi_m\rangle$ can be found using the corresponding diagonal element ρ_{mm} of the density matrix such that [86],

$$\rho_{mm} = \sum_{n} W_n \left|a_m^{(n)}\right|^2 . \tag{4.4}$$

The density matrix $\hat{\rho}$ is a Hermitian operator. Moreover, it can be used to obtain the expectation value of any operator $\hat{Q}$ using the trace of the product of $\hat{\rho}$ and $\hat{Q}$ as,

$$\langle\hat{Q}\rangle = \mathrm{Tr}\left(\hat{\rho}\hat{Q}\right) , \tag{4.5}$$

The density matrix is said to contain all physically significant information of a quantum mechanical system as it can be used to obtain the expectation value of any operator as above [5, 86].

For a quantum mechanical system in a pure state $|\psi\rangle$, the density operator is obtainable as,

$$\hat{\rho} = |\psi\rangle \langle\psi| , \tag{4.6}$$

and a sufficient and necessary condition for a given density matrix $\hat{\rho}$ to describe

a pure system is given by [86],

$$\mathrm{Tr}\left(\hat{\rho}^2\right) = (\hat{\rho})^2 . \tag{4.7}$$

Such pure states $|\psi\rangle$ can always be expressed as a linear or completely coherent superposition of basis states.

4.2 Time Evolution of the Density Matrix

4.2.1 Time Evolution in the Schrödinger picture

The time evolution of a quantum mechanical state $\Psi(t)$ can be described by the Schrödinger equation [79,86,87],

$$\mathrm{i}\hbar\frac{\partial}{\partial t}|\Psi(t)\rangle = \hat{\mathcal{H}}\,|\Psi(t)\rangle\,, \tag{4.8}$$

where $\hat{\mathcal{H}}$ and $\Psi(t)$ are the system Hamiltonian and the state in the Schrödinger picture. Using the quantum mechanical adjoint of (4.8), we obtain [81],

$$-\mathrm{i}\hbar\frac{\partial}{\partial t}\langle\Psi(t)| = \langle\Psi(t)|\,\hat{\mathcal{H}}, \tag{4.9}$$

Obtaining the time derivative of (4.1) using the product differential rule,

$$\begin{aligned}\frac{\partial}{\partial t}\hat{\rho} &= \sum_{\mathrm{n}} W_{\mathrm{n}}\frac{\partial}{\partial t}\left(|\Psi_{\mathrm{n}}(t)\rangle\langle\Psi_{\mathrm{n}}(t)|\right)\\ &= \sum_{\mathrm{n}} W_{\mathrm{n}}\left\{\left(\frac{\partial}{\partial t}|\Psi_{\mathrm{n}}(t)\rangle\right)\langle\Psi_{\mathrm{n}}(t)| + |\Psi_{\mathrm{n}}(t)\rangle\left(\frac{\partial}{\partial t}\langle\Psi_{\mathrm{n}}(t)|\right)\right\}\end{aligned}$$

Substituting from (4.8) and (4.9),

$$\frac{\partial}{\partial t}\hat{\rho} = \sum_{\mathrm{n}} W_{\mathrm{n}}\left\{-\frac{\mathrm{i}}{\hbar}\hat{\mathcal{H}}\,|\Psi_{\mathrm{n}}(t)\rangle\langle\Psi_{\mathrm{n}}(t)| + \frac{\mathrm{i}}{\hbar}|\Psi_{\mathrm{n}}(t)\rangle\langle\Psi_{\mathrm{n}}(t)|\,\hat{\mathcal{H}}\right\}$$

$$= -\frac{\mathrm{i}}{\hbar}\left\{\hat{\mathcal{H}}\hat{\rho} - \hat{\rho}\hat{\mathcal{H}}\right\}.$$

Using the standard notation for commutation operation, we arrive at [5],

$$\frac{\partial}{\partial t}\hat{\rho} = -\frac{\mathrm{i}}{\hbar}\left[\hat{\mathcal{H}}, \hat{\rho}\right]. \tag{4.12}$$

where $\hat{\rho}$ is the system density matrix/operator in the Schrödinger picture.

4.2.2 Moving to the Interaction Picture

Let us now assume that the total system Hamiltonian under a small external time-dependent perturbation can be written in the form,

$$\hat{\mathcal{H}}(t) = \hat{\mathcal{H}}_0 + \hat{\mathcal{V}}(t). \tag{4.13}$$

It is assumed that $\hat{\mathcal{H}}_0$ is time-independent and $\hat{\mathcal{V}}(t)$ is caused by a coherent external electric field incident on the system which causes transitions between the eigenstates of $\hat{\mathcal{H}}_0$. The state vectors of the system in the Schrödinger and interaction pictures are related such that [86],

$$|\Psi(t)\rangle = e^{-(\mathrm{i}/\hbar)\hat{\mathcal{H}}_0 t}\,|\Psi(t)\rangle_{\mathrm{I}}. \tag{4.14}$$

Thus, using the Schrödinger equation (4.8) with (4.14) for a Hamiltonian of the form (4.13) yields,

$$\mathrm{i}\hbar\frac{\partial}{\partial t}\left\{e^{-(\mathrm{i}/\hbar)\hat{\mathcal{H}}_0 t}\,|\Psi(t)\rangle_{\mathrm{I}}\right\} = \left\{\hat{\mathcal{H}}_0 + \hat{\mathcal{V}}(t)\right\} e^{-(\mathrm{i}/\hbar)\hat{\mathcal{H}}_0 t}\,|\Psi(t)\rangle_{\mathrm{I}}. \tag{4.15}$$

By simplifying the above equation, we can finally obtain the the equation for time evolution of the interaction picture state vector $|\Psi(t)\rangle_{\mathrm{I}}$,

$$\mathrm{i}\hbar\frac{\partial}{\partial t}|\Psi(t)\rangle_{\mathrm{I}} = \hat{\mathcal{V}}_{\mathrm{I}}(t)\,|\Psi(t)\rangle_{\mathrm{I}}\,, \tag{4.16}$$

where $\hat{\mathcal{V}}_{\mathrm{I}}(t) = e^{(\mathrm{i}/\hbar)\hat{\mathcal{H}}_0 t}\hat{\mathcal{V}}(t)e^{-(\mathrm{i}/\hbar)\hat{\mathcal{H}}_0 t}$. From (4.16) it is evident that the time dependence of $|\Psi(t)\rangle_{\mathrm{I}}$ is entirely caused by the external perturbation $\hat{\mathcal{V}}(t)$. Moreover, when $\hat{\mathcal{V}}(t)$ is small compared to $\hat{\mathcal{H}}_0$, $|\Psi(t)\rangle$ will slowly vary against time, enabling (4.16) to possess an approximate solution with time-dependent perturbation theory which is more practically calculable compared to its Schrödinger picture counterpart. Such solvability is achieved due to the removal of rapidly varying factors due to the Hamiltonian component $\hat{\mathcal{H}}_0$ from the system states [86].

Applying the unitary transformations (4.18) and (4.14) to the Schrödinger picture density operator and states in (4.1) yields,

$$\hat{\rho}_{\mathrm{I}}(t) = \sum_{\mathrm{n}} W_{\mathrm{n}}\,|\Psi_{\mathrm{n}}(t)\rangle_{\mathrm{I}}\,\langle\Psi_{\mathrm{n}}(t)|_{\mathrm{I}} \tag{4.17}$$

As an operator $\hat{\mathcal{O}}(t)$ in the Schrödinger picture can be transformed to the interaction picture using the following transformation,

$$\hat{\mathcal{O}}(t)_{\mathrm{I}} = e^{(\mathrm{i}/\hbar)\hat{\mathcal{H}}_0 t}\hat{\mathcal{O}}(t)e^{-(\mathrm{i}/\hbar)\hat{\mathcal{H}}_0 t}, \tag{4.18}$$

we can substitute $\hat{\rho}(t) = e^{-(\mathrm{i}/\hbar)\hat{\mathcal{H}}_0 t}\hat{\rho}_{\mathrm{I}}(t)e^{(\mathrm{i}/\hbar)\hat{\mathcal{H}}_0 t}$ to obtain the *Liouville equation* in the interaction picture (see appendix C.1),

$$\frac{\partial}{\partial t}\hat{\rho}_{\mathrm{I}}(t) = -\frac{\mathrm{i}}{\hbar}\left[\hat{\mathcal{V}}_{\mathrm{I}}(t), \hat{\rho}_{\mathrm{I}}(t)\right]. \tag{4.19}$$

In the chapters that follow, both Schrödinger and interaction picture interpretations presented above would be used interchangeably for the ease of calculation.

Up to this point, our concern was focused on *closed quantum systems* which are assumed to be isolated from the external environment. However, realistic modeling mandates taking the environmental influences, such as bath induced excitations, decays and dephasing, into account [2]. Thus, the next section will focus on *open quantum systems* which interact with the submerging environment.

4.3 Open Quantum Systems

A realistic quantum system would be in continuous contact with its environment, which leads to changes in the system properties such as energy and polarization. The gradual evolution of a system initially in a non-equilibrium state, to a state of equilibrium determined by external environmental (bath) conditions (such as temperature) is known as a *relaxation process*. Unlike the Schrödinger and Liouville equations which denote fundamental equations of motion of closed quantum systems, such relaxation phenomena represent irreversible processes attributable to open quantum systems [86]. Two popular approaches of modeling the time evolution of the system density matrix in the presence of such irreversible phenomena are, the *Lindblad* and *Redfield* formalisms.

4.3.1 The Lindblad Formalism

The *Lindblad equation* [88] is a versatile tool usable for the treatment of irreversible and non-unitary evolutions ranging from dissipation and decoherence to quantum measurements [87, 89]. It is considered the "workhorse of open quantum systems" due to its well-behaved mathematical properties and relative simplicity [90]. A common example relevant to our context would be the modeling of spontaneous emission of a two-level atom using the Lindblad formalism. Lindblad terms in the time-evolution of an open quantum system represent effects

caused by the system-bath interaction, and they naturally arise as a consequence of the Markov approximation. For a detailed derivation of the emergence of Lindbladians, the reader is referred to [89]. The current section of the thesis will only outline the summary required by the subsequent exciton-plasmon models.

The general form of the Lindblad equation is [2, 13, 89],

$$\frac{\partial}{\partial t}\hat{\rho}_{\text{sys}} = -\frac{\mathrm{i}}{\hbar}\left[\hat{\mathcal{H}}_{\text{sys}}, \hat{\rho}_{\text{sys}}\right] + \sum_j \lambda_j \left(2\hat{L}_j \hat{\rho}_{\text{sys}} \hat{L}_j^\dagger - \left\{\hat{L}_j^\dagger \hat{L}_j, \hat{\rho}_{\text{sys}}\right\}\right), \tag{4.20}$$

where $\hat{\rho}_{\text{sys}}$ and $\hat{\mathcal{H}}_{\text{sys}}$ are the density matrix and the relevant Hamiltonian of the quantum system under study, which should be appropriately selected pertaining to our earlier discussions. For given two system operators $\hat{\mathcal{A}}$ and $\hat{\mathcal{B}}$, $\{\hat{\mathcal{A}}, \hat{\mathcal{B}}\} = \hat{\mathcal{A}}\hat{\mathcal{B}} + \hat{\mathcal{B}}\hat{\mathcal{A}}$ denotes the anti-commutation. The system operators $\hat{L}_j$ are called Lindblad operators and the factors λ_j represent system parameters attributable to relevant relaxation processes.

It can be readily observed that the first term on the RHS resembles the unitary evolution of the density operator which we discussed in the previous sections. If the Lindblad operators, $\hat{L}_j$ represent Hermitian observables, the above Lindblad equation is usable to model the measurement processes. When $\hat{L}_j$ represent non-Hermitian operators such as an excitation annihilation operator, it is usable to model phenomena such as dissipation, decay or decoherence [89].

From the general equation (4.20), we can observe that for a given system operator $\hat{L}_j$, the Lindblad term $\mathcal{L}(\hat{L}_j)$ can be expanded as follows,

$$\mathcal{L}(\hat{L}) = \lambda_j \left(2\hat{L}_j \hat{\rho}_{\text{sys}} \hat{L}_j^\dagger - \hat{L}_j^\dagger \hat{L}_j \hat{\rho}_{\text{sys}} - \hat{\rho}_{\text{sys}} \hat{L}_j^\dagger \hat{L}_j\right), \tag{4.21}$$

which accounts for the contribution of one relaxation process.

Having obtained the general idea, let us now walk through a specific example of the Lindblad equation relevant to the context of this thesis, in order to obtain a deeper understanding of the concept. Consider the example of a two-level atom

which is allowed to have three types of interactions with the submerging bath, namely, incoherent decay of the excited state into the atomic ground state, bath induced incoherent excitation of the ground to excited state and bath induced elastic scattering processes.

Let $\hat{\sigma}$ be the ladder operator which causes transition from the atomic excited state to the ground state. Quantum mechanical master equation for the atom, modeled as an open quantum system, with Lindblad terms for each of the three aforementioned interactions takes the form [5],

$$\frac{\partial}{\partial t}\hat{\rho}_{\text{sys}} = -\frac{\mathrm{i}}{\hbar}\left[\hat{\mathcal{H}}_{\text{sys}}, \hat{\rho}_{\text{sys}}\right] + \lambda_1\mathcal{L}(\hat{\sigma}) + \lambda_2\mathcal{L}(\hat{\sigma}^\dagger) + \lambda_3\mathcal{L}(\hat{\sigma}^\dagger\hat{\sigma}). \tag{4.22}$$

In the above equation $\lambda_1\mathcal{L}(\hat{\sigma})$, $\lambda_2\mathcal{L}(\hat{\sigma}^\dagger)$ and $\lambda_3\mathcal{L}(\hat{\sigma}^\dagger\hat{\sigma})$ are attributable to the three relaxation processes; bath induced decay, bath induced excitation and elastic scattering, respectively.

Using (4.21), (4.22) can be expanded as,

$$\begin{aligned}\frac{\partial}{\partial t}\hat{\rho}_{\text{sys}} = -\frac{\mathrm{i}}{\hbar}\left[\hat{\mathcal{H}}_{\text{sys}}, \hat{\rho}_{\text{sys}}\right] + \lambda_1\left(2\hat{\sigma}\hat{\rho}_{\text{sys}}\hat{\sigma}^\dagger - \hat{\sigma}^\dagger\hat{\sigma}\hat{\rho}_{\text{sys}} - \hat{\rho}_{\text{sys}}\hat{\sigma}^\dagger\hat{\sigma}\right) + \\ \lambda_2\left(2\hat{\sigma}^\dagger\hat{\rho}_{\text{sys}}\hat{\sigma} - \hat{\sigma}\hat{\sigma}^\dagger\hat{\rho}_{\text{sys}} - \hat{\rho}_{\text{sys}}\hat{\sigma}\hat{\sigma}^\dagger\right) + \\ \lambda_3\left(2\hat{\sigma}^\dagger\hat{\sigma}\hat{\rho}_{\text{sys}}\hat{\sigma}^\dagger\hat{\sigma} - \hat{\sigma}^\dagger\hat{\sigma}\hat{\rho}_{\text{sys}} - \hat{\rho}_{\text{sys}}\hat{\sigma}^\dagger\hat{\sigma}\right)\end{aligned} \tag{4.23}$$

where we have use the simplification $(\hat{\sigma}^\dagger\hat{\sigma})(\hat{\sigma}^\dagger\hat{\sigma}) = \hat{\sigma}^\dagger\hat{\sigma}$ for $\hat{\sigma} = |g\rangle\langle e|$.

4.3.2 Bloch-Redfield Formalism

A summary of the Bloch-Redfield formalism is presented below to provide a complete picture of the density matrix and its time evolution in our background study. Readers are referred to [90] for a thorough understanding of the derivation and details. The Bloch-Redfield Formalism assumes a system-bath Hamiltonian of

the form,

$$\hat{\mathcal{H}}_{\text{sys-bath}} = \hat{\mathcal{H}}_{\text{sys}} + \hat{\mathcal{H}}_{\text{bath}} + \hat{\mathcal{H}}_{\text{int-SB}}, \tag{4.24}$$

where $\hat{\mathcal{H}}_{\text{sys}}$ is the Hamiltonian of the quantum system of our interest, $\hat{\mathcal{H}}_{\text{bath}}$ denotes the Hamiltonian of the submerging bath and $\hat{\mathcal{H}}_{\text{int-SB}}$ is the Hamiltonian attributable to the interaction between the system and bath which takes the form,

$$\hat{\mathcal{H}}_{\text{int-SB}} = \sum_j \hat{s}_j \hat{B}_j. \tag{4.25}$$

Bath operators and system operators are denoted by $\hat{B}_j$ and $\hat{s}_j$, respectively. It is assumed that the eigenstates of the system Hamiltonian $\hat{\mathcal{H}}_{\text{sys}} \left|\psi_{\text{sys}}\right\rangle_{\text{n}} = E_{\text{n}} \left|\psi_{\text{sys}}\right\rangle_{\text{n}}$ are connected to an arbitrary basis $\left|\phi\right\rangle_{\text{n}}$ by the transformation matrix,

$$\hat{V} = \sum_{\text{n}} \left|\psi_{\text{sys}}\right\rangle_{\text{n}} \left\langle\phi\right|_{\text{n}}. \tag{4.26}$$

For the system described above, the general and compact form of the Bloch-Redfield equations is given by [90],

$$\frac{\partial}{\partial t}\hat{\rho}_{\text{sys}} = -\frac{\text{i}}{\hbar}\left[\hat{\mathcal{H}}_{\text{sys}}, \hat{\rho}_{\text{sys}}\right] + \frac{1}{\hbar^2}\sum_{j,k}\big(- \hat{s}_j \hat{V}\hat{r}_{jk}\hat{V}^\dagger\hat{\rho}_{\text{sys}} + \hat{V}\hat{r}_{jk}\hat{V}^\dagger\hat{\rho}_{\text{sys}}\hat{s}_j - \hat{\rho}_{\text{sys}}\hat{V}\hat{q}_{jk}\hat{V}^\dagger\hat{s}_j + \hat{s}_j\hat{\rho}_{\text{sys}}\hat{V}\hat{q}_{jk}\hat{V}^\dagger\big) \tag{4.27}$$

where $\hat{r}_{jk}$ and $\hat{q}_{jk}$ are obtained such that they abide by the relationships,

$$\left\langle\phi\right|_{\text{n}} \hat{r}_{jk} \left|\phi\right\rangle_{\text{m}} = \left\langle\phi\right|_{\text{n}} \hat{V}^\dagger \hat{s}_k \hat{V} \left|\phi\right\rangle_{\text{m}} \frac{1}{2} C_{jk}(E_{\text{m}} - E_{\text{n}}), \tag{4.28a}$$

$$\left\langle\phi\right|_{\text{n}} \hat{q}_{jk} \left|\phi\right\rangle_{\text{m}} = \left\langle\phi\right|_{\text{n}} \hat{V}^\dagger \hat{s}_k \hat{V} \left|\phi\right\rangle_{\text{m}} \frac{1}{2} C_{kj}(E_{\text{n}} - E_{\text{m}}), \tag{4.28b}$$

$$C_{jk}(\omega) = \int_{-\infty}^{\infty} d\tau e^{i\omega\tau} \langle \tilde{B}_j(\tau)\tilde{B}_k(0)\rangle. \tag{4.28c}$$

where the Fourier transform of the correlation function in the interaction picture $\left(\tilde{B}_j(\tau) = e^{\mathrm{i}\hat{B}\tau}\hat{B}_j e^{-\mathrm{i}\hat{B}\tau}\right)$ is used to obtain the spectral function $C_{jk}(\omega)$ which characterizes the submerging bath.

Bloch-Redfield formalism does not guarantee the positivity of the density matrix and is computationally complex compared to the Lindblad formalism [91]. Thus, the Lindblad formalism presented in the earlier section was selected to model the relaxation processes included in the chapters that follow.

Chapter 5
Analytical Study of Exciton Behaviour in a Plasmonic Near Field

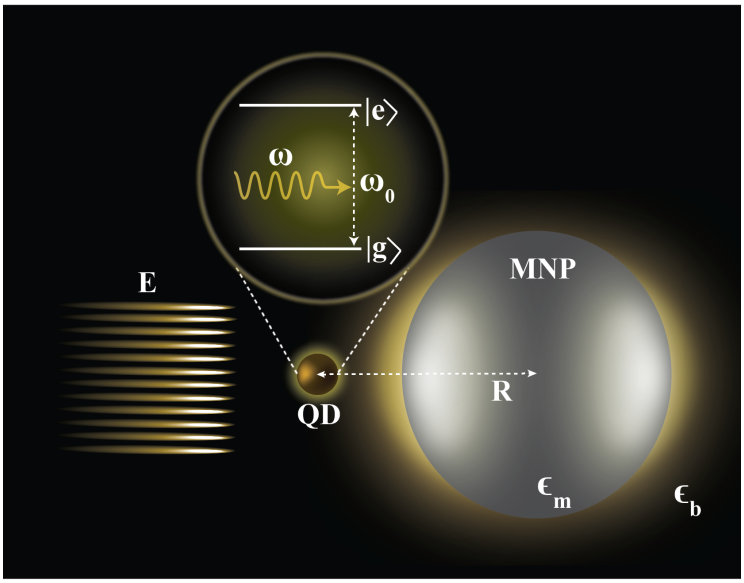

Figure 5.1: The schematic diagram of a quantum dot (QD) in the vicinity of a metal nanoparticle (MNP). The MNP-QD nanohybrid is illuminated by a coherent external electric field with magnitude E and angular frequency ω. The exciton in the QD undergoes dipole interaction with the coherent external drive and the near field of the localized surface plasmon resonances in the MNP. The bare excitonic energy of the QD is $\hbar\omega_{\mathrm{qd}}$. The MNP-QD centre separation distance is R. The dielectric permittivities of the MNP and the host medium are ϵ_{m} and ϵ_{b}, respectively.

The objective of this chapter is to analytically characterize the influence of a neighboring metal MNP on the behavioral trends of a QD using a GNOR method

based approach, taking the MNP distance dependent modifications to the QD population relaxation and dephasing rates into account. As it was discussed earlier, the GNOR model is a recent generalization and an extension of the hydrodynamic Drude model (HDM), which goes beyond the HDM by taking into account, both the convection current and electron diffusion in the MNPs. It allows unified theoretical explanation of some experimentally observed plasmonic phenomena which otherwise would require *ab initio* analysis as the conventional local response approximation (LRA) fails to account for them. Attempts to incorporate MNP nonlocal effects in the analytical characterization of vicinal excitons found in literature [92] utilize the phenomenological hydrodynamic model and assume the absence of MNP inter-band effects. Moreover, they are only applicable to narrow parameter regions [13].

This chapter presents a complete analytical characterization which overcomes these drawbacks and lends to the perusal of the system over wide continua of various parameters, enabling to get an elevated view at a much lesser level of complexity compared to the conventional LRA based numerical methods or the *ab initio* methods of accounting for the nonlocal effects.

5.1 Model Overview

Let us consider an MNP-QD hybrid nanosystem consisting of an MNP with radius r_{m} and a QD with a relatively negligible radius, separated by a distance R, as depicted in Fig. 5.1. Throughout this chapter, bold fonts, hat notation, tilde notation and bolded hat notation are used to indicate vectors, quantum mechanical operators, slowly varying amplitudes and unit vectors, respectively.

The system is submerged in an environment of relative permittivity ϵ_{b} and experiences an externally applied coherent electric field $\vec{E} = \hat{z}E_0(e^{-\mathrm{i}\omega t} + e^{\mathrm{i}\omega t})/2 = \hat{z}E$, where i is the imaginary unit, ω is the angular frequency and $\hat{z}$ is a unit vector

along or perpendicular to the MNP-QD axis. The direction of the incident field is chosen to be parallel/perpendicular to the axis of the MNP-QD system. All distances are assumed to be small enough for the retardation effects to be ignored and ephemeral thermal effects [93, 94] are assumed to be negligible in the model.

When the QD is irradiated with an external field nearly resonant with the energy gap between its valence and the first conduction bands, a bound electron-hole pair (an exciton) is created [95]. The QD is modeled as a spherical semiconductor with a dielectric constant ϵ_s, containing a two-level atom-like quantum system (exciton) at the centre. This is a good approximation when studying optical processes at frequencies that are nearly resonant with the frequency corresponding to the lowest excitonic transition energy of the QD [96, 97]. The dipole moment operator element of the QD is denoted by μ and the bare excitonic energy is $\hbar\omega_{\text{qd}}$.

In cases where inter-band effects are absent and only the conduction band electrons contribute to the optical properties of the material, it can be assumed that that $\epsilon_{\text{core}} = 1$, following the usual procedure in literature [92]. However, in common plasmonic material such as gold and silver, inter-band transitions play an important role in determining the plasmonic response. Therefore, this work uses a Drude-like dielectric function $\epsilon_{\text{m}}(\omega)$ which takes the inter-band effects of the MNP into account, pertaining to our discussions in Sec. 2.2.

5.2 The Quantum Dot as an Open Quantum System

Let $\hat{\sigma} = |g\rangle\langle e|$ and $\hat{\sigma}^{\dagger} = |e\rangle\langle g|$ be the exciton creation and annihilation operators, where $|g\rangle$ and $|e\rangle$ are the energy eigen vectors of the unperturbed atomic Hamiltonian representing the exciton ground and excited states, respectively.

Using (3.11) and (3.12), Hamiltonian of the QD under the influence of the

MNP and the externally applied electric field can be given as [23, 98–100],

$$\hat{\mathcal{H}}_{\mathrm{qd}} = \hbar\omega_{\mathrm{qd}}\hat{\sigma}^{\dagger}\hat{\sigma} - E_{\mathrm{qd}}\mu\left(\hat{\sigma} + \hat{\sigma}^{\dagger}\right) \tag{5.1}$$

where E_{qd} is the (magnitude of) the total electric field experienced by the exciton at the centre of QD. We model dipolar polarizability of the MNP using the GNOR based approach presented in Sec 2.2. In this context the LRA based dipolar polarizability β_{LRA} of the conventional dipole response model is replaced by β_{NL}. E_{qd} comprises the influence of the externally incident coherent illumination E and the dipole response field of the vicinal MNP at the QD location given by [2],

$$E_{\mathrm{res}} = \frac{s_{\alpha}P_{\mathrm{mnp}}}{(4\pi\epsilon_0\epsilon_{\mathrm{b}}R^3)}, \tag{5.2}$$

where ϵ_0 denotes the free space permittivity, $s_{\alpha} = 2(-1)$ is an orientation parameter which indicates that the external field is parallel(perpendicular) to the axis connecting the MNP and QD centres.

The field experienced by the quantum system at the centre of the QD will be screened due to ϵ_{s} such that $E_{\mathrm{qd}} = (E + E_{\mathrm{res}})/\epsilon_{\mathrm{effS}}$ where $\epsilon_{\mathrm{effS}} = (2\epsilon_{\mathrm{b}} + \epsilon_{\mathrm{s}})/3\epsilon_{\mathrm{b}}$ [23]. Magnitude of the MNP polarizarion denoted by P_{mnp} is given by [5, 13],

$$P_{\mathrm{mnp}} = 4\pi\epsilon_0\epsilon_{\mathrm{b}}{r_{\mathrm{m}}}^3\left(\beta_{\mathrm{NL}}\tilde{E}^{+}_{\mathrm{mnp}}e^{-\mathrm{i}\omega t} + \beta^{*}_{\mathrm{NL}}\tilde{E}^{-}_{\mathrm{mnp}}e^{\mathrm{i}\omega t}\right) \tag{5.3}$$

where $\tilde{E}^{+}_{\mathrm{mnp}}$ and $\tilde{E}^{-}_{\mathrm{mnp}}$ are the positive and negative frequency coefficients of E_{mnp}, which is the electric field felt by the MNP, given by,

$$E_{\mathrm{mnp}} = E + \frac{1}{4\pi\epsilon_0\epsilon_{\mathrm{b}}}\frac{s_{\alpha}P_{\mathrm{qd}}}{\epsilon_{\mathrm{effS}}R^3} \tag{5.4}$$

with the QD polarization denoted as $P_{\mathrm{qd}} = \mu\left(\rho_{12} + \rho_{21}\right)$ [24, 101], using the off diagonal density matrix elements ρ_{12} and ρ_{21} of the QD. Both MNP and QD po-

larize along the incoming radiation $\vec{E}$. By factoring out the high frequency time dependence of the off diagonal density matrix elements of the QD where [5],

$$\rho_{12} = \tilde{\rho}_{12} e^{\mathrm{i}\omega t}, \tag{5.5a}$$

$$\rho_{21} = \rho_{12}^{*}, \tag{5.5b}$$

E_{qd} can be recast as,

$$E_{\mathrm{qd}} = \frac{\hbar}{\mu} \left\{ \Omega_{12}^{\mathrm{eff}} + \mathcal{G}\tilde{\rho}_{21} \right\} e^{-\mathrm{i}\omega t} + h.c. = \tilde{E}_{\mathrm{qd}}^{+} e^{-\mathrm{i}\omega t} + h.c. \tag{5.6}$$

Throughout this thesis, *h.c.* stands for hermitian conjugate. The Rabi frequency in the absence of quantum coherence is denoted by $\Omega_{12}^{\mathrm{eff}}$ [102] and $\mathcal{G}$ arises due to the MNP electric field component induced as a result of the QD dipole response field incident on the MNP, hence can be thought of as the self interaction of the QD [5]. These quantities can be obtained in terms of the MNP dipolar polarizability as [5, 13],

$$\Omega_{12}^{\mathrm{eff}} = \Omega_0 \left(1 + \frac{s_\alpha \beta_{\mathrm{NL}} {r_{\mathrm{m}}}^3}{R^3} \right) \tag{5.7a}$$

$$\mathcal{G} = \frac{s_\alpha^2 \beta_{\mathrm{NL}} {r_{\mathrm{m}}}^3 \mu^2}{4\pi\epsilon_0 \epsilon_{\mathrm{b}} \hbar \epsilon_{\mathrm{effS}}^2 R^6} \tag{5.7b}$$

where,

$$\Omega_0 = (\mu E_0)/(2\hbar\epsilon_{\mathrm{effS}}) \tag{5.8}$$

is the Rabi frequency of the bare external field when the MNP and QD are isolated (large R). The factor $1/\epsilon_{\mathrm{effS}}$ arises due to the screening of the externally incident field by the QD permittivity, as the excitonic system is assumed to form at the centre of the QD.

We obtain the effective or normalized Rabi frequency [103, 104] of the QD under the influence of both MNP and the external field using the effective field

incident on the QD exciton given by (5.6) as [102],

$$\Omega_{12}^{r} = \frac{\mu}{\hbar}\tilde{E}_{\mathrm{qd}}^{+} = \Omega_{12}^{\mathrm{eff}} + \mathcal{G}\tilde{\rho}_{21}, \tag{5.9}$$

where $\tilde{E}_{\mathrm{qd}}^{+}$ is the positive frequency coefficient of E_{qd}. Using the Rabi frequencies under bare external illumination and in the presence of the MNP, the coherent plasmonic field enhancement (CPFE) experienced by the excitonic system in the QD is defined as [29,105],

$$\mathrm{CPFE} = \frac{\left|\Omega_{12}^{r}\right|}{\Omega_{0}^{2}}. \tag{5.10}$$

The Hamiltonian of the QD given by equation (5.1) describes a closed quantum system where the effects of the environment are not yet taken into account. The QD couples with the environment, forming an open quantum system with irreversible dynamics [2].

Quantum dynamics of the system coupled with the environments can be accounted for by solving the following master equation for the QD density matrix $\hat{\rho}$ [5], which is assumed to take the form presented in (4.23) with $\hat{\rho}_{\mathrm{sys}} = \hat{\rho}$ and $\hat{\mathcal{H}}_{\mathrm{sys}} = \hat{\mathcal{H}}_{\mathrm{qd}}$ in the Schröinger picture. Matrix form of the aforementioned master equation in the basis space formed by $|g\rangle, |e\rangle$ reads (refer appendix D.1 for the derivation),

$$\begin{aligned}\frac{\partial}{\partial t}\hat{\rho} = \frac{\mathrm{i}}{\hbar}&\begin{bmatrix} -\mu E_{\mathrm{qd}}(\rho_{12}-\rho_{21}) & -\mu E_{\mathrm{qd}}(\rho_{11}-\rho_{22}) + \hbar\omega_{\mathrm{qd}}\rho_{12} \\ -\mu E_{\mathrm{qd}}(\rho_{22}-\rho_{11}) - \hbar\omega_{\mathrm{qd}}\rho_{21} & -\mu E_{\mathrm{qd}}(\rho_{21}-\rho_{12}) \end{bmatrix} \\ &- \begin{bmatrix} 2\lambda_2\rho_{11} - 2\lambda_1\rho_{22} & (\lambda_1+\lambda_2+\lambda_3)\rho_{12} \\ (\lambda_1+\lambda_2+\lambda_3)\rho_{21} & 2\lambda_1\rho_{22} - 2\lambda_2\rho_{11} \end{bmatrix}\end{aligned} \tag{5.11}$$

where the latter component is the relaxation matrix $\Gamma(\hat{\rho})$ of the quantum system. For optical frequencies, $\lambda_2 \approx 0$ even near room temperature [5]. Let,

$$\tau = 1/(2\lambda_1) \tag{5.12a}$$

$$T = 1/(\lambda_1 + \lambda_3). \tag{5.12b}$$

Using (5.12a), (5.12b) and $\rho_{11} + \rho_{22} = 1$,

$$\Gamma(\hat{\rho}) \approx \begin{bmatrix} (\rho_{11} - 1)/\tau & \rho_{12}/T \\ \rho_{21}/T & \rho_{22}/\tau \end{bmatrix} \tag{5.13}$$

where ρ_{mn} refers to the density matrix element located at the m^{th} row and n^{th} column. Therefore, the master equation can be approximated using (5.13) for optical frequencies of our interest as,

$$\frac{\partial}{\partial t}\hat{\rho} = \frac{\mathrm{i}}{\hbar}\left[\hat{\rho}, \hat{\mathcal{H}}_{\mathrm{qd}}\right] - \Gamma(\hat{\rho}). \tag{5.14}$$

where $\Gamma(\hat{\rho})$ is given by (5.13) and its matrix form is now simplified to,

$$\begin{bmatrix} \frac{\partial}{\partial t}\rho_{11} & \frac{\partial}{\partial t}\rho_{12} \\ \frac{\partial}{\partial t}\rho_{21} & \frac{\partial}{\partial t}\rho_{22} \end{bmatrix} = \begin{bmatrix} \left\{-\frac{\mathrm{i}}{\hbar}\mu E_{\mathrm{qd}}(\rho_{12} - \rho_{21}) - \frac{(\rho_{11}-1)}{\tau}\right\} & \left\{-\frac{\mathrm{i}}{\hbar}\mu E_{\mathrm{qd}}\Delta + \mathrm{i}\omega_{\mathrm{qd}}\rho_{12} - \frac{\rho_{12}}{T}\right\} \\ \left\{\frac{\mathrm{i}}{\hbar}\mu E_{\mathrm{qd}}\Delta - \mathrm{i}\omega_{\mathrm{qd}}\rho_{21} - \frac{\rho_{21}}{T}\right\} & \left\{-\frac{\mathrm{i}}{\hbar}\mu E_{\mathrm{qd}}(\rho_{21} - \rho_{12}) - \frac{\rho_{22}}{\tau}\right\} \end{bmatrix} \tag{5.15}$$

where the QD population difference is denoted as $\Delta = (\rho_{11} - \rho_{22})$.

The energy or population relaxation time of the QD which will lead to a mixing between ρ_{11} and ρ_{22} is denoted by τ. The relaxation time τ includes a contribution from non radiative decay to the dark states [106]. T refers to the polarization relaxation or dephasing time [92, 105] which will cause losses in the off diagonal density matrix elements of the QD. Both population relaxation and dephasing causes loss of coherence in the system [5].

The normalized decay rates in the vicinity of the MNP can be expressed as follows, taking the nonlocal effects of the MNP into account, according to the

two linearly independent orientations of the QD dipole moment [107, 108];

$$\left(\frac{1/\tau}{1/\tau_0}\right)_{\perp} = 1 + \frac{3}{2k^3}\sum_{\mathrm{n}=1}^{\infty}\left[\frac{\mathrm{Im}\{\alpha_{\mathrm{n}}(\omega)\}(\mathrm{n}+1)^2}{(a+R)^{2(\mathrm{n}+2)}}\right] \tag{5.16a}$$

$$\left(\frac{1/\tau}{1/\tau_0}\right)_{\parallel} = 1 + \frac{3}{2k^3}\sum_{\mathrm{n}=1}^{\infty}\left[\frac{\mathrm{Im}\{\alpha_{\mathrm{n}}(\omega)\}\mathrm{n}(\mathrm{n}+1)}{2(a+R)^{2(\mathrm{n}+2)}}\right] \tag{5.16b}$$

where τ_0 is the population relaxation time of the QD in the absence of the MNP, $k = \omega/c$ is the wave number and α_{n} is the n^{th} polarizability of the MNP and $\perp$ and $\parallel$ denote the radial ($s_\alpha = 2$) and tangential ($s_\alpha = -1$) orientations of the QD dipole with respect to the MNP. Using above equations, it can be shown that, in the dipole limit where $\mathrm{n} = 1$ and $\alpha = \beta_{\mathrm{NL}}(\omega)a^3$, the QD relaxation time depends on the MNP nonlocal dipolar polarizability as,

$$\tau(\omega) = \frac{\tau_0}{1 + f\,\mathrm{Im}\{\alpha(\omega)\}/\{k^3(r_{\mathrm{m}}+R)^6\}} \tag{5.17}$$

where the factor $f = 6$ when $s_\alpha = 2$ and $f = 3/2$ when $s_\alpha = -1$. Using (5.12a), (5.12b) and $t_{\mathrm{p}} = 1/\lambda_3$ where t_{p} corresponds to pure dephasing due to elastic scattering, the relationship between the QD dephasing rate and the MNP nonlocal dipolar polarizability can be arrived at as [13, 92],

$$T(\omega) = \frac{2\tau(\omega)t_p}{t_p + 2\tau(\omega)}. \tag{5.18}$$

Using $R \to \infty$ in (5.17) and (5.18) [13],

$$t_{\mathrm{p}} = 2\tau_0 T_0/(2\tau_0 - T_0). \tag{5.19}$$

5.3 Steady State Analytical Solution

As a majority of QD related applications operate well away from the rise time of the applied field where the transients have settled-down [4,30,102,105], we focus on the steady state solution of the system in this chapter.

Let us first define the following relations to be used when solving the master equation (5.14),

$$\tilde{\rho}_{12} = \mathcal{A} + \mathrm{i}\mathcal{B} \tag{5.20a}$$

$$\tilde{\rho}_{21} = \mathcal{A} - \mathrm{i}\mathcal{B} \tag{5.20b}$$

$$\Omega_{12}^{\mathrm{eff}} = \Omega_{\mathrm{re}} + \mathrm{i}\Omega_{\mathrm{im}} \tag{5.20c}$$

$$\mathcal{G} = \mathcal{G}_{\mathrm{re}} + \mathrm{i}\mathcal{G}_{\mathrm{im}}. \tag{5.20d}$$

Using element-wise comparison on (5.15) and by substituting for E_{qd}, we can arrive at the system Bloch equations defining the behavior of the QD under the influence of the MNP and the externally incident field (see appendix D.2),

$$\frac{\partial}{\partial t}\rho_{22} \approx -\frac{\rho_{22}}{\tau(\omega)} + \mathrm{i}\Omega_{12}^{r}\tilde{\rho}_{12} - \mathrm{i}\Omega_{12}^{r*}\tilde{\rho}_{21} \tag{5.21a}$$

$$\frac{\partial}{\partial t}\rho_{11} \approx \frac{\rho_{22}}{\tau(\omega)} - \mathrm{i}\Omega_{12}^{r}\tilde{\rho}_{12} + \mathrm{i}\Omega_{12}^{r*}\tilde{\rho}_{21} \tag{5.21b}$$

$$\frac{\partial}{\partial t}\tilde{\rho}_{21} \approx -\left[\mathrm{i}(\omega_{\mathrm{qd}} - \omega) + 1/T(\omega)\right]\tilde{\rho}_{21} + \mathrm{i}\Omega_{12}^{r}\Delta. \tag{5.21c}$$

By rearranging (5.21) using (5.20), we can arrive at the following form of the system Bloch equations [5,13],

$$\frac{\partial}{\partial t}\mathcal{A} = -\frac{\mathcal{A}}{T(\omega)} + \delta_{\mathrm{qd}}\mathcal{B} - \left(\Omega_{\mathrm{im}} + \mathcal{G}_{\mathrm{im}}\mathcal{A} - \mathcal{G}_{\mathrm{re}}\mathcal{B}\right)\Delta \tag{5.22a}$$

$$\frac{\partial}{\partial t}\mathcal{B} = -\frac{\mathcal{B}}{T(\omega)} - \delta_{\mathrm{qd}}\mathcal{A} - \left(\Omega_{\mathrm{re}} + \mathcal{G}_{\mathrm{re}}\mathcal{A} + \mathcal{G}_{\mathrm{im}}\mathcal{B}\right)\Delta \tag{5.22b}$$

$$\frac{\partial}{\partial t}\Delta = \frac{1-\Delta}{\tau(\omega)} + 4\left[\Omega_{\mathrm{im}}\mathcal{A} + \Omega_{\mathrm{re}}\mathcal{B} + \mathcal{G}_{\mathrm{im}}\left(\mathcal{A}^2 + \mathcal{B}^2\right)\right] \tag{5.22c}$$

where $\delta_{qd} = \omega - \omega_{qd}$ denotes the detuning of the external field with the QD excitonic transition. In the steady state where the temporal derivatives approach zero, using (5.22a) and (5.22b),

$$\mathcal{A} = \frac{-(\delta_{qd}\Omega_{re} + \Omega_{im}/T(\omega))\Delta - (\mathcal{G}_{im}\Omega_{im} + \Omega_{re}\mathcal{G}_{re})\Delta^2}{(\mathcal{G}_{im}\Delta + 1/T(\omega))^2 + (\delta_{qd} + \mathcal{G}_{re}\Delta)^2} \tag{5.23a}$$

$$= -\mathrm{Re}\left(\frac{\Omega_{12}^{eff}\Delta}{\delta_{qd} + \mathcal{G}\Delta + i/T(\omega)}\right) \tag{5.23b}$$

$$\mathcal{B} = \frac{(\delta_{qd}\Omega_{im} - \Omega_{re}/T(\omega))\Delta + (\mathcal{G}_{re}\Omega_{im} - \Omega_{re}\mathcal{G}_{im})\Delta^2}{(\mathcal{G}_{im}\Delta + 1/T(\omega))^2 + (\delta_{qd} + \mathcal{G}_{re}\Delta)^2} \tag{5.23c}$$

$$= \mathrm{Im}\left(\frac{\Omega_{12}^{eff}\Delta}{\delta_{qd} + \mathcal{G}\Delta + i/T(\omega)}\right) \tag{5.23d}$$

It is evident that if we solve (5.22) for Δ in the steady state, we can easily find $\mathcal{A}$ and $\mathcal{B}$ using the above equations. Hence by solving (5.22c) for Δ in the steady state, let us obtain [92],

$$w_3\Delta^3 + w_2\Delta^2 + w_1\Delta + w_0 = 0, \tag{5.24}$$

where,

$$\begin{aligned}
w_3 &= T(\omega)^2\left(\mathcal{G}_{re}^2 + \mathcal{G}_{im}^2\right), \\
w_2 &= 2T(\omega)^2\delta_{qd}\mathcal{G}_{re} + 2T(\omega)\mathcal{G}_{im} - T(\omega)^2\left(\mathcal{G}_{re}^2 + \mathcal{G}_{im}^2\right), \\
w_1 &= T(\omega)(4\tau(\omega)|\Omega_{12}^{eff}|^2 - 2\mathcal{G}_{im}) + T(\omega)^2(\delta_{qd}^2 - 2\delta_{qd}\mathcal{G}_{re}) + 1, \\
w_0 &= -T(\omega)^2\delta_{qd}^2 - 1.
\end{aligned}$$

Setting $\tilde{w}_i = w_i/w_3$ for $i = 0, 1$ and 2,

$$\Delta^3 + \tilde{w}_2\Delta^2 + \tilde{w}_1\Delta + \tilde{w}_0 = 0. \tag{5.25}$$

Using Cardano's method for solving cubic equations [109] we can obtain the three

possible solutions for Δ as,

$$\Delta_1 = (p_1 + p_2) - \tilde{w}_2/3, \tag{5.26a}$$

$$\Delta_2 = -(p_1 + p_2)/2 - \tilde{w}_2/3 + i\sqrt{3}(p_1 - p_2)/2, \tag{5.26b}$$

$$\Delta_3 = -(p_1 + p_2)/2 - \tilde{w}_2/3 - i\sqrt{3}(p_1 - p_2)/2. \tag{5.26c}$$

In the above equation,

$$p_1 = \mathcal{P}_1^{1/3}, \text{ where } \mathcal{P}_1 = r + \sqrt{q^3 + r^2}, \tag{5.27a}$$

$$p_2 = \mathcal{P}_2^{1/3}, \text{ where } \mathcal{P}_2 = r - \sqrt{q^3 + r^2}, \tag{5.27b}$$

where $q = \tilde{w}_1/3 - \tilde{w}_2^2/9$ and $r = (\tilde{w}_1\tilde{w}_2 - 3\tilde{w}_0)/6 - \tilde{w}_2^3/27$.

As $\Delta = \rho_{11} - \rho_{22}$ is the QD population difference, only the real roots of Δ satisfying the condition $-1 \leq \Delta \leq 1$ are useful [92]. The first Cardano root of (5.25), Δ_1, given by (5.26a), holds the only real root which readily satisfies this condition when $q^3 + r^2 >= 0$, where we have easily picked the real cubic roots of $\mathcal{P}_1$ and $\mathcal{P}_2$ as p_1 and p_2 respectively.

However, when $q^3 + r^2 < 0$, $\mathcal{P}_1$ possesses three complex cubic roots, the complex conjugates of which will appear as the cubic roots of $\mathcal{P}_2$. Careful observation of (5.26) reveals that, all three roots of Δ (Δ_1, Δ_2 and Δ_3) are real in such conditions. Under this condition, the physically valid root of Δ in (5.25) is given by Δ_1 in (5.26a) when the cubic roots of $\mathcal{P}_1$ and $\mathcal{P}_2$ are picked using De Moivre's nth root theorem for complex numbers as (see appendix D.3),

$$p_1 = |\mathcal{P}_1|^{1/3} \left[\cos(\theta_1/3) + \mathrm{i}\sin(\theta_1/3)\right] \text{ and } p_2 = p_1^*, \tag{5.28}$$

where $\mathcal{P}_1 = |\mathcal{P}_1|\angle\theta_1$ in the polar form. The above analytical results were verified for the large parameter space considered in chapter 6, against the steady state numerical solutions of (5.22) and (5.23). Thus, the complete and physically valid

analytical solution of (5.25) for the aforementioned parameter region is given by $\Delta = p_1 + p_2 - \tilde{w}_2/3$ [13] where,

$$p_1 = (\mathcal{P}_1)^{1/3} \in \mathbb{R} \text{ and } p_2 = (\mathcal{P}_2)^{1/3} \in \mathbb{R} \text{ for } q^3 + r^2 >= 0,$$
$$p_1 = |\mathcal{P}_1|^{1/3} \cos(\theta_1/3) \text{ and } p_2 = p_1^* \text{ for } q^3 + r^2 < 0.$$

5.4 Absorption, Energy and Dephasing Rate Normalizations

Variation of optical properties such as QD absorption, red and blue shifts of exciton energy and dephasing rates in the presence of plasmonic nanocavities could be exploited for the development of nanoscale plasmonic devices particularly for chemical and biological sensing applications [30,102]. We now proceed to analytically characterize such QD properties using the GNOR based approach.

The energy absorption of the QD can be obtained using the QD population difference as [5],

$$Q_{\text{qd}} = \hbar\omega_{\text{qd}}\rho_{22}/\tau(\omega) = \hbar\omega_{\text{qd}}(1-\Delta)/(2\tau(\omega)), \tag{5.30}$$

where we have replaced the conventional LRA based population difference with the newly suggested GNOR based Δ.

The system Bloch equation (5.21c) for the off diagonal density matrix element ρ_{21} can be recast as (see appendix D.4) [13,102],

$$\frac{\partial}{\partial t}\tilde{\rho}_{21} \approx -\left[\mathrm{i}(\Pi_{21} - \omega) + \Lambda_{21}\right]\tilde{\rho}_{21} + \mathrm{i}\Omega_{12}^{\text{eff}}\Delta. \tag{5.31}$$

The astute reader will notice that Π_{21} and Λ_{21} denote the normalized energy and the Föster-enhanced broadening (normalized dephasing rate) of the QD excitonic transition caused by the presence of the vicinal MNP [102] given by $\Pi_{21} =$

$\omega_{qd} - \mathcal{G}_{re}\Delta$ and $\Lambda_{21} = 1/T(\omega) + \mathcal{G}_{im}\Delta$. We call the two factors $\Pi_f = \mathcal{G}_{re}\Delta$ and $\Lambda_f = \mathcal{G}_{im}\Delta$ the exciton transition energy (red) shift and FRET rate factor (or the dephasing rate blue shift) respectively.

5.5 Quantum State Purity

Recently, there has been considerable progress in investigating the potential of using semiconductor quantum dots as qubits, where identifying and ameliorating sources of decoherence are important steps in understanding and improving system performance [110, 111]. It has also been proposed that directed nanoscale information transfer can be achieved by coupling qubits, for example in QDs, to plasmonic nanostructures [24]. To exploit this paradigm, it is vital to understand the effects of MNP-QD coupling on the properties of QD, including how non-classical phenomena such as the MNP nonlocal response could affect the quantum information. A GNOR based analytical characterization of the quantum state purity of the QD could be useful in this context.

A system's ability to exhibit quantum interference or "coherence" is a characteristic of a system in a pure quantum state that is maximally specified within quantum mechanics [112], whereas mixed states are classical statistical mixtures [81]. Coherence is represented by the off-diagonal elements of the system density matrix, which will be zero for a system in a completely mixed state and non-zero for a system with partial or full coherence. However, as the presence or absence of off-diagonal density matrix elements could be basis-dependent, it is always considered more appropriate to check purity as [81, 112],

$$\text{Purity} = \text{Tr}(\hat{\rho}^2), \tag{5.32}$$

where the bounds of system purity are set such that,

$$1/d \leq \text{Purity} \leq 1. \tag{5.33}$$

The dimension of the associated Hilbert space is denoted by d. If the system's quantum state is pure (Purity $= 1$), it spans a one-dimensional subspace of the system Hilbert space [112]. A state that falls within the bounds without being pure or completely mixed (Purity $= 1/d$) is a "partially coherent state" [81].

For the excitonic system of our concern, using (5.32), (5.20a) and (5.20b) it can be shown that (see appendix D.5) [13],

$$\text{Purity} = \frac{1+\Delta^2}{2} + 2(\mathcal{A}^2 + \mathcal{B}^2) = \frac{1+\Delta^2}{2} + 2|\rho_{12}|^2. \tag{5.34}$$

Then the mixedness of the system can be naturally defined as the complement of system purity such that [112],

$$\text{Mixedness} = 1 - \text{Purity}\,. \tag{5.35}$$

It is important to note that both purity and mixedness are invariant under transformations of the form $\hat{\rho} \rightarrow \hat{U}\hat{\rho}\hat{U}^\dagger$, where $\hat{U}$ is a unitary operator. For example, this invariance holds under the dynamical mapping $\hat{U}(t, t_0) = e^{-\frac{\mathrm{i}}{\hbar}\hat{\mathcal{H}}(t-t_0)}$ where $\hat{\mathcal{H}}$ is the system Hamiltonian [112]. Moreover, when $\mathcal{A}^2, \mathcal{B}^2 \ll 1$ and $\Delta \approx 1$ (5.34) reduces to,

$$\text{Purity} \approx \frac{1+\Delta^2}{2} \approx \Delta^2 \approx \Delta. \tag{5.36}$$

Hence, purity is expected to roughly follow the behaviour of Δ under such conditions.

Finally, for comparison purposes, we derive the system purity in the absence of the vicinal MNP. We nullify the effect of the MNP by setting $R \rightarrow \infty$, $T \rightarrow T_0$ and $\tau \rightarrow \tau_0$. Then from (5.7a) and (5.7b), $\mathcal{G} \rightarrow 0$ and $\Omega_{12}^{\text{eff}} \rightarrow \Omega_0$. This leads to the

reduction of the cubic equation (5.24) to a linear equation with the coefficients,

$$w_0 \to -T_0^2\delta_{\mathrm{qd}}^2 - 1, \tag{5.37a}$$

$$w_1 \to 4\tau_0 T_0 |\Omega_0|^2 + T_0^2\delta_{\mathrm{qd}}^2 + 1, \tag{5.37b}$$

$$w_2 \to 0, \tag{5.37c}$$

$$w_3 \to 0, \tag{5.37d}$$

where we recall that T_0 and τ_0 denote the dephasing and decay rates of the isolated QD, respectively. Substituting these back in (5.24) yields the steady state analytical population difference of the isolated QD as,

$$\Delta_{\mathrm{iqd}} = -\frac{w_0}{w_1} = \frac{T_0^2\delta_{\mathrm{qd}}^2 + 1}{4T_0\tau_0|\Omega_0|^2 + T_0^2\delta_{\mathrm{qd}}^2 + 1}. \tag{5.38}$$

The steady state expressions for the real and imaginary parts of the slowly time varying off diagonal density matrix element of the isolated QD then become [13],

$$\mathcal{A}_{\mathrm{iqd}} = -\mathrm{Re}\left(\frac{\Omega_0\Delta_{\mathrm{iqd}}}{\delta_{\mathrm{qd}} + \mathrm{i}/T_0}\right), \tag{5.39a}$$

$$\mathcal{B}_{\mathrm{iqd}} = \mathrm{Im}\left(\frac{\Omega_0\Delta_{\mathrm{iqd}}}{\delta_{\mathrm{qd}} + \mathrm{i}/T_0}\right), \tag{5.39b}$$

$$\{\mathrm{Purity}\}_{\mathrm{iqd}} = \left(1 + \Delta_{\mathrm{iqd}}^2\right)/2 + 2(\mathcal{A}_{\mathrm{iqd}}^2 + \mathcal{B}_{\mathrm{iqd}}^2). \tag{5.39c}$$

5.6 Summary and Conclusion

This chapter presented a fully analytical characterization of a quantum dot placed in the vicinity of an MNP, and illuminated by an external coherent driving field. The presented analytical equations were verified for the full parameter space used in chapter 6.

Note that if one sets $\delta_{\mathrm{NL}} \to 0$ in the presented model, the GNOR based nonlocal β_{NL} of the MNP approaches the Clausius Mossotti factor β_{LRA} defined in the LRA given by (2.7). Thus, using $\delta_{\mathrm{NL}} \to 0$, $\tau \to \tau_0$ and $T \to T_0$, the conventional LRA based equation set [5, 23, 24, 26, 28, 30, 102, 105, 106] can be obtained. Using $R \to \infty$, $\tau \to \tau_0$ and $T \to T_0$, the relevant equations for the isolated QD can be obtained [13].

Chapter 6
Numerical Simulation of Exciton Behaviour in a Plasmonic Near Field

6.1 Numerical Model Overview

Using the analytical model presented in chapter 5, let us now study the behavior of an exciton situated in a plasmonic near-field, over continua of several system parameters. Unless specifically mentioned otherwise, the default parameters used for the generated results are as follows: incident field intensity $I_0 = 1 \times 10^3\,\mathrm{W\,cm^{-2}}$, orientation parameter $s_\alpha = 2$, polarization relaxation (dephasing) time of the isolated quantum dot (QD) $T_0 = 0.3\,\mathrm{ns}$, energy or population relaxation time of the isolated QD $\tau_0 = 0.8\,\mathrm{ns}$ [106], dielectric constant of the submerging medium $\epsilon_b = 1$, dielectric constant of the QD material $\epsilon_s = 6$ [106] and QD resonance frequency $\omega_{\mathrm{qd}} = 3.5\,\mathrm{eV}$ [113] such that the quantum dot, metal nanoparticle (MNP) and the incoming coherent radiation are near-resonantly coupled. The analysis uses a silver MNP where the bulk plasma frequency $\hbar\omega_p = 8.99\,\mathrm{eV}$, bulk damping rate $\hbar\gamma = 0.025\,\mathrm{eV}$, Fermi velocity $v_f = 1.39 \times 10^6\,\mathrm{m\,s^{-1}}$ [11], D $\approx 9.624 \times 10^{-4}\,\mathrm{m^2\,s^{-1}}$ [114] and the experimental bulk dielectric data ϵ_{exp} are obtained from the tabulations by Johnson and Christy [60]. The amplitude E_0 and the intensity I_0 of the coherent external field are related using $E_0 = \sqrt{2I_0/(\epsilon_0 c)}$, where c is the speed of light in vacuum [92]. As the main objective of this chapter is to study the behaviour of an exciton in a

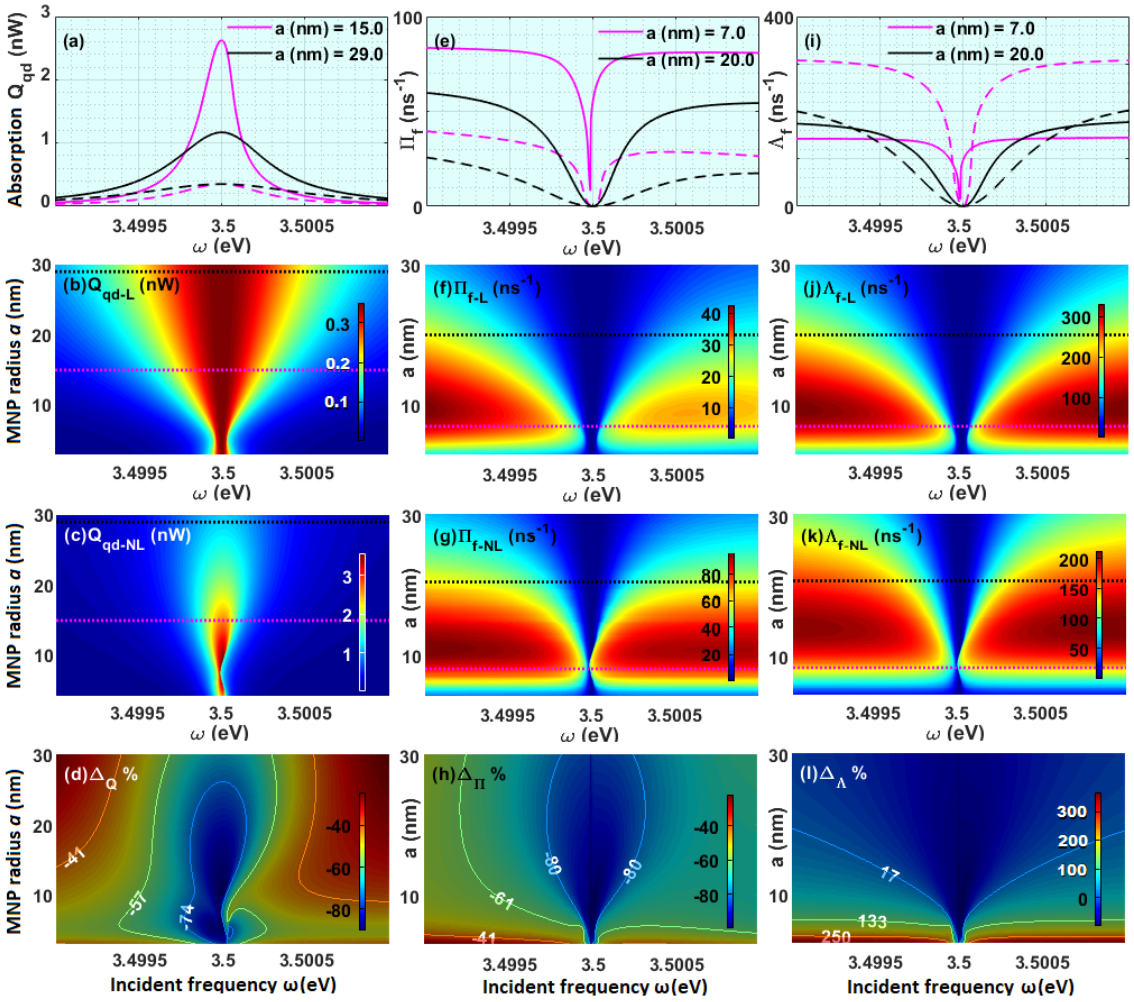

Figure 6.1: Second and third rows depict the top view of the $x = \omega$ (range: $3.499 - 3.501$ eV), $y = a$ (range: $3 - 30$ nm) surface plots of LRA based (subscript L) and the GNOR based (subscript NL) results of Q_{qd} (first column), Π_f (second column) and Λ_f (third column), respectively. The first row depicts the line plots corresponding to the cross sections marked in black and pink on the respective surface plots in the same column. Solid lines represent the GNOR based plots whereas the dashed lines are the conventional LRA based plots. The final row depicts the signed percentage difference $\Delta_X = (X_L - X_{NL})/X_{NL}\%$ where X denotes the physical quantity of the relevant column. For all subplots, $R = a + 10$ nm and $\mu = 1.3$ e nm where e denotes the elementary charge.

nanohybrid over continua of system parameters, we have not restricted the analysis to a given type of quantum dot.

6.2 Absorption, Field Enhancement, Exciton Energy and Dephasing Rate

Let us analyse the variation of QD absorption rate Q_{qd} (in the vicinity of an MNP), MNP induced red-shift of the QD excitonic energy Π_f and MNP induced blue-shift of the QD dephasing rate Λ_f with varying MNP radius a and coherent external illumination frequency ω, as depicted in Fig. 6.1. Sub-figures in the second and third rows depict the LRA based and GNOR based results of the three aforementioned QD properties, presented in the form of colour-coded surface plots (top view). Sub-figures in the first row depict the line plots corresponding to the cross sections indicated in pink and black on the LRA and GNOR based surface plots in the two successive rows of the same column. The solid lines represent the GNOR based results whereas the dashed lines represent the relevant LRA based results. The final row shows the surface plots of the percentage difference between the respective LRA and GNOR based results (normalized by the GNOR based result).

Fig. 6.1(a) reveals that Q_{qd} follows a singly-peaked distribution along ω (in both LRA and GNOR based models) with a peak near the QD resonance 3.5 eV. It can be observed using subplots 6.1(a), (b) and (c) that the LRA based model suggests smaller peak amplitudes and larger absorption line-widths along the frequency axis compared to the respective GNOR based counterparts. Moreover, as seen in 6.1(c), the GNOR model suggests a higher asymmetry of peaks along the frequency axis compared to the LRA based model. The signed percentage difference $\Delta_{\text{Q}} = (\Delta_{\text{qd-L}} - \Delta_{\text{qd-NL}})/\Delta_{\text{qd-NL}}\%$ depicted in Fig. 6.1(d) reveals that the LRA based model underestimates the QD absorption by more than 23% com-

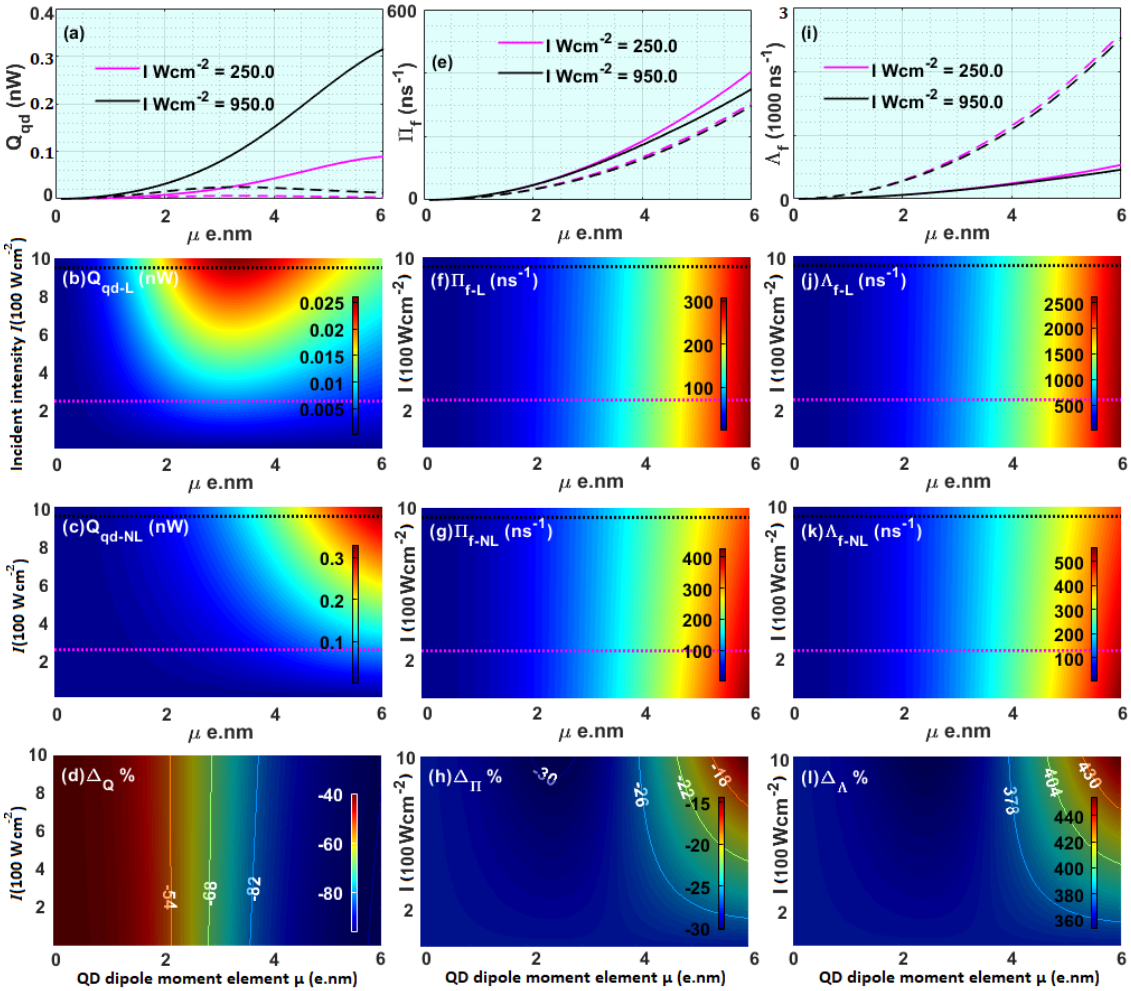

Figure 6.2: Second and third rows depict the top view of the $x = \mu, y = I$ surface plots of LRA based (subscript L) and the GNOR based (subscript NL) results of the QD energy absorption Q_{qd} (first column), excitonic energy (red) shift Π_f (second column) and dephasing rate (blue) shift Λ_f (third column), respectively. The first row depicts the line plots corresponding to the cross sections marked in black and pink on the respective surface plots in the same column. Solid lines represent the GNOR based plots whereas the dashed lines are the conventional LRA based plots. The final row depicts the signed percentage difference $\Delta_{\text{X}} = (\text{X}_{\text{L}} - \text{X}_{\text{NL}})/\text{X}_{\text{NL}}\%$ where X denotes the physical quantity of the relevant column. For all subplots, the MNP radius $a = 3\,\text{nm}$, MNP-QD centre separation $R = 13\,\text{nm}$, frequency of the coherent external illumination $\omega = 3.4995\,\text{eV}$.

pared to the GNOR based model, in the entire region under study.

From the second and third columns of Fig. 6.1, it can be seen that both Π_f and Λ_f possess singly dipped distributions along the ω axis (under both LRA and GNOR based models). From Fig. 6.1(h), it can be seen that $\Delta_\Pi = (\Pi_{\text{f-L}} - \Pi_{\text{f-NL}})/\Pi_{\text{f-NL}}\%$ is $< -20\%$ in the entire region under consideration, implying that the LRA based model under-estimates the MNP induced red-shift of the excitonic resonance frequency by more than 20%. Fig. 6.1(h) indicates that this percentage difference exceeds 80% in magnitude when the external field frequency ω gets close to the bare excitonic resonance ω_{qd} implying the dominance of nonlocal effects in the region. Fig. 6.1(l) shows that, a substantial over-estimation of the LRA based Λ_f over the GNOR based result is suggested for MNP radius $a < 10\,\text{nm}$ when the dark blue region with very small detunings from the exciton resonance is exceeded [13].

We then study the behavior of Q_{qd}, Π_f and Λ_f when the coherent external field intensity I and the QD dipole moment μ are varied in continua, using Fig. 6.2. All subplots are in the same constellation as Fig. 6.1. From Fig. 6.2(d), it is evident that $\Delta_{\text{Q}} = (Q_{\text{L}} - Q_{\text{NL}})/Q_{\text{NL}}\% < -40\%$ in the entire region, suggesting that the LRA based model under-estimates the QD absorption compared to the case where the nonlocal effects are taken into account. It can also be observed that this percentage difference is almost invariant along the I axis for a given value of μ.

From the second and third columns of Fig. 6.2, it can be seen that both Π_f and Λ_f are almost invariant along the I axis for a given μ. Fig. 6.2(h) shows that $\Delta_\Pi = (\Pi_{\text{f-L}} - \Pi_{\text{f-NL}})/\Pi_{\text{f-NL}}\% < -14\%$ in the entire parameter region suggesting that the GNOR based model results in higher red-shifts to the exciton resonance when in the near field of an MNP. From Fig. 6.2(I), it is evident that the GNOR based model suggests smaller blue shifts to the QD dephasing compared to the LRA based model, resulting in $\Delta_\Lambda = (\Lambda_{\text{f-L}} - \Lambda_{\text{f-NL}})/\Lambda_{\text{f-NL}}\% > 350\%$ in the entire

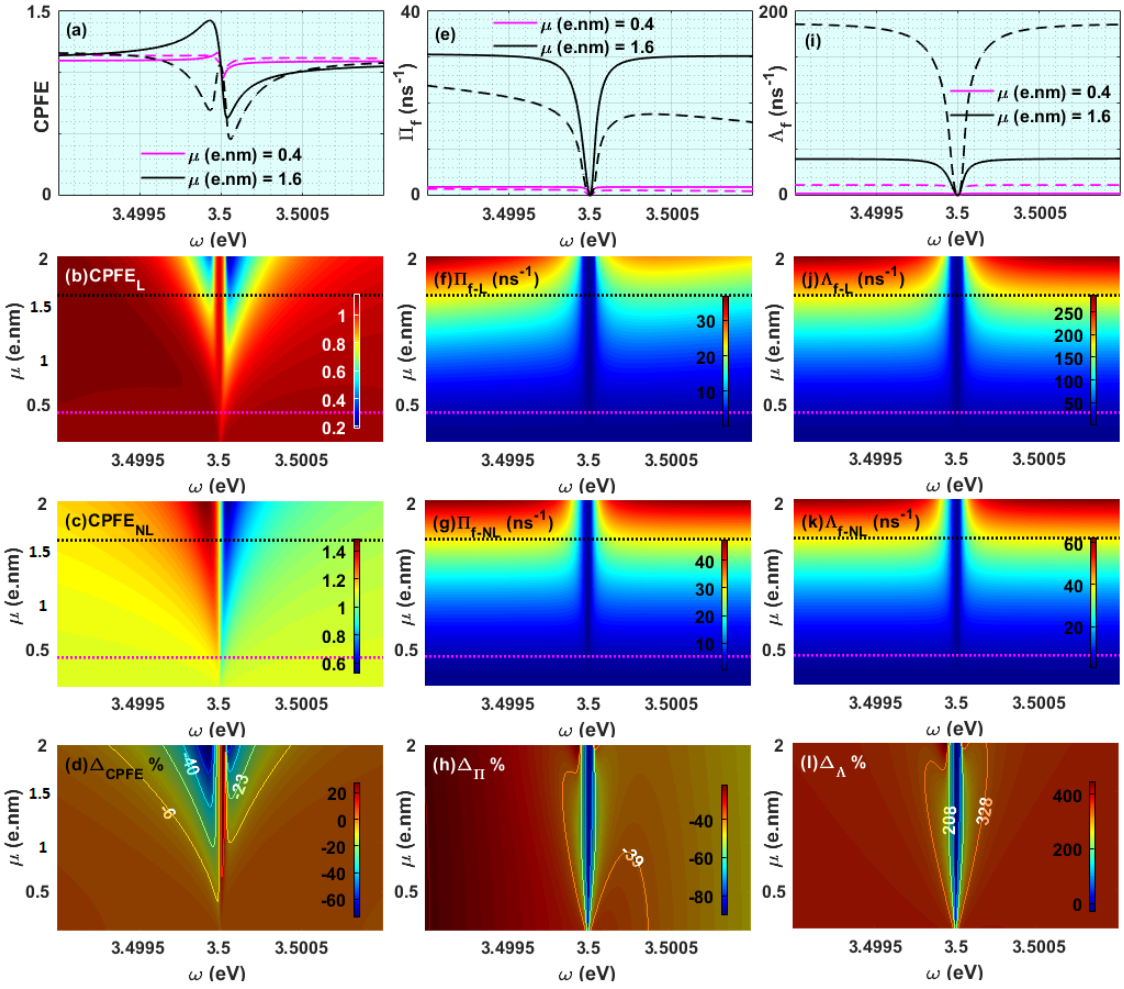

Figure 6.3: Second and third rows depict the top view of the $x = \omega, y = \mu$ surface plots of LRA based (subscript L) and the GNOR based (subscript NL) results of CPFE (first column), Π_f (second column) and Λ_f (third column), respectively. The first row depicts the line plots corresponding to the cross sections marked in black and pink on the respective surface plots in the same column. Solid lines represent the GNOR based plots whereas the dashed lines are the conventional LRA based plots. The final row depicts the signed percentage difference $\Delta_X = (X_L - X_{NL})/X_{NL}\%$ where X denotes the physical quantity of the relevant column. For all subplots, $a = 3\,\text{nm}$, $R = 13\,\text{nm}$.

region under consideration.

Using Fig. 6.3, we can study the variation of coherent plasmonic field enhancement (CPFE) experienced by the QD, Π_f and Λ_f when μ and ω are varied, using the usual arrangement of sub-figures. The first column depicts the LRA and GNOR based predictions (both as line and surface plots) of CPFE and their percentage difference. From Fig. 6.3(a)-(c), it can be observed that the GNOR based model suggests a Fano-like distribution for CPFE whereas the LRA based model suggests a modified Fano-like distribution. From Fig. 6.3(d), it is evident that the GNOR based model entails significant modification of CPFE from the LRA based model as μ increases and the detuning of ω from ω_{qd} decreases. The second and third columns of Fig. 6.3 correspond to Π_f and Λ_f respectively, both of which follow narrow, singly dipped frequency distributions for all μ, under both LRA and GNOR based models. In line with the observations in the earlier parameter spaces, the GNOR model suggests higher red-shifts (Π_f) to the exciton resonance in the entire parameter region. It suggests lower blue-shifts (Λ_f) to the QD dephasing rate compared to the LRA based model, except at coherent illumination frequencies extremely close to ω_{qd} [13].

6.3 Effects of Centre Separation Variation

We then study the behavior of the QD as the MNP-QD centre separation (R) and the QD dipole moment (μ) are varied. The first, second and third columns of Fig. 6.4 correspond to the real component of the normalized QD Rabi frequency $\mathrm{Re}\left[\Omega_{12}^{r}\right]$, the QD population difference Δ and QD absorption Q_{qd} in the usual arrangement of subplots.

The solid lines of Fig. 6.4(a) which correspond to the GNOR based prediction have four distinguishable features, especially when $\mu > 1\,\mathrm{e\,nm}$; (i) For large R, it can be seen that $\mathrm{Re}\left[\Omega_{12}^{r}\right] \rightarrow \Omega_0$, and the field experienced by the QD approaches

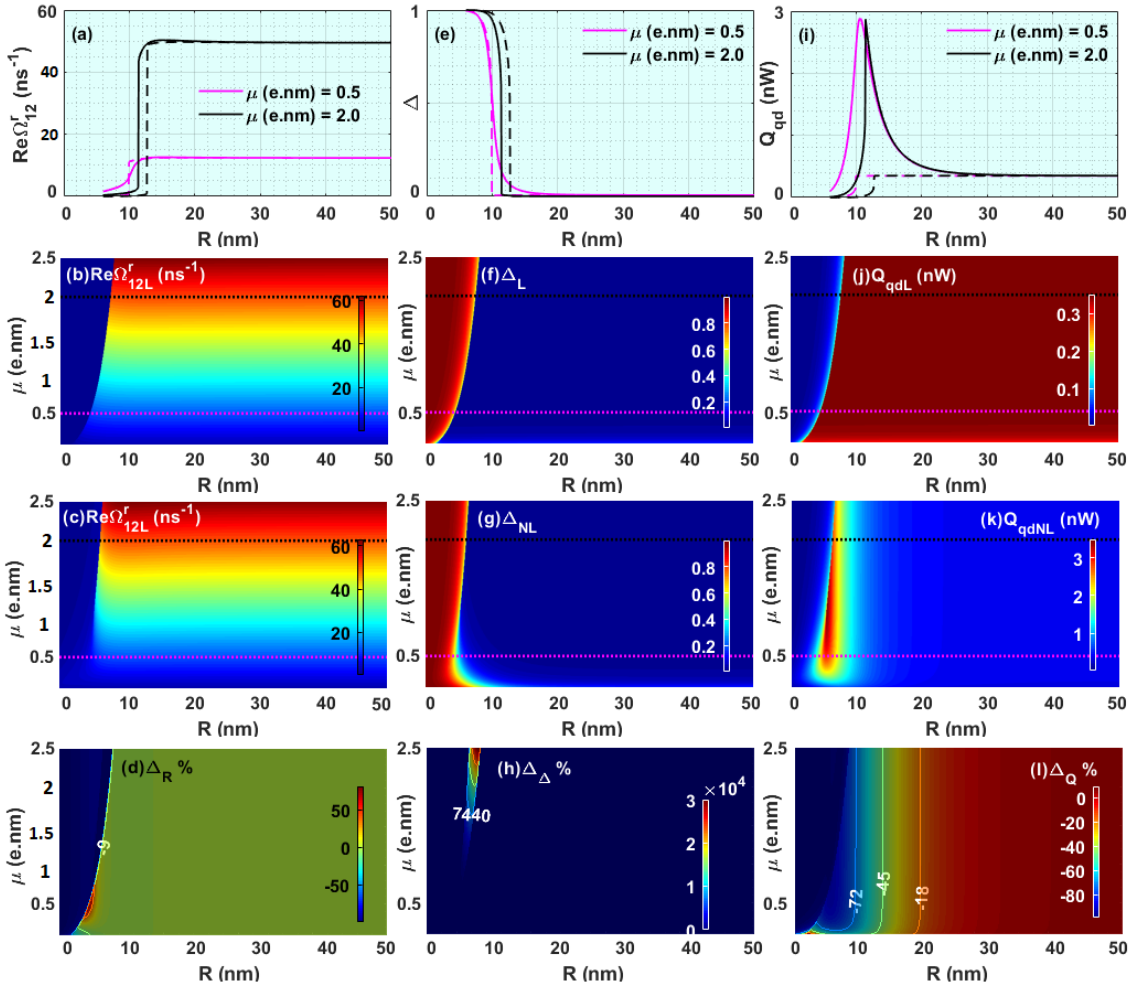

Figure 6.4: Second and third rows depict the top view of the $x = R, y = \mu$ surface plots of LRA based (subscript L) and the GNOR based (subscript NL) results of $\mathrm{Re}\,\Omega_{12}^{r}$ (first column), Δ (second column) and Q_{qd} (third column), respectively. The first row depicts the line plots corresponding to the cross sections marked in black and pink on the respective surface plots in the same column. Solid lines represent the GNOR based plots whereas the dashed lines are the conventional LRA based plots. The final row depicts the signed percentage difference $\Delta_{\mathrm{X}} = (\mathrm{X_L} - \mathrm{X_{NL}})/\mathrm{X_{NL}}\%$ where X denotes the physical quantity of the relevant column. For all subplots $a = 3\,\mathrm{nm}$, $\omega = \omega_{\mathrm{qd}}$.

the externally applied field. (ii) Re $\left[\Omega_{12}^{r}\right]$, and hence the field experienced by the QD slightly increases above Ω_0 as R decreases. (iii) This enhancement reaches a peak and then starts to decrease with further decrease of R, which is an indication of the competition between Förster energy transfer from QD to MNP and the plasmonic field enhancement near QD. (iv) This follows by an encounter of an abrupt and significant decrease of Re $\left[\Omega_{12}^{r}\right]$, and hence the field experienced by the QD, as R decreases further. This could be identified as near PMR(plasmonic meta-resonance)-like behavior of the MNP-QD hybrid nano-system [105]. PMR corresponds to a "molecular-type" resonance which is quite different from the conventional atomic resonances. It occurs under strong exciton-plasmon coupling, when separately distinguishable bright and dark states are experienced by the QD. The dark state which corresponds to dramatic screening of the effective field experienced by the QD, due to the presence of the MNP, is an indication of the PMR. PMR-like behavior of MNP-QD nanohybrids has recently been under study for a multitude of applications such as in-vivo nanoscale switching [29, 105]. Plasmonic metaresonances will be further investigated in detail in chapter 7.

Juxtaposition of Fig. 6.4(c), (g) and (k) reveal that the dip in the distribution of Δ along R axis and the corresponding peak of Q_{qd} coincide with the relevant PMR related dip along the R axis in (c) for $\mu > 1\,\mathrm{e\,nm}$. Moreover, the percentage difference plots (Fig. 6.4(d), (h) and (I)) indicate that both LRA and GNOR based models converge towards the same values when R exceeds 30 nm.

6.4 Population Difference and Quantum State Purity

We then study the resemblance of QD population difference Δ to its quantum state purity using Fig. 6.5. In this figure, subplots (b), (c) and (d) in the first column depict the variation of the LRA based (Δ_{L}), GNOR based (Δ_{NL}) and the

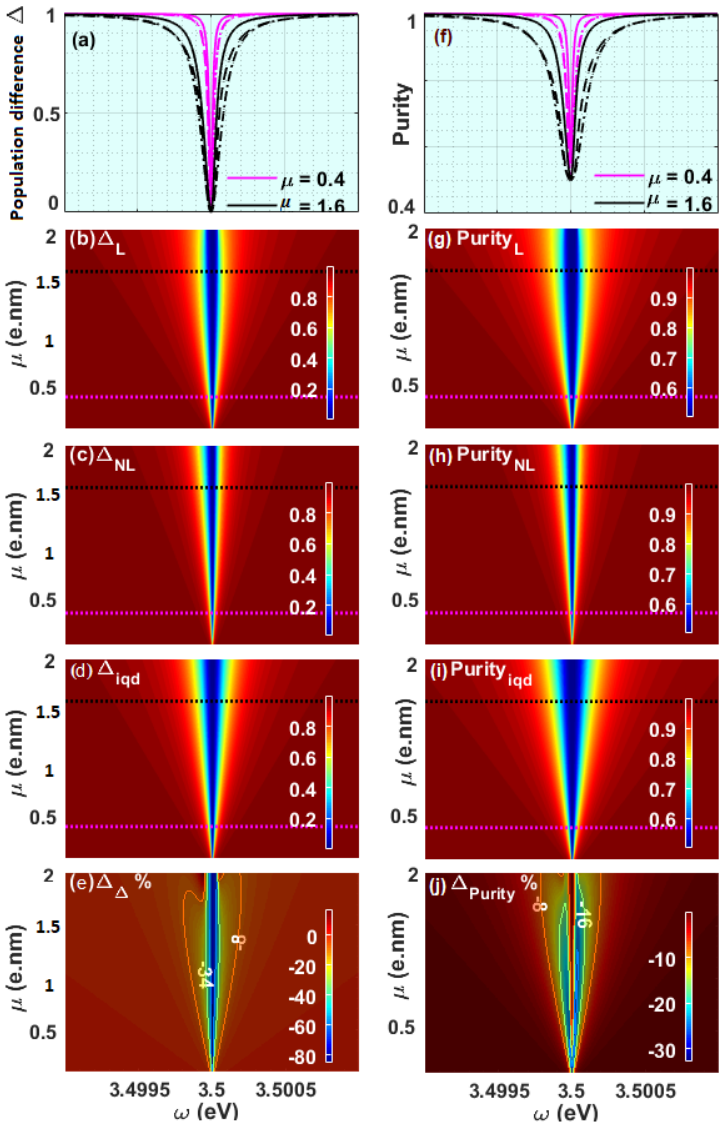

Figure 6.5: Second, third and fourth rows depict the top view of the $x = \omega, y = \mu$ surface plots of LRA based (subscript L), GNOR based (subscript NL) and isolated QD (subscript iqd) results of Δ (first column) and Purity (second column), respectively. The first row depicts the line plots corresponding to the cross sections marked in black and pink on the respective surface plots in the same column. Solid lines represent the GNOR based plots whereas the dashed lines are the conventional LRA based plots and the dotted-dashed lines are the isolated QD plots.The final row depicts the signed percentage difference $\Delta_X = (X_L - X_{NL})/X_{NL}\%$ where X denotes the physical quantity of the relevant column. For all subplots, $a = 3\,\text{nm}$, $R = 13\,\text{nm}$.

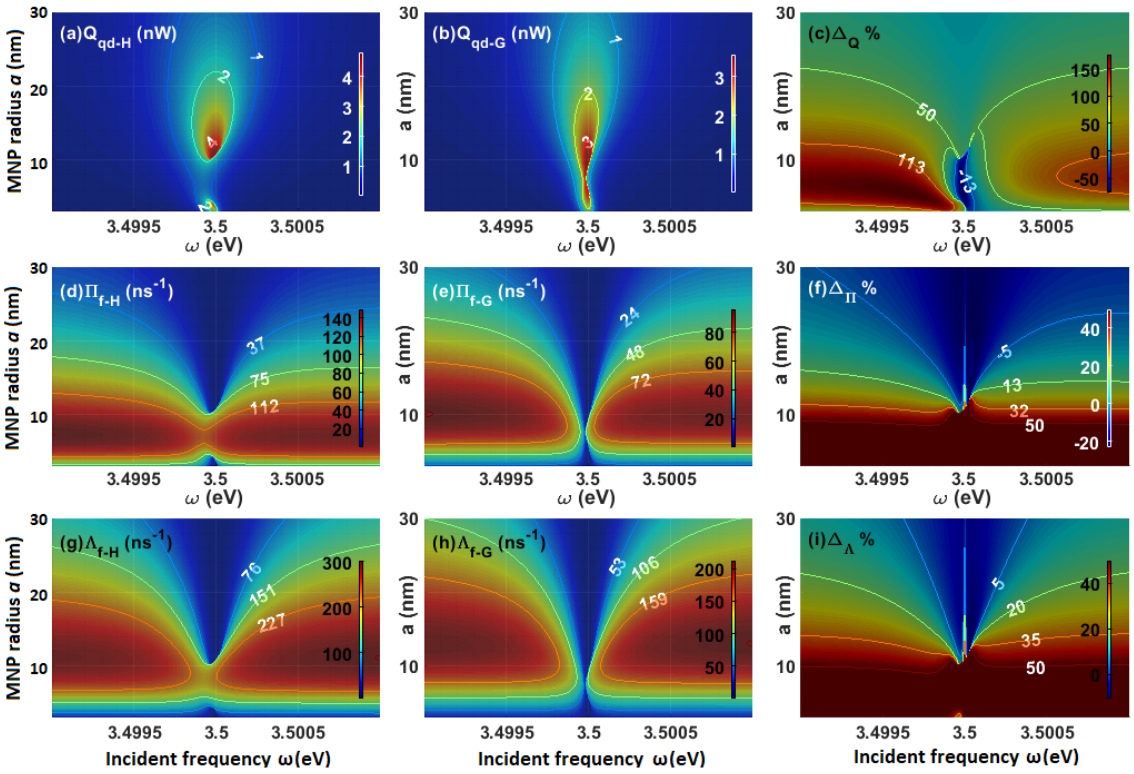

Figure 6.6: Comparison of sample HDM and GNOR based results. Figures depict the top view of the $x = \omega$ (range: $3.499 - 3.501\,\text{eV}$), $y = a$ (range: $3 - 30\,\text{nm}$) surface plots of HDM based (subscript H) and the GNOR based (subscript G) results of Q_{qd} (first row), Π_f (second row) and Λ_f (third row), respectively. The final column depicts the signed percentage difference $\Delta_{\text{X}} = (\text{X}_{\text{H}} - \text{X}_{\text{G}})/\text{X}_{\text{G}}\%$ where X denotes the physical quantity of the relevant row. For all subplots, $R = a + 10\,\text{nm}$ and $\mu = 1.3\,\text{e nm}$.

isolated QD (Δ_{iqd}) population differences, respectively, with varying ω and μ. Fig. 6.5(a) depicts the line-plots corresponding to the cross-sections marked in pink and black on the three subsequent surface plots. The solid, dashed and dotted-dashed lines correspond to the GNOR based, LRA based and the isolated QD cases, respectively. Fig. 6.5(e) shows the usual surface-contour plot of the LRA and GNOR percentage difference $\Delta_{\Delta} = (\Delta_{\text{L}} - \Delta_{\text{NL}})/\Delta_{\text{NL}}\%$. The second column of Fig. 6.5 depicts the same constellation of subplots as the preceding column for the quantum state purity of the QD.

Comparison of the first column to the corresponding plots of the second re-

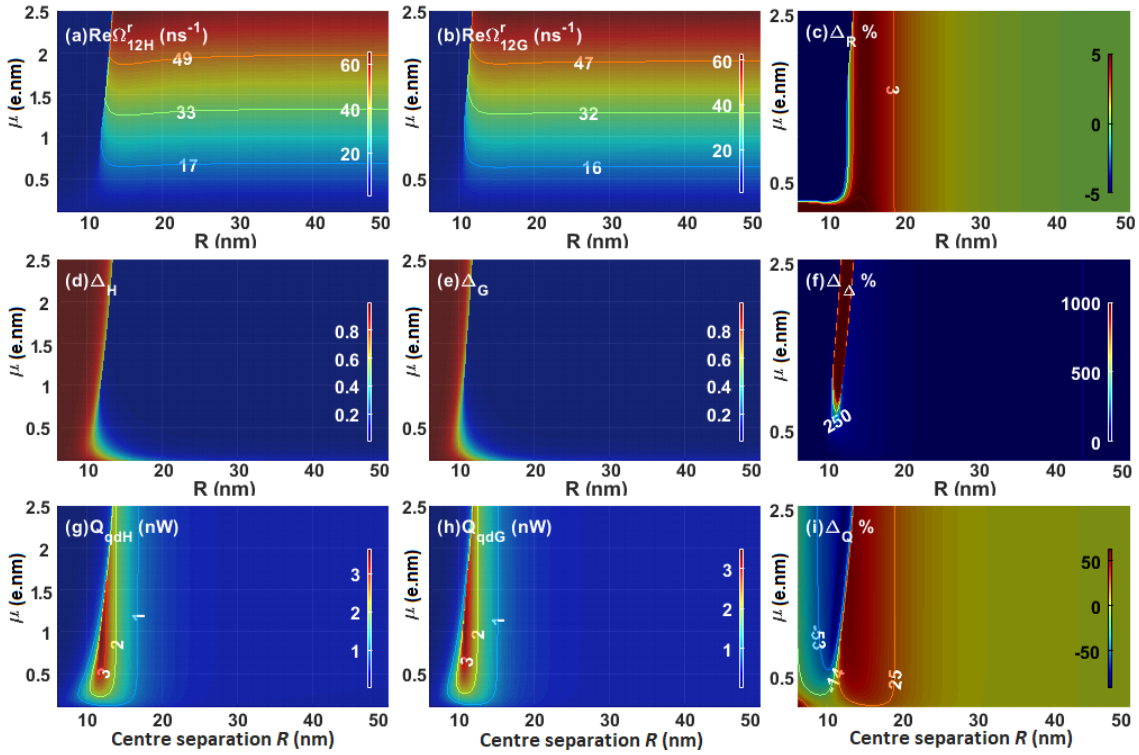

Figure 6.7: Comparison of sample HDM and GNOR based results. Figures depict the top view of the $x = R$, $y = \mu$ surface plots of HDM based (subscript H) and the GNOR based (subscript G) results of normalized Rabi frequency Ω^r_{12} (first row), population difference Δ (second row) and QD absorption rate Q_{qd} (third row), respectively. The final column depicts the signed percentage difference $\Delta_X = (X_H - X_G)/X_G\%$ where X denotes the physical quantity of the relevant row. For all subplots $a = 3\,\text{nm}$.

veals that the plot shapes of population difference bear a high resemblance to the respective quantum state purity plots. It can also be observed that when $\Delta \to 1, \text{Purity} \to \Delta$ suggesting the existence of the QD in a completely pure state where the state occupation probabilities, $\rho_{11} \to 1$ and $\rho_{22} \to 0$. In contrast, when $\Delta \to 0, \text{Purity} \to 0.5$ (the minimum possible value of purity of a two state system) suggesting that $\rho_{11} \to 0.5$ and $\rho_{22} \to 0.5$, leading the QD to a completely mixed state. Observation of the first three sub-plots of each column reveals that both Δ and Purity possess singly dipped frequency distributions for each value of μ where $\Delta \to 0$ (and Purity $\to 0.5$) when the detuning of the external field

with the QD resonance decreases, for all three cases under study. The isolated QD spectra for Δ and Purity exhibit a symmetric dip near ω_{qd} which constantly broadens with increasing μ. The LRA based model suggests a symmetric dip around ω_{qd}, the broadening of which is lesser than that of the isolated QD case, towards higher values of μ. In contrast, the GNOR based model suggests a dip around ω_{qd} with growing asymmetry as μ increases. Fig. 6.5(e) indicates that the percentage difference between the LRA and GNOR based Δ predictions become significant as the detuning of the external field (with respect to ω_{qd}) decreases. Δ and Purity values from both models tend to coincide at high detunings from ω_{qd} [13].

6.5 Comparison between HDM and GNOR

Finally, let us peruse a comparison between HDM based and the proposed GNOR based characterizations of the QD influenced by a near-field MNP. From Fig. 6.6, it is evident that the observed differences are quite significant for MNP radii less than 10 nm, where the experimentally observed size dependent resonance shifts of metal nanoparticles (attributed to nonlocal effects) are most significant [36]. The differences observed between the HDM and GNOR based results mainly arise as the GNOR model accounts for the electron diffusion phenomenon in the MNP which arises mainly due to surface effects such as Landau damping [11]. From a similar analysis in the μ vs R space using Fig. 6.7, it was observable that the difference between HDM and GNOR based results are significant in the near-PMR region and both models tend to give similar predictions when R increases beyond 30 nm (when $a = 3$ nm), due to the decreased impact of the MNP [13].

6.6 Summary of Physical Observations

Using the above results and discussion, it can be concluded that the GNOR based characterization of a QD exciton situated in the near field of an MNP displays higher levels of energy absorption (Q_{qd}), compared to its LRA based counterpart, at least in the large parameter space under study. It also suggests steeper spectral line-widths along the frequency axis for Q_{qd} and larger MNP induced red-shifts (Π_f) to the excitonic resonance frequency compared to the LRA based model. The following interesting phenomena (left unrevealed by the LRA based model) were also displayed by the proposed GNOR based model, in the selected parameter regime. It suggests a Fano-like spectrum near the bare excitonic resonance for the coherent plasmonic field enhancement (CPFE) experienced by the QD. Moreover, incorporation of the nonlocal effects introduces an asymmetry to the dips of QD population Δ and quantum state purity near the bare excitonic resonance ω_{qd}. Overall, it is evident that the GNOR based model predicts strong modifications to various QD properties such as population difference, absorption, MNP induced shifts to excitonic energy and Förster enhanced broadening, coherent plasmonic field enhancement and quantum state purity, compared to the conventional LRA based predictions. Such modifications are prominent with small MNP radii, high QD dipole moments, small detunings (of the coherent external illumination from the bare excitonic resonance) and near parameter regions exhibiting plasmonic meta resonance (PMR)-like behavior.

Chapter 7
Plasmonic Metaresonances

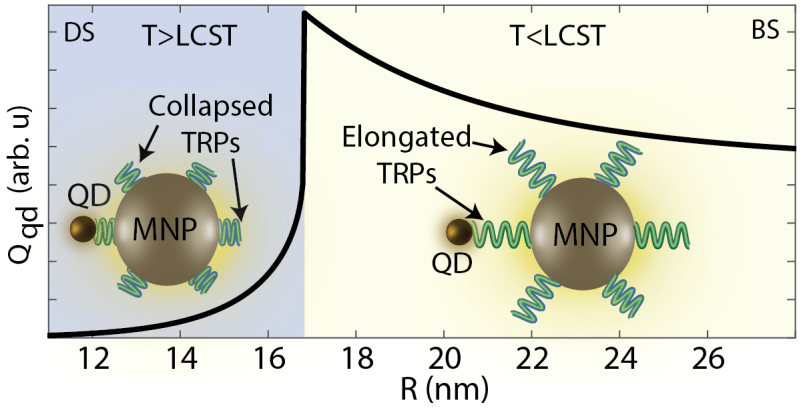

Figure 7.1: Graphical illustration of an example of the near-plasmonic metaresonant switching action of exciton-plasmon nanohybrids. This figure depicts the usability of thermoresponsive polymer conjugated metal nanoparticle (MNP)-quantum dot (QD) metamolecules for temperature sensing, based on the MNP-QD centre separation. The solid black line corresponds to the QD absorption rate curve for a silver-based metamolecule with QD dipole moment 1 e nm (same as the solid blue curve in Fig. 7.5), where e denotes the elementary charge. T denotes the temperature of the submerging medium and LCST is the lower critical solution temperature of the mediating polymer strand.

In this section, let us study the plasmonic metaresonances encountered in section 6.7 in detail. It has been revealed that, when a quantum dot (QD) is placed in the near field of a metal nanoparticle (MNP) with both being driven by a coherent optical field, molecular-like collective states or "resonances" that are different from localized surface plasmons could form in the system due to the quantum coherence generated in the QD by the external field and its ability to dramatically

influence the plasmonic field (coherent plasmonic effects) [105,115]. Such molecular resonances are known as plasmonic metaresonances (PMRs). These PMRs are not analogous to frequency domain resonances such as excitons in QDs and plasmons in MNPs, and primarily occur in the space/time domain [116]. PMRs form a class of optical events gaining increasing popularity due to their promising prospects in sensing and switching applications.

When influenced by the plasmonic near-field of an MNP, the interaction of a QD with a time-dependent coherent optical field constitutes a two-stage coupling process [115]. At the first stage, the optical field experienced by the QD is dramatically suppressed, leading to a plasmonically induced time delay τ_p. At the second stage, the QD is driven with a Rabi frequency normalized by the plasmonic effects. A nanohybrid experiences PMR when system parameters such as QD dipole moment, MNP-QD centre separation or submerging medium permittivity reach critical values, resulting in the plasmonically induced time delay of the effective Rabi frequency experienced by the QD asymptotically tending to infinity, leaving the system in the first stage [115]. In this chapter τ_p is obtained as the time required for the effective Rabi frequency Ω_{12}^r of the system to reach half of its steady state value, in response to a step-like rise of the amplitude (E_0) of the externally incident field.

In near-PMR regions where selected parameters are tuned to be on the verge of their "critical" values, the QD coupled to the MNP and the external field acts as an ultra-fast nano-switch that exhibits highly sensitive transitions between coherent "dark" and "bright" metaresonant states. In the bright state, the effective field experienced by the QD is enhanced and in the dark state which corresponds to PMR (where $\tau_p \to \infty$ as stated earlier), the optical field felt by the QD is significantly screened [105]. Thus, Plasmonic metaresonances can potentially form the basis for a wide range of chemically, biologically or physically triggered optical nanoswitches that are sensitive to ultra-small variations in the environment [105].

For example, given that the refractive index of the host medium and other system properties are kept constant, PMR occurs when the MNP-QD centre separation reaches a critical value (R_c) which enables the detection of distance variations at sub-nanometer resolution using optical techniques, as illustrated in Fig. 7.1(b).

All previous theoretical studies on PMR encountered so far utilize the conventional local response approximation (LRA) [11] when modeling the plasmonic near-field, and MNP-independent decay and dephasing rates when modeling the QD [29,30,102,105,115,116]. This chapter focuses on addressing these limitations via improved modeling of plasmonic metaresonances, by taking the nonlocal plasmonic response, and MNP polarization dependent QD decay and dephasing into account. An approach based on the generalized nonlocal optical response (GNOR) theory [11,11,13,114] is utilized for this purpose. When referring to the proposed nonlocal and the conventional local models, the plasmonically induced time delay τ_p will be referred to as τ_{NL} and τ_L, respectively, throughout this chapter.

7.1 Numerical Model Overview

Both analytical and numerical solutions to the modified system Bloch equations in (5.22) were used to obtain the steady state and temporal simulation results presented in this section. The numerical solutions were obtained using the ODE45 solver in MATLAB software. The default set of parameters used throughout this chapter is as follows. The input to the system is an external coherent electric field with an angular frequency $\omega = 2.28\,\text{eV}$ and a step amplitude E_0 with a 10 ns delay (during which $E_0 = 0$) and a steady state value of $2 \times 10^4\,\text{V m}^{-1}$. This field is assumed to be polarized parallel to the hybrid molecular axis ($s_\alpha = 2$). Polarization and population relaxation times of the isolated QD are $T_0 = 0.37\,\text{ns}^{-1}$ and $\tau_0 = 0.8\,\text{ns}^{-1}$, respectively [105]. The relative dielectric constant of the QD,

$\epsilon_s = 6$ [13]. The angular frequency of the QD excitonic resonance, $\omega_{qd} = 2.28\,\text{eV}$ and the QD is assumed to be in exact resonance with the externally incident field ($\omega = \omega_{qd}$). The nanohybrid used in this study comprises a silver MNP with radius $a = 8\,\text{nm}$, bulk plasma frequency $\omega_p = 8.99\,\text{eV}$, bulk damping rate $\gamma = 0.025\,\text{eV}$, Fermi velocity $v_F = 1.39 \times 10^6\,\text{m}\,\text{s}^{-1}$ and diffusion constant $D \approx 9.624 \times 10^{-4}\,\text{m}^2\,\text{s}^{-1}$ [11, 114] whereas the experimental dielectric permittivity of silver (ϵ_{exp}) is obtained using the tabulations of Johnson and Christy in Ref. [60]. The centre separation between the MNP and QD is initially fixed at $R = 18\,\text{nm}$ and the permittivity of the submerging aqueous medium is assumed to be $\epsilon_b = 1.8$ [115, 116]. The above set of parameters would be used throughout this section except where it is specifically mentioned otherwise.

7.2 Impact of Submerging Permittivity Variations

Fig. 7.2 portrays the QD behavior when the host medium permittivity is varied in the close vicinity of $\epsilon_b = 1.8$, as predicted by both LRA and GNOR based approaches. Fig. 7.2(b), (e) and (h) depict the top view of the $x = \epsilon_b$, $y = \mu$ surface plots of the real part of the normalized Rabi frequency experienced by the QD (Re $\left[\Omega_{12}^r\right]$), QD population difference (Δ) and QD absorption rate (Q_{qd}), respectively, in the presence of a near-field MNP modeled using the conventional LRA based framework. Sub-figures (c), (f) and (i) depict the respective quantities obtained using the GNOR based formalism.

From equation (5.9), it is evident that Ω_{12}^r is a direct measure of the effective field felt by the QD. As PMR relates to the dramatic screening of the effective field experienced by the QD due to coherent plasmonic effects, the dark blue areas where Re $\left[\Omega_{12}^r\right] \approx 0$ in Fig. 7.2(b) and (c) correspond to the PMR predictions by the LRA and GNOR models. Close inspection of the aforementioned sub-figures reveals that the regimes of transition from the dark (PMR) to bright metastates are

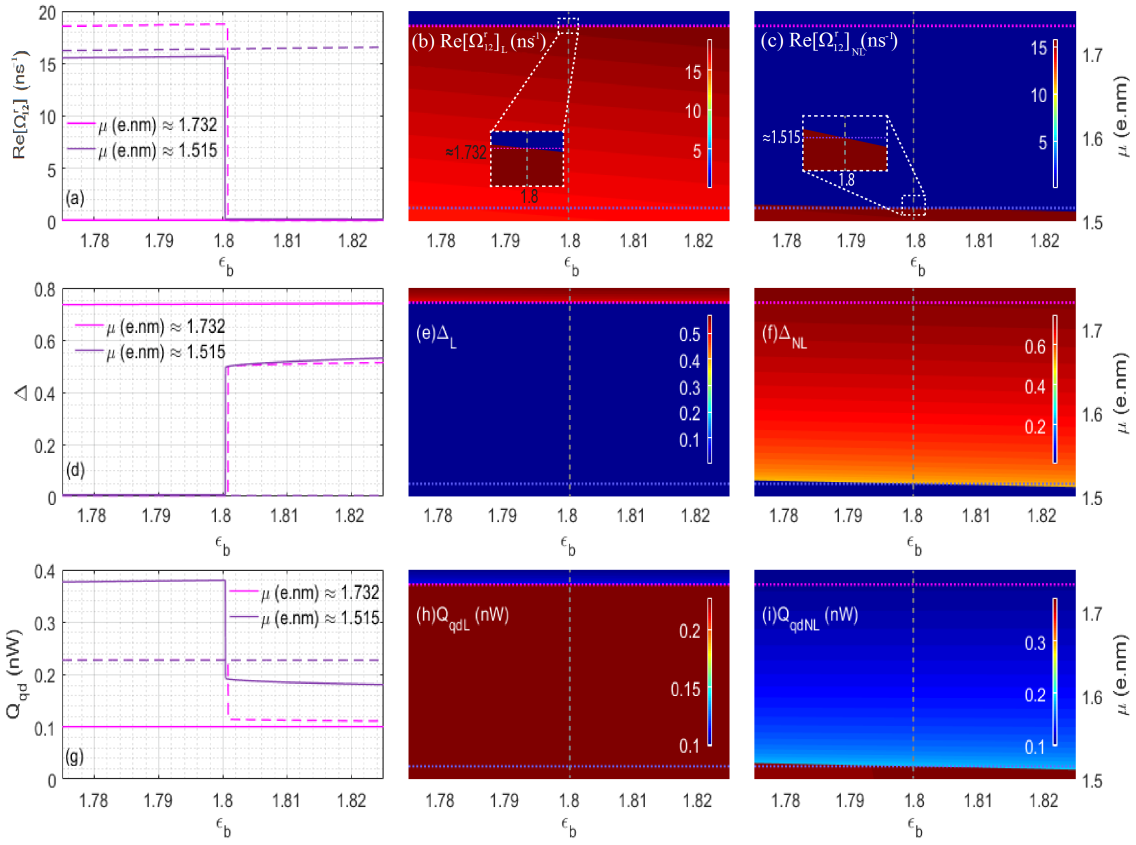

Figure 7.2: The steady state near-PMR behavior of the QD with varying permittivity of the submerging aqueous medium, analyzed using the conventional LRA and the proposed GNOR based approaches. Second and third columns depict the top view of $x = \epsilon_b$ (range: 1.775-1.825), $y = \mu$ (range: 1.5-1.75 e nm) color coded surface plots of the LRA based (subscript L) and GNOR based (subscript NL) results for the real part of the effective Rabi frequency experienced by the QD Re $\left[\Omega_{12}^{r}\right]$ (first row), QD population difference Δ (second row), and QD absorption rate Q_{qd} (third row), respectively. The pink and purple dotted lines in all surface plots correspond to the cross sections with the μ values where the PMR-related phase change is predicted when $\epsilon_b = 1.8$, by the LRA and GNOR models, respectively. The first column depicts the line-plots corresponding to the cross sections marked in pink and purple on the surface plots in the same row where solid lines represent the GNOR based plots (cross sections of the third column) and the dashed lines represent the conventional LRA based plots (cross sections of the second column).

observable as nearly horizontal (slant) boundaries near $\mu \approx 1.732\,\mathrm{e\,nm}$ (where e denotes the elementary charge) and $\mu \approx 1.515\,\mathrm{e\,nm}$ for the LRA and GNOR based predictions, respectively, for our chosen system parameter space. For the purpose of comparison in the context of PMR-related applications suggested in Sec. 11, we focus on the surface plot cross section where PMR-related phase transition occurs when the submerging permittivity reaches $\epsilon_\mathrm{b} = 1.8$. The two relevant cross sections are marked as pink (at $\mu = \mu_\mathrm{L} \approx 1.732\,\mathrm{e\,nm}$) and purple (at $\mu = \mu_\mathrm{NL} \approx 1.515\,\mathrm{e\,nm}$) dotted lines on both surface plots in Fig. 7.2(b) and (c). The line-plots corresponding to these surface-plot cross sections are shown in Fig. 7.2(a), where the dashed lines correspond to the LRA based cross sections (pink and purple) and the solid lines correspond to the respective GNOR based results. When the QD dipole moment $\mu = \mu_\mathrm{L}$, the LRA based model predicts a state shift from bright to dark state at $\epsilon_\mathrm{b} = 1.8$, whereas the GNOR based model states that the system remains in the dark state for all host permittivities considered. In contrast, at $\mu = \mu_\mathrm{NL}$ where the GNOR based model predicts the bright to dark state shift at $\epsilon_\mathrm{b} = 1.8$, the LRA based model predicts the system to be remaining in the bright state for all host permittivities, as shown in Fig. 7.2(a). Comparison between the above LRA and GNOR based results reveals that omitting the MNP nonlocal response substantially over-estimates the QD dipole moment needed to achieve near-PMR state switching for the submerging medium of our interest.

The second and third rows of Fig. 7.2 depict similar analyses for the QD population difference Δ and QD absorption rate Q_qd. Juxtaposition of Fig. 7.2(a) and (d) reveals that the bright to dark state switching maps to a QD population difference shift from 0 to (approximately) 0.5. Moreover, as shown in Fig. 7.2(g), the predictions for Q_qd obtained using both LRA and GNOR formalisms are qualitatively similar to the respective Re $\left[\Omega_{12}^r\right]$ counterparts.

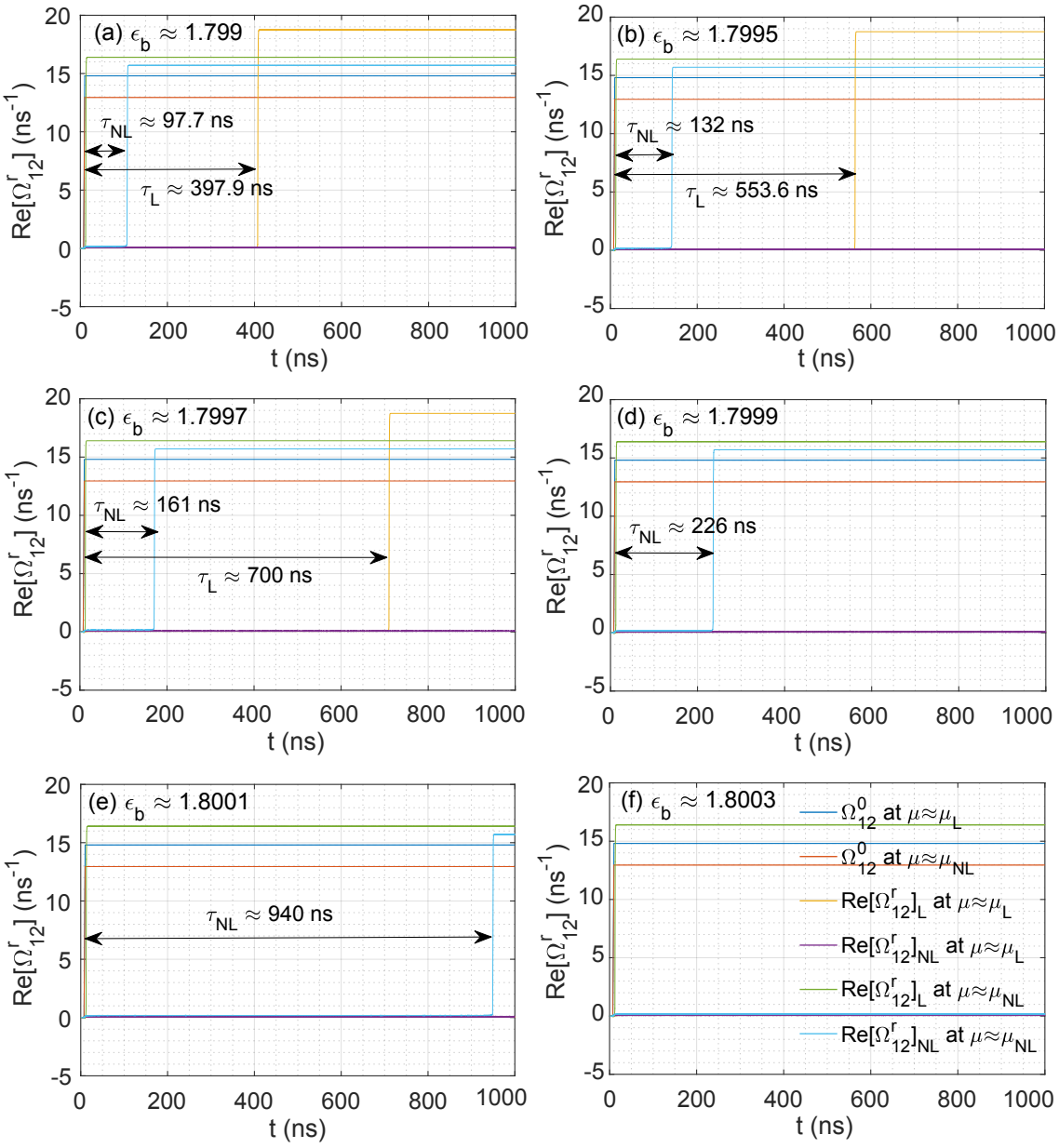

Figure 7.3: Analysis of the temporal dynamics predicted by the conventional LRA based (subscript L) and GNOR based (subscript NL) analyses for $\mu = \mu_{\text{L}} \approx 1.732\,\text{e}\,\text{nm}$ and $\mu = \mu_{\text{NL}} \approx 1.515\,\text{e}\,\text{nm}$, for different submerging medium permittivities in the close vicinity of $\epsilon_{\text{b}} = 1.8$.

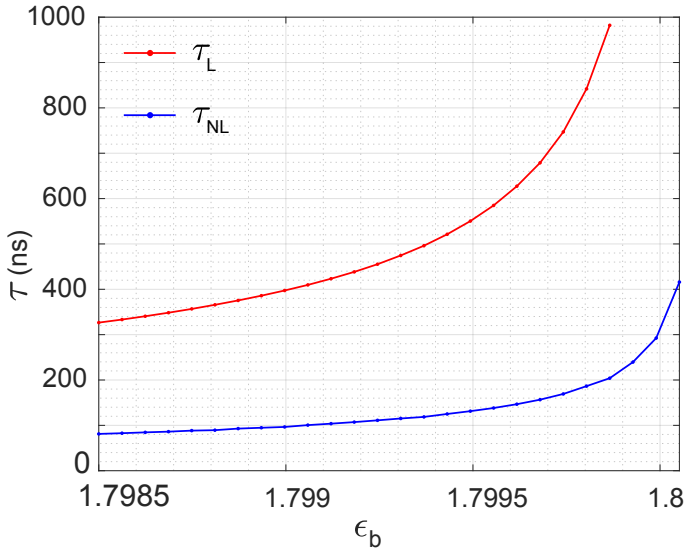

Figure 7.4: Variation of the plasmonically induced response delay for the LRA (subscript L) and GNOR (subscript NL) based nanoswitches operating at $\epsilon_b = 1.8$.

7.3 Environmental Impact on Temporal Dynamics

In this section, using Fig. 7.3, let us analyse the near-PMR temporal dynamics corresponding to the four line-plots observed in Fig. 7.2(a), where we identified μ_L and μ_{NL} as the two dipole moment values corresponding to the LRA and GNOR based selections for μ to achieve PMR switching at $\epsilon_b = 1.8$, when all other parameters are kept common. The bare Rabi frequencies experienced by isolated QDs with dipole moments μ_L and μ_{NL} upon the incidence of an electric field with amplitude E_0 (which has a delay time of 10 ns) results in the respective blue and red solid lines replicated in all subplots, Fig. 7.3(a)-(f). It can be observed that the bare Rabi frequency (Ω_0) follows the same step-rise as the input signal amplitude in the absence of any plasmonic influence.

The steady state values of the solid lines in each sub-figure of Fig. 7.3 correspond to dots extracted from Fig. 7.2(a) for six different ϵ_b values in the close vicinity of $\epsilon_b = 1.8$. The plasmonically induced time delay τ_p is labeled as τ_L for the LRA based case and as τ_{NL} for the GNOR based case, in each sub-figure. The

yellow and blue solid lines of Fig. 7.3 correspond to the two scenarios with PMR switching at $\epsilon_b = 1.8$. For the solid yellow lines which depict the temporal variation of Re $\left[\Omega_{12}^r\right]$ as predicted by the LRA based model for $\mu = \mu_L \approx 1.732\,\mathrm{e\,nm}$, the predicted response delay for $\epsilon_b \approx 1.799$ is approximately 398 ns. The same exceeds 1000 ns when the value of ϵ_b tends to 1.7999. This behaviour mimics the fall of the corresponding steady state curve depicted by the pink dashed line in Fig. 7.2(a) from the bright to dark state. Similarly, the variation of the solid blue temporal curves in Fig. 7.3 mimic the PMR switching of the GNOR based ($\mu = \mu_{NL} \approx 1.515\,\mathrm{e\,nm}$) purple solid line in Fig. 7.2(a). For these curves, the GNOR based plasmonic time delay $\tau_{NL} \approx 98$ ns at $\epsilon_b \approx 1.799$ which subsequently exceeds 1000 ns at $\epsilon_b \approx 1.8003$.

The green curves in Fig. 7.3(a)-(f) represent the temporal variation of Re $\left[\Omega_{12}^r\right]$ obtained using the LRA based formalism for $\mu = \mu_{NL} \approx 1.515\,\mathrm{e\,nm}$. It is readily observable that these curves display nearly zero plasmonic time delay for all near-PMR ϵ_b values considered, which mimics the system residing in the bright state for all submerging permittivities as shown in the purple dashed line of Fig. 7.2(a). In contrast, the GNOR based curves for $\mu = \mu_L \approx 1.732\,\mathrm{e\,nm}$ (pink) in Fig. 7.3(a)-(f) comprise $\tau_p > 1000$ ns for all considered ϵ_b values, which is a clear indication of the system residing in the dark or PMR state, as indicated by the pink solid line in Fig. 7.2(a).

Finally, using Fig. 7.4, we peruse the variation of the plasmonically induced time delays of the LRA (τ_L) and GNOR (τ_{NL}) based nanoswitches operating at $\epsilon_b = 1.8$. It is evident that τ_L far exceeds τ_{NL} for all near-PMR ϵ_b values considered.

7.4 Distance Dependent Plasmonic Metaresonances

As it was outlined earlier in the introduction section, PMRs occur in the space/time domain and switching can be achieved by tuning different nanohybrid and host

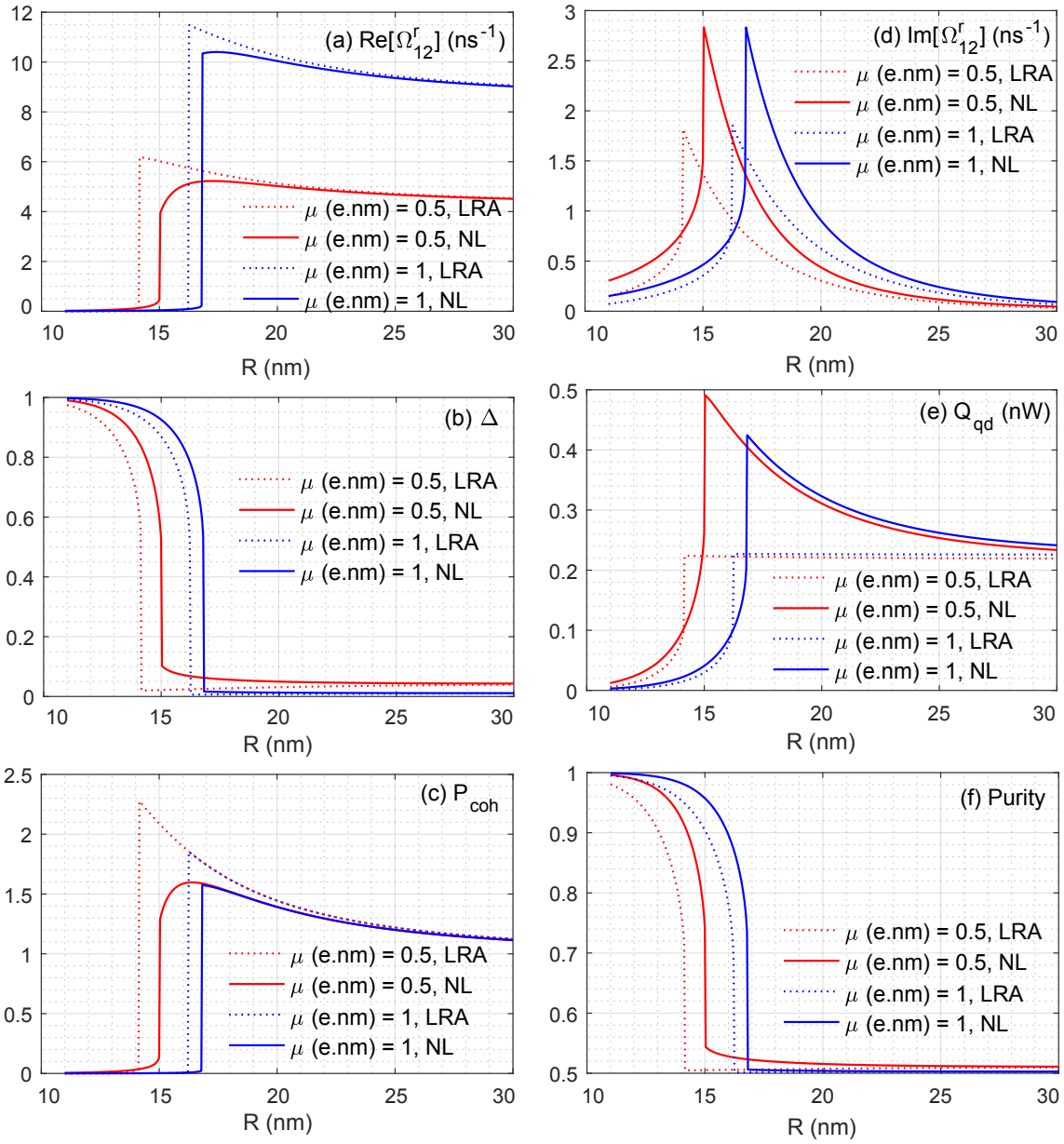

Figure 7.5: The steady analysis of the system as a function of MNP-QD centre separation R, for two different values of the QD dipole moment μ, in an aqueous submerging medium with $\epsilon_b = 1.8$. The solid red and blue lines depict the GNOR based results for nanohybrids with QD dipole moments $\mu = 0.5\,\mathrm{e\,nm}$ and $1\,\mathrm{e\,nm}$, respectively. The dashed curves depict the corresponding LRA based results. (a) Variation of the real part of effective Rabi frequency Ω^r_{12} experienced by the QD in the presence of coherent plasmonic effects (b) Variation of QD population difference Δ (c) Coherent plasmonic field enhancement P_{coh} experienced by the QD (d) Imaginary part of the effective Rabi frequency Ω^r_{12} (e) QD energy absorption rate Q_{qd} (f) Variation of the quantum state purity of the QD under the influence of the MNP

medium properties such as the QD dipole moment, submerging permittivity and MNP-QD centre separation. In this section, let us focus on analyzing the MNP-QD centre separation dependence of plasmonic metaresonances.

Fig. 7.5 depicts the real and imaginary parts of the effective Rabi frequency Ω_{12}^r, QD population difference Δ, coherent plasmonic field enhancement $\mathrm{P_{coh}}$, QD absorption rate Q_{qd} and the quantum state purity as functions of the MNP-QD centre separation R, in the temporal steady state. It is assumed that the MNP-QD nanohybrid is be submerged in the same aqueous host medium with permittivity $\epsilon_{\mathrm{b}} = 1.8$. The displayed results have been obtained for $\mu = 0.5\,\mathrm{e\,nm}$ and $\mu = 1\,\mathrm{e\,nm}$, using both LRA and GNOR based approaches.

Fig. 7.5(a) shows the variation of $\mathrm{Re}\left[\Omega_{12}^r\right]$ which adheres to the distinct near PMR behavior of the effective Rabi frequency identified in literature [105]. For both values of μ considered (μ_{L} and μ_{NL}), and for both LRA and GNOR based models, $\mathrm{Re}\left[\Omega_{12}^r\right] \approx \Omega_0$ for large R, and the field experienced by the QD is approximately equal to the externally incident field. When R is decreased, $\mathrm{Re}\left[\Omega_{12}^r\right]$ (and hence the effective field experienced by the QD) shows an overall increasing trend. When R is decreased further, we reach a critical distance R_{c} where the effective field exhibits an abrupt, significant decrease. Thus, R_{c} marks the transition from the bright state (where QD experiences a sizable effective plasmonic field) to the dark state (where the effective field experienced by the QD is dramatically screened), which is an indication of the system reaching a PMR. For $\mu = 0.5\,\mathrm{e\,nm}$ the LRA based model predicts $R_{\mathrm{c}} \approx 14.2\,\mathrm{nm}$ whereas the GNOR based model predicts $R_{\mathrm{c}} \approx 15\,\mathrm{nm}$. Similarly, the approximate LRA and GNOR based predictions for R_{c} when $\mu = 1\,\mathrm{e\,nm}$ are 16.2 nm and 16.8 nm, respectively. Moreover, as portrayed in Fig. 7.5(c), all curves of coherent plasmonic field enhancement $\mathrm{P_{coh}}$ display qualitatively similar variations to the respective $\mathrm{Re}\left[\Omega_{12}^r\right]$ in Fig. 7.5(a), with scaled magnitudes due to normalization by the bare Rabi frequency Ω_0. When $R \to \infty$, $\mathrm{P_{coh}} \to 1$ as $\Omega_{12}^r \to \Omega_0$.

It is evident from Fig. 7.5(d) that the effective Rabi frequency (and hence the effective field) experienced by the QD becomes complex valued for MNP-QD centre separations close to R_c. The physical interpretation of this observation would be that the coherent plasmonic effects induced by the neighboring MNP cause the generation of an extra phase in the effective field [105]. It can be observed that Im $\left[\Omega_{12}^r\right] \rightarrow 0$ when $R \rightarrow \infty$ resulting in $\Omega_{12}^r \rightarrow \Omega_0$, due to diminishing plasmonic impact. When R is gradually decreased, Im $\left[\Omega_{12}^r\right]$ non-linearly increases, reaching a peak at R_c. It experiences an abrupt decrease at R_c after which it gradually tends to zero. This qualitative behavior of Im $\left[\Omega_{12}^r\right]$ is commonly followed by all four curves portrayed in Fig. 7.5(d). It is interesting to note that, under both LRA and GNOR based modeling, the value of μ seems to have negligible contribution to the peak magnitude of Im $\left[\Omega_{12}^r\right]$, in contrast to its real valued component. It can also be observed that the LRA model significantly under-estimates the peak values of Im $\left[\Omega_{12}^r\right]$ for both values of μ considered.

Fig. 7.5(b) depicts the variation of QD population difference Δ as a function of MNP-QD centre separation R. At small values of R preceding R_c which map to the PMR (dark) state where the effective field on QD is dramatically screened, $\Delta \approx 1$, which implies a high probability of the QD residing in the excitonic ground state. As R is increased, Δ decreases gradually until it encounters a dramatic vertical drop at $R = R_c$ and the nanohybrid switches to the bright state where $\Delta \rightarrow 0$ and QD exhibits nearly equal probabilities of residing in the excitonic ground or excited states ($\rho_{11} \approx \rho_{22}$). It can be observed that the LRA model predicts the bright state Δ values to be more closer to 0 compared to the relevant GNOR based predictions. Moreover, both models predict lower bright state Δ values at the higher μ value.

Comparison of Fig. 7.5(b) with Fig. 7.5(f) reveals that the variation of population difference bears a high (qualitative) resemblance to the respective quantum state purity plots. We can also observe that when $\Delta \rightarrow 1$ with decreasing R in

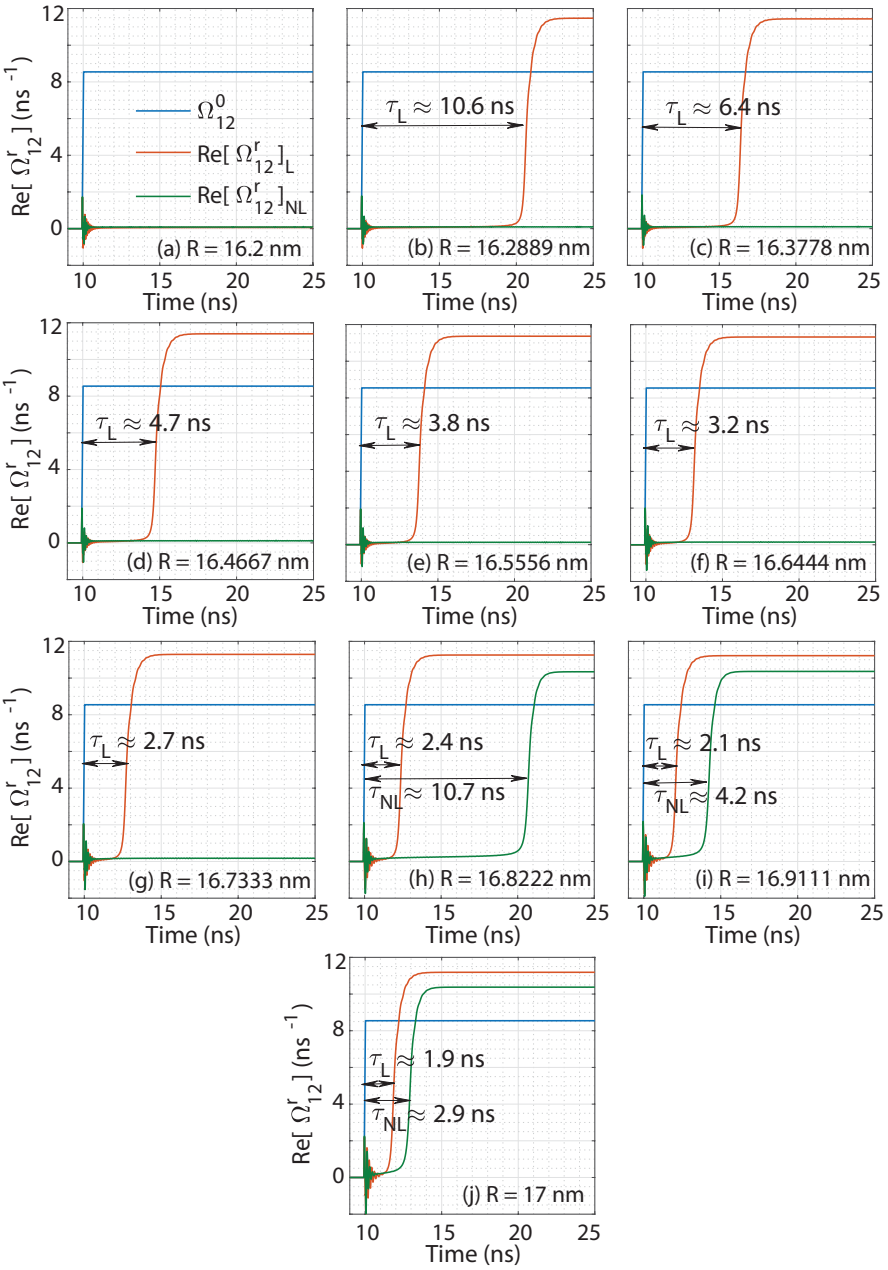

Figure 7.6: Analysis of the temporal dynamics predicted by the conventional LRA based (subscript L) and GNOR based (subscript NL) methods for $\mu = 1\,\mathrm{e\,nm}$ at different near PMR centre separation distances. In all sub-figures, the solid blue line shows the Rabi frequency experienced by the isolated QD, which follows the step-rise of the input field amplitude E_0. The orange and green curves represent the LRA and GNOR based results, respectively whereas τ_{L} and τ_{NL} refer to the plasmonically induced time delay τ_{p} as predicted by the two models.

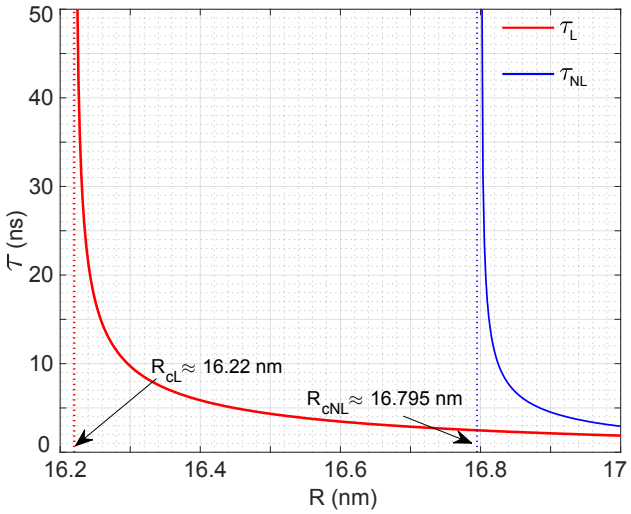

Figure 7.7: Variation of the plasmonically induced response delay for the LRA (subscript L) and GNOR (subscript NL) based nanoswitches operating at $\epsilon_b = 1.8$ and $\mu = 1\,\mathrm{e\,nm}$. R_{cL} and R_{cNL} refer to the LRA and GNOR based predictions for the critical centre separation where PMR switching occurs.

Table A1: Comparison of near-PMR response delays predicted by LRA and GNOR based models for different R

R(nm)	τ_L(ns)	τ_{NL}(ns)
16.2	> 2000	> 2000
16.2889	10.6185	> 2000
16.3778	6.3925	> 2000
16.4667	4.7429	> 2000
16.5556	3.8098	> 2000
16.6444	3.1837	> 2000
16.7333	2.7304	> 2000
16.8222	2.3815	10.6989
16.9111	2.1036	4.2486
17	1.8849	2.9372

the dark (PMR) state, Purity $\rightarrow 1$ which is an indication of the QD residing in a completely pure quantum state [13]. Moreover, when $\Delta \rightarrow 0$ in the bright state, Purity $\rightarrow 0.5$ where $\rho_{11} \rightarrow 0.5$ and $\rho_{22} \rightarrow 0.5$ leading the QD to a completely mixed quantum state.

Let us finally study the variation of Q_{qd} depicted in Fig. 7.5(e). It reveals that the LRA based model substantially underestimates the QD absorption rate in the

bright state ($R > R_c$). The GNOR based plots also reveal that the peak absorption rate (observed at the relevant R_c) for $\mu = 0.5\,\mathrm{e\,nm}$ surpasses the peak absorption rate at $\mu = 1\,\mathrm{e\,nm}$ which could be attributable to the incomplete vanishing of Δ for $\mu = 0.5\,\mathrm{e\,nm}$ near R_c.

Impact of Centre Separation on Temporal Dynamics

Using Fig. 7.6, we can analyse the near-PMR temporal dynamics of the $\mu = 1\,\mathrm{e\,nm}$ system introduced earlier in section 7.4, using both LRA and GNOR based formalisms. The bare Rabi frequency experienced by the isolated QD, which undergoes the same step-like variation as E_0, is shown by a solid blue line in each sub-figure. At the onset of its step-rise, both orange and green curves that correspond to the respective LRA and GNOR based predictions of Re $\left[\Omega_{12}^r\right]$ display transient oscillations, after which both systems predict a period of plasmonically induced screening of the effective field. We study the temporal variation at different centre separation values from $16.2 - 17\,\mathrm{nm}$ using ten subplots where we have labeled the plasmonically induced time delay τ_p predicted by the LRA and GNOR models as τ_L and τ_{NL} respectively, following our usual convention. It can be observed that both τ_L and τ_{NL} decrease with increasing R, and that $\tau_L < \tau_{NL}$, for the selected parameter region. These results are summarized using Table A1.

Fig. 7.7, depicts the variation of τ_L and τ_{NL} as functions of R, where asymptotes are observable near the R_c values predicted by the LRA (R_{cL}) and GNOR (R_{cNL}) models. The values of centre separations at the asymptotes closely match the respective R values where the abrupt drops of Re $\left[\Omega_{12}^r\right]$ were observed in Fig. 7.5(a), as both scenarios indicate the system switching from the bright to the dark (PMR) state.

7.5 Summary of Physical Observations

The aim of this chapter was to peruse numerically modeled plasmonic metaresonances (PMRs) in a coherently illuminated quantum dot (QD), coupled to a neighboring metal nanoparticle (MNP), using a generalized nonlocal optical response (GNOR) method based approach, taking the MNP dependence of the QD decay and dephasing rates into account. It revealed the impact of different system parameters such as QD dipole moment, MNP-QD centre separation and submerging medium permittivity on the formation of PMRs, under both the conventional LRA based and the improved GNOR based approaches. Comparison of the improved GNOR based results with the conventional LRA based counterparts clearly indicated that the omission of MNP nonlocal response and MNP induced decay and dephasing rate modifications causes implications such as significant over-estimation of the QD dipole moment required to achieve PMR, underestimation of the critical centre separation and prediction of significantly lower near-PMR QD absorption rates, in comparison to the GNOR based predictions. Later in this thesis, chapter 11 will utilize the GNOR based approach of modeling PMRs to demonstrate the prospects of using PMR based nanoswitches in prospective biomedical applications.

Chapter 8

Cavity-QED based Characterization of Nanohybrid Scattering Spectra

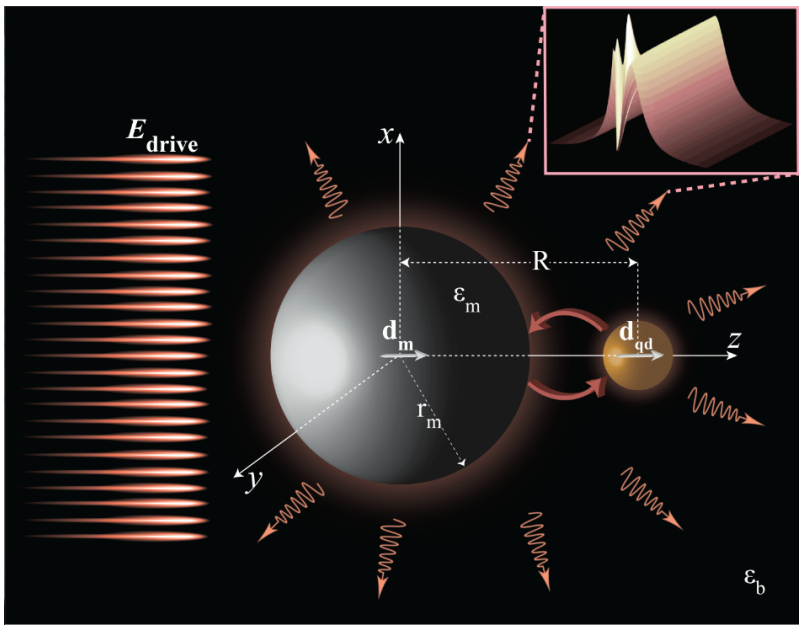

Figure 8.1: The schematic diagram of the MNP-QD hybrid molecule in the external driving field [2]. The right insert shows an example Rayleigh scattering spectrum of the hybrid molecule.

Taking a step further from the previous semi-classical descriptions, where the quantum dot (QD) is treated quantum mechanically and the metal nanoparticle (MNP) is treated classically, this chapter is dedicated to analytically modeling the entire MNP-QD hybrid molecule incident by an external driving field as an open quantum system using a cavity-QED approach. The process incorporates quan-

tum mechanically modeling the dipole moment operator and the dipole response field of the metal nanoparticle taking the nonlocal effects into account using the usual GNOR based approach.

When a hybrid MNP-QD nanomolecule is optically excited, an additional electric field superposed on the external driving field is experienced by the MNP due to the dipole moment of the optical transitions in the QD. The resulting electric field induces a dipole moment in the MNP which in turn alters the field experienced by the QD leading to a self-feedback [117]. Due to this interaction, artificial hybrid nanomolecules formed by placing MNPs in close proximity with QDs exhibit fascinating scattering properties. This chapter presents an analytical model usable to study such scattering spectra.

8.1 Overview of the Model

Pertaining to our earlier discussions, this chapter too considers a hybrid molecule comprising a spherical, non-magnetic MNP of radius r_{m} coupled to a QD of radius r_{qd} embedded in a homogenous dielectric bath with a real positive relative permittivity ϵ_{b} as shown in Fig. 8.1. The MNP and QD are separated by a distance R, allowing no direct tunneling between them ($R - r_{\mathrm{m}} - r_{\mathrm{qd}} > 2 \times 10^{-9}\,\mathrm{m}$) [97]. The hybrid molecule is excited by an external electric field $\boldsymbol{E}_{\mathrm{drive}} = \tilde{\boldsymbol{\epsilon}}(E_0^+ e^{-\mathrm{i}\omega t} + E_0^- e^{\mathrm{i}\omega t})$ where i is the imaginary unit, ω is the angular frequency and $\tilde{\boldsymbol{\epsilon}}$ is a unit vector along or perpendicular to the axis of the hybrid molecule. Let us recall that the physics sign convention where a positive energy $\hbar\omega$ maps to a positive frequency component, oscillating as $e^{-\mathrm{i}\omega t}$ [118] is used throughout this thesis. Therefore, E_0^+ and E_0^- are the respective positive and negative frequency coefficients, where $E_0^+ = E_0^- = E_0$ for the case of $\boldsymbol{E}_{\mathrm{drive}}$. The applied field polarizes both the MNP and the QD, allowing a dipole-dipole coupling between them.

8.2 Cavity QED based Analysis of the Nanohybrid

Let us now analyse our hybrid molecule in the external driving field (see Fig. 8.1) quantum mechanically, with the aid of cavity QED methods.

In this chapter, the field arising due to the surface plasmons (SPs) in the metal nanoparticle is quantized by associating each mode with a quantum simple harmonic oscillator. For each oscillator mode k, n_k and $|n_k\rangle$ denote the number of surface plasmons and the Fock (or number) state, respectively. For subwavelength particles, SP resonance corresponds to a dipole mode [119]. Assuming the resemblance to a cavity mode with the the vacuum state placed at zero energy level, the Schrödinger picture Hamiltonian of the unperturbed SP dipole mode can be written as,

$$\hat{\mathcal{H}}_{\mathrm{m}}^{\mathrm{Sch}} = \hbar\omega_{\mathrm{m}}\hat{a}^{\dagger}\hat{a}, \tag{8.1}$$

where ω_{m}, $\hat{a}$ and $\hat{a}^{\dagger}$ denote the plasmonic resonance energy, SP annihilation and creation operators, respectively [120]. Then, the Hamiltonian of our coupled quantum system in the Schrödinger picture is obtainable as follows,

$$\hat{\mathcal{H}}_{\mathrm{sys}}^{\mathrm{Sch}} = \hat{\mathcal{H}}_{\mathrm{m}}^{\mathrm{Sch}} + \hat{\mathcal{H}}_{\mathrm{qd}}^{\mathrm{Sch}} + \hat{\mathcal{H}}_{\mathrm{int}}^{\mathrm{Sch}} + \hat{\mathcal{H}}_{\mathrm{drive}}^{\mathrm{Sch}}. \tag{8.2}$$

where $\hat{\mathcal{H}}_{\mathrm{qd}}^{\mathrm{Sch}}$, $\hat{\mathcal{H}}_{\mathrm{int}}^{\mathrm{Sch}}$ and $\hat{\mathcal{H}}_{\mathrm{drive}}^{\mathrm{Sch}}$ denote the unperturbed QD Hamiltonian, the interaction Hamiltonian between the QD and MNP, and the interaction Hamiltonian of the total hybrid molecule with the external driving field, respectively.

In chapter 5, the QD state raising and lowering operators were obtained as $\hat{\sigma}^{\dagger} = |e\rangle\langle g|$ and $\hat{\sigma} = |g\rangle\langle e|$. Re-defining ω_{qd} as the frequency of the excitonic transition between $|e\rangle$ and $|g\rangle$ (to easily distinguish QD and MNP resonances) and the energy of the ground state to be zero, we can obtain $\hat{\mathcal{H}}_{\mathrm{qd}}^{\mathrm{Sch}} = \hbar\omega_{\mathrm{qd}}\hat{\sigma}^{\dagger}\hat{\sigma}$ [2].

The Hamiltonian component $\hat{\mathcal{H}}_{\mathrm{int}}^{\mathrm{Sch}}$ can be calculated as the dipole energy of the QD kept in the dipole response field created by the MNP. In the cavity QED

treatment of the hybrid molecule, the electric field operator of the surface plasmon $\hat{E}_{\mathrm{m}}$ is approximated by a cavity mode [97], where its positive frequency component relates to the plasmon field annihilation operator as [121–123],

$$\hat{E}_{\mathrm{m}}^{+} \approx \mathrm{i}\mathcal{E}\hat{a}. \tag{8.3}$$

An expression for the coefficient $\mathcal{E}$ will be derived towards the end of this section.

The optical decay of the QD from the excited state $|e\rangle$ to the ground state $|g\rangle$ is associated with the transition dipole operator $\hat{d}_{\mathrm{qd}} = \mu_{\mathrm{qd}}^{*}\hat{\sigma} + \mu_{\mathrm{qd}}\hat{\sigma}^{\dagger}$. With the dipole moment element μ_{qd} assumed real, this simplifies to [124],

$$\hat{d}_{\mathrm{qd}} = \mu_{\mathrm{qd}}\left(\hat{\sigma} + \hat{\sigma}^{\dagger}\right) = \hat{d}_{\mathrm{qd}}^{+} + \hat{d}_{\mathrm{qd}}^{-}, \tag{8.4}$$

where $\hat{d}_{\mathrm{qd}}^{+} = \mu_{\mathrm{qd}}\hat{\sigma}$ and $\hat{d}_{\mathrm{qd}}^{-} = \mu_{\mathrm{qd}}\hat{\sigma}^{\dagger}$ denote the positive and negative frequency components that will oscillate as $e^{-\mathrm{i}\omega t}$ and $e^{\mathrm{i}\omega t}$ respectively, when converted to the interaction picture. Following the description of atom-light coupling within the dipole approximation [76, 98], $\hat{\mathcal{H}}_{\mathrm{int}}^{\mathrm{Sch}}$ can be written as,

$$\hat{\mathcal{H}}_{\mathrm{int}}^{\mathrm{Sch}} = -\hat{d}_{\mathrm{qd}}.\hat{E}_{\mathrm{m}} \approx -\left(\hat{d}_{\mathrm{qd}}^{+}\hat{E}_{\mathrm{m}}^{-} + \hat{d}_{\mathrm{qd}}^{-}\hat{E}_{\mathrm{m}}^{+}\right), \tag{8.5}$$

where the non-energy conserving fast oscillating terms have been eliminated using the rotating wave approximation. Substituting (8.3) and (8.4) in (8.5), we arrive at,

$$\hat{\mathcal{H}}_{\mathrm{int}}^{\mathrm{Sch}} = \mathrm{i}\hbar g\left(\hat{\sigma}\hat{a}^{\dagger} - \hat{\sigma}^{\dagger}\hat{a}\right), \tag{8.6}$$

where the coupling constant g is defined as [97],

$$g = \frac{\mu_{\mathrm{qd}}\mathcal{E}}{\hbar}. \tag{8.7}$$

Let us now proceed to derive an expression for the Hamiltonian term $\hat{\mathcal{H}}_{\mathrm{drive}}^{\mathrm{Sch}}$

which results from the dipole interaction of the MNP and QD with E_{drive}. We first define the dipole moment operator of the MNP as,

$$\hat{d}_{\text{m}} = \hat{d}_{\text{m}}^{+} + \hat{d}_{\text{m}}^{-} = \mu_{\text{m}}^{*}\hat{a} + \mu_{\text{m}}\hat{a}^{\dagger}, \tag{8.8}$$

where μ_{m} is the dipole moment element of $\hat{d}_{\text{m}}$. This enables us to write,

$$\hat{\mathcal{H}}_{\text{drive}}^{\text{Sch}} = -E_{\text{drive}}(\hat{d}_{\text{qd}} + \hat{d}_{\text{m}}) \tag{8.9}$$

By substituting for E_{drive}, $\hat{d}_{\text{qd}}$, $\hat{d}_{\text{m}}$ and applying the rotating wave approximation, we can arrive at,

$$\hat{\mathcal{H}}_{\text{drive}}^{\text{Sch}} = -E_0\left(\mu_{\text{m}}\hat{a}^{\dagger}e^{-\text{i}\omega t} + \mu_{\text{m}}^{*}\hat{a}e^{\text{i}\omega t}\right) - E_0\mu_{\text{qd}}\left(\hat{\sigma}^{\dagger}e^{-\text{i}\omega t} + \hat{\sigma}e^{\text{i}\omega t}\right). \tag{8.10}$$

Substituting these results in (8.2) yields the complete expression for the system Hamiltonian in the Schrödinger picture. For the ease of proceeding with the calculations, we can then convert it to the interaction picture where the interaction frame rotates at the driving field frequency ω. Let us first recast the system Hamiltonian in the Schrödinger picture to the following form,

$$\hat{\mathcal{H}}_{\text{sys}}^{\text{Sch}} = \hat{\mathcal{H}}_0 + \hbar\Delta_{\text{m}}\hat{a}^{\dagger}\hat{a} + \hbar\Delta_{\text{qd}}\hat{\sigma}^{\dagger}\hat{\sigma} + \hat{\mathcal{H}}_{\text{int}}^{\text{Sch}} + \hat{\mathcal{H}}_{\text{drive}}^{\text{Sch}}, \tag{8.11}$$

where $\hat{\mathcal{H}}_0 = \hbar\omega\hat{a}^{\dagger}\hat{a} + \hbar\omega\hat{\sigma}^{\dagger}\hat{\sigma}$. The two detunings of the MNP and QD from E_{drive} are given the notations $\Delta_{\text{m}} = (\omega_{\text{m}} - \omega)$ and $\Delta_{\text{qd}} = (\omega_{\text{qd}} - \omega)$, respectively.

The interaction picture Hamiltonian in a frame rotating at frequency ω is defined as [125],

$$\hat{\mathcal{H}}_{\text{sys}}^{\text{Int}} = \hat{\mathcal{U}}_0^{\dagger}\hat{\mathcal{V}}\hat{\mathcal{U}}_0, \tag{8.12}$$

where $\hat{\mathcal{U}}_0 = e^{-\text{i}\hat{\mathcal{H}}_0 t/\hbar}$ and $\hat{\mathcal{V}} = \hat{\mathcal{H}}_{\text{sys}}^{\text{Sch}} - \hat{\mathcal{H}}_0$.

Simplification of (8.12) using a procedure similar to that outlined in section

3.2.2 results in the complete expression for the system Hamiltonian in the interaction picture [2],

$$\hat{\mathcal{H}}_{\text{sys}}^{\text{Int}} = \hbar\Delta_{\text{m}}\hat{a}^{\dagger}\hat{a} + \hbar\Delta_{\text{qd}}\hat{\sigma}^{\dagger}\hat{\sigma} + \text{i}\hbar g(\hat{a}^{\dagger}\hat{\sigma} - \hat{a}\hat{\sigma}^{\dagger}) - E_0\left(\hat{d}_{\text{m}} + \hat{d}_{\text{qd}}\right). \tag{8.13}$$

$\hat{\mathcal{H}}_{\text{sys}}^{\text{Int}}$ possesses dressed eigenstates [126] which govern the behaviour of the hybrid system.

The above Hamiltonian describes a closed quantum system where we have not yet taken the effects of the environment or the reservoir into account. However, the nanohybrid couples with the environment forming an open quantum system with irreversible dynamics. This interaction is modelled as a Markovian process [87]. The full quantum dynamics of the coupled nanosystem can be derived using the following master equation for the interaction picture density operator [97, 127],

$$\frac{\partial}{\partial t}\hat{\rho} = \frac{\text{i}}{\hbar}\left[\hat{\rho}, \hat{\mathcal{H}}_{\text{sys}}^{\text{Int}}\right] + \hat{\mathcal{L}}_{\text{qd}} + \hat{\mathcal{L}}_{\text{m}}, \tag{8.14}$$

where the Liouvillian terms $\hat{\mathcal{L}}_{\text{qd}}$ and $\hat{\mathcal{L}}_{\text{m}}$ are given by [87, 97, 127],

$$\hat{\mathcal{L}}_{\text{qd}} = \frac{\gamma_{\text{qd}}}{2}\left(2\hat{\sigma}\hat{\rho}\hat{\sigma}^{\dagger} - \hat{\sigma}^{\dagger}\hat{\sigma}\hat{\rho} - \hat{\rho}\hat{\sigma}^{\dagger}\hat{\sigma}\right), \tag{8.15a}$$

$$\hat{\mathcal{L}}_{\text{m}} = \frac{\gamma_{\text{m}}}{2}\left(2\hat{a}\hat{\rho}\hat{a}^{\dagger} - \hat{a}^{\dagger}\hat{a}\hat{\rho} - \hat{\rho}\hat{a}^{\dagger}\hat{a}\right), \tag{8.15b}$$

where the Markovian interaction with the reservoirs determines the decay rates γ_{qd} and γ_{m} for the QD exciton and the MNP surface plasmon respectively [97].

Recall that the expectation value of an observable $\hat{Q}$ can be obtained using the trace of the product of $\hat{\rho}$ and $\hat{Q}$ as $\langle\hat{Q}\rangle = \text{Tr}[\hat{\rho}\hat{Q}]$ [86]. Using this claim, we can obtain the equation of motion of $\langle\hat{a}\rangle$ in the interaction picture as,

$$\frac{\partial}{\partial t}\langle\hat{a}\rangle = \frac{\partial}{\partial t}\,\text{Tr}[\hat{a}\hat{\rho}] = \text{Tr}\left[\frac{\partial}{\partial t}\left(\hat{a}\hat{\rho}\right)\right] = \text{Tr}\left[\hat{a}\frac{\partial}{\partial t}\hat{\rho}\right]. \tag{8.16}$$

By inserting (8.13) in (8.14) and obtaining the trace of the entire expression multiplied by $\hat{a}$ yields,

$$\frac{\partial}{\partial t}\langle\hat{a}\rangle = \mathrm{Tr}\left[\hat{a}\left(\frac{\mathrm{i}}{\hbar}[\hat{\rho}, \hat{\mathcal{H}}_{\mathrm{sys}}^{\mathrm{Int}}] + \hat{\mathcal{L}}_{\mathrm{qd}} + \hat{\mathcal{L}}_{\mathrm{m}}\right)\right]. \tag{8.17}$$

Assuming the QD and MNP operators commute and using bosonic commutator relations for the MNP operators together with the cyclic property of trace, we can simplify (8.17) to obtain (see appendix E.1),

$$\frac{\partial}{\partial t}\langle\hat{a}\rangle = -\mathcal{D}_{\mathrm{m}}\langle\hat{a}\rangle + g\langle\hat{\sigma}\rangle + \mathcal{M}_{\mathrm{m}}, \tag{8.18}$$

where $\mathcal{D}_{\mathrm{m}} = \left(\mathrm{i}\Delta_{\mathrm{m}} + \gamma_{\mathrm{m}}/2\right)$ and $\mathcal{M}_{\mathrm{m}} = \mathrm{i}\mu_{\mathrm{m}}E_0/\hbar$. Solving (8.18) for the steady state by setting $\frac{\partial}{\partial t}\langle\hat{a}\rangle = 0$ yields [2],

$$\langle\hat{a}\rangle = \left(g\langle\hat{\sigma}\rangle + \mathcal{M}_{\mathrm{m}}\right)/\mathcal{D}_{\mathrm{m}}. \tag{8.19}$$

Similarly, as $\langle\hat{\sigma}\rangle = \mathrm{Tr}\left[\hat{\sigma}\hat{\rho}\right]$ we can write,

$$\frac{\partial}{\partial t}\langle\hat{\sigma}\rangle = \mathrm{Tr}\left[\hat{\sigma}\left(\frac{\mathrm{i}}{\hbar}[\hat{\rho}, \hat{\mathcal{H}}_{\mathrm{sys}}^{\mathrm{Int}}] + \hat{\mathcal{L}}_{\mathrm{qd}} + \hat{\mathcal{L}}_{\mathrm{m}}\right)\right]. \tag{8.20}$$

Using the definitions of $\hat{\sigma}$, $\hat{\sigma}^{\dagger}$ and the orthogonality relation of $|e\rangle$, $|g\rangle$ in the simplification of (8.20) we can arrive at the equation of motion for $\langle\hat{\sigma}\rangle$ as (see appendix E.2),

$$\frac{\partial}{\partial t}\langle\hat{\sigma}\rangle = -\mathcal{D}_{\mathrm{qd}}\langle\hat{\sigma}\rangle - \left(1 - 2\langle\hat{\sigma}^{\dagger}\hat{\sigma}\rangle\right)\left(g\langle\hat{a}\rangle - \mathcal{M}_{\mathrm{qd}}\right), \tag{8.21}$$

where $\mathcal{D}_{\mathrm{qd}} = \left(\mathrm{i}\Delta_{\mathrm{qd}} + \gamma_{\mathrm{qd}}/2\right)$ and $\mathcal{M}_{\mathrm{qd}} = \mathrm{i}\mu_{\mathrm{qd}}E_0/\hbar$. In the semiclassical formalism where the fields are well-defined (noise-free), the expectation values of the products of MNP and QD operators are separable [128]. The latter property was utilized in arriving at the result in (8.21).

For weak fields where the excitonic populations are minute ($\langle\hat{\sigma}^\dagger\hat{\sigma}\rangle \ll 1$) [97], we obtain the coupled expression for $\langle\hat{\sigma}\rangle$ at steady state as,

$$\langle\hat{\sigma}\rangle \approx \left(-g\langle\hat{a}\rangle + \mathcal{M}_{\mathrm{qd}}\right)/\mathcal{D}_{\mathrm{qd}}. \tag{8.22}$$

Solving the two coupled equations (8.19) and (8.22) we can obtain the decoupled analytical solutions for $\langle\hat{a}\rangle$ and $\langle\hat{\sigma}\rangle$ for weak fields, at steady state [2],

$$\langle\hat{a}\rangle \approx \frac{\mathcal{M}_{\mathrm{m}}\mathcal{D}_{\mathrm{qd}} + g\mathcal{M}_{\mathrm{qd}}}{\mathcal{D}_{\mathrm{m}}\mathcal{D}_{\mathrm{qd}} + g^2}, \tag{8.23a}$$

$$\langle\hat{\sigma}\rangle \approx \frac{\mathcal{M}_{\mathrm{qd}}\mathcal{D}_{\mathrm{m}} - g\mathcal{M}_{\mathrm{m}}}{\mathcal{D}_{\mathrm{m}}\mathcal{D}_{\mathrm{qd}} + g^2}. \tag{8.23b}$$

Let us now proceed to obtain expressions for the plasmon field amplitude $\mathcal{E}$ and the dipole matrix element μ_{m}. If the electric field operator is replaced with its mean value, we obtain the classical electric field that satisfies the Maxwell's equations [129]. Note that $\langle\hat{a}\rangle$ in (8.23a) is the expectation value of the Schrödinger picture annihilation operator, obtained using the interaction picture density matrix. Hence, $\langle\hat{a}\rangle$ yields the slowly varying amplitude of the expectation value of the interaction picture annihilation operator, $\langle\hat{a}_{\mathrm{I}}(t)\rangle = \langle\hat{a}\rangle e^{-\mathrm{i}\omega t}$. Similarly, for the QD, $\langle\hat{\sigma}_{\mathrm{I}}(t)\rangle = \langle\hat{\sigma}\rangle e^{-\mathrm{i}\omega t}$.

Let us first model the MNP under the LRA [11] where the nonlocal effects are neglected and the optical response is described by the LRA based polarizability (2.7). In this context, the classical positive electric field coefficient of the surface plasmon field felt by the QD is given in the LRA as (see appendix E.3),

$$E^{+}_{\mathrm{res}}\Big|_{r=R} \approx \frac{s_\alpha d^{+}_{\mathrm{m}}}{4\pi\epsilon_0\epsilon_b R^3}. \tag{8.24}$$

where d^{+}_{m} is the positive frequency component of the MNP's classical dipole mo-

ment,

$$d_{\mathrm{m}}^{+} \approx 4\pi\epsilon_0\epsilon_{\mathrm{b}}\beta_{\mathrm{LRA}}r_{\mathrm{m}}^{3}\left(E_0 + \frac{s_\alpha d_{\mathrm{qd}}^{+}}{4\pi\epsilon_0\epsilon_{\mathrm{b}}R^3}\right). \tag{8.25}$$

Equating the classical positive electric field coefficient of the surface plasmon field felt by the QD in (8.24), with the expectation value of the relevant quantum mechanical operator in (8.3), we obtain: $E_{\mathrm{res}}^{+}\big|_{r=R} = \langle \hat{E}_{\mathrm{m}}^{+} \rangle = \mathrm{i}\mathcal{E}\langle \hat{a} \rangle$. Similarly, from the expectation value of (8.4), we can obtain $d_{\mathrm{qd}}^{+} = \langle \hat{d}_{\mathrm{qd}}^{+} \rangle = \mu_{\mathrm{qd}}\langle \hat{\sigma} \rangle$.

Substituting for $E_{\mathrm{res}}^{+}\big|_{r=R}$ using (8.24) and (8.25), for $\langle \hat{a} \rangle$ using (8.19) and by separately equating the MNP response field components arising due to the QD and E_{drive}, we can arrive at the following under the LRA,

$$\mathcal{E} = \frac{s_\alpha}{R^3}\sqrt{\frac{\beta_{\mathrm{LRA}}r_{\mathrm{m}}^{3}\hbar\mathcal{D}_{\mathrm{m}}}{4i\pi\epsilon_0\epsilon_{\mathrm{b}}}}, \tag{8.26a}$$

$$\mu_{\mathrm{m}} = -\sqrt{4i\pi\epsilon_0\epsilon_{\mathrm{b}}\,\beta_{\mathrm{LRA}}r_{\mathrm{m}}^{3}\hbar\mathcal{D}_{\mathrm{m}}}. \tag{8.26b}$$

Let us now use (8.26b) and (8.19) to obtain an expression for $-\mu_{\mathrm{m}}\langle \hat{a} \rangle$ and compare the result with (8.25) as,

$$-\mu_{\mathrm{m}}\langle \hat{a} \rangle = 4\pi\epsilon_0\epsilon_{\mathrm{b}}\beta_{\mathrm{LRA}}r_{\mathrm{m}}^{3}\left(E_0 + \frac{s_\alpha d_{\mathrm{qd}}^{+}}{4\pi\epsilon_0\epsilon_b R^3}\right) = d_{\mathrm{m}}^{+}. \tag{8.27}$$

The astute reader will recall that obtaining the expectation value of (8.8) results in $d_{\mathrm{m}}^{+} = \langle \hat{d}_{\mathrm{m}}^{+} \rangle = \mu_{\mathrm{m}}^{*}\langle \hat{a} \rangle$. Therefore, $-\mu_{\mathrm{m}} \approx \mu_{\mathrm{m}}^{*}$ is the necessary condition for a given MNP to be successfully modeled by the cavity QED model. In the following section, we derive the approximate expression for μ_{m} of metals exhibiting good plasmonic properties that will meet this criteria [2].

8.3 Good Plasmonic Approximations

This section will present an overview of the good plasmonic materials that will be useful in our subsequent derivations.

A necessary condition for the existence of surface plasmons is $\mathrm{Re}\left[\epsilon_{\mathrm{m}}(\omega)\right] \in \mathbb{R}^{-}$ [130]. Such material show good plasmonic properties when [131],

$$\mathrm{Im}\left[\epsilon_{\mathrm{m}}(\omega)\right] \ll -\mathrm{Re}\left[\epsilon_{\mathrm{m}}(\omega)\right]. \tag{8.28}$$

Let us recall that the dipolar polarizability of the MNP α abides by the proportionality relation $\alpha \propto r_{\mathrm{m}}^{3}\beta_{\mathrm{LRA}} = r_{\mathrm{m}}^{3}\left(\epsilon_{\mathrm{m}}-\epsilon_{\mathrm{b}}\right)/\left(\epsilon_{\mathrm{m}}+2\epsilon_{\mathrm{b}}\right)$ [9]. It is evident that the polarizability experiences a resonant enhancement when $|\epsilon_{\mathrm{m}}(\omega)+2\epsilon_{\mathrm{b}}|$ is a minimum. For small $\mathrm{Im}[\epsilon_{\mathrm{m}}(\omega)]$ around the resonance, this simplifies to the Frölich condition in the LRA [9, 131],

$$\mathrm{Re}\left[\epsilon_{\mathrm{m}}(\omega_{\mathrm{m}})\right] \approx -2\epsilon_{\mathrm{b}}. \tag{8.29}$$

The magnitude of α at resonance is limited by the incomplete vanishing of its denominator, since $\mathrm{Im}[\epsilon_{\mathrm{m}}(\omega)] \neq 0$.

The rate of energy loss from the SP mode is proportional to $\mathrm{Im}\left[\epsilon_{\mathrm{m}}(\omega)\right]$ [132]. This leads to a finite lifetime of the SPs leading to a near-resonance decay rate [97, 131],

$$\gamma_{\mathrm{m}} \approx 2\eta\,\mathrm{Im}\left[\epsilon_{\mathrm{m}}(\omega_{\mathrm{m}})\right], \tag{8.30}$$

where,

$$\eta = \left(\frac{\mathrm{d}\,\mathrm{Re}\left[\epsilon_{\mathrm{m}}(\omega)\right]}{\mathrm{d}\,\omega}\right)^{-1}_{\omega=\omega_{\mathrm{m}}}. \tag{8.31}$$

When the dielectric losses are relatively small (which is applicable to the entire plasmonic region of noble metals), the Kramers-Kronig relations for $\epsilon_{\mathrm{m}}(\omega)$ [131] predicts that $\eta > 0$.

Applying (8.28), (8.29) and (8.30) in (8.26a) and (8.26b) when $\Delta_{\mathrm{m}} \approx 0$, we can obtain (see appendix E.4),

$$\mathcal{E} \approx \frac{s_\alpha}{R^3}\sqrt{\frac{3\hbar\eta r_{\mathrm{m}}^3}{4\pi\epsilon_0}}, \tag{8.32a}$$

$$\mu_{\mathrm{m}} \approx -i\epsilon_b\sqrt{12\pi\epsilon_0\eta r_{\mathrm{m}}^3\hbar}, \tag{8.32b}$$

where $-\mu_{\mathrm{m}} \approx \mu_{\mathrm{m}}^*$ and hence $d_{\mathrm{m}}^+ \approx \mu_{\mathrm{m}}^*\langle\hat{a}\rangle$.

8.4 The Nonlocal Correction

As suggested by our discussion so far, energy (or the frequency) of surface plasmon resonances in the MNP is determined by its polarizability using the Frölich condition. In the classical LRA, the polarizability of the MNP at a given point was modelled to be locally related to the electric field. In this section, we introduce a correction to the earlier analytical results using the GNOR based polarizability discussed in section 2.2, to account for the nonlocal effects of the MNP.

By substituting the nonlocal β_{NL} introduced in section 2.2 in place of β_{LRA} in (8.26a) and (8.26b), we can obtain the exact versions of $\mathcal{E}$ and μ_{m} with the nonlocal correction (let us call them $\mathcal{E}^{\mathrm{NL}}$ and $\mu_{\mathrm{m}}^{\mathrm{NL}}$). However, for the same reason outlined in the section 8.2, $-\mu_{\mathrm{m}}^{\mathrm{NL}} \approx (\mu_{\mathrm{m}}^{\mathrm{NL}})^*$ criteria must be met for the MNP-QD molecule to be modelled within the cavity QED approach with a reasonable accuracy, where we have defined $\mu_{\mathrm{m}}^{\mathrm{NL}}$ as the MNP dipole moment operator element in the nonlocal case. We then show that this criteria is met near resonance for good plasmonic materials when $\mathrm{Re}(1+\delta_{\mathrm{NL}}) \gg |\,\mathrm{Im}(1+\delta_{\mathrm{NL}})|$.

The modified nonlocal Frölich condition where $\alpha_{\mathrm{NL}} \propto r_{\mathrm{m}}^3\beta_{\mathrm{NL}}$ undergoes a resonant enhancement is given by [11],

$$\mathrm{Re}\left[\epsilon_{\mathrm{m}}(\omega_{\mathrm{m}})\right] \approx -2\epsilon_{\mathrm{b}}\,\mathrm{Re}\left(1+\delta_{\mathrm{NL}}\right), \tag{8.33}$$

for $\mathrm{Re}(1+\delta_{\mathrm{NL}}) \gg |\,\mathrm{Im}(1+\delta_{\mathrm{NL}})|$. When this resonant enhancement occurs, $\mathrm{Re}\left[\epsilon_{\mathrm{m}}(\omega)\right]$ can be approximated using its first order Taylor expansion near ω_{m} as,

$$\mathrm{Re}\left[\epsilon_{\mathrm{m}}\left(\omega\right)\right] \approx \mathrm{Re}\left[\epsilon_{\mathrm{m}}\left(\omega_{\mathrm{m}}\right)\right] + \left(\omega-\omega_{\mathrm{m}}\right)/\eta. \tag{8.34}$$

We can use this to approximate β_{NL} introduced in (2.18) around the SP resonance frequency ω_{m} by a complex Lorentzian using (8.28), (8.30), (8.33) and (8.34) as follows [2],

$$\beta_{\mathrm{NL}} \approx 3i\epsilon_{\mathrm{b}}\eta\,\mathrm{Re}(1+\delta_{\mathrm{NL}})/\mathcal{D}_{\mathrm{m}}. \tag{8.35}$$

Substituting β_{cm}^{NL} from (8.35) in (8.26a) and (8.26b) yields [2],

$$\mathcal{E}^{\mathrm{NL}} \approx \frac{s_{\alpha}}{R^3}\sqrt{\frac{3\hbar\eta r_{\mathrm{m}}^3\,\mathrm{Re}(1+\delta_{\mathrm{NL}})}{4\pi\epsilon_0}}, \tag{8.36a}$$

$$\mu_{\mathrm{m}}^{\mathrm{NL}} \approx -i\epsilon_{\mathrm{b}}\sqrt{12\pi\epsilon_0\eta r_{\mathrm{m}}^3\hbar\,\mathrm{Re}(1+\delta_{\mathrm{NL}})}. \tag{8.36b}$$

The equations (8.35), (8.36a) and (8.36b) capture the main results of this chapter. It is evident that good plasmonic materials fulfill the $-\mu_{\mathrm{m}}^{\mathrm{NL}} \approx (\mu_{\mathrm{m}}^{\mathrm{NL}})^*$ criteria required by the cavity QED model near resonance, given the condition $\mathrm{Re}(1+\delta_{\mathrm{NL}}) \gg |\,\mathrm{Im}(1+\delta_{\mathrm{NL}})|$ is satisfied.

In summary, it should be highlighted that the approximated $\mathcal{E}^{\mathrm{NL}}$ and $\mu_{\mathrm{m}}^{\mathrm{NL}}$ hold the following relationships with their approximated LRA counterparts $\mathcal{E}$ and μ_{m}.

$$\mathcal{E}^{\mathrm{NL}} \approx \mathcal{E}\sqrt{\mathrm{Re}\left(1+\delta_{\mathrm{NL}}\right)}, \tag{8.37a}$$

$$\mu_{\mathrm{m}}^{\mathrm{NL}} \approx \mu_{\mathrm{m}}\sqrt{\mathrm{Re}\left(1+\delta_{\mathrm{NL}}\right)} \tag{8.37b}$$

8.5 Scattering of Light By the Hybrid Molecule

Let us now calculate the Rayleigh scattering of the hybrid molecule which is prominent when the size of the scattering object is much smaller than the wavelength of the incident light [25]. The output scattered light comprises coherent and incoherent components. The coherent part is due to the elastic Rayleigh scattering where the radiated electromagnetic energy has the same frequency as the incoming field [133]. For low incident light intensities, elastic scattering is dominant. We can use this claim to model the Rayleigh scattering by the hybrid molecule, using the cavity QED solutions for the system in the weak field limit given by (8.23a) and (8.23b). The coherent part of the scattered intensity is proportional to [2,97,117],

$$I \approx \left| d_{\mathrm{qd}}^{+} + d_{\mathrm{m}}^{+} \right|^2 = \left| \mu_{\mathrm{qd}} \langle \hat{\sigma} \rangle + \mu_{\mathrm{m}}^{*} \langle \hat{a} \rangle \right|^2, \tag{8.38}$$

under the LRA. Similarly, for the nonlocal case [2,4],

$$I^{\mathrm{NL}} \approx \left| \mu_{\mathrm{qd}}^{\mathrm{NL}} \langle \hat{\sigma} \rangle^{\mathrm{NL}} + (\mu_{\mathrm{m}}^{\mathrm{NL}})^{*} \langle \hat{a} \rangle^{\mathrm{NL}} \right|^2, \tag{8.39}$$

where the superscript NL denotes the relevant quantities calculated using the nonlocally corrected equations. These results will be amply used in the numerical results chapter that follows.

8.6 The Tolerance Factor of the Nonlocal Model

With the aim of conducting a validity region analysis for the suggested nonlocal cavity QED model in the numerical chapter that follows, a tolerance factor is introduced in this section. As we have already discussed, the successful use of the cavity QED model to analyse the MNP-QD hybrid molecule requires the

fulfillment of the condition $-\mu_{\mathrm{m}}^{\mathrm{NL}} \approx (\mu_{\mathrm{m}}^{\mathrm{NL}})^*$. With this in mind, we can define [2],

$$\mathcal{T} = \left| \frac{|\mu_{\mathrm{m\_u}}^{NL}| - |\mu_{\mathrm{m\_a}}^{\mathrm{NL}}|}{|\mu_{\mathrm{m\_u}}^{\mathrm{NL}}|} \right| \times 100\%, \tag{8.40}$$

where $\mu_{\mathrm{m\_u}}^{\mathrm{NL}}$ is the unapproximated version of $\mu_{\mathrm{m}}^{\mathrm{NL}}$ in the nonlocal model obtained by substituting β_{NL} from (2.18) in (8.26b) and $\mu_{m\_a}^{NL}$ is the approximated $\mu_{\mathrm{m}}^{\mathrm{NL}}$ in the nonlocal model obtained using (8.36b). This in turn demands that both the conditions $\mathrm{Im}(\epsilon_{\mathrm{m}}(\omega)) \ll -\mathrm{Re}(\epsilon_{\mathrm{m}}(\omega))$ and $\mathrm{Re}(1+\delta_{\mathrm{NL}}) \gg |\mathrm{Im}(1+\delta_{\mathrm{NL}})|$ are met. The equation (8.40) can be used as a *de-facto* tolerance for the presented nonlocal cavity-QED model. Note that the absolute values are used for the comparison (to obtain a real percentage value) due to μ_{m} being a complex quantity.

Chapter 9
Nanohybrids Comprising Different Plasmonic Materials

In this chapter, let us analyse the scattered intensity spectra of MNP-QD hybrid molecules comprising noble, transition, post transition and alkali metal based nano-resonators. The five metals Au, Ag, Cu, Al and Na are used as representative plasmonic materials, and the GNOR based cavity QED approach outlined in the earlier chapter is utilized to obtain the nanohybrid scattering spectra. The plasmonic material used in an MNP-QD hybrid molecule plays a vital role in determining its spectrum. Thus, let us start with a brief overview of plasmonic materials used for the nanohybrids, to get a glimpse of their suitability in different applications.

9.1 Overview of Different Plasmonic Materials

9.1.1 Au and Ag

Due to their large plasma frequencies and high free electron density, metals are often regarded the materials of choice for plasmonics [134]. The two noble metals, silver (Ag) and gold (Au), are the two most commonly used plasmonic materials among metals as they have relatively low losses in the visible and NIR ranges [134] and relatively low resistivities (hence high conductivities) [135].

Au is considered the material of choice at lower NIR frequencies due to its mechanical properties, ease of implementation and very high resistance against oxidation by the common surrounding medium [136]. Researchers are just beginning to fully realize the vast range of medical diagnostic and therapeutic capabilities of Au nanoparticle (AuNP) based devices in applications such as cancer imaging and therapy [137]. Due to their potentially noncytotoxic and facile immunotargeting capabilities and nonsusceptibility to photobleaching or chemical/thermal denaturation, colloidal gold nanoparticles have recently been given a high research focus as alternatives for dyes and contrast agents used in in vivo imaging procedures [4,138].

Ag is more efficient than Au as a plasmonic material [136] as it possesses a larger plasmonic field enhancement factor over the visible and NIR wavelength range [119]. It has been amply studied and experimented with for various optoelectronic nano devices such as spasers [8], real-time nano optical sensors [139], nanoantennas [140] and solar cells [141]. Moreover, Ag nanoparticles (AgNPs) are being extensively investigated for their therapeutic and diagnostic capabilities [4,142].

9.1.2 Cu, Al and Na

Let us recall that a metal needs to possess small Im $[\epsilon_m(\omega)]$ with Re $[\epsilon_m(\omega)] \in \mathbb{R}^-$ for the existence of surface plasmon resonances [130,131]. Although it is well established that localized surface plasmon resonances that can be tuned throughout the UV to NIR regions are spanned by noble metal nanoplarticles such as Ag and Au [143, 144], a number of other metals (such as Cu, Al, Na) possess the ability to satisfy the above requirement at least partially [134]. Therefore, they can span localized surface plasmon resonances for at least a part of the UV to NIR region [145]. However, they have received much less attention compared to Ag

and Au in plasmonic applications as some of them are unstable (highly reactive) hence difficult to work with [146], or prone to surface oxidation that can significantly affect the optical properties [134,145]. However, they could be better suited for certain applications than Ag and Au due to their certain desirable properties and lower cost. Thus various methods of protection against these challenges (e.g. oxidation), such as embedding nanoparticles in different media [145, 147] are being investigated by researchers. These studies directly motivate the investigation of such metals to learn and harness their plasmonic abilities [4].

Copper (Cu), which is a transition metal, is the most commonly used metal in a plethora of electronic applications owing to its high conductivity and low cost. It possesses the second-best conductivity among metals (next to Ag). The imaginary part of the dielectric function of Cu is comparable to that of Au from 600-750 nm [134]. Different approaches of versatile protection against oxidation have been successfully demonstrated using Cu nanoparticles (CuNPs). Thus, CuNPs are being investigated as viable alternatives to the more expensive AgNPs and AuNPs [4, 134, 145].

Aluminium (Al), which is a post transition metal, is a cheap and abundant metal compared to noble metals such as Ag and Au. Al shows a reasonably strong interband transition localized in a narrow range of energy around 1.5 eV (800 nm) which causes a large imaginary dielectric function resulting in high losses in the visible wavelength range [134, 148]. In the ultra-violet wavelength range, the real part of the dielectric function of Al is negative and the imaginary part is relatively low, even at wavelengths smaller than 200 nm. Therefore, Al behaves as a better plasmonic material than both Au and Ag in the blue and UV ranges. Therefore, Al nanoparticles (AlNPs) are expected to support localized surface plasmon resonances with high optical cross sections tunable over a wide range of energy, deep into the UV [4, 149].

The high reactivity of bulk alkali metals in atmospheric conditions has re-

sulted in a very limited amount of experimental attention [147,150] towards them despite the availability of some theoretical examinations of their localized surface plasmon resonances [146,151]. However, some alkali metals such as sodium (Na) have shown losses much smaller than those of Ag (which is the material of choice for many plasmonic applications), giving rise to comparatively better plasmonic properties [152]. Moreover, Na and K nanoshells have shown high absorption efficiencies over both Ag and Au nanoshells (upto 86% increase over Au and 240% increase over Ag) [146], suggesting that further investigation of their abilities as plasmonic materials may be worth the additional inconveniences of handling these reactive metals. Therefore, alkali metal based nano devices, protected using inactive environments, should be investigated for their potential to replace the conventional metals in the context of plasmonic applications requiring higher efficiencies [4].

9.2 Numerical Results and Discussion

Having obtained a general idea of the different plasmonic materials to be used in place of the nano-resonator (MNP), let us now numerically analyse the Rayleigh scattering spectra resulting from such different exciton-plasmon nanohybrids. The parameters used to generate the numerical results are presented in Table A1. These will be the default parameters used for all results in this chapter except where specified otherwise. In this chapter and in the one that follows, we obtain the diffusion constant of the MNP using the *Halevi formalism* [2, 11], as $D = 4\gamma v_F^2/15\left(\omega^2 + \gamma^2\right)$, due to the unavailability of experimentally measured diffusion constants for all metals under consideration. Using Ag based nanohybrids, it was verified that the use of *Halevi* D is justified, as we are interested in the resonance shifts of the nanoparticles and normalized scattering spectra.

Table A1: The default set of parameters

Variable	Value	Reference
Incident field amplitude	$100\,\mathrm{V\,m^{-1}}$	-
Orientation parameter (s_α)	2	-
MNP-QD detuning ($\Delta = \omega_\mathrm{m} - \omega_\mathrm{qd}$)	20 meV	-
MNP-QD distance (R)	15 nm	-
MNP radius (r_m)	8 nm	-
Relative bath permittivity (ϵ_b)	5	-
QD decay rate (γ_qd)	50 meV	[97]
QD dipole moment element (μ_{qd})	33.62 Debye	[97]
Bulk plasmon frequency (ω_p)		
Au	9.02 eV	[11]
Ag	8.99 eV	[11]
Cu	8.7 eV	[134]
Al	15.8 eV	[11]
Na	6.04 eV	[11]
Bulk damping rate (γ)		
Au	0.071 eV	[11]
Ag	0.025 eV	[11]
Cu	0.07 eV	[134]
Al	0.6 eV	[11]
Na	0.16 eV	[11]
Fermi velocity (v_F)		
Au	$1.39 \times 10^6\,\mathrm{m\,s^{-1}}$	[11]
Ag	$1.39 \times 10^6\,\mathrm{m\,s^{-1}}$	[11]
Cu	$1.57 \times 10^6\,\mathrm{m\,s^{-1}}$	[153]
Al	$2.03 \times 10^6\,\mathrm{m\,s^{-1}}$	[11]
Na	$1.07 \times 10^6\,\mathrm{m\,s^{-1}}$	[11]
Bulk (experimental) permittivity (ϵ_exp)		
Au, Ag, Cu	-	[60]
Au	-	[154]
Au	-	[155]

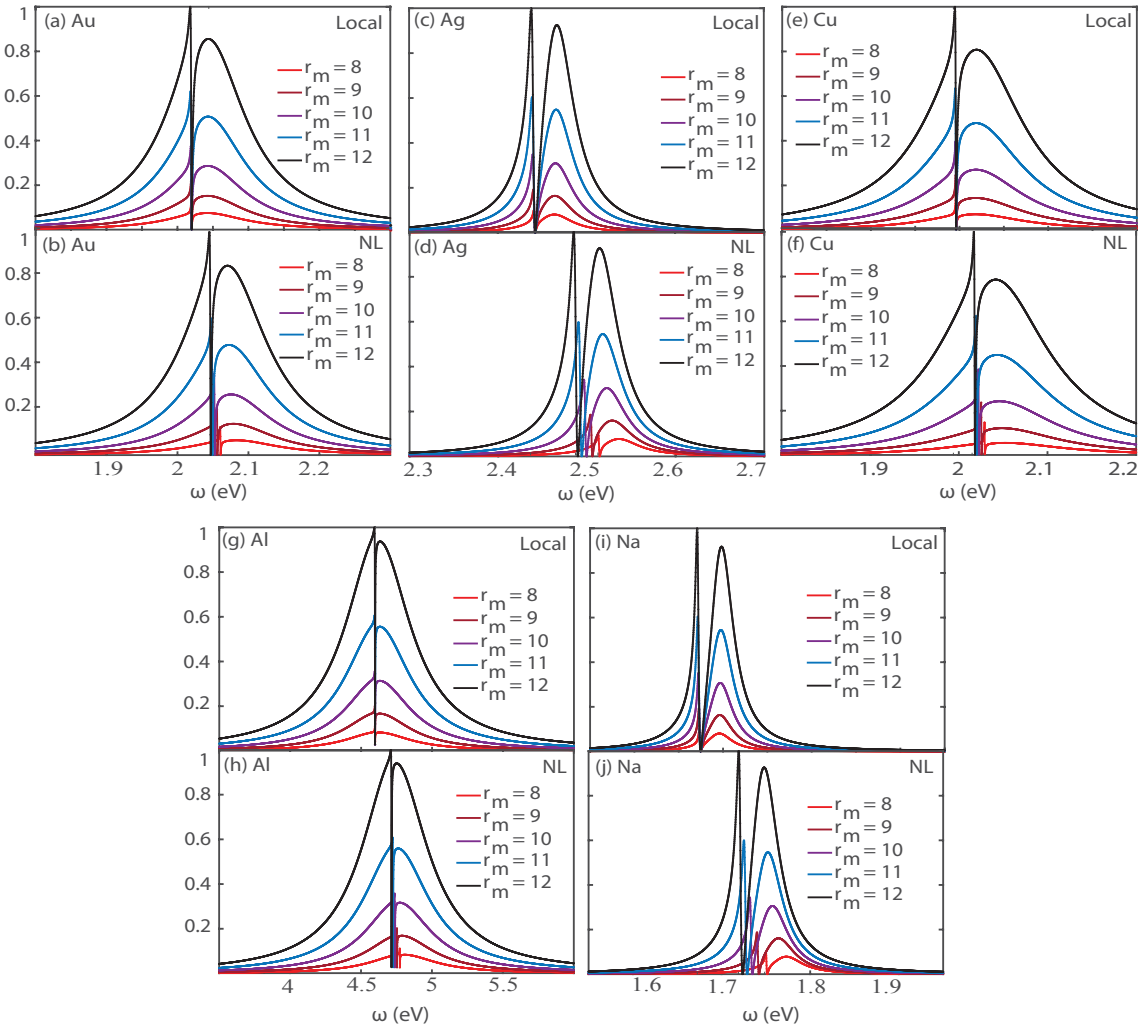

Figure 9.1: Variation of the coherent Rayleigh scattering spectra of nanohybrids with varying r_{m}, for different materials, obtained using the local (LRA) and non-local (GNOR) models. The Y axis of each sub-figure shows the normalized scattered intensity and the X axis shows frequency in eV. Curves are normalized by the largest peak in the respective sub figure. The sub-figures (a), (c), (e), (g), and (i) capture the spectra generated using the LRA based model whereas the sub-figures (b), (d), (f), (h), and (j) capture the spectra generated using the GNOR based model. For all sub-figures, $\epsilon_{\mathrm{b}} = 5$, $\Delta = \omega_{\mathrm{m}} - \omega_{\mathrm{qd}} = 20\,\mathrm{meV}$ and $R = 15\,\mathrm{nm}$ are used.

9.2.1 Impact of Varying Metal Nanoparticle Radius

Fig. 9.1 depicts the variation of the normalized coherent Rayleigh scattering curves of MNP-QD hybrid molecules comprising different metal based MNPs. The results of both LRA based (8.38) and GNOR based (8.39) scattered intensity formulae are perused for their response to varying MNP radius r_{m}. The depicted results consider a set of r_{m} values in the vicinity of 10 nm where the effects of nonlocal response are expected to be visible. The sub-figures (a), (c), (e), (g), and (i) depict the conventional LRA based spectra whereas the sub-figures (b), (d), (f), (h), and (j) depict GNOR based spectra.

For all five metals considered, both LRA and GNOR based models predict an increase of the Rayleigh scattering intensity with increasing r_{m}, as intuitively expected. It is evident that the GNOR based model captures the blueshift of resonance energy that occurs with the decreasing particle size, which tallies with the studies done using isolated MNPs in [36,45]. This blueshift is not revealed by the conventional LRA based model. In addition to the aforementioned MNP radius-dependent blueshift, the GNOR based model predicts a generally blueshifted set of spectra compared to the relevant LRA based counterparts for all metals under study. Observation of the spectra reveals that different metal based nanohybrids are usable for applications operating in different frequency regimes. For example, Al based nanohybrids are well suited for applications in the ultraviolet frequency regime whereas other four metal based nanohybrids operate in the optical frequency regime. It can also be seen that the spectral shape and operational frequency regimes of Au and Cu based nanohybrids bear a close resemblance to each other. Moreover, the spectral shapes of Ag and Na based nanohybrids too bear a high level of resemblance. Given the ability to tune the resonance frequencies using other parameters such as the submerging permittivity, these observations suggest that the potential investigation of the usability of Cu and Na as alternatives for Au and Ag could prove to be useful in the future [4].

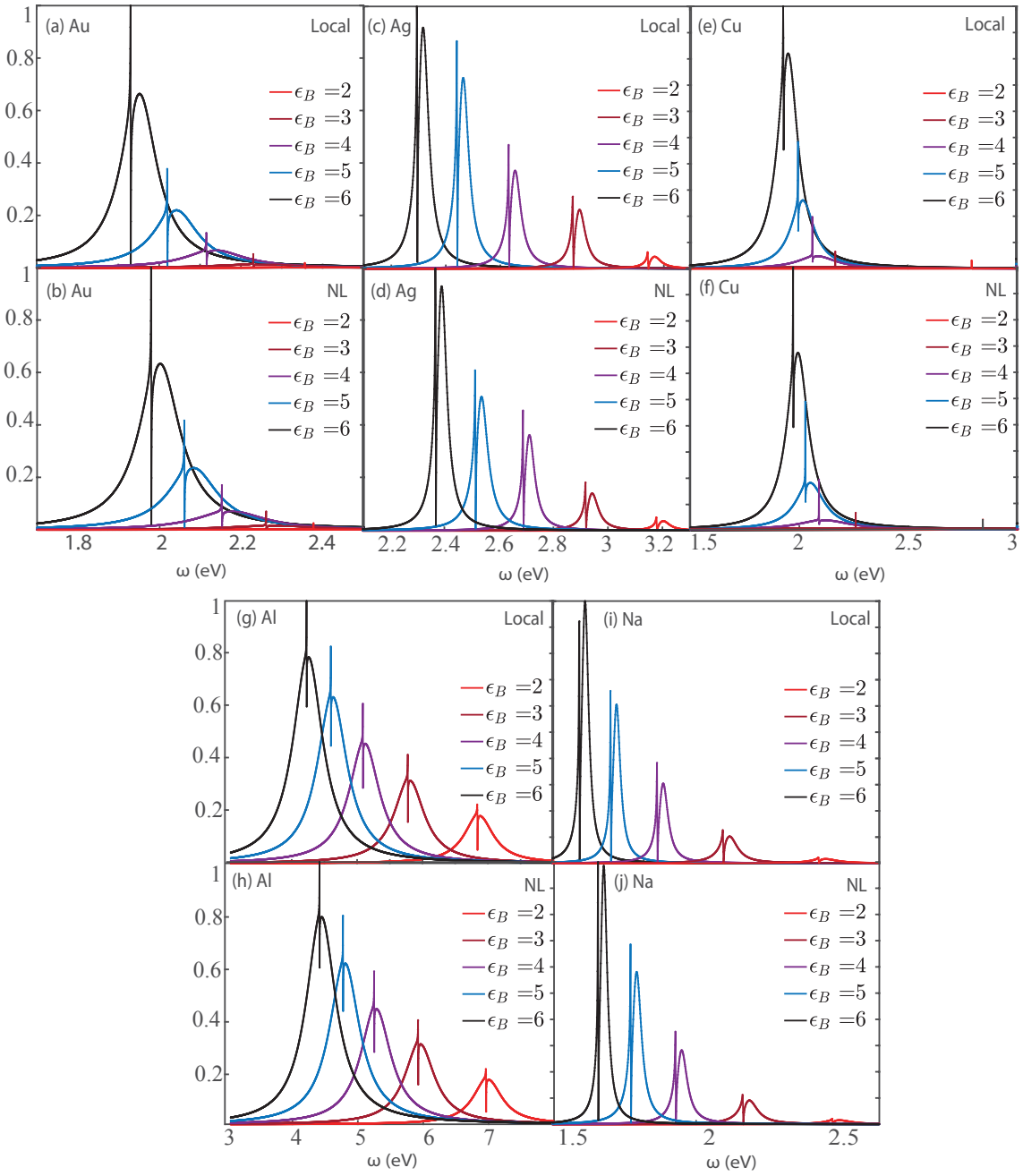

Figure 9.2: Variation of coherent Rayleigh scattering spectra of the nanohybrid with varying ϵ_b, for different materials, obtained using both local (LRA) and non-local (GNOR) models. The Y axis of each sub-figure shows the normalized scattered intensity and the X axis shows frequency in eV. Curves are normalized by the largest peak in the respective sub figure. The sub-figures in the top row capture the spectra generated using the LRA based model whereas the sub-figures in the bottom row capture the spectra generated using the GNOR based model. For all sub-figures, $r_m = 8\,\text{nm}$, $\Delta = \omega_m - \omega_{qd} = 20\,\text{meV}$ and $R = 15\,\text{nm}$ are used.

9.2.2 Impact of Varying Submerging Permittivity

Fig. 9.2 shows how the intensity spectra of different metal based nanohybrids vary with the permittivity of the surrounding medium. Fig. 9.2(a), (c), (e), (g), and (i) depict the LRA based plots for Au, Ag, Cu, Al, and Na nanohybrids respectively, whereas Fig. 9.2(b), (d), (f), (h) and (j) show the same set of plots obtained using the GNOR based formalism.

Recall that the resonance frequency is decided by the Frölich condition given by (8.29) and (8.33) in the local and nonlocal cases respectively. Increasing ϵ_b moves the resonance frequency leftwards, along the Drude-like dielectric curve (2.2) in the optical region for metals such as gold and silver. Observations of the scattered intensity plots reveals that this frequency red-shift which occurs with increasing ϵ_b is seen to be captured by both LRA and GNOR based models.

It is evident that all curves red-shift along the frequency axis and increase in height, as the permittivity of the submerging bath increases. It is also observable that both LRA and GNOR based models predict that the resonance frequency and the peak scattered intensity show a high sensitivity to the permittivity of the host medium, which can be exploited in applications such as bio-sensing [133]. As an example, the permittivity of cancer tissue are known to be much higher than that of the surrounding normal tissue [156], which should result in a red-shifted, amplified spectrum enabling tumour detection using optical techniques at earliest stages.

The trend of increasing spectrum height with submerging medium permittivity also suggests that metals such as gold, copper and aluminium which generally exhibit lower plasmonic peaks compared to metals such as silver and Na [4] are expected to behave as better plasmonic materials at high environmental permittivities. It can also be seen that Au and Cu based nanohybrids exhibit a higher amplitude sensitivity to ϵ_b compared to other metal based counterparts and hence could emerge as better candidates for sensing applications.

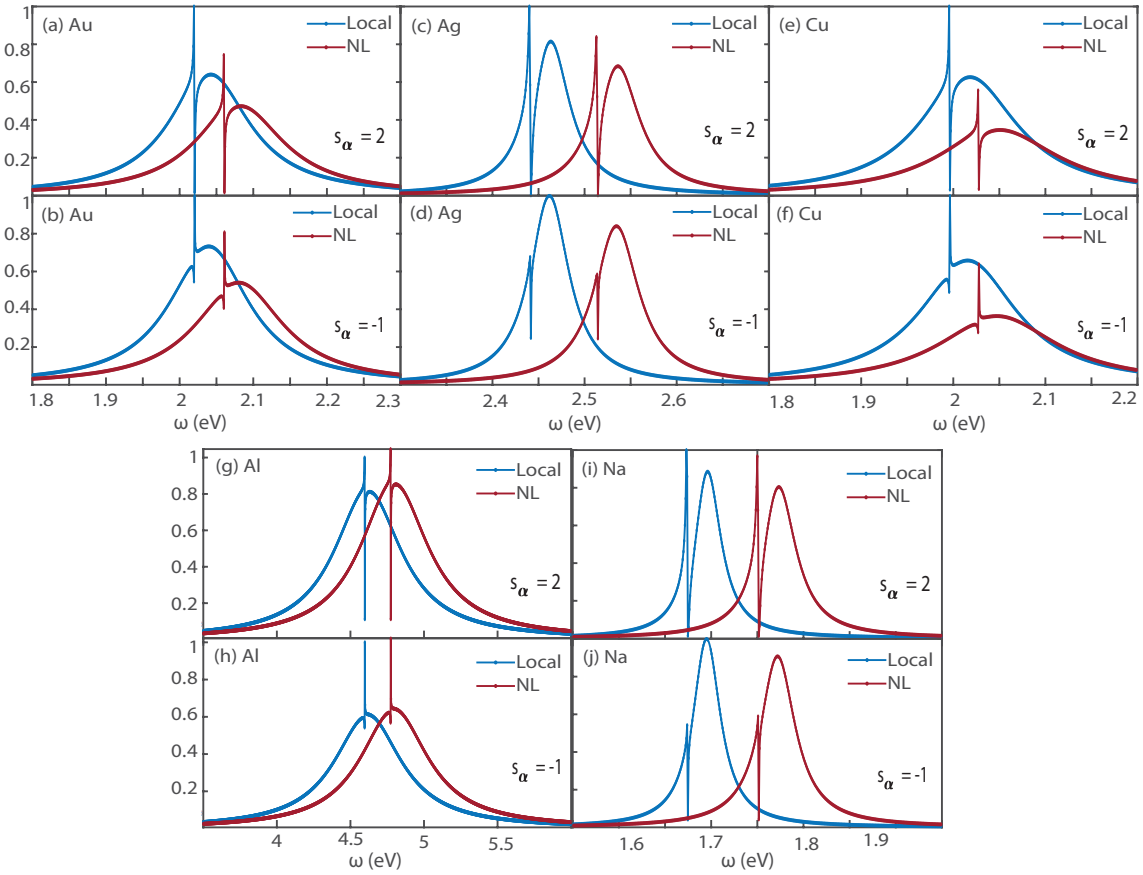

Figure 9.3: LRA and GNOR based coherent Rayleigh scattering spectra for $s_\alpha = 2$ (parallel polarization conditions) and $s_\alpha = -1$ (perpendicular polarization conditions) for different materials. The Y axis of each sub-figure shows the normalized Rayleigh scattering intensity and the X axis shows the frequency in eV. Other parameters used include $\epsilon_\mathrm{b} = 5$, $r_\mathrm{m} = 8\,\mathrm{nm}$, $R = 15\,\mathrm{nm}$ and $\Delta = \omega_\mathrm{m} - \omega_\mathrm{qd} = 20\,\mathrm{meV}$. All curves are normalized by the peak intensity of the associated sub-figure.

9.2.3 Orientation Dependence of Scattering Spectra

The dependence of the normalized Rayleigh scattering intensities of different MNP based nanohybrids on the orientation parameter s_α is depicted in Fig. 9.3. Note that the sub-figures (a), (c), (e), (g), and (i) depict the scattering spectra for parallel polarization ($s_\alpha = 2$) for both LRA and GNOR based cases, for nanohybrids comprising Au, Ag, Cu, Al, and NA nanoresonators, respectively. The sub-figures (b), (d), (f), (h), and (j) depict the same set of plots for perpendicular polarization conditions ($s_\alpha = -1$).

A scaling of the GNOR based nonlocal scattered intensity in comparison to the respective LRA based counterparts can be observed for all metals, under both polarization conditions. This can be identified as a consequence of the introduction of the $\mathrm{Re}(1 + \delta_{\mathrm{NL}})$ component to the approximate expression of μ_{m} in the GNOR based case. It can also be observed that the interference between the MNP and QD spectra, and the resulting kink depends on the external driving field orientation, s_α, for all MNP-QD hybrid molecules based on different plasmonic materials.

In all nanohybrid spectra studied so far, we could observe that a sharp enhancement and a suppression of the scattered intensity occur in a small region near the resonance frequency of the QD, due to the respective constructive and destructive interferences of the MNP and QD spectra. Both LRA and GNOR based plots depicted in Fig. 9.3 show that this interference effect is highly dependent on the external driving field orientation s_α. For example, for AgMNP based nanohybrids, a substantial hindering of constructive interference, which results in drastically reduced kink height, is observed for perpendicular polarization ($s_\alpha = -1$), in comparison to the parallel polarization conditions ($s_\alpha = 2$).

Moreover, close observation reveals that a line broadening effect is present in the GNOR based spectra in comparison to the respective LRA based counterparts, as expected by plasmonic experiments [2, 31].

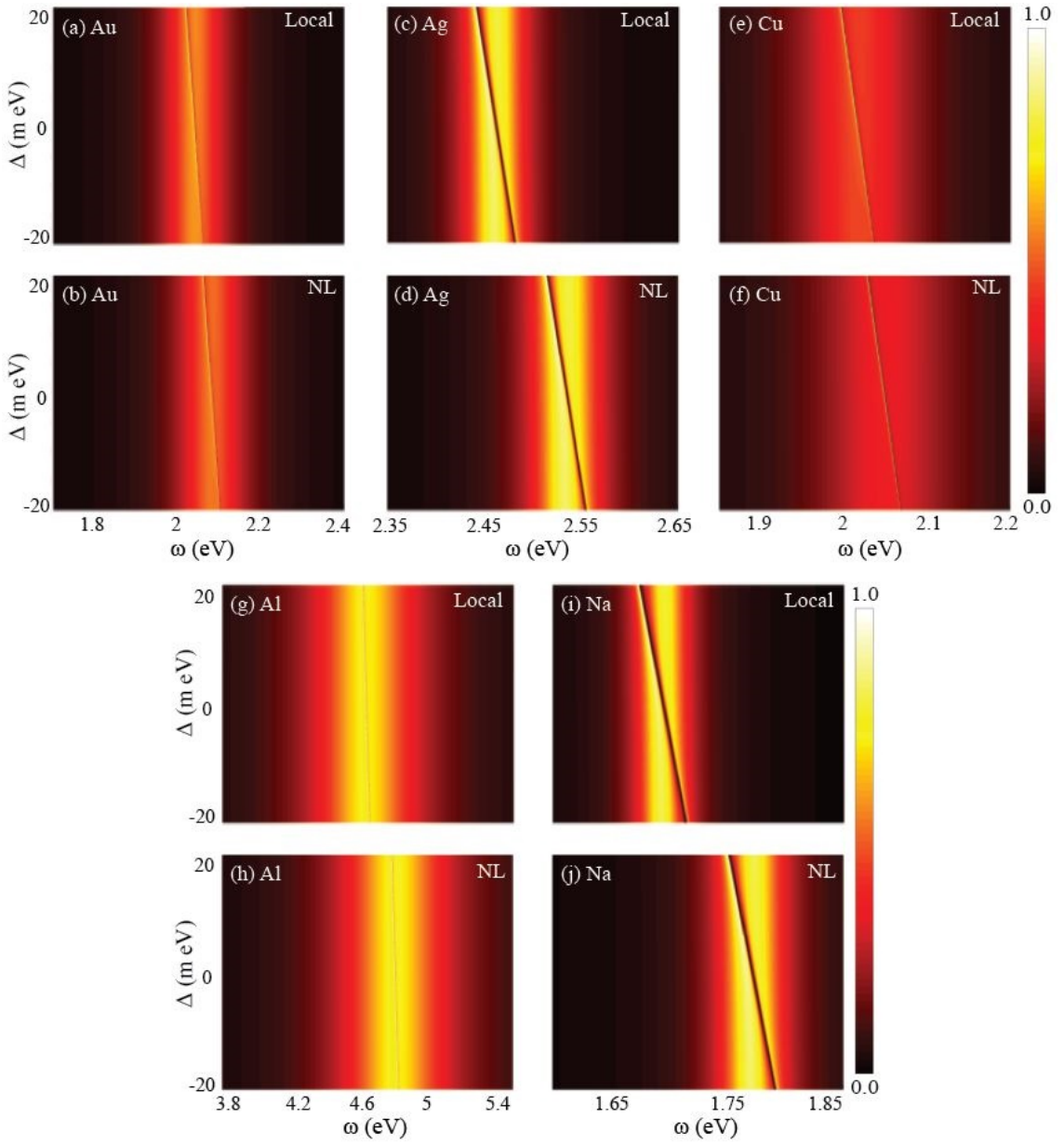

Figure 9.4: Two dimensional plots for the coherent scattered intensity of the hybrid molecule, normalized by the maximum intensity of each sub-figure for $\epsilon_b = 5$ and $r_m = 8\,\text{nm}$. The Y axis of each sub-figure depicts the detuning between the MNP and QD resonance frequencies ($\Delta = \omega_m - \omega_{qd}$) in units meV and the X axis reads the frequency in eV. The color indicates the normalized scattered intensity. Both locally (LRA based) and non-locally (GNOR based) modelled plots are depicted for each metal.

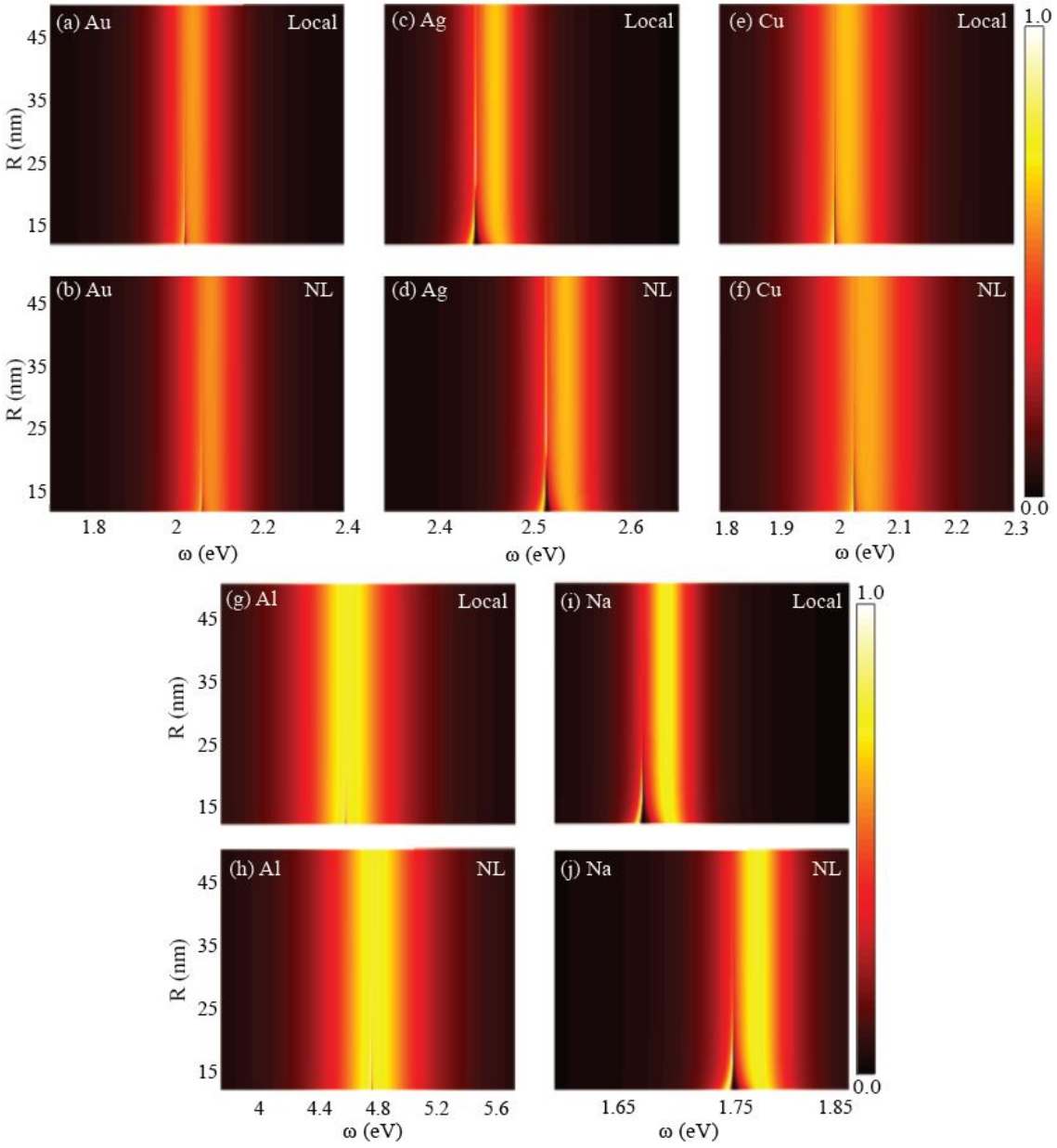

Figure 9.5: Two dimensional plots for the coherent scattered intensity of the hybrid molecule, normalized by the maximum intensity of each sub-figure for $\epsilon_b = 5$ and $r_m = 8\,\text{nm}$. The Y axis of each sub-figure depicts the MNP-QD centre separation R in units nm and the X axis reads the frequency in eV. The color indicates the normalized scattered intensity. Both locally (LRA based) and non-locally (GNOR based) modelled plots are depicted for each metal.

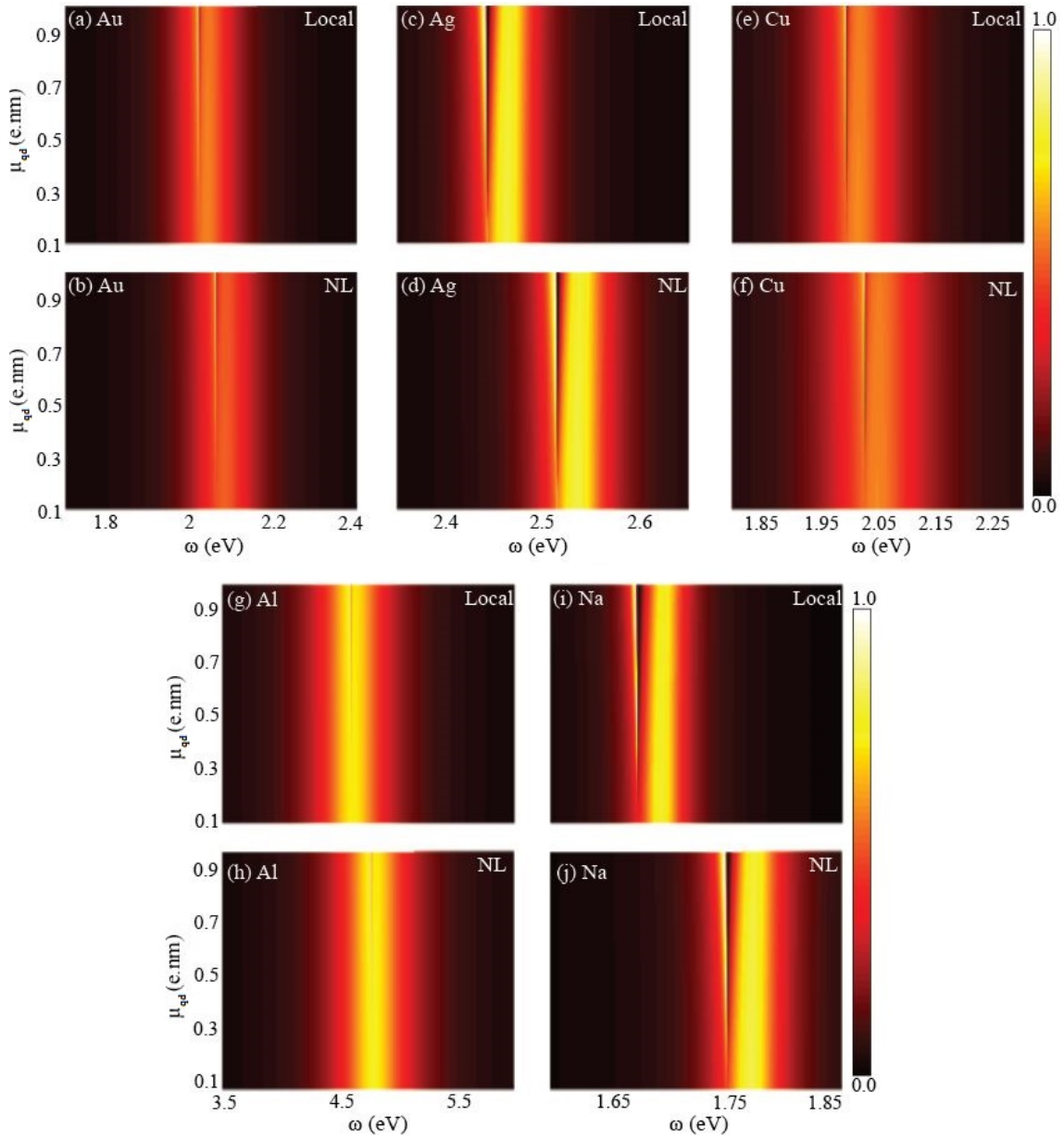

Figure 9.6: Two dimensional plots for the coherent scattered intensity of the hybrid molecule, normalized by the maximum intensity of each sub-figure for $\epsilon_b = 5$ and $r_m = 8\,\text{nm}$. The Y axis of each sub-figure depicts the dipole moment element of the QD μ_{qd} in units e nm and the X axis reads the frequency in eV. The color indicates the normalized scattered intensity. Both locally (LRA based) and non-locally (GNOR based) modelled plots are depicted for each metal.

9.2.4 Impact of MNP-QD Detuning, Centre Separation and QD Dipole Moment

Fig. 9.4 shows two dimensional plots of the scattered intensity against the MNP-QD detuning Δ and the external driving field frequency ω, given by the local and nonlocal models respectively. The slanted line across each spectrum shows the movement of the steep enhancement-suppression pattern (seen earlier in the line-plots) towards higher frequencies following the movement of the resonance position of the QD along the frequency axis. It is evident that this pattern is distinctly visible in Ag and Na based nanohybrids, compared to the other three metal based nanohybrids under study.

Figures 9.5 and 9.6 show similar two dimensional plots for scattered intensity in the R vs ω and μ_{qd} vs ω parameter spaces, respectively, in the usual constellation of sub-figures. It is observable that decreasing the MNP-QD centre separation and increasing the QD dipole moment has similar impacts on the scattered intensity of the nanohybrid, where both result in sharper kinks spread along a wider area of the spectrum.

The strength of interference (and hence the kink sharpness and width) tends to decrease with decreasing QD dipole moment and increasing MNP-QD centre separation as intuitively expected. Similar to our observations in Fig. 9.4, Ag and Na based nanohybrids exhibit sharper interference patterns compared to Au, Cu and Na. From all three figures 9.4, 9.5, and 9.6, it can be observed that the GNOR based spectra are relatively blue-shifted along the frequency axis compared to the respective LRA based counterparts. It can also be observed that the spectra of Al based nanohybrids are much wider compared to all the other metal based nanohybrids under study, and reside near the ultra-violet frequency range. Moreover, all thee plots support our earlier observation of Cu and Na based nanohybrids closely resembling the qualitative behaviour of Au and Ag based nanohybrids.

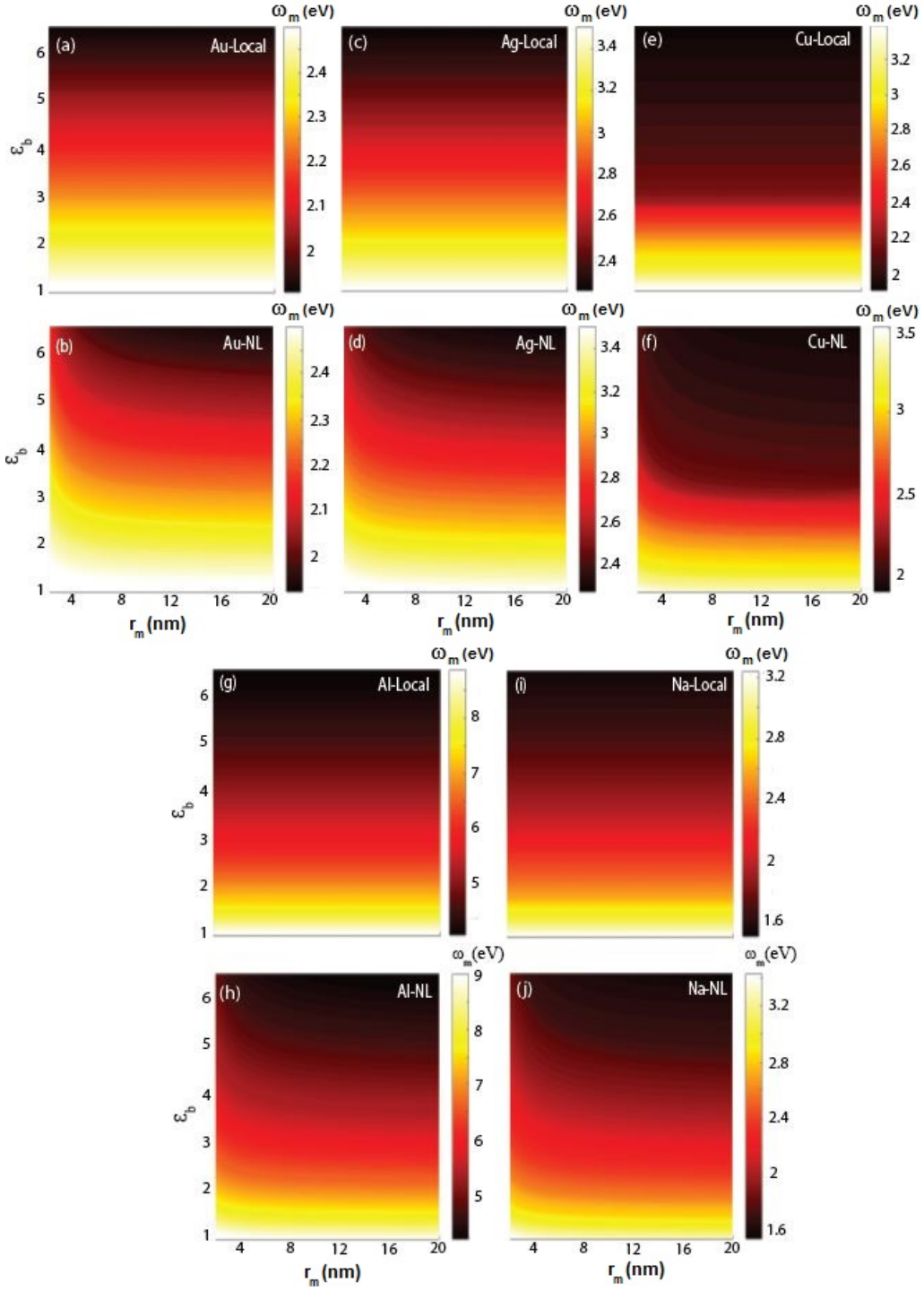

Figure 9.7: The variation of ω_{m} against r_{m} and ϵ_{b}, as predicted by the LRA (local) and GNOR (nonlocal) based models. The Y axis of each plot reads ϵ_{b} and the X axis reads the radius of the MNP r_{m} in nm. The color shows the resonance frequency of the MNP ω_{m} at the respective (r_{m}, ϵ_{b}) coordinate in eV.

9.2.5 MNP Size Dependent Resonance Variation

Using Fig. 9.7, we can study the how the MNP resonance frequency varies with the MNP radius r_m and the submerging medium permittivity ϵ_b, as predicted by both LRA and GNOR based models. The sub-figures are arranged in the usual constellation where (a), (c), (e), (g), and (i) depict the LRA based ω_m predictions for Au, Ag, Cu, Al and Na MNPs, whereas (b), (d), (f), (h), and (j) depict the same in the GNOR based formalism. It is evident that the LRA does not capture the radius dependence of the MNP resonance which is quite significant for sub-wavelength nanoparticles. The GNOR plots readily capture this radius dependence where it can be observed that the dependence of ω_m on r_m increases with decreasing r_m, for all five types of nanohybrids considered.

For the convenience of future research, the resonance frequencies for different nanoparticles were calculated using the GNOR based Frölich condition (8.33) taking the MNP radius dependence into account, and tabulated as follows.

Table A2: Surface plasmon resonance frequencies (ω_m) for gold nanospheres (AuMNPs) calculated using the presented GNOR based formalism and tabulated against the submerging bath permittivity ϵ_b and the MNP radius r_m.

ϵ_b	3 nm	5 nm	7 nm	9 nm	11 nm	13 nm	15 nm	17 nm	19 nm
3	2.34	2.3	2.29	2.28	2.27	2.27	2.27	2.26	2.26
3.5	2.29	2.25	2.23	2.22	2.22	2.21	2.21	2.21	2.2
4	2.24	2.2	2.18	2.17	2.16	2.16	2.15	2.15	2.15
4.5	2.2	2.15	2.13	2.12	2.11	2.11	2.11	2.1	2.1
5	2.16	2.11	2.09	2.08	2.07	2.06	2.06	2.06	2.06
5.5	2.12	2.07	2.05	2.03	2.03	2.02	2.02	2.02	2.01
6	2.09	2.03	2.01	1.99	1.99	1.98	1.98	1.97	1.97
6.5	2.05	1.99	1.97	1.95	1.95	1.94	1.94	1.93	1.93
7	2.02	1.96	1.93	1.92	1.91	1.9	1.9	1.89	1.89
7.5	1.99	1.92	1.89	1.88	1.87	1.86	1.86	1.85	1.85
8	1.96	1.89	1.86	1.84	1.83	1.83	1.82	1.82	1.81
8.5	1.93	1.86	1.83	1.81	1.8	1.79	1.79	1.78	1.78
9	1.91	1.83	1.8	1.78	1.77	1.76	1.75	1.75	1.75
9.5	1.88	1.8	1.77	1.75	1.74	1.73	1.72	1.72	1.72
10	1.85	1.77	1.74	1.72	1.71	1.7	1.69	1.69	1.69

Table A3: Surface plasmon resonance frequencies (ω_m) for silver nanospheres (AgMNPs) calculated using the presented GNOR based formalism and tabulated against the submerging bath permittivity ϵ_b and the MNP radius r_m.

ϵ_b	3 nm	5 nm	7 nm	9 nm	11 nm	13 nm	15 nm	17 nm	19 nm
1	3.55	3.53	3.52	3.52	3.51	3.51	3.51	3.51	3.51
1.5	3.41	3.37	3.36	3.35	3.35	3.34	3.34	3.34	3.34
2	3.27	3.22	3.21	3.2	3.19	3.19	3.18	3.18	3.18
2.5	3.13	3.09	3.07	3.06	3.05	3.05	3.04	3.04	3.04
3	3.02	2.97	2.95	2.93	2.93	2.92	2.92	2.91	2.91
3.5	2.92	2.85	2.82	2.81	2.8	2.79	2.79	2.78	2.78
4	2.82	2.75	2.72	2.7	2.69	2.69	2.68	2.68	2.68
4.5	2.73	2.66	2.63	2.61	2.6	2.6	2.59	2.59	2.58
5	2.66	2.58	2.55	2.53	2.51	2.51	2.5	2.5	2.49
5.5	2.59	2.5	2.47	2.45	2.44	2.43	2.42	2.42	2.41
6	2.52	2.44	2.4	2.38	2.37	2.36	2.35	2.35	2.35
6.5	2.46	2.38	2.34	2.32	2.31	2.3	2.29	2.29	2.29

Table A4: Surface plasmon resonance frequencies (ω_m) for copper nanospheres (CuMNPs) calculated using the presented GNOR based formalism and tabulated against the submerging bath permittivity ϵ_b and the MNP radius r_m.

ϵ_b	3 nm	5 nm	7 nm	9 nm	11 nm	13 nm	15 nm	17 nm	19 nm
4	2.18	2.13	2.12	2.11	2.1	2.1	2.1	2.09	2.09
4.5	2.14	2.1	2.08	2.07	2.07	2.07	2.06	2.06	2.06
5	2.11	2.07	2.05	2.04	2.04	2.04	2.03	2.03	2.03
5.5	2.08	2.04	2.03	2.02	2.01	2.01	2	2	2
6	2.06	2.02	2	1.99	1.98	1.98	1.97	1.97	1.97
6.5	2.04	1.99	1.97	1.96	1.95	1.94	1.94	1.94	1.93
7	2.02	1.96	1.94	1.93	1.92	1.91	1.91	1.91	1.9
7.5	2	1.94	1.91	1.9	1.89	1.88	1.88	1.87	1.87
8	1.98	1.91	1.88	1.87	1.86	1.85	1.85	1.84	1.84
8.5	1.96	1.89	1.86	1.84	1.83	1.82	1.82	1.81	1.81
9	1.94	1.86	1.83	1.81	1.8	1.79	1.79	1.78	1.78
9.5	1.91	1.84	1.8	1.78	1.77	1.76	1.76	1.76	1.76
10	1.89	1.81	1.78	1.76	1.76	1.76	1.76	1.76	1.76

Table A5: Surface plasmon resonance frequencies (ω_m) for aluminum nanospheres (AlMNPs) calculated using the presented GNOR based formalism and tabulated against the submerging bath permittivity ϵ_b and the MNP radius r_m.

ϵ_b	3 nm	5 nm	7 nm	9 nm	11 nm	13 nm	15 nm	17 nm	19 nm
2	7.19	7.06	7	6.97	6.95	6.93	6.92	6.92	6.91
2.5	6.62	6.48	6.42	6.38	6.36	6.34	6.33	6.33	6.32
3	6.19	6.03	5.96	5.93	5.9	5.89	5.87	5.86	5.86
3.5	5.83	5.67	5.6	5.56	5.53	5.51	5.5	5.49	5.48
4	5.54	5.37	5.29	5.25	5.23	5.21	5.19	5.18	5.18
4.5	5.3	5.12	5.04	5	4.97	4.95	4.93	4.92	4.92
5	5.09	4.9	4.82	4.77	4.75	4.73	4.71	4.7	4.69
5.5	4.91	4.71	4.63	4.58	4.55	4.53	4.52	4.51	4.5
6	4.75	4.55	4.46	4.41	4.38	4.36	4.35	4.34	4.33
6.5	4.61	4.4	4.31	4.27	4.23	4.21	4.2	4.19	4.18
7	4.48	4.27	4.18	4.13	4.1	4.08	4.06	4.05	4.04
7.5	4.37	4.16	4.06	4.01	3.98	3.96	3.94	3.93	3.92
8	4.27	4.05	3.95	3.9	3.87	3.84	3.83	3.81	3.8
8.5	4.18	3.95	3.85	3.8	3.8	3.8	3.8	3.8	3.8
9	4.09	3.86	3.8	3.8	3.8	3.8	3.8	3.8	3.8
9.5	4.02	3.8	3.8	3.8	3.8	3.8	3.8	3.8	3.8
10	3.95	3.8	3.8	3.8	3.8	3.8	3.8	3.8	3.8

Table A6: Surface plasmon resonance frequencies (ω_m) for sodium nanospheres (NaMNPs) calculated using the presented GNOR based formalism and tabulated against the submerging bath permittivity ϵ_b and the MNP radius r_m.

ϵ_b	3 nm	5 nm	7 nm	9 nm	11 nm	13 nm	15 nm	17 nm	19 nm
1.5	2.93	2.87	2.84	2.82	2.81	2.8	2.8	2.8	2.79
2	2.64	2.57	2.55	2.54	2.53	2.52	2.52	2.51	2.51
2.5	2.45	2.38	2.36	2.34	2.33	2.33	2.32	2.32	2.32
3	2.31	2.24	2.21	2.19	2.18	2.17	2.16	2.16	2.16
3.5	2.19	2.1	2.06	2.05	2.03	2.03	2.02	2.02	2.01
4	2.07	1.99	1.95	1.93	1.92	1.91	1.91	1.9	1.9
4.5	1.98	1.9	1.86	1.84	1.83	1.82	1.82	1.81	1.81
5	1.91	1.82	1.78	1.76	1.75	1.74	1.73	1.73	1.72
5.5	1.84	1.75	1.71	1.69	1.68	1.67	1.67	1.66	1.66
6	1.78	1.69	1.66	1.64	1.63	1.62	1.61	1.61	1.61
6.5	1.73	1.64	1.61	1.59	1.58	1.57	1.56	1.56	1.55
7	1.68	1.6	1.56	1.54	1.52	1.51	1.51	1.5	1.5

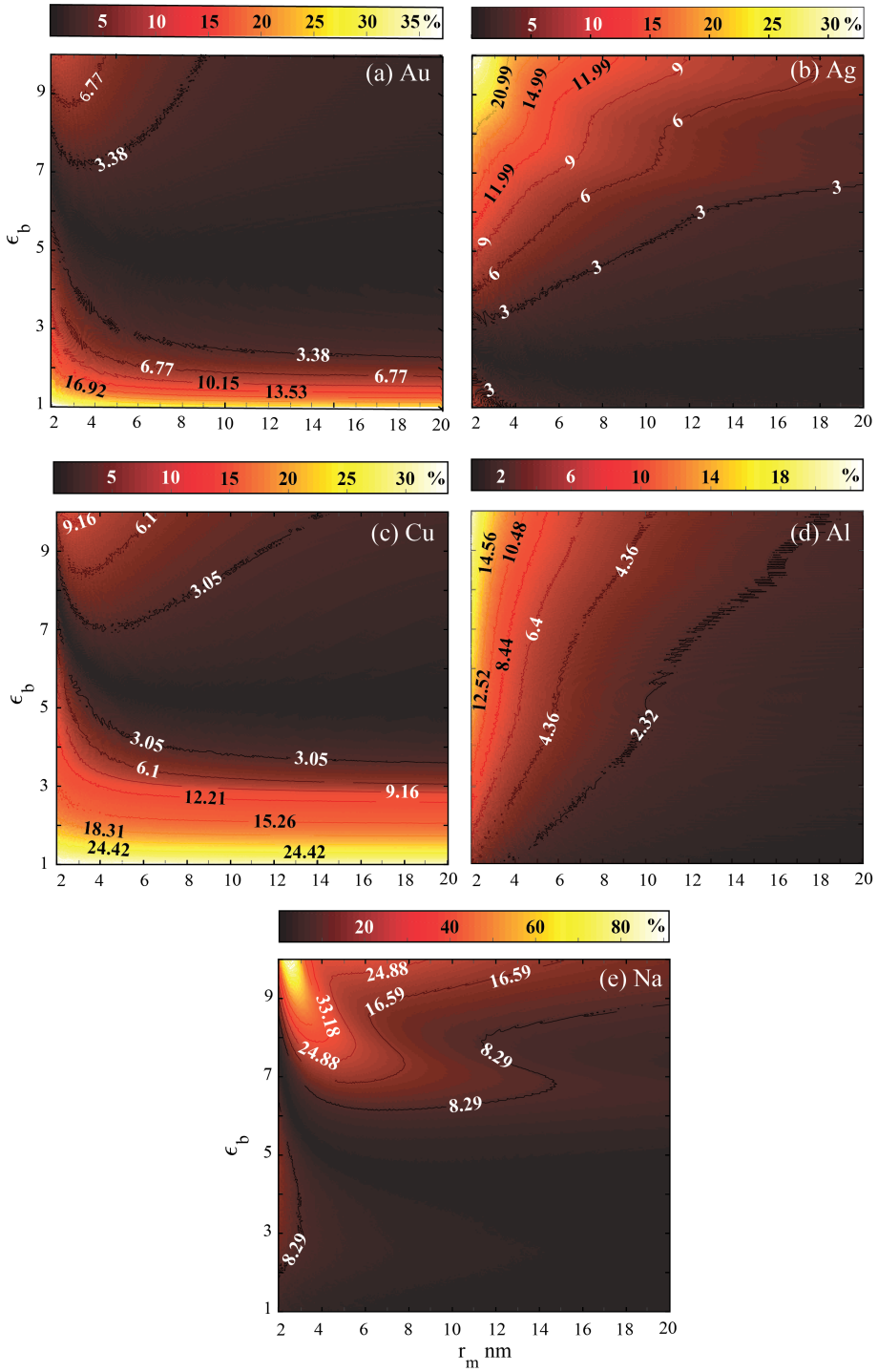

Figure 9.8: The factor $\mathcal{T}$ (which represents the *de-facto* tolerance level for the cavity QED model presented in chapter 8) calculated using (8.40) for different materials at the respective resonance frequencies for different MNP radii and environment permittivities. The Y axis reads the environment permittivity ϵ_b and the X axis reads the MNP radius r_m in nm. The colorbar reads $\mathcal{T}$ as a percentage.

9.3 Summary and Conclusion

In this chapter, we numerically analysed the metal nanoparticle-quantum dot (MNP-QD) hybrid molecule in an external driving field using a cavity-QED approach and presented a comprehensive comparison between the behaviour suggested by the local response approximation (LRA) and the generalized nonlocal optical response (GNOR) based methods.

Optical signatures of the scattering spectra and their variation with the tunable system properties were observed and discussed in this numerical analysis for nanohybrids based on five different metals. It was also evident that the LRA fails to capture some features such as the size dependent resonance shifts, line-width broadening and amplitude scaling where the GNOR model succeeds. The nonlocal GNOR model captures the blueshift of resonance energy that occurs with the decreasing particle size, which tallies with experimental studies done using isolated and dimer MNPs.

This chapter also presented tables summarising the GNOR based resonance energies of different metal based MNPs for varying MNP radius and submerging permittivity. Finally in Fig. 9.8 the tolerance level $\mathcal{T}$ given by (8.40) was plotted against the bath permittivity ϵ_{b} and the MNP radius r_{m} for all five types of MNP-QD hybrid systems under consideration.

Chapter 10

Optoelectronic Figure of Merit for Nanohybrid Scattering Prowess

From the analyses so far, it is evident that the fano-like spectrum of a MNP-QD hybrid molecule is highly tunable using properties such as the composition and sizes of the constituents, MNP-QD distance, QD dipole moment, MNP and QD damping rates and the permittivity of the surrounding medium. Due to this high tunability, a given MNP-QD based sensing application possesses a large number of eligible configurations. However, the lack of a simple way to compare one MNP-QD configuration against another considering the fano-like spectra makes it difficult to the rank viable options for an optimal selection. This chapter aims to fill this void by proposing a metric that aids to rank nanohybrid configurations in the order of their scattering prowess/suitability for a given scattered intensity based sensing application. For the purpose of comparison of a given set of nanohybrid spectra, this chapter introduces a simple but elegant relative figure of merit (RFoM) which simultaneously takes into account, the scattered intensity at the constructive interference point and the refractive index sensitivity of the nanohybrid. To demonstrate the use of the proposed RFoM, the same five metal based nanohybrids (modeled using the GNOR based formalism) studied in the earlier chapter would be utilized. This chapter also aims to incite the interest in using MNP-QD nanohybrids, which possess sensing capabilities superior to those of the individual constituents, for sensing applications that rely on scat-

tered light.

10.1 The Relative Figure of Merit (RFoM)

For the purpose of comparison of the scattered intensity spectra resulting from a set of candidate MNP-QD nanohybrid configurations for a given sensing application, let us now introduce a RFoM which focuses on maximizing the scattered intensity (near MNP and QD resonances, when the MNP and QD have a small detuning from each other) and the refractive index sensitivity, as follows.

Suppose a set of n fano-like MNP-QD scattered intensity spectra for n different MNP-QD configurations that we aim to compare against each other are contained in a set,

$$\mathrm{S_I} = \{I_1(\omega), I_2(\omega), ..., I_\mathrm{k}(\omega), ...I_\mathrm{n}(\omega)\}, \tag{10.1}$$

where each scattered intensity curve $I_\mathrm{k}(\omega)$ is a function of the angular frequency of the incoming radiation, ω.

Similarly, let the corresponding isolated MNP scattered intensity spectra (in the absence of the QD) be denoted by the set,

$$\mathrm{S_M} = \{M_1(\omega), M_2(\omega), ..., M_\mathrm{k}(\omega), ...M_\mathrm{n}(\omega)\}. \tag{10.2}$$

Let us define a normalizer for this set as,

$$\|I\| = \max\{[\max(I_\mathrm{k}(\omega))]_{\mathrm{k}=1,...,\mathrm{n}}\}, \tag{10.3}$$

which is the maximum out of the maximum intensity values of all spectra in the set $\mathrm{S_I}$.

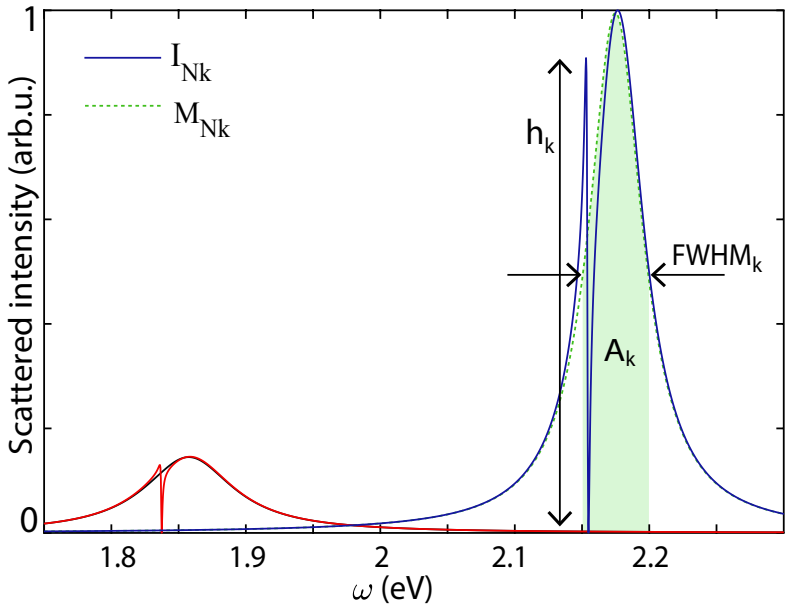

Figure 10.1: Illustration of the parameters used in the proposed relative figure of merit of the kth candidate MNP-QD configuration (RFoM$_k$) given by equation (10.8). Here we illustrate the calculation of RFoM for a set comprising two configurations for demonstration purposes. Plots are normalized by the maximum intensity in the set. For a given normalized configuration, FWHM$_k$ stands for the full width at half maximum of the relevant (normalized) isolated MNP curve M_{Nk}. A_k depicts the area of the isolated MNP curve falling within FWHM, whereas h_k depicts the maximum kink height of the normalized nanohybrid spectrum I_{Nk} in the vicinity of the QD resonance frequency.

Using the defined normalizer, we obtain the two normalized sets,

$$\{S_I\}_N = \{I_{N1}(\omega), I_{N2}(\omega), ..., I_{Nk}(\omega), ...I_{Nn}(\omega)\}, \tag{10.4a}$$

$$\{S_M\}_N = \{M_{N1}(\omega), M_{N2}(\omega), ..., M_{Nk}(\omega), ...M_{Nn}(\omega)\}, \tag{10.4b}$$

where the kth normalized nanohybrid spectrum is denoted by

$$I_{Nk}(\omega) = I_k(\omega)/\|I\|, \tag{10.5}$$

and the k^{th} normalized isolated MNP spectrum is denoted by

$$M_{Nk}(\omega) = M_k(\omega)/\|I\|. \tag{10.6}$$

Let the height of the kink in the normalized fano-like curve $I_{Nk}(\omega)$ caused by the quantum dot's interference (in the vicinity of the QD resonance frequency) be denoted by h_{Nk}.

For each $M_{Nk}(\omega)$, let the two angular frequency values corresponding to the level where $M_{Nk}(\omega) = M_{Nk}(\omega_m)/2$ (ω_m is the MNP resonance frequency) be denoted by ω_{1k} and ω_{2k}, with $\omega_{1k} < \omega_{2k}$. The full width at half maximum ($FWHM_k$) of the spectrum $M_{Nk}(\omega)$ is defined as,

$$FWHM_k = \omega_{2k} - \omega_{1k}. \tag{10.7}$$

Using the above definitions, the RFoM for the k^{th} fano-like nanohybrid scattering spectrum is defined as [4],

$$RFoM_k = A_k/FWHM_k + h_k, \tag{10.8}$$

where $A_k = \int_{\omega_{1k}}^{\omega_{2k}} M_{Nk}(\omega)d\omega$. The components of $RFoM_k$ are graphically illustrated in Figure 10.1.

$RFoM_k$ is a measure of the scattered intensity within $FWHM_k$, with $A_k/FWHM_k$ being representative of the MNP's scattered intensity and h_k being representative of the scattered intensity caused by the QD's interference.

Using (10.8), one can form a set of RFoMs as,

$$S_{RFoM} = \{RFoM_1, RFoM_2, ..., RFoM_k, ..., RFoM_n\} \tag{10.9}$$

the elements of which correspond to, and can be used to compare the set of n different MNP-QD configurations of our interest. A higher $RFoM_k$ value suggests

a better suitability of one configuration over another, with respect to the scattered intensity at the interference point and submerging medium sensitivity [4].

The mathematically defined $\mathrm{RFoM_k}$ is intuitive, and the rationale behind it is as follows. It considers the area under the $\mathrm{FWHM_k}$ of the isolated MNP, as many scattered intensity based applications are concerned of the near-resonant behaviour of the nanohybrid, where the QD, MNP and the externally incident radiation are in close resonance with each other. Division by $\mathrm{FWHM_k}$ (of the MNP) is carried out on the basis that a narrow MNP spectrum is preferred for higher refractive index sensitivity [157]. Large $A_\mathrm{k}/\mathrm{FWHM_k}$ values therefore ensure easy detection of submerging refractive index changes at high resolution, by tracking the MNP resonance point. A tall kink (high h_k value) shows a high level of enhancement of the nanohybrid scattering spectrum at the MNP-QD interference point making the nanohybrid easily detectable at the QD resonance which would be useful in applications such as tumour imaging, especially at parallel polarization conditions [4]. It considers only the single value, kink height, instead of the area as the QD spectrum is much narrower than the MNP spectrum [158].

It was verified that the suggested metric gives meaningful results for a known special case which compares the scattered intensities of isolated Au and Ag spheres (when QDs are not turned on). It ranked the performance of the Ag sphere above Au, agreeing with the widely accepted MNP figure of merit indicators [131].

In the next section, the defined RFoM is demonstrated using the same five MNP-based nanohybrids we encountered in the earlier chapter.

10.2 Numerical Demonstration

Unless specified otherwise, the following parameters are used in the numerical analysis: incident field amplitude of $100\,\mathrm{V\,m^{-1}}$, $s_\alpha = 2$ (parallel polarization), MNP-QD detuning of 20 meV, $R = 15\,\mathrm{nm}$, $r_\mathrm{m} = 8\,\mathrm{nm}$, $\epsilon_\mathrm{b} = 6.5$, $\gamma_\mathrm{qd} = 50\,\mathrm{meV}$

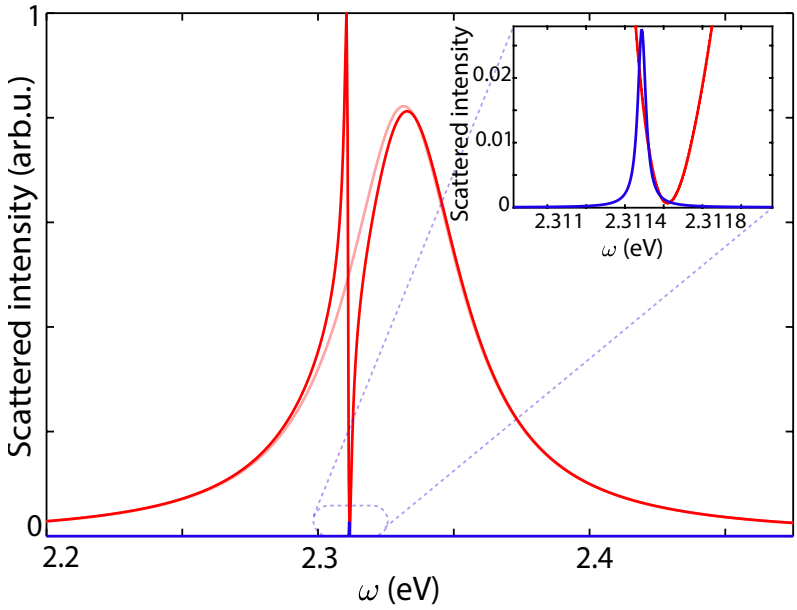

Figure 10.2: Scattered intensity spectrum (red) of an Ag based nanohybrid representing the modification of the MNP spectrum (pink) due to the interference with the QD spectrum (blue). The right insert depicts an enlarged version of the QD spectrum for better visibility.

and $\mu_{\mathrm{qd}} = 33.62$ D. The metal specific parameters are the same as those mentioned in Table A1.

10.2.1 Superior Scattering Prowess of Nanohybrids

Let us first confirm the suitability of MNP-QD nanohybrids for scattered intensity based sensing applications over their individual constituents using Fig. 10.2. It can be clearly seen that, even when the scattering intensity of the isolated QD is much smaller compared to the MNP, it is sufficient to dramatically modify the scattering spectrum of the nanohybrid via constructive and destructive interference resulting in a narrow fano-like kink. This modification produces an enhanced scattered intensity near the frequency of the excitonic transition, rendering MNP-QD nanohybrids (often) superior to the conventional QD-only or MNP-only sensors. When the polarization of the incoming field aligns with the

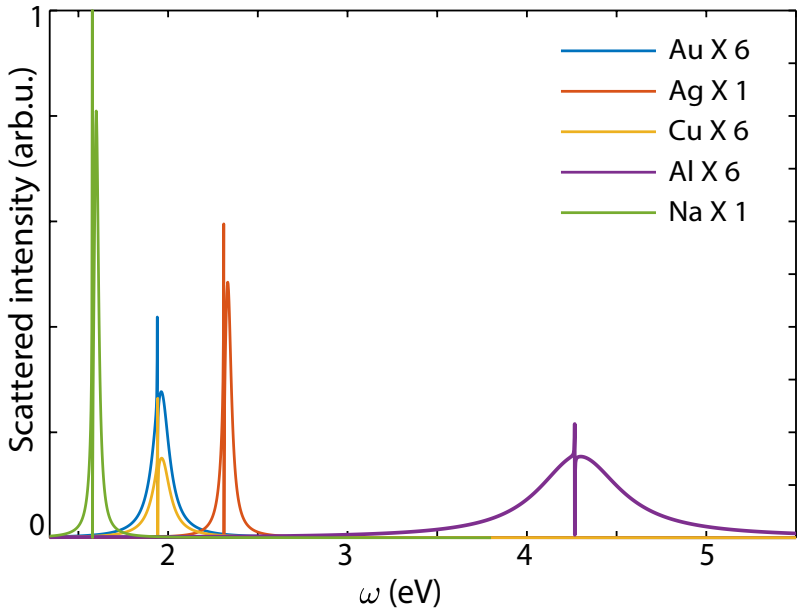

Figure 10.3: Normalized scattered intensity spectra for MNP-QD nanohybrids based on different metals when $s_\alpha = 2$ (parallel polarization). Plots for Au, Cu and Al are scaled by a factor of 6 for better visibility.

axis connecting the MNP and QD centres, the scattered intensity at the QD resonance was often observed to exceed both isolated MNP and isolated QD peak intensities. Moreover, the plasmonic peak of the nanohybrid spectrum is highly sensitive to the changes of the permittivity of the surrounding dielectric medium, hence the detection of shifts of the plasmonic peak reveals information about the composition of the submerging medium. Therefore it is evident that MNP-QD nanohybrids hold promise for superior and more informative scattered intensity based sensing applications compared to conventional isolated MNP and QD based sensors [4].

10.2.2 Ranking Different Metal Based Nanohybrids

Fig. 10.3 depicts normalized scattered intensities for MNP-QD nanohybrids based on different metals when $s_\alpha = 2$. If these five MNP-QD nanohybrid configurations are potential candidates of a sensing application, they can be compared

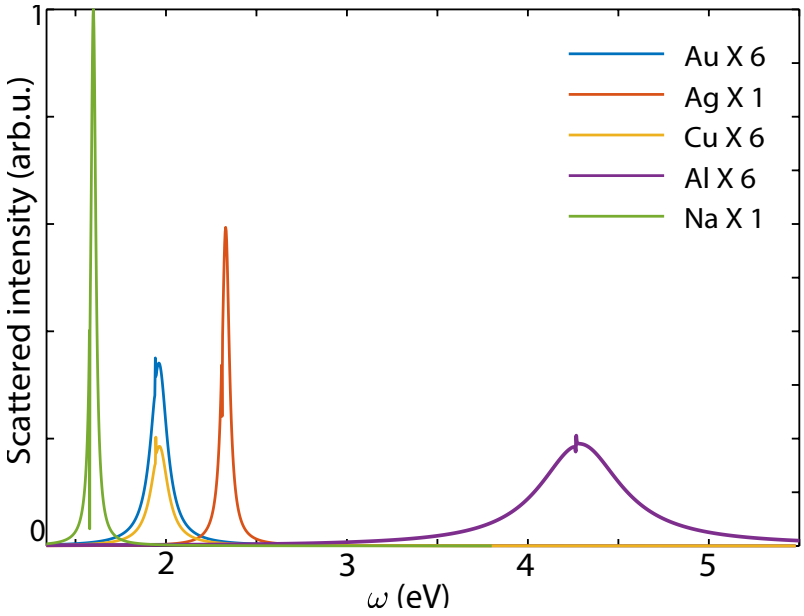

Figure 10.4: Normalized scattered intensity for MNP-QD nanohybrids based on different metals under perpendicular polarization conditions ($s_\alpha = -1$). All plots are normalized by the maximum intensity in the window. Plots for Au, Cu and Al are scaled by a factor of 6 for better visibility.

Table A1: RFoM results for curves depicted in Figure 10.3 ($s_\alpha = 2$ case) and Figure 10.4 ($s_\alpha = -1$ case)

RFoM	$s_\alpha = 2$	$s_\alpha = -1$
Au	0.106	0.105
Ag	0.981	0.856
Cu	0.064	0.064
Al	0.057	0.079
Na	1.643	1.31

using the proposed RFoM to pick the best option based on the intensity at kink position and refractive index sensitivity. The RFoM values obtained for this scenario are given in the second column of Table A1. They can be arranged in the order of their scattering prowess as Na $>$ Ag $>$ Au $>$ Cu $>$ Al. The third column gives the RFoM values calculated for the $s_\alpha = -1$ case, for the set of spectra depicted in Fig. 10.4. For this case, the ranking remains the same, except for the swap of Cu and Al. However, the RFoM values shown in Table A1 have

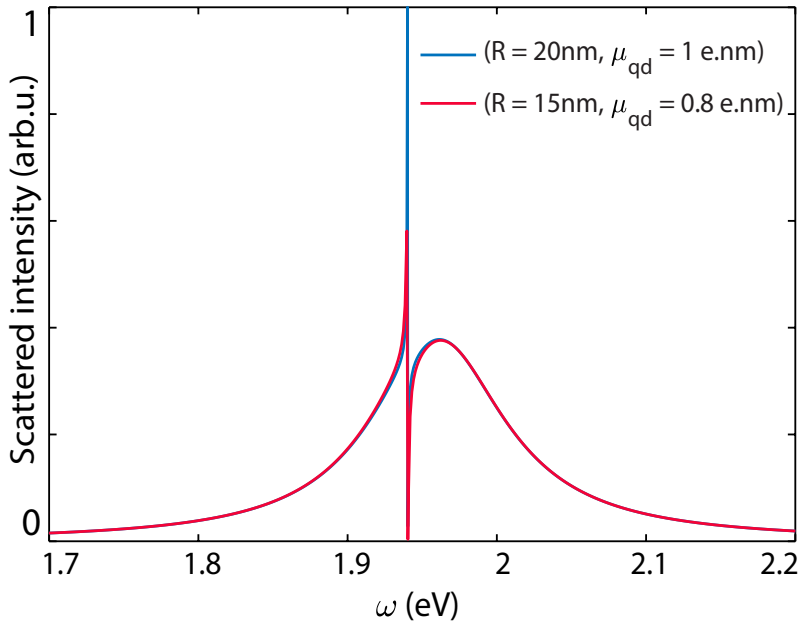

Figure 10.5: Comparison of the scattering spectra of two MNP-QD configurations based on Au. In the first configuration, MNP-QD separation R is 20 nm and the QD dipole moment element (μ_{qd}) is 1 e nm. In the second configuration, R = 15 nm and $\mu_{\mathrm{qd}} = 0.8$ e nm.

been obtained by separately normalizing the two set of spectra for the $s_\alpha = 2$ and $s_\alpha = -1$ cases, hence cannot be directly compared. If we use a common normalizer for all 10 curves, it can be observed that $\mathrm{RFoM}_{s_\alpha=2} > \mathrm{RFoM}_{s_\alpha=-1}$ (for each metal) due to the diminished kink height in the perpendicular polarization ($s_\alpha = -1$) case [4]. This feature of prominent and diminished kink heights in the respective $s_\alpha = 2$ and $s_\alpha = -1$ cases makes the MNP-QD nanohybrid usable as an orientation sensor to determine the relative locations of the QD and MNP or to observe polarization-dependent photon statistics of light scattered from the nanohybrid [159].

10.2.3 Different QD based Nanohybrids

Fig. 10.5 depicts two MNP-QD nanohybrid configurations based on Au, first with 20 nm interparticle distance and 1 e nm QD dipole moment, and the second

with 15 nm interparticle distance and 0.8 e nm QD dipole moment, which could be candidates for a tumour detection application. RFoM values calculated for configurations 1 and 2 are $\mathrm{RFoM}_1 = 1.30$ and $\mathrm{RFoM}_2 = 0.88$, respectively, which encourage the use of configuration 1 for the application. Although the choice seems trivial for the example picked, this method is pivotal when comparing a large set of potential configurations for a similar MNP-QD based sensing application.

10.3 Summary and Conclusions

This chapter proposed a simple, elegant relative figure of merit (RFoM) metric to compare a set of candidate MNP-QD nanohybrids for a given sensing application, and to rank them in their order of scattering prowess to select the best candidate. The effectiveness of the proposed RFoM was evaluated using the scattering spectra calculated by the QED assisted generalized nonlocal optical response (GNOR) method. The RFoM was used to compare various optical spectra generated by noble, alkali, transition and post transition metal based MNP-QD nanohybrids, using Au, Ag, Cu, Al and Na as the representative plasmonic materials. This chapter also highlighted the superiority and versatility of the scattered intensity based sensing capabilities of MNP-QD nanohybrids compared to their individual constituents.

Chapter 11
Prospects of Bio-Sensing

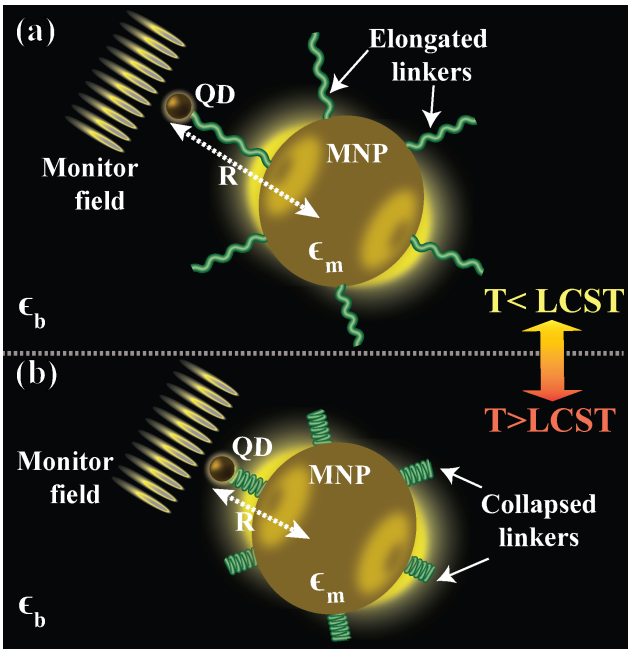

Figure 11.1: Behaviour of thermoresponsive polymer capped metal MNP-QD nanohybrids under coherent optical illumination. (a) The state of the nanohybrid at temperatures below the lower critical solution temperature (LCST) of the thermoresponsive polymer, where the polymer strands remain elongated. (b) The state of the nanohybrid at temperatures above the LCST where the polymer strands are collapsed such that the separation distance (R) between the MNP and QD is reduced.

Multifunctional nanodevices possess an unprecedented potential to contribute towards early cancer diagnosis, imaging and treatment. Such nanodevices can act as agents for tumor targeting, classification, sensing pathophysiological de-

fects in tumors, targeted delivery of therapeutic drugs, imaging, sensing of external triggers such as temperature and monitoring therapeutic response [4, 160]. These nanodevices can comprise constituents such as quantum dots (QDs) [161] and metal nanoparticles (MNPs) [4]. MNPs and QDs, which are two classes of powerful and versatile nanoparticles whose optical properties are highly tunable, have been amply investigated in literature for a wide array of bio-sensing applications [162–164]. In the earlier chapters of this thesis, it was observed that MNP-QD nanohybrids can be engineered to possess superior and versatile sensing capabilities compared to their individual constituents. They can also be tuned to behave as ultra-sensitive nanoswitches in the near-PMR regions. This chapter presents an overview of the bio-sensing prospects of MNP-QD nanohybrids, in light of the earlier observations.

11.1 Exploiting Plasmonic Metaresonances

The ability to fabricate nanohybrids where MNPs are coupled to QDs using bio-linkers has already been experimentally demonstrated in the literature [165]. The next section investigates the promising prospects of PMR-based nanoswitches, formed by attaching QDs to MNPs via bio-linkers, in sensing applications.

11.1.1 Prospects of PMR-based *In-vitro* Cancer Screening

Aptamers are a class of synthetic ligands which possess a remarkable ability to bind to specific targets with high specificity and affinity [166]. Such binding is achieved by folding these short, single-strand nucleic acid-based ligands into a target-specific three-dimensional conformation that enables precise molecular recognition of the given target [167]. Due to their excellent properties compared to conventional antibodies, aptamers have recently gained recognition as a new

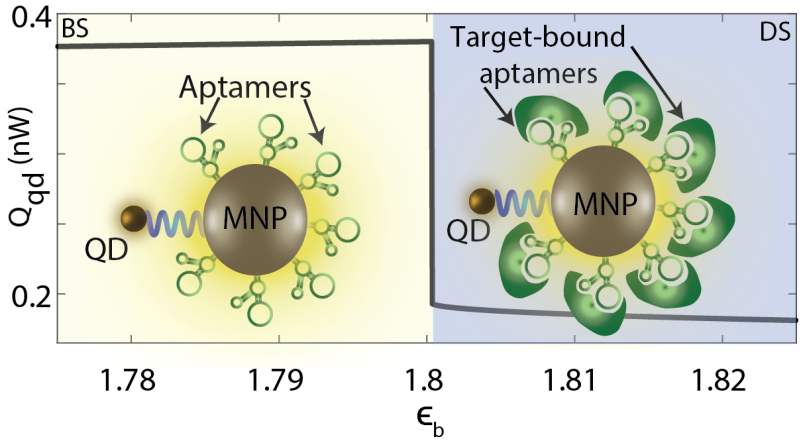

Figure 11.2: The artistic illustration of the prospective use of PMR related phase change in an aptamer-conjugated MNP-QD nanohybrid (where the MNP and QD are connected using a bio-linker) for the detection of cancer-markers in blood serum. The solid black line represents the QD absorption rate curve obtained using the GNOR formalism for $\mu \approx 1.515\,\mathrm{e\,nm}$ in Fig. 7.2(g). Submerging blood serum is assumed to be a water-like medium with relative permittivity $\epsilon_b \approx 1.8$. The abbreviations BS and DS refer to the near-PMR bright and dark states.

class of agents for the delivery of therapeutic drugs to malignant cells by targeting specific cancer-associated bio-markers. Aptamers that can target bio-markers such as the carcinoembryonic antigen (CEA) have already been developed [166]. Moreover, it has been shown that they can be structurally modified to be conjugated to other agents such as nanomaterials usable in cancer therapy [166]. Aptamer conjugated metallic nanoparticles have recently been demonstrated to have high potential for molecular targeting applications [168].

As early detection remains the most promising approach to improve the long-term survival of patients, blood-based cancer markers usable for the early identification of different types of cancer have been readily investigated [169,170]. Such bio-marker-specific aptamer-conjugated MNPs coupled to QDs using bio-linkers have promising prospects for ultra sensitive PMR-based in-vitro cancer screening. The proposed configuration is artistically illustrated in Fig. 11.2. The solid black line represents the QD absorption rate curve obtained using the GNOR

based formalism for $\mu \approx 1.515\,\mathrm{e\,nm}$ in Fig. 7.2(g).

The system is tuned such that it undergoes PMR when $\epsilon_\mathrm{b} \rightarrow 1.8$. In a host medium where aptamer-specific bio-markers (target molecules) are absent, or before target-binding occurs, the effective host medium permittivity in the immediate vicinity of the nanohybrid will be less. We assume that $\epsilon_\mathrm{b} \approx \epsilon_\mathrm{w} = 1.77$ in such conditions [29] and the nanohybrid remains in the bright state (BS), as indicated in Fig. 11.2.

When target molecules are bound to the conjugated aptamers, the effective host medium permittivity in the immediate vicinity of the nanohybrid increases. Considering a small hypothetical spherical volume in the immediate vicinity of the nanohybrid, the effective host medium permittivity felt by the nanohybrid can be crudely approximated using the Maxwell-Garnett effective medium theory [171] as follows,

$$\epsilon_\mathrm{b} \approx \epsilon_\mathrm{w} \frac{2\delta_\mathrm{i}(\epsilon_\mathrm{i} - \epsilon_\mathrm{w}) + \epsilon_\mathrm{i} + 2\epsilon_\mathrm{w}}{2\epsilon_\mathrm{w} + \epsilon_\mathrm{i} - \delta_\mathrm{i}(\epsilon_\mathrm{i} - \epsilon_\mathrm{w})}, \tag{11.1}$$

where ϵ_w is the permittivity of the submerging aqueous medium in the absence of aptamer-bound bio-markers, ϵ_i denotes the permittivity of the dry bio-marker inclusions and δ_i represents the volume fraction of the bio-marker inclusions in the spherical volume considered around the nanohybrid. For an assumed volume fraction as small as 0.1 and $\epsilon_\mathrm{i} \approx 2.5$ for the biological insertions [172], we obtain $\epsilon_\mathrm{b} \approx 1.835$ from equation (11.1) which switches the nanohybrid system to the dark state (DS) as depicted in Fig. 11.2.

It is evident that such ultra-sensitive switching capabilities could inspire in-vitro early cancer screening procedures conductible on a droplet of blood extracted from a patient which possess the potential to become routine health checks that could drastically reduce mortalities due to cancer.

11.1.2 Prospects of PMR-based *In-vivo* Temperature Monitoring

Enhanced permeability and retention (EPR) effect [173] based plasmonic photothermal therapy (PPTT), which induces cellular hyperthermia using heating agents such as plasmonic nanorods, is under extensive research to selectively target and destroy malignant tissue [174]. Hyperthermia refers to heating a tissue to temperatures in the range $41 - 47\,^{\circ}\mathrm{C}$ for tens of minutes which causes cell death by loosening the cell membranes and denaturing proteins [175]. PPTT is an attractive alternative (with comparatively less morbidity) to procedures such as surgical treatment or radiation therapy, as they preserve the anatomic functional integrity of many organs. Metal nanoparticle assisted plasmonic photothermal therapy is a minimally-invasive oncological treatment which aims to selectively target malignant tissue where photon energy is converted into heat, which induces cellular hyperthermia. It has been experimentally demonstrated that even deep tissue malignancies in mice can be selectively destroyed via *in vivo* PPTT treatment, employing plasmonic gold nanorods (GNRs) and a small, portable, inexpensive, low power near-infrared (NIR) laser [174]. Monitoring and feedback control of the tumor temperature during PPTT will further minimize the heat induced damage to the surrounding healthy tissue in close vicinity to the targeted tumor. For hyperthermia therapies to be successfully used for cancer therapeutics with minimal damage to the surrounding healthy tissue, precise temperature regulation is vital [176].

It has been shown in literature that the lower critical solution temperature (LCST) of thermo-responsive polymers such as PNIPAM (upon exceeding which the polymer strands undergo a phase change from elongated to collapsed state) can be tuned to desired levels of temperature using the molecular structure and composition. This has been demonstrated in literature by varying the molecular weight, end-groups, architecture and branching [177, 178]. PNIPAM-MNP nanocomposites have already been experimentally synthesized and widely stud-

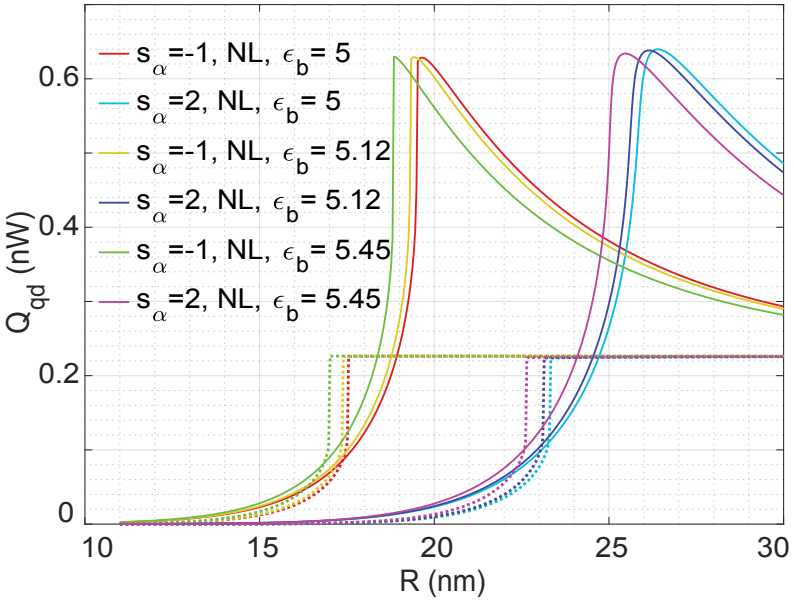

Figure 11.3: Absorption properties of a QD with $\omega_0 \approx 2.28\,\text{eV}$, $T_0 \approx 0.37\,\text{ns}^{-1}$, $\tau_0 \approx 0.8\,\text{ns}^{-1}$, $\epsilon_s = 6$ and $\mu = 2\,\text{e}\,\text{nm}$ located in the near-field of a spherical gold nanoparticle with $a = 8\,\text{nm}$, under resonant external illumination with $E_0 = 6.366 \times 10^3\,\text{V}\,\text{m}^{-1}$. The solid curves are obtained using the generalized nonlocal optical response (GNOR) method based approach whereas the dashed curves with the corresponding colors represent the respective local response approximation (LRA) based curves.

ied in literature [179, 180]. We suggest using PMR-based MNP-QD nanoswitches which are conjugated with thermoresponsive polymers as potential candidates for versatile *in-vivo* thermometers that could provide highly precise and ultra-sensitive feedback for EPR based hyperthermia therapy.

As a starting point to demonstrate the prospective *in-vivo* thermometer action, we study the absorption properties of a QD with $\omega_0 \approx 2.28\,\text{eV}$, $T_0 \approx 0.37\,\text{ns}^{-1}$, $\tau_0 \approx 0.8\,\text{ns}^{-1}$, $\epsilon_s = 6$ and $\mu = 2\,\text{e}\,\text{nm}$ [5] connected to a spherical gold nanoparticle with $a = 8\,\text{nm}$ using a thermoresponsive polymer strand. We study the system under resonant external illumination with $E_0 = 6.366 \times 10^3\,\text{V}\,\text{m}^{-1}$ at three different submerging medium permittivities $\epsilon_b \approx 5, 5.12$ and 5.45. The variation of Q_{qd} of the above system is depicted in Fig. 11.3. The solid lines in the subfigure correspond to the GNOR based curves whereas the dashed lines represent

the respective LRA based curves. It can be observed that the GNOR based curves predict higher Q_{qd} levels which non-linearly increase with decreasing MNP-QD centre separation until the system enters the dark state, resulting in a steep decline of Q_{qd}. In contrast, the LRA based curves display a seemingly steady bright state intensity. Extending the simulation towards $R = 100\,\mathrm{nm}$ reveals that both GNOR and LRA based predictions converge at higher values of MNP-QD centre separation.

The Two-dimensional Skin Tumor Model

We then develop a two-dimensional skin tumor model using which we aim to demonstrate the prospect of using plasmonic metaresonances in thermoresponsive polymer conjugated MNP-QD nanohybrids for tumor detection and hyperthermia temperature monitoring.

Fig. 11.4(a) depicts an artistic illustration of a skin tumor where we assume that the gray-scale pixel intensities linearly (and positively) correlate to the tissue water content, with the lightest areas representing a total water content of 65% and the darkest areas indicating a water content of 81.6%.

It has been experimentally observed that the dielectric permittivity of a tissue (measured at microwave frequencies) shows an approximately linear rise with the volume fraction of water [181]. We safely assume that this observation holds in the optical permittivity regime of our interest, as is also indicated by the optical permittivity data presented in Table II of [172]. The optical permittivities of the skin epidermis/dermis (E-D) tissue with a total water content of 65% is estimated as $\epsilon_{\mathrm{b}} \approx 5$, the same with a total water content of 70% is estimated as $\epsilon_{\mathrm{b}} \approx 5.12$ and the permittivity of an embedded tumor is (which has a total water content of 81.6%) is estimated as $\epsilon_{\mathrm{b}} \approx 5.45$ [172]. It has long been known that tumor-bearing tissue often contain a significantly higher volume fraction of water compared to the normal tissue from which they have been derived [182]. It has also been

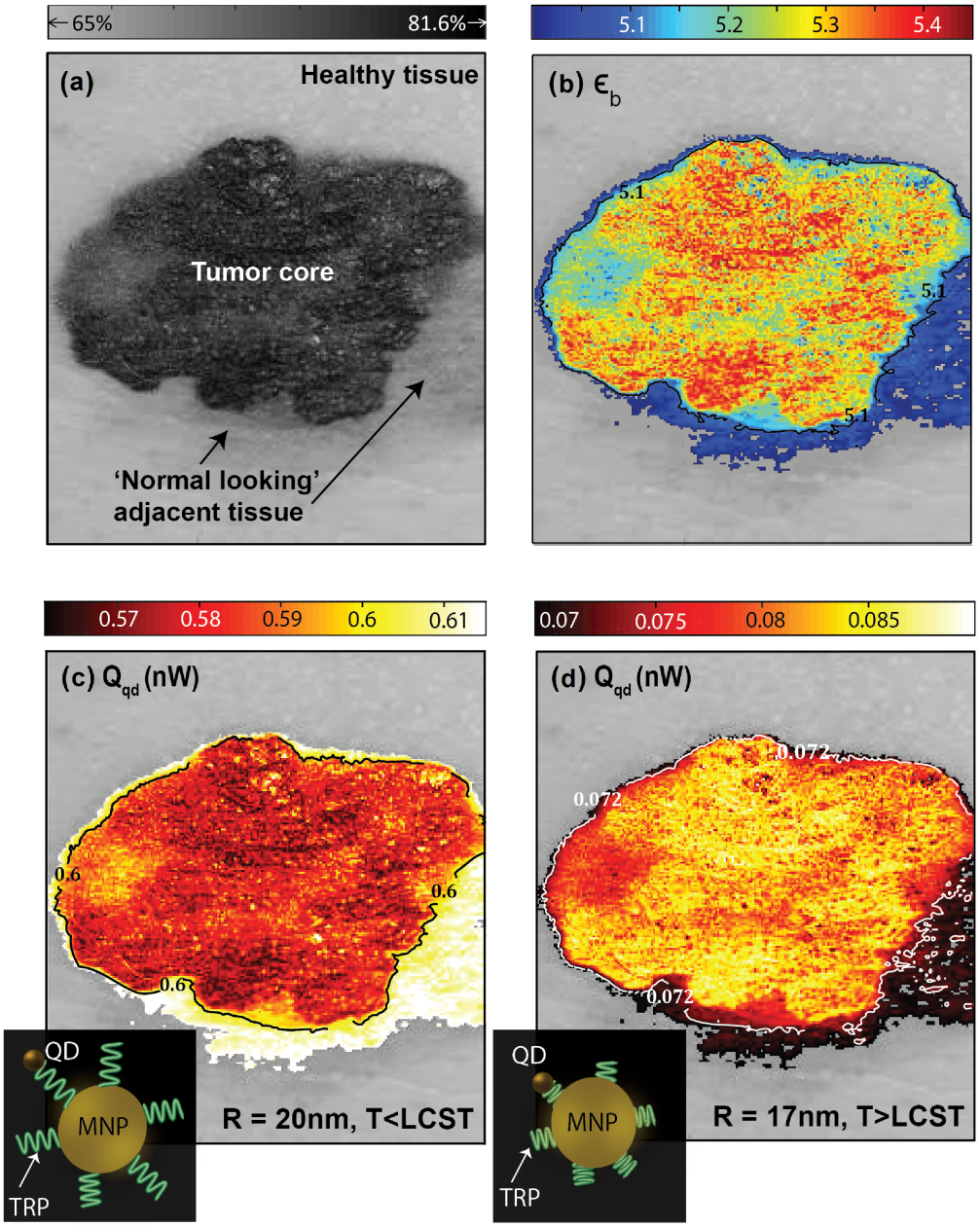

Figure 11.4: (a) An artistically illustrated skin tumor where the gray-scale pixel intensities are linearly mapped to the volume fraction of tissue water content (b) Tumor permittivity model (c) Q_{qd} when the thermoresponsive polymers remain in the elongated state (d) Q_{qd} when the thermoresponsive polymers remain in the collapsed state.

observed that "normal looking" cells adjacent to a hepatoma contain a higher water content than the healthy liver cells [182]. Hence we assume that the tissue volume fraction of water in our proposed skin tumor model is associated with the likelihood of the particular tissue being cancerous.

In light of the aforementioned evidence, we build the tumor permittivity profile depicted in Fig. 11.4(b) by linearly mapping the levels of hydration indicated by the gray-scale pixel intensities of the tumor depicted in sub-figure (a) to permittivities from $\epsilon_b = 5$ to 5.45. The model is devised such that the tissue in the vicinity of the tumor boundary possess lower volume fractions of water, hence lower dielectric permittivities and vice versa. We also assume that the tumor is two-dimensionally distributed along the E-D layer, for purposes of demonstration.

Our thermoresponsive polymer conjugated MNP-QD nanohybrids can passively target the tumor by exploiting the EPR effect. The defective leaky vascular anatomy and poor lymphatic drainage at tumor sites cause intravenously injected nanoparticles to home on the tumor [183, 184] as illustrated in Fig. 11.5, after which the tumor permittivity profile indicated in Fig. 11.4(b) will be the same as the submerging medium permittivity profile felt by the nanohybrids that are assumed to be evenly distributed across the tumour.

Margin pattern reversing phenomenon

Having developed a two-dimensional tumor model which is passively targeted by TRP-conjugated MNP-QD nanohybrids, we now assume its perpendicular illumination by an external electric field with conditions similar to the $s_\alpha = -1$ scenario indicated in Fig. 11.3. The TRP strands mediating the MNPs and QDs are assumed to be engineered to possess an LCST similar to the desired maximum hyperthermia temperature as discussed in an earlier section. The impact of environmental temperature variations (in the hyperthermia regime) on the optical

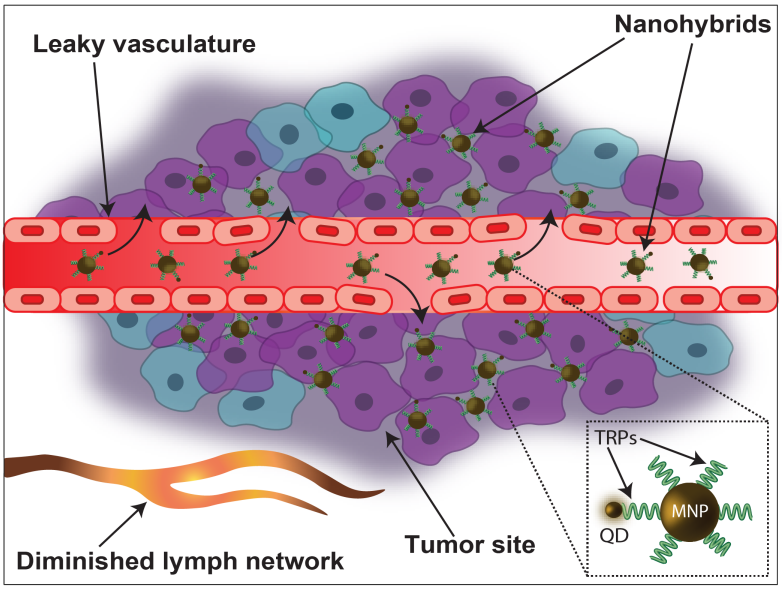

Figure 11.5: Schematic diagram illustrating the enhanced permeability and retention (EPR) effect based passive targeting of thermoresponsive nanohybrids

properties of MNPs and QDs are safely neglected due to their high temperature stability [185–187].

Fig. 11.4(c) depicts the variation of Q_{qd} when the temperature (T) of the tumor is less than the LCST of the TRP strands. When T $<$ LCST, TRP strands remain in their elongated state, hence the MNP-QD centre separation $R \approx 20\,\mathrm{nm}$. Juxtaposition of Fig. 11.4(c) and the relevant $s_\alpha = -1$ lineplots in Fig. 11.3 reveals that all nanohybrids homing the tumor, which experience submerging medium permittivities ranging from $\epsilon_{\mathrm{b}} = 5$ to 5.45, remain in their bright state, resulting in high levels of Q_{qd} when T $<$ LCST. It is interesting to note that the boundary areas of the tumor, which map to lower permittivities in Fig. 11.4(b), display higher levels of Q_{qd}, which is explainable by the respective lineplot values in Fig. 11.3 at $R = 20\,\mathrm{nm}$. This results in sharply highlighting the tumor boundary when the nanohybrids remain in their bright state, which would assist the accurate identification of the territory to be treated.

When the tumor temperature rises above the engineered LCST, the TRP strands

would abruptly collapse, reducing the distance between the QD and the MNP. We suggest selecting the TRP strand length such that nanohybrids submerged in all permittivities from 5 to 5.45 reach the PMR dark state, as indicated at $R \approx 17\,\text{nm}$ in Fig. 11.3. The resulting Q_{qd} profile of the tumor is illustrated in Fig. 11.4(d). It can be observed that the Q_{qd} levels observed throughout the tumor are significantly lower than the corresponding values in Fig. 11.4(c) due the nanohybrids now residing in the dark state. More interestingly, we can observe that the tumor absorption pattern which had the boundary highlighted in the bright state has now reversed, with the tumor core exhibiting higher levels of Q_{qd} compared to the boundary. Let us name this phenomenon as the "margin pattern reversal" caused by submerged nanohybrids entering the PMR dark state.

Post-theraputic clearance

The focus of the presented simulation-based study is to demonstrate the vivid prospects of exploiting plasmonic metaresonances in carefully engineered TRP-capped MNP-QD nanohybrids for *in-vivo* temperature monitoring on a purely theoretical basis, aiming to incite applied research that would investigate the concept further. Such research should take the following outlook and concerns into account.

After the hyperthermia temperature monitoring procedure, clearance of the nanoparticles or their degradation into biologically benign components is necessary to avoid any potential amplification of toxicity caused by their retention in the body [188]. It has been experimentally demonstrated that it is possible to prepare degradable PNIPAM oligomers possessing molecular weights below the renal cutoff that are nontoxic at biomedically relevant concentrations [189]. Efficient renal clearance has also been demonstrated for quantum dots smaller than 5.5 nm [188]. However, as it has been shown that gold nanoparticles exceeding a hydrodynamic diameter of 5.5 nm are eliminated from blood by the reticuloen-

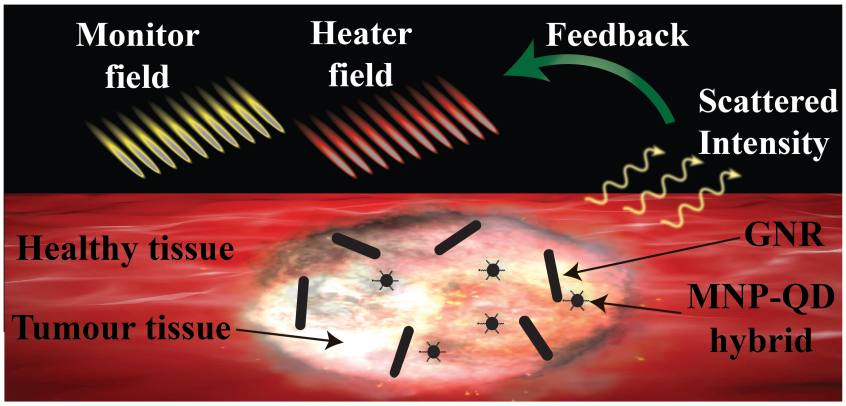

Figure 11.6: The artistic illustration of the proposed hyperthermia therapy and temperature monitoring procedure. Gold nanorods and MNP-QD nanohybrids are accumulated in the tumor tissue due to the enhanced permeability and retention effect of the tumors. The scattered intensity in the monitor field frequency window is used as a feedback signal to control the amplitude of the heater field, retaining the tumor tissue at the minimum temperature needed for cellular hyperthermia, such that the surrounding healthy tissue undergo minimal heat induced damages.

dothelial system instead of the renal system, and thus could tend to accumulate in the spleen and liver [190]. Due to reasons highlighted above, future research aimed at achieving ultimate *in-vivo* operation of the proposed procedures should not only focus on the successful experimental realization and PEGylation [191] of the nanohybrids but also on their successful post-theraputic clearance.

11.2 Exploiting Scattered Intensity Variations

This section demonstrates the prospect of using the scattered intensity variations of thermoresponsive polymer capped MNP-QD nanohybrids (an alternative to PMR based switching) for minimally invasive detection of cancerous tissue and for feedback control of tumor temperature in localized hyperthermia therapy conducted using gold nanorods, to minimize heat induced damage to the surrounding healthy tissue. The generalized nonlocal optical response method based cav-

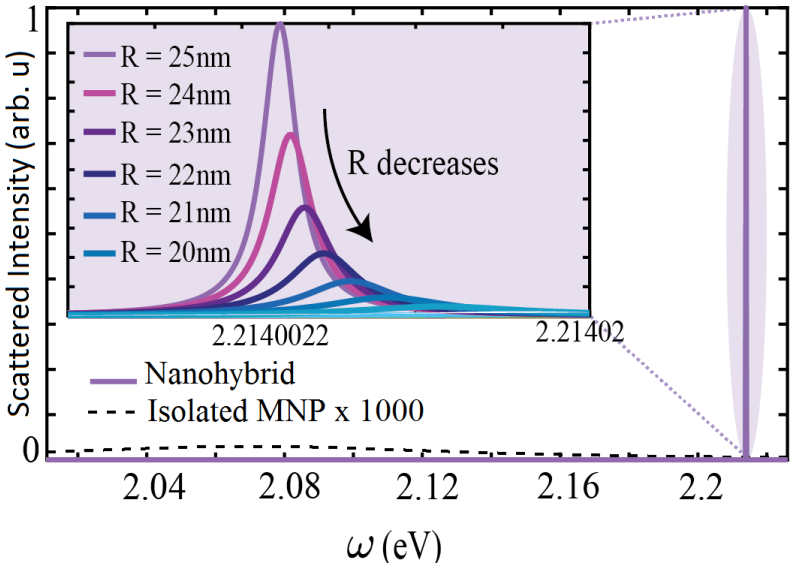

Figure 11.7: The normalized Rayleigh scattering spectra of the MNP-QD nanohybrid and the isolated gold MNP (magnified 1000 times), calculated using the cavity-QED formalism, in arbitrary units. The inset shows the zoomed versions of the nanohybrid spectra in close vicinity of the QD resonance frequency, for different values of MNP-QD centre separation R. It can be observed that the peak intensity reduces and the constructive interference maxima undergo a frequency blue-shift as R decreases. All curves are normalized by the maximum intensity in the respective subplot.

ity quantum electrodynamical formalism introduced in chapter 8 is used to obtain the Rayleigh scattering spectra of the nanohybrids.

Pertaining to our earlier discussions, let us assume a scenario where EPR assisted PPTT is conducted using gold nanorods and thermoresponsive polymer conjugated MNP-QD nanohybrids are used to monitor the tumour. Two non-overlapping near-optical frequency windows are used for the purposes of heating and monitoring the tumour, which would be called the *heater field* and *monitor field* from this point onwards. The proposed procedure is artistically illustrated in Fig. 11.6.

We can estimate the GNR absorbance, in an NIR window that does not overlap with the monitor field frequency window, using Gan's theory as follows [179,

192]:

$$\mathcal{A} \propto \frac{2\pi V \epsilon_{\mathrm{b}}^{3/2}}{3\lambda} \sum_{j} \frac{(1/P_j)^2 \,\mathrm{Im}\{\epsilon_{\mathrm{m}}\}}{\left(\mathrm{Re}\{\epsilon_{\mathrm{m}}\} + \frac{1-P_j}{P_j}\epsilon_{\mathrm{b}}\right)^2 + \mathrm{Im}\{\epsilon_{\mathrm{m}}\}^2}, \tag{11.2}$$

where V is the GNR volume and λ is the wavelength of the heater field. P_j are the depolarization factors of the three GNR axes A, B, C defined as,

$$P_A = \frac{1-e^2}{e^2}\left[\frac{1}{2e}\ln\left(\frac{1+e}{1-e}\right) - 1\right], \tag{11.3a}$$

$$P_B = P_C = \frac{1-P_A}{2}, \tag{11.3b}$$

where, $e = \sqrt{1-(B/A)^2}$ and A/B denotes the aspect ratio. GNR semi-axes are related such that $A > B = C$.

Fig. 11.1 (a) and (b) depict the two phases of a thermoresponsive polymer conjugated MNP-QD nanohybrid incident by coherent optical illumination, at temperatures above and below the LCST of the linker, respectively. For the numerical study that follows, the nanohybrid is submerged in a medium with optical permittivity $\epsilon_{\mathrm{b}} = 5.45$ [172]. It is assumed that the polymer strand is engineerd to achieve LCST at the maximum desired hyperthermia temperature, as discussed in the earlier section. The simulated nanohybrids are assumed to be formed of gold MNPs linked to CdTe QDs with excitonic energy 2.214 eV [193], transition dipole moment 50D [194] and excitonic decay rate $0.055\,\mathrm{ns}^{-1}$ [195]. Among various QDs, protein capped cadmium telluride (CdTe) QDs are considered as promising probes in the bio-imaging of living cells due to their tunable photoluminescence upon optical excitation, higher photostability, water solubility, more controllable and narrower emission bands and higher quantum yields compared to the conventional fluorescent dyes [193]. The radius of the MNP is kept at 5 nm. Parallel polarization condition where the MNP-QD axis lies along the coherent optical illumination is assumed for the presented results. It was verified that similar results hold for perpendicular polarization conditions and hence for any

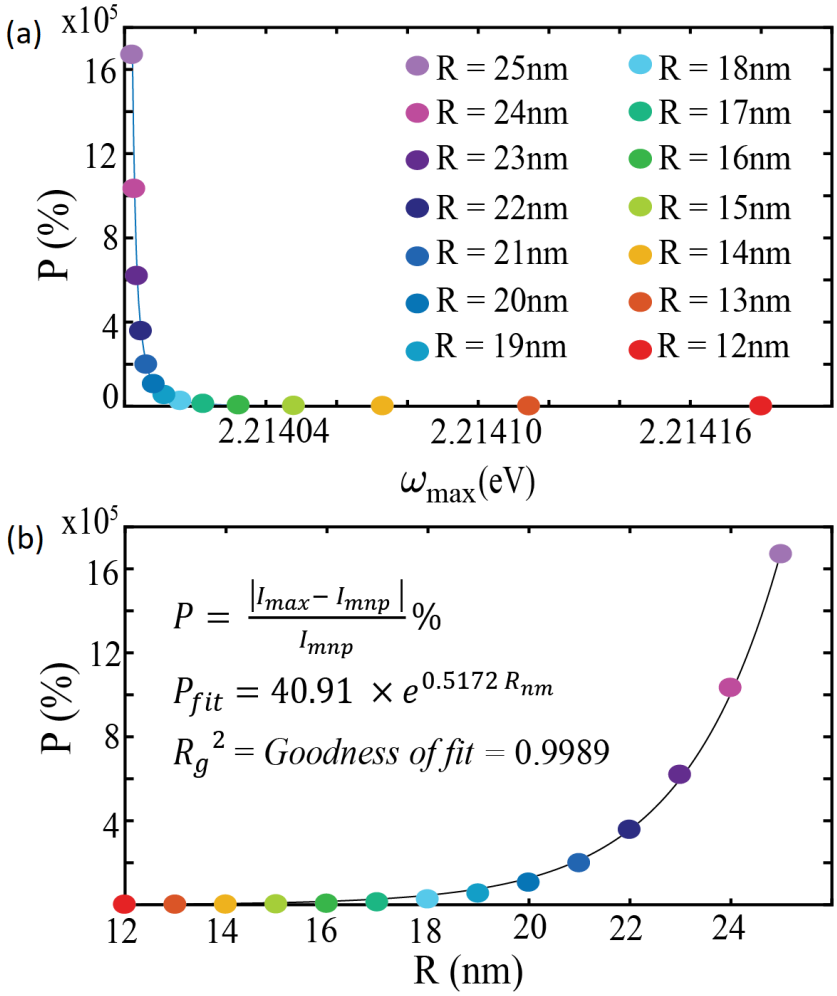

Figure 11.8: (a) Percentage Rayleigh scattering enhancement (P) of the nanohybrid over the quasi-constant (in a narrow frequency window around the resonance of the QD) scattered intensity of the isolated gold nanosphere (I_{mnp}), at the position where the nanohybrid scattering reaches its maximum (I_{max}), plotted against the frequency at the scattering maximum of the nanohybrid (ω_{max}). Each dot corresponds to the peak point of the same colored curve of the earlier subplot. (b) shows P plotted against the the gold nanosphere-QD centre separation (R), with the dot colors bearing the same meaning as earlier. The solid line depicts the fitted exponential model with a goodness of fit 0.9989, for the parameter set considered for this study.

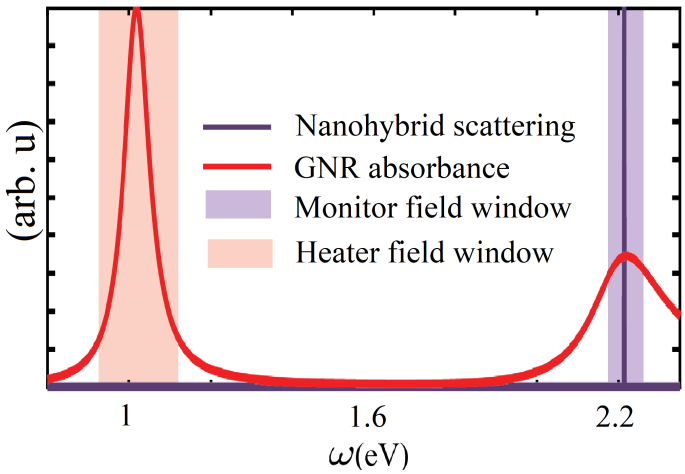

Figure 11.9: The nanohybrid Rayleigh scattering spectrum for any given centre separation distance considered earlier in Fig. 11.7, and the absorbance curve for gold nanorods with aspect ratio 4 and any given constant volume, submerged in the same dielectric medium as the nanohybrids obtained using Gan's theory [3]. Both plots are normalized using the own maximum intensity. The areas highlighted in pink and purple represent the two non-overlapping frequency windows used for heating and monitoring, respectively.

random orientation which is readily expressible using parallel and perpendicular orientations.

The Rayliegh scattering spectra of the nanohybrid and the isolated MNP, depicted in Fig. 11.7 were calculated using GNOR assisted cavity QED formalism discussed in chapter 8. Fig. 11.8 (a) depicts the Rayleigh scattering enhancement (P) over the isolated MNP at the scattering maximum of the MNP-QD nanohybrid plotted against the angular frequencies at scattering maxima. Fig. 11.8 (b) shows that P follows an exponential scaling with the MNP-QD centre separation distance R. Moreover, it can be observed from Fig. 11.7, 11.8(a) and (b), that the peaks exhibit a blue-shift with decreasing R, which could form the basis for a multitude of MNP-QD nanohybrid based sensing applications.

Normalized GNR absorbance spectrum for gold nanorods with aspect ratio 4, obtained using Gan's theory, is depicted in Fig. 11.9. From the same figure, it is clearly evident that the monitoring (optical) and heating (NIR) frequency

windows are non-overlapping and hence can be utilized simultaneously, with minimal interference to each other.

These observations reveal the promising prospects of the minimally invasive tumor detection, treatment and monitoring procedure depicted in Fig. 11.10. In this procedure, intravenously injected gold nanorods and aforementioned gold MNP-CdTe QD nanohybrids are allowed to home on the malignant tissue due to the EPR effect as depicted in Fig. 11.6. Monitor field (in the optical frequency window indicated in Fig. 11.9) is illuminated on the tumor-bearing area and the Rayliegh scattering of homing nanohybrids are used to image the tumor. As this is done at the body temperature (37 °C), below the LCST, PNIPAM strands reside in their elongated state (large R), favorably resulting in a high scattered intensity. Once the tumor is precisely located, a targeted heater field in the near infrared (NIR) frequency regime around the longitudinal plasmon resonance of the GNRs, as indicated in Fig. 11.6, is turned on to conduct PPTT. In this minimally-invasive therapeutic procedure, photon energy is converted into heat by the accumulated GNRs, selectively destroying the cancer tissue. GNRs are ideal candidates for PPTT, as they strongly absorb photons in the NIR range and generate heat energy much faster than gold nanospheres [3]. When the tumor gradually reaches the minimal hyperthermia temperature sufficient for denaturation of cells which is same as the engineered LCST, the binding PNIPAM strands abruptly collapse, reducing the MNP-QD centre separation R, followed by the scattered intensity. This could be used as a feedback signal to regulate the heater field amplitude at the minimum required level, minimizing heat-induced damage to the surrounding healthy tissue.

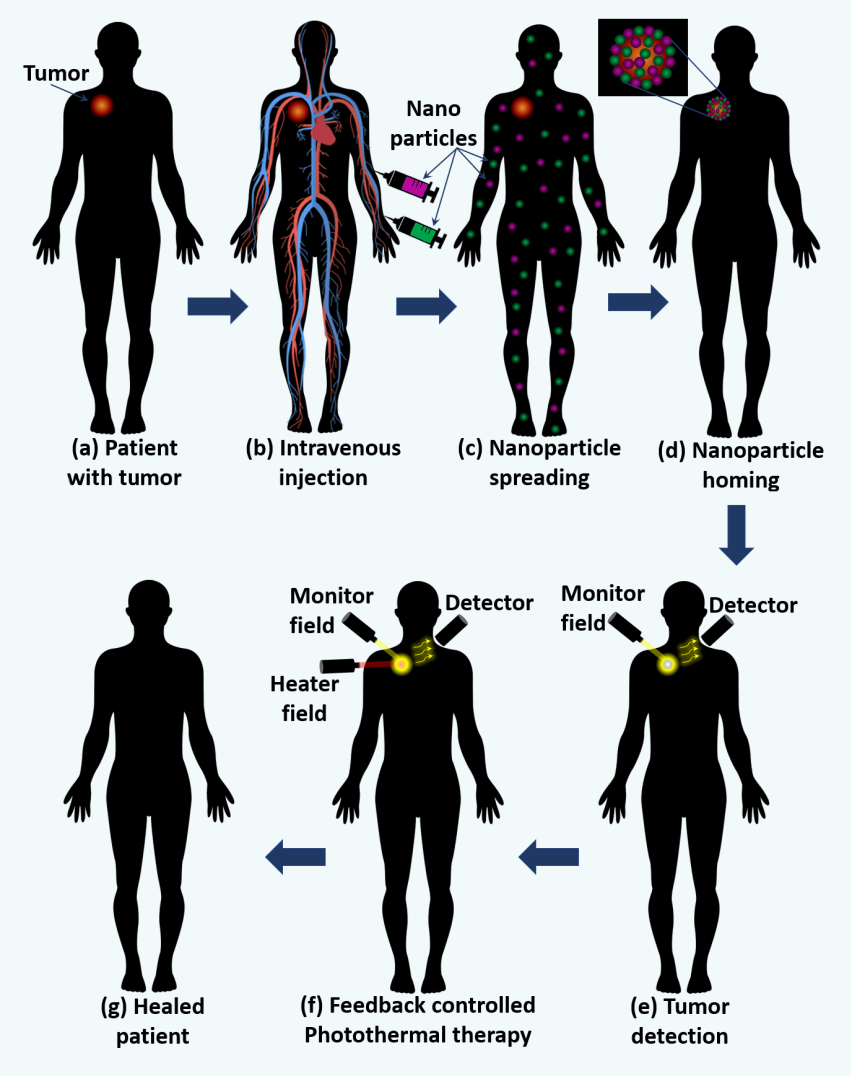

Figure 11.10: (a) Patient with a tumor. (b) Intravenously injecting two types of nanoparticles (MNP-QD nanohybrids and gold nanorods) (c) The injected nanoparticles are expected to flow throughout the patient's body with the bloodstream. (d) The nanoparticles home on the tumor due to the enhanced permeability and retention effect of the tumor tissue. (e) Monitor field is illuminated on the suspected tumorous area to localize the tumor. (f) Once the tumor is precisely located, the heater field is turned on, and the monitor field sustained to the obtain feedback using which the heater field amplitude is controlled at the minimal level required to achieve hyperthermia at the tumor. (g) Tumor tissue is selectively destroyed with minimal damage to the healthy tissue in the vicinity.

11.3 Summary and Conclusions

This chapter presented the prospects of exploiting MNP-QD nanohybrids for biosensing applications in the forms of PMR-based nanoswitches and scattered intensity based sensors. The first section suggested two applications of PMR-based nanoswitches, namely, aptamer based in-vitro cancer screening and thermoresponsive polymer based temperature sensing. To demonstrate the latter application, a proof of concept (two dimensional) skin tumor model, homogeneously populated by MNP-QD nanohybrids, was utilized. The simulations revealed a novel near-PMR physical phenomenon observable under perpendicular illumination, which we named as the *margin pattern reversal*, where the spatial absorption pattern reverses as the near-PMR QDs switch from their bright to dark state.

The second section was dedicated to demonstrate the prospect of exploiting the scattering spectra of MNP-QD nanohybrids for minimally invasive detection of cancerous tissue and for feedback control of tumor temperature in localized hyperthermia therapy conducted using gold nanorods, to minimize damage to the surrounding healthy tissue. Here, we used the generalized nonlocal optical response method based cavity quantum electrodynamical formalism and showed that the enhancement of the Rayleigh scattering intensity of the nanohybrid over that of the isolated gold nanosphere follows an exponential scaling with varying nanohybrid centre separation distance, in the close vicinity of the QD resonance frequency. Such behaviour makes polymer mediated MNP-QD nanohybrids ideal candidates for a multitude of distance based sensing applications.

Chapter 12

Contributions and Future work

12.1 Summary of Contributions

Research objective 1 - Development of a GNOR assisted cavity QED model of an MNP-QD hybrid molecule

In this stage, we analytically modelled an MNP-QD nanohybrid in an external driving field, as an open quantum system, using a GNOR assisted cavity-QED approach. In the process, we quantum mechanically modelled the dipole moment operator and the dipole response field of the metal nanoparticle, taking the nonlocal effects into account. This model accounts for the nonlocal optical response of the MNP plasmons and its impact on the behaviour of the nanohybrid without needing to invoke computationally demanding *ab initio* approaches of accounting for nonlocality. Moreover, it is computationally much less demanding than the conventional local response approximation based numerical approaches amply utilized in the literature.

This stage was successfully completed and the results were published in the journal *Physical Review B*

Research objective 2 - Analysis and comparison of different resonator based nanohybrids

In this stage, we presented a simple, elegant relative figure of merit (RFoM), which focuses on maximizing the scattered intensity and the refractive index sensitivity of MNP-QD nanohybrids, to rank them in the order of their scattering prowess for sensing applications. The proposed RFoM was used to analyse the optical spectra of noble, transition, post transition and alkali metal based MNP-QD nanohybrids using the representative metals Au, Ag, Cu, Al and Na, adopting the generalized nonlocal optical response (GNOR) method based cavity QED approach developed in the earlier stage. This stage also produced numerical evidence to the superior and versatile sensing capabilities of the MNP-QD nanohybrids, in comparison to the individual constituents, proving that such nanohybrids possess better prospects in sensing applications.

This stage was successfully completed and the results were communicated in the *Journal of Physics: Condensed Matter*.

Research objective 3 - Investigating the effects of nonlocal plasmonic response on the coherent dynamics of vicinal excitons

This stage entailed analytically characterizing the influence of a neighboring metal nanoparticle (MNP) on the behavioral trends of a quantum dot (QD) using a generalized nonlocal optical response (GNOR) method based approach, taking the MNP distance dependent modifications to the QD population relaxation and dephasing rates into account. The proposed GNOR based model predicted strong modifications to various QD properties such as the population difference, absorption, MNP induced shifts to excitonic energy and Förster enhanced broadening, coherent plasmonic field enhancement, and quantum state purity, compared to the conventional LRA based predictions. Such modifications were seen to be

prominent with small MNP radii, high QD dipole moments, small detunings (of the coherent external illumination from the bare excitonic resonance), and near parameter regions exhibiting plasmonic meta resonance (PMR)-like behavior.

Upon successful completion of this stage, the findings were communicated in the journal *Physical Review B*.

Research objective 4 - Improved modeling of plasmonic metaresonances

In this stage, we modeled the plasmonic metaresonances in an exciton-plasmon nanohybrid using an approach based on the GNOR formalism and compared the results to those obtained using the conventional local response approximation. The results indicated that, omission of the MNP nonlocal response and the associated decay/dephasing rate modifications of the QD tend to raise implications such as significant over-estimation of the QD dipole moment required to achieve PMR, under-estimation of the critical centre separation and prediction of significantly lower near-PMR QD absorption rate, in comparison to the improved GNOR based predictions. In light of the observations, we suggested two prospective applications of PMR based nanoswitches, namely, aptamer based *in-vitro* cancer screening and thermoresponsive polymer based temperature sensing. To demonstrate the latter application, we developed and utilized a proof of concept (two dimensional) skin tumor model homogeneously populated by MNP-QD nanohybrids. The simulations revealed a novel near-PMR physical phenomenon observable under perpendicular illumination, which was named the *margin pattern reversal*, where the spatial absorption pattern reverses when the near-PMR QDs switch from the bright to dark state.

This stage was successfully completed. The resulting (accepted) journal article is currently in production in the *Journal of Physics: Condensed Matter*.

Research objective 5 - Further investigation of the bio-sensing prospects of exciton-plasmon nanohybrids

In this stage, we theoretically demonstrated the prospect of using thermoresponsive polymer capped MNP-QD nanohybrids for minimally invasive detection of skin cancer tissue and for feedback control of tumor temperature in localized hyperthermia therapy conducted using gold nanorods, to minimize damage to the surrounding healthy tissue. Here, we used the GNOR based cavity QED model developed earlier and showed that the enhancement of the Rayleigh scattering intensity of the nanohybrid over that of the isolated gold nanosphere could exhibit an exponential-like scaling with varying nanohybrid centre separation distance, in the close vicinity of the QD resonance frequency.

This stage was successfully completed and the resulting conference article was published in the IEEEXplore Digital Library, proceedings of the *12th IEEE Conference on Nano/Molecular Medicine and Engineering*.

12.2 Suggestions for Future Work

The work presented in this thesis can be extended in a number of theoretical and experimental pathways. We have outlined a few suggested directions below.

Investigating the impact of nonlocal multipolar response on exciton-plasmon interaction

This thesis focused on the interaction of a semiconductor quantum dot with a small metal nanoparticle operating in the nonlocal dipole regime. It has been shown that nonlocal effects on the dipole mode of a small metallic sphere dominates for diameters in the order of 20 nm, in the quasi static regime [11]. However, different sources of excitation such as the swift electron used in EELS (electron en-

ergy loss microscopy) could produce significantly inhomogeneous electric-field distributions which can excite higher-order multipoles even in metal spheres with diameters below 20 nm [11,196,197]. Thus, we believe that future research considering the nonlocal resonance condition for all multipoles given in the nonretarded limit [196] will certainly be useful in the context of device design.

Investigating the interaction of differently shaped nanoresonators with quantum dots

Although several studies in the literature have concerned the interaction of semiconductor quantum dots with differently shaped metal nanoparticles such as nanorods, nanodisks and ellipsoids [102,198,199], we did not encounter fully analytical studies which quantum mechanically model the entire nanohybrid while taking the non-classical effects of the resonator into account. We believe that such studies will prove to be useful in many areas of application.

Modeling the interaction of three and multi-level quantum dots with metal nanoparticles

Similar to the earlier scenario, the interaction of a three-level quantum dot with a metal nanoparticle modeled using the local response approximation has been the focus of several studies [199,200]. To the best of our knowledge, the development of a fully quantum mechanical, analytical model that takes the resonator nonclassical effects into account is yet to be done.

Investigating the size effects of quantum dots in exciton-plasmon nanohybrids

Quantum dots are regarded as zero-dimensional material [201, 201] which has resulted in almost all theoretical studies in literature [5,23,24,26,106,115,200], including ours, neglecting their size effects. However, in a reality, quantum dots too

are finite dimensional and accounting for their size effects in theoretical studies would be useful in the context of practical applications.

Investigating exciton-plasmon interactions in all-carbon nanohybrids

The possibility of inducing localized surface plasmons in graphene nanoflakes and excitons in carbon nanotubes have been recently investigated in the literature [202, 203]. It has also been shown that nanohybrids where graphene nanoflakes are optically coupled to carbon nanotubes could potentially possess enhanced sensing capabilities compared to the individual constituents whilst inheriting their high biocompatibility, favourable electrical, mechanical and spectroscopic properties. All-carbon nanohybrids are also believed to be competitive candidates for bio-sensing applications due to their potentially high biocompatibility and tunability compared to metal-resonator based sensors [204].

Further investigations on all-carbon exciton-plasmon nanosuperstructures may be extremely helpful for the future development of sensors and spasers with a plethora of favorable physical properties.

Fully analytical characterization of nanohybrids comprising multiple quantum dots and metal nanoparticles

During our extensive literature review, we encountered a handful of research which model the interaction between multiple metal nanoparticles and quantum dots [127, 205], none of which take non-classical effects such as the nonlocal response or plasmon hybridization [206] into account.

Attempts to develop analytical models that overcome the aforementioned limitations will be worth the mathematical complexities encountered, as they will help realistic modeling with drastically reduced computational complexity compared to *ab initio* methods such as density functional theory.

Theoretical and experimental investigation of the prospects of exciton-plasmon nanohybrids in practical applications

This thesis numerically demonstrated a few prospects of exciton-plasmon nanohybrids in bio-sensing applications. Endless future research can be carried out to investigate the prospects of such nanohybrids in areas of light harvesting, quantum computing, nanoelectronics and spasing.

These are only a few examples of the possible future advancements in the context investigated in this thesis. As a final remark, we can assure that the readers will only realize how wise the words of *Richard Feynman* were, once they start investigating along the path.

"There is plenty of room at the bottom..."

Appendix A
Localized Surface Plasmons

A.1 Solving Laplace's Equation for Azimuthal Symmetry

In the spherical coordinate system r, θ and ϕ, the *Laplace's equation* reads [207],

$$\frac{1}{r^2}\frac{\partial}{\partial r}\left(r^2\frac{\partial}{\partial r}\mathcal{V}\right)+\frac{1}{r^2\sin(\theta)}\frac{\partial}{\partial\theta}\left(\sin(\theta)\frac{\partial}{\partial\theta}\mathcal{V}\right)+\frac{1}{r^2\sin^2(\theta)}\frac{\partial^2}{\partial\phi^2}\mathcal{V}=0. \tag{A.1}$$

Due to the azimuthal symmetry of our configuration, $\mathcal{V}$ is independent of ϕ, hence (A.1) reduces to,

$$\frac{1}{r^2}\frac{\partial}{\partial r}\left(r^2\frac{\partial}{\partial r}\mathcal{V}\right)+\frac{1}{r^2\sin(\theta)}\frac{\partial}{\partial\theta}\left[\sin(\theta)\frac{\partial}{\partial\theta}\mathcal{V}\right]=0. \tag{A.2}$$

We are interested in separable solutions of the form, $\mathcal{V}(r,\theta)=\mathcal{R}(r)\Theta(\theta)$. We substitute the above equation in (A.2) and divide by $\mathcal{R}\Theta$ to arrive at,

$$\frac{1}{\mathcal{R}}\frac{\partial}{\partial r}\left(r^2\frac{\partial}{\partial r}\mathcal{R}\right)+\frac{1}{\Theta\sin(\theta)}\frac{\partial}{\partial\theta}\left(\sin(\theta)\frac{\partial}{\partial\theta}\Theta\right)=0. \tag{A.3}$$

The addends of (A.3) should be separately zero for the sum to be null, as they depend on different independent variables. Hence we arrive at the Radial equation,

$$\frac{d}{dr}\left(r^2\frac{d}{dr}\mathcal{R}\right)=n(n+1)\mathcal{R}, \tag{A.4}$$

which has the general solution,

$$\mathcal{R} = Ar^n + \frac{B}{r^{n+1}} \tag{A.5}$$

and the Angular equation,

$$\frac{d}{d\theta}\left(\sin(\theta)\frac{d}{d\theta}\Theta\right) = -n(n+1)\Theta\sin(\theta) \tag{A.6}$$

the solutions of which are *Legendre polynomials* of the variable $\cos(\theta)$,

$$\Theta(\theta) = P_n(\cos(\theta)). \tag{A.7}$$

$P_n(x)$ in (A.7) is given by the Rodrigue's formula,

$$P_n(x) = \frac{1}{2^n n!}\left(\frac{d}{dx}\right)^n (x^2-1)^n. \tag{A.8}$$

Rodrigue's formula works only for non-negative integers n and the Angular equation possesses two independent solutions for every value of n. However, there is only one physically acceptable solution as the other solutions tend to blow up at $\theta = 0$ and $\theta = \phi$. Thus, in the case of azimuthal symmetry, the most general, physically acceptable separable solution is,

$$\mathcal{V}(r,\theta) = \left(Ar^n + \frac{B}{r^{n+1}}\right) P_n(\cos(\theta)). \tag{A.9}$$

The general solution would a linear combination of the separable solutions,

$$\mathcal{V}(r,\theta) = \sum_{n=0}^{\infty}\left(A_n r^n + \frac{B_n}{r^{n+1}}\right) P_n(\cos(\theta)). \tag{A.10}$$

A.2 Boundary Conditions of Electric Scalar Potential

We obtained the unsimplified expression for electric potential as (2.5),

$$\mathcal{V}(r,\theta) = \begin{cases} \sum_{n=0}^{\infty} \left[\mathcal{A}_n \left(\frac{r}{a}\right)^n + \mathcal{B}_n \left(\frac{a}{r}\right)^{n+1}\right] P_n\left[\cos(\theta)\right], & \text{for } r < a \\ \sum_{n=0}^{\infty} \left[\mathcal{A}'_n \left(\frac{r}{a}\right)^n + \mathcal{B}'_n \left(\frac{a}{r}\right)^{n+1}\right] P_n\left[\cos(\theta)\right], & \text{for } r \geq a \end{cases}$$

It can be seen that nonzero values of $\mathcal{B}_n$ leads to unphysical infinite potentials inside the MNP when $r \to 0$. Hence $\forall n$, $\mathcal{B}_n = 0$. Moreover, when $r \to \infty$, $E \to E_{\text{drive}} = E_0\hat{z}$. Therefore, as $\boldsymbol{E} = -\nabla\mathcal{V}$, using simple integration, we arrive at $\mathcal{V} \to -E_0 r\cos(\theta)$ when $r \to \infty$. As $P_n[\cos(\theta)] = \cos(\theta)$ only for $n = 1$, $\mathcal{A}'_1 = -aE_0$ and $\mathcal{A}'_n = 0\ \forall n \neq 1$. Using these boundary conditions, we arrive at [5],

$$\mathcal{V}(r,\theta) = \begin{cases} \sum_{n=0}^{\infty} \mathcal{A}_n \left(\frac{r}{a}\right)^n P_n\left[\cos(\theta)\right], & \text{for } r < a \\ \sum_{n=0}^{\infty} \mathcal{B}'_n \left(\frac{a}{r}\right)^{n+1} P_n\left[\cos(\theta)\right] - E_0 r\cos(\theta), & \text{for } r \geq a \end{cases} \tag{A.11}$$

For the continuity of $\mathcal{V}$ at the particle boundary, the two conditional expressions for $r < a$ and $r \geq a$ should be equal when $r = a$. Thus,

$$\sum_{n=0}^{\infty} \mathcal{A}_n P_n \cos(\theta) = \sum_{n=0}^{\infty} \mathcal{B}'_n P_n \cos(\theta) - E_0 a\cos(\theta). \tag{A.12}$$

For the continuity of the radial displacement field $\boldsymbol{D}$ across the dielectric surface, when $r = a$,

$$\epsilon_{\text{b}} \frac{\partial}{\partial r}\mathcal{V}\Big|_{\text{outside}} = \epsilon_{\text{m}} \frac{\partial}{\partial r}\mathcal{V}\Big|_{\text{inside}} \tag{A.13}$$

Obtaining the partial derivative of r for both sides of (A.11) and setting $r = a$ gives,

$$\frac{\partial}{\partial r}\left[\epsilon_{\mathrm{b}}\sum_{n=0}^{\infty}\mathcal{B}'_n\left(\frac{a}{r}\right)^{n+1}P_n\left[\cos(\theta)\right]-E_0 r\cos(\theta)\right]=\frac{\partial}{\partial r}\left[\epsilon_{\mathrm{m}}\sum_{n=0}^{\infty}\mathcal{A}_n\left(\frac{r}{a}\right)^{n}P_n\left[\cos(\theta)\right]\right]$$

$$\frac{\epsilon_{\mathrm{m}}}{\epsilon_{\mathrm{b}}}\sum_{n=1}^{\infty}n\mathcal{A}_n\frac{1}{a}P_n\left[\cos(\theta)\right]=\sum_{n=1}^{\infty}-(n+1)\mathcal{B}'_n\frac{1}{a}P_n\left[\cos(\theta)\right]-E_0\cos(\theta) \quad \text{(A.14)}$$

where the $n=0$ summation component has disappeared from both sides due to the factor n on the L.H.S.

Legendre polynomials are orthogonal with respect to their L^2 inner product in the interval $-1\leq x\leq 1$ such that [208],

$$\int_{-1}^{1}P_{\mathrm{m}}(x)P_{\mathrm{n}}(x)dx=\frac{2}{2n+1}\delta_{\mathrm{mn}} \quad \text{(A.15)}$$

where δ_{mn} denotes the Kronecker delta function. From (2.5), for continuity of $\mathcal{V}$ at the dielectric interface ($r=a$),

$$\sum_{n=0}^{\infty}(\mathcal{A}_n+\mathcal{B}_n)P_n\left[\cos(\theta)\right]=\sum_{n=0}^{\infty}(\mathcal{A}'_n+\mathcal{B}'_n)P_n\left[\cos(\theta)\right], \quad \text{(A.16)}$$

When we multiply both sides by $P_0\cos(\theta)$,

$$\sum_{n=0}^{\infty}(\mathcal{A}_n+\mathcal{B}_n)P_n\left[\cos(\theta)\right]P_0\left[\cos(\theta)\right]=\sum_{n=0}^{\infty}(\mathcal{A}'_n+\mathcal{B}'_n)P_n\left[\cos(\theta)\right]P_0\left[\cos(\theta)\right],$$

only the $n=0$ terms survive due to the orthogonality of Legendre polynomials, leading to $(\mathcal{A}_0+\mathcal{B}_0)=(\mathcal{A}'_0+\mathcal{B}'_0)$. As we showed earlier, $\mathcal{A}'_0=\mathcal{B}_0=0$. Hence we arrive at $\mathcal{A}_0=\mathcal{B}'_0$. Similarly, multiplying (A.16) by $P_1\cos(\theta)$ and $P_n\cos(theta)$ respectively, we can arrive at $\mathcal{A}_1=\mathcal{B}'_1-aE_0$ and $\mathcal{A}_n=\mathcal{B}'_n\ \forall n>1$. Moreover, by multiplying both sides of (A.14) by $P_1\cos(\theta)$ and $P_{\mathrm{m}}\cos(\theta)$ respectively, and exploiting the orthogonality of Legendre polynomials, we can obtain the boundary conditions $\epsilon_{\mathrm{m}}\mathcal{A}_1/\epsilon_{\mathrm{b}}=-2\mathcal{B}'_1-E_0a$ and $n\epsilon_{\mathrm{m}}\mathcal{A}_n/\epsilon_{\mathrm{b}}=-(n+1)\mathcal{B}'_n$. Simultane-

ously solving these equations, the following can be obtained,

$$\mathcal{A}_1 = \frac{-3\epsilon_\mathrm{b}}{2\epsilon_\mathrm{b} + \epsilon_\mathrm{m}} E_0 a \tag{A.17a}$$

$$\mathcal{B}'_1 = \frac{\epsilon_\mathrm{m} - \epsilon_\mathrm{b}}{2\epsilon_\mathrm{b} + \epsilon_\mathrm{m}} E_0 a \tag{A.17b}$$

$$\frac{n+1}{n}\mathcal{A}_n = -\frac{\epsilon_\mathrm{m}}{\epsilon_\mathrm{b}}\mathcal{A}_n,\ n > 1 \tag{A.17c}$$

We can readily observe that the equation (A.17c) would not hold for the complex dielectric permittivity ϵ_m and non-absorbing ϵ_b unless $\mathcal{A}_n = 0$ for all $n > 1$.

Hence the final solution for the electric scalar potential becomes [5],

$$\mathcal{V}(r,\theta) = \begin{cases} -\frac{3\epsilon_\mathrm{b}}{(2\epsilon_\mathrm{b}+\epsilon_\mathrm{m})} E_0 r\cos(\theta), & \text{for } r < a \\ \frac{\epsilon_\mathrm{m}-\epsilon_\mathrm{b}}{2\epsilon_\mathrm{b}+\epsilon_\mathrm{m}} a^3 E_0 \frac{1}{r^2}\cos(\theta) - E_0 r\cos(\theta), & \text{for } r \geq a \end{cases} \tag{A.18}$$

A.3 Electric Field of an Illuminated Metal Nanoparticle

By solving the *Laplace's equation* for azimuthal symmetry and and applying the appropriate boundary conditions, we arrived at the electric scalar potential created due to an illuminated metal nanoparticle in (A.18). We now use the fundamental relation $\boldsymbol{E} = -\nabla\mathcal{V}$ to obtain the relevant electric field in the *quasi-static* limit [5,9,12].

The ∇ operator in spherical coordinates reads [12],

$$\nabla f = \frac{\partial}{\partial r} f\hat{r} + \frac{1}{r}\frac{\partial}{\partial\theta} f\hat{\theta} + \frac{1}{r\sin(\theta)}\frac{\partial}{\partial\phi} f\hat{\phi} \tag{A.19}$$

By applying (A.19) separately to the $r < a$ and $r \geq a$ cases of (A.18) and simplify-

ing, we arrive at,

$$\boldsymbol{E} = \begin{cases} \frac{3\epsilon_b}{2\epsilon_b+\epsilon_m} E_0(\cos(\theta)\hat{r} - \sin(\theta)\hat{\theta}), & \text{for } r < a \\ \left(1 + \frac{2(\epsilon_m-\epsilon_b)a^3}{r^3(2\epsilon_b+\epsilon_m)}\right) E_0 \cos(\theta)\hat{r} + \left(\frac{(\epsilon_m-\epsilon_b)a^3}{r^3(2\epsilon_b+\epsilon_m)} - 1\right) E_0 \sin(\theta)\hat{\theta}, & \text{for } r \geq a \end{cases} \tag{A.20}$$

As $\hat{z} = \cos(\theta)\hat{r} - \sin(\theta)\hat{\theta}$ in spherical coordinates, the above equation can be written in the form [5],

$$\boldsymbol{E} = \begin{cases} \frac{3\epsilon_b}{2\epsilon_b+\epsilon_m} E_0 \hat{z}, & \text{for } r < a \\ \frac{2(\epsilon_m-\epsilon_b)a^3}{r^3(2\epsilon_b+\epsilon_m)} E_0 \cos(\theta)\hat{r} + \frac{(\epsilon_m-\epsilon_b)a^3}{r^3(2\epsilon_b+\epsilon_m)} E_0 \sin(\theta)\hat{\theta} + E_0\hat{z}, & \text{for } r \geq a \end{cases} \tag{A.21}$$

It is observable that the field induced by the MNP in response to the incident field outside the MNP is given by,

$$\begin{aligned} \boldsymbol{E}_{\text{res}}(r \geq a) &= \frac{(\epsilon_m - \epsilon_b)a^3 E_0}{(2\epsilon_b + \epsilon_m)r^3} \left[2\cos(\theta)\hat{r} + \sin(\theta)\hat{\theta}\right] \\ &= \frac{(\epsilon_m - \epsilon_b)a^3 E_0}{(2\epsilon_b + \epsilon_m)r^3} \left[2\cos(\theta)\hat{r} + \sin(\theta)\hat{\theta} + \cos(\theta)\hat{r} - \cos(\theta)\hat{r}\right] \\ &= \frac{(\epsilon_m - \epsilon_b)a^3 E_0}{(2\epsilon_b + \epsilon_m)r^3} \left[3\cos(\theta)\hat{r} - \hat{z}\right] \\ &= \frac{(\epsilon_m - \epsilon_b)a^3}{(2\epsilon_b + \epsilon_m)r^3} \left[3(\boldsymbol{E}_{\text{drive}}.\hat{r})\hat{r} - \boldsymbol{E}_{\text{drive}}\right]. \end{aligned}$$

as $\hat{z}.\hat{r} = \cos(\theta)$ and $\boldsymbol{E}_{\text{drive}} = E_0\hat{z}$.

Appendix B
Quantum Dots as Artificial Atoms

B.1 Wavefunction and Energy of a *Particle in a Box*

As per our detailed discussion in section 3.1 the conduction band of a QD can be modeled using the *infinite square well* or the *particle in a box* model. We will start the derivation of equations for the relevant wave equation (3.1) and the corresponding eigen energy equation (3.2) by obtaining the equations for a one dimensional infinite square well potential. For this purpose, we will follow the approach presented in [75]:

A particle, such as an electron, in a one-dimensional square well potential is completely free to move along the selected dimension inside the well due to the potential being zero ($V(x) = 0$) except beyond the two ends ($x = 0$ and $x = l_x$) where an infinite potential prevents it from escaping ($V(x) \rightarrow \infty$), as depicted in Fig. 3.1(b). Therefore, the probability of finding the particle outside the well is zero, which results in $\Psi(x) = 0 \; \forall x < 0$ and $x > l_x$. The time-dependent Schrödinger equation inside the potential well reads [75],

$$\frac{-\hbar^2}{2m}\frac{d^2}{dx^2}\Psi = E\Psi \implies \frac{d^2}{dx^2}\Psi = -\mathcal{K}^2\Psi \text{ where } \mathcal{K} = \frac{\sqrt{2mE}}{\hbar} \tag{B.1}$$

with the eigen energy $E \neq 0$. In the above equation, $\hbar$ is the reduced Planck constant and m is the electronic mass. We can readily observe that (B.1) takes the

form of a classical simple harmonic oscillator which has the solution,

$$\Psi(x) = A\sin(\mathcal{K}x) + B\cos(\mathcal{K}x), \tag{B.2}$$

where A and B are coefficients to be found using appropriate boundary conditions.

Although the wavefunction Ψ and its derivative $d\Psi/dx$ are both usually continuous, only the first condition would apply when the potential $V(x) \to \infty$. This would lead to,

$$\Psi(0) = \Psi(x) = 0 \implies B = 0 \implies \Psi(x) = A\sin(x). \tag{B.3}$$

Ruling out the trivial and non-normalizable solution where $\Psi = 0$ due to $A = 0$, we arrive at $\sin(\mathcal{K}l_x) = 0$, which means $\mathcal{K}l_x = \{\pm\pi, \pm 2\pi, \pm 3\pi ...\}$ It is evident that $\mathcal{K}$ takes distinct values of the form, $\mathcal{K}_n = n\pi/l_x$ where $n = \{1, 2, 3...\}$ where the negative sign has been incorporated into the yet to be found coefficient A. Thus, the permitted discrete eigen energies of the one-dimensional infinite potential well would be,

$$E_n = \frac{\hbar^2\mathcal{K}^2}{2m} = \frac{\hbar^2\pi^2 n^2}{2l_x^2 m}. \tag{B.4}$$

In attempt to find the coefficient A, we use the normalization of the wavefunction such that,

$$\int_0^{l_x} |A|^2 \sin^2(\mathcal{K}x)dx = 1 \implies |A|^2 = 2/l_x, \tag{B.5}$$

which only leaves us with the magnitude of the required coefficient. As the phase of the coefficient has no physical significance, we pick the real positive root, hence $A = \sqrt{2/l_x}$. This leads to the infinite set of possible wavefunctions of a particle (electron in this case) confined in a one-dimensional infinite potential well,

$$\frac{2}{l_x}\sin\left(\frac{n\pi x}{l_x}\right), \text{ where } n = 1, 2, 3... \tag{B.6}$$

The above one-dimensional solution can be straightforwardly extended for a three dimensional particle in a box using the three dimensional time-independent Schrödinger equation [75],

$$-\frac{\hbar^2}{2m}\nabla^2\Psi = E\Psi. \tag{B.7}$$

Assuming a separable solution of the form,

$$\Psi(x,y,z) = \mathcal{X}(x)\mathcal{Y}(y)\mathcal{Z}(z) \tag{B.8}$$

and plugging (B.8) back in (B.7) leads to,

$$\frac{-\hbar^2}{2m}\left[\frac{1}{\mathcal{X}}\frac{d^2}{dx^2}\mathcal{X} + \frac{1}{\mathcal{Y}}\frac{d^2}{dy^2}\mathcal{Y} + \frac{1}{\mathcal{Z}}\frac{d^2}{dz^2}\mathcal{Z}\right] = E \tag{B.9}$$

For constant energy E, the three addends of the above equations should separately be constant as they depend on different independent variables. With the influence from the one-dimensional case, we can write,

$$\frac{d^2}{dx^2}\mathcal{X} = \mathcal{K}_x^2\mathcal{X} \implies \frac{1}{\mathcal{X}}\frac{d^2}{dx^2}\mathcal{X} = -\mathcal{K}_x^2 \tag{B.10a}$$

$$\frac{d^2}{dy^2}\mathcal{Y} = \mathcal{K}_y^2\mathcal{Y} \implies \frac{1}{\mathcal{Y}}\frac{d^2}{dy^2}\mathcal{Y} = -\mathcal{K}_y^2 \tag{B.10b}$$

$$\frac{d^2}{dz^2}\mathcal{Z} = \mathcal{K}_z^2\mathcal{Z} \implies \frac{1}{\mathcal{Z}}\frac{d^2}{dz^2}\mathcal{Z} = -\mathcal{K}_z^2 \tag{B.10c}$$

By substituting the above in (B.9), we can obtain,

$$\frac{\hbar^2}{2m}\left[\mathcal{K}_x^2 + \mathcal{K}_y^2 + \mathcal{K}_z^2\right] = E. \tag{B.11}$$

Using

$$\mathcal{K}_x = \frac{n_x\pi}{l_x},\ \mathcal{K}_y = \frac{n_y\pi}{l_y},\ \mathcal{K}_z = \frac{n_z\pi}{l_z} \tag{B.12}$$

where, $n = 1, 2, 3...$ we can arrive at,

$$E(n_x, n_y, n_z) = \frac{\hbar^2 \pi^2}{2m} \left[\left(\frac{n_x}{l_x} \right)^2 + \left(\frac{n_y}{l_y} \right)^2 + \left(\frac{n_z}{l_z} \right)^2 \right]$$

and

$$\begin{aligned} \Psi x, y, z &= \mathcal{X}(x)\mathcal{Y}(y)\mathcal{Z}(z) \\ &= \sqrt{\frac{8}{l_x l_y l_z}} \sin\left(\frac{n_x \pi x}{l_x} \right) \sin\left(\frac{n_y \pi y}{l_y} \right) \sin\left(\frac{n_z \pi z}{l_z} \right) \end{aligned}$$

which represent the possible discrete eigen energies and the corresponding wave-functions of an electron trapped in a three-dimensional infinite potential well.

Appendix C
Density Matrix Theory and Open Quantum Systems

C.1 Interaction picture *Liouville equation*

Time evolution of the density operator in the Schrödinger picture is given by the commutator relation,

$$\frac{\partial}{\partial t}\hat{\rho}(t) = -\frac{\mathrm{i}}{\hbar}\left[\hat{\mathcal{H}}_0 + \hat{\mathcal{V}}(t), \hat{\rho}(t)\right]$$

by Substituting

$$\hat{\rho}(t) = e^{-(\mathrm{i}/\hbar)\hat{\mathcal{H}}_0 t}\hat{\rho}_{\mathrm{I}}(t)e^{(i/\hbar)\hat{\mathcal{H}}_0 t}$$

we can obtain,

$$\frac{\partial}{\partial t}\left\{e^{-(\mathrm{i}/\hbar)\hat{\mathcal{H}}_0 t}\hat{\rho}_{\mathrm{I}}(t)e^{(\mathrm{i}/\hbar)\hat{\mathcal{H}}_0 t}\right\} = -\frac{\mathrm{i}}{\hbar}\left[\hat{\mathcal{H}}_0 + \hat{\mathcal{V}}(t), \hat{\rho}(t)\right].$$

Expansion of the product differential and simplification using the commutation relation of $\hat{\mathcal{H}}_0$ and $e^{\pm(\mathrm{i}/\hbar)\hat{\mathcal{H}}_0 t}$ walks us through the following major steps,

$$\frac{-\mathrm{i}}{\hbar}e^{-(\mathrm{i}/\hbar)\hat{\mathcal{H}}_0 t}\left\{\hat{\mathcal{H}}_0\hat{\rho}_{\mathrm{I}} - \hat{\rho}_{\mathrm{I}}\hat{\mathcal{H}}_0\right\}e^{(\mathrm{i}/\hbar)\hat{\mathcal{H}}_0 t} + e^{-(\mathrm{i}/\hbar)\hat{\mathcal{H}}_0 t}\frac{\partial}{\partial t}\hat{\rho}_{\mathrm{I}}(t)e^{(\mathrm{i}/\hbar)\hat{\mathcal{H}}_0 t} = -\frac{\mathrm{i}}{\hbar}\left[\hat{\mathcal{H}}, \hat{\rho}(t)\right]$$

$$= -\frac{\mathrm{i}}{\hbar}\Big\{ e^{(\mathrm{i}/\hbar)\hat{\mathcal{H}}_0 t}\hat{\mathcal{V}}e^{-(i/\hbar)\hat{\mathcal{H}}_0 t}e^{(\mathrm{i}/\hbar)\hat{\mathcal{H}}_0 t}\hat{\rho}e^{-(\mathrm{i}/\hbar)\hat{\mathcal{H}}_0 t} - e^{(\mathrm{i}/\hbar)\hat{\mathcal{H}}_0 t}\hat{\rho}e^{-(\mathrm{i}/\hbar)\hat{\mathcal{H}}_0 t}e^{(i/\hbar)\hat{\mathcal{H}}_0 t}\hat{\mathcal{V}}e^{-(\mathrm{i}/\hbar)\hat{\mathcal{H}}_0 t}\Big\}$$

which finally result in the interaction picture *Liouville equation*,

$$\frac{\partial}{\partial t}\hat{\rho}_{\mathrm{I}}(t) = -\frac{\mathrm{i}}{\hbar}\left\{\hat{\mathcal{V}}_{\mathrm{I}}(t)\hat{\rho}_{\mathrm{I}}(t) - \hat{\rho}_{\mathrm{I}}(t)\hat{\mathcal{V}}_{\mathrm{I}}(t)\right\} = -\frac{\mathrm{i}}{\hbar}\left[\hat{\mathcal{V}}_{\mathrm{I}}(t), \hat{\rho}_{\mathrm{I}}(t)\right]$$

Appendix D
Analytical Characterization of Exciton Behaviour in a Plasmonic Near Field

D.1 Matrix Form of the Atomic Master Equation

In the Hilbert space where $|e\rangle$ and $|g\rangle$ form an independent basis set, the ladder operators ($\hat{\sigma}$ and $\hat{\sigma}^\dagger$) of the QD and $\hat{\sigma}^\dagger\hat{\sigma}$ can be expressed in their matrix form as,

$$\hat{\sigma} = |g\rangle\langle e| = \begin{pmatrix} 1 \\ 0 \end{pmatrix}\begin{pmatrix} 0 & 1 \end{pmatrix} = \begin{pmatrix} 0 & 1 \\ 0 & 0 \end{pmatrix} \tag{D.1a}$$

$$\hat{\sigma}^\dagger = |e\rangle\langle g| = \begin{pmatrix} 0 \\ 1 \end{pmatrix}\begin{pmatrix} 1 & 0 \end{pmatrix} = \begin{pmatrix} 0 & 0 \\ 1 & 0 \end{pmatrix} \tag{D.1b}$$

$$\hat{\sigma}^\dagger\hat{\sigma} = |e\rangle\langle e| = \begin{pmatrix} 0 \\ 1 \end{pmatrix}\begin{pmatrix} 0 & 1 \end{pmatrix} = \begin{pmatrix} 0 & 0 \\ 0 & 1 \end{pmatrix} \tag{D.1c}$$

With the above description, we can recast the Hamiltonian of the QD interacting with the plasmonic and external coherent fields given by (5.1) as,

$$\hat{\mathcal{H}}_{\mathrm{qd}} = \hbar\omega_{\mathrm{qd}}\hat{\sigma}^\dagger\hat{\sigma} - E_{\mathrm{qd}}\mu\left(\hat{\sigma} + \hat{\sigma}^\dagger\right) = \begin{pmatrix} 0 & -\mu E_{\mathrm{qd}} \\ -\mu E_{\mathrm{qd}} & \hbar\omega_{\mathrm{qd}} \end{pmatrix} \tag{D.2a}$$

We can then use the matrix of (4.23),

$$\frac{\partial}{\partial t}\hat{\rho} = -\frac{\mathrm{i}}{\hbar}\left[\hat{\mathcal{H}}_{\mathrm{qd}}, \hat{\rho}\right] + \lambda_1\left(2\hat{\sigma}\hat{\rho}\hat{\sigma}^\dagger - \hat{\sigma}^\dagger\hat{\sigma}\hat{\rho} - \hat{\rho}\hat{\sigma}^\dagger\hat{\sigma}\right) + \lambda_2\left(2\hat{\sigma}^\dagger\hat{\rho}\hat{\sigma} - \hat{\sigma}\hat{\sigma}^\dagger\hat{\rho} - \hat{\rho}\hat{\sigma}\hat{\sigma}^\dagger\right) + \lambda_3\left(2\hat{\sigma}^\dagger\hat{\sigma}\hat{\rho}\hat{\sigma}^\dagger\hat{\sigma} - \hat{\sigma}^\dagger\hat{\sigma}\hat{\rho} - \hat{\rho}\hat{\sigma}^\dagger\hat{\sigma}\right)$$

to finally arrive at,

$$\dot{\hat{\rho}} = \frac{\mathrm{i}}{\hbar}\begin{bmatrix} -\mu E_{\mathrm{qd}}(\rho_{12} - \rho_{21}) & -\mu E_{\mathrm{qd}}(\rho_{11} - \rho_{22}) + \hbar\omega_{\mathrm{qd}}\rho_{12} \\ -\mu E_{\mathrm{qd}}(\rho_{22} - \rho_{11}) - \hbar\omega_{\mathrm{qd}}\rho_{21} & -\mu E_{\mathrm{qd}}(\rho_{21} - \rho_{12}) \end{bmatrix} - \begin{bmatrix} 2\lambda_2\rho_{11} - 2\lambda_1\rho_{22} & (\lambda_1 + \lambda_2 + \lambda_3)\rho_{12} \\ (\lambda_1 + \lambda_2 + \lambda_3)\rho_{21} & 2\lambda_1\rho_{22} - 2\lambda_2\rho_{11} \end{bmatrix},$$

where ρ_{ij} denotes the $(i,j)^{\mathrm{th}}$ element of the QD density matrix $\hat{\rho}$.

D.2 Derivation of QD Bloch Equations

Matrix form of the density matrix time evolution of the QD under the influence of the MNP and the externally incident field is given by (5.15) as,

$$\begin{bmatrix} \dot{\rho}_{11} & \dot{\rho}_{12} \\ \dot{\rho}_{21} & \dot{\rho}_{22} \end{bmatrix} = \begin{bmatrix} \left\{-\frac{\mathrm{i}}{\hbar}\mu E_{\mathrm{qd}}(\rho_{12} - \rho_{21}) - \frac{(\rho_{11}-1)}{\tau}\right\} & \left\{-\frac{\mathrm{i}}{\hbar}\mu E_{\mathrm{qd}}\Delta + i\omega_{\mathrm{qd}}\rho_{12} - \frac{\rho_{12}}{T}\right\} \\ \left\{\frac{\mathrm{i}}{\hbar}\mu E_{qd}\Delta - i\omega_{\mathrm{qd}}\rho_{21} - \frac{\rho_{21}}{T}\right\} & \left\{-\frac{\mathrm{i}}{\hbar}\mu E_{qd}(\rho_{21} - \rho_{12}) - \frac{\rho_{22}}{\tau}\right\} \end{bmatrix}$$

Equating the first elements of LHS and RHS, substituting for E_{qd} from (5.9) and factoring out the high frequency time dependencies of ρ_{12} and ρ_{21},

$$\dot{\rho}_{11} = -\frac{\mathrm{i}}{\hbar}\mu\left(\frac{\hbar}{\mu}\Omega_{12}^r e^{-\mathrm{i}\omega t} + \frac{\hbar}{\mu}\Omega_{12}^{r*} e^{\mathrm{i}\omega t}\right)(\tilde{\rho}_{12}e^{\mathrm{i}\omega t} - \tilde{\rho}_{21}e^{-\mathrm{i}\omega t}) - \frac{(\rho_{11}-1)}{\tau} \tag{D.3}$$

using the rotating wave approximation to eliminate the high frequency time dependencies,

$$\dot{\rho}_{11} \approx -\mathrm{i}\Omega_{12}^r\tilde{\rho}_{12} + \mathrm{i}\Omega_{12}^{r*}\tilde{\rho}_{21} + \frac{\rho_{22}}{\tau(\omega)} \tag{D.4}$$

Using a similar steps, it can be shown that,

$$\dot{\rho}_{22} \approx \mathrm{i}\Omega_{12}^{r}\tilde{\rho}_{12} + \mathrm{i}\Omega_{12}^{r*}\tilde{\rho}_{21}. \tag{D.5}$$

By comparing ρ_{21} on the LHS and RHS of (5.15), substituting for E_{qd} and factoring the high frequency time dependence of off diagonal density matrix elements as earlier,

$$\frac{\partial}{\partial t}\left\{\tilde{\rho}_{21}e^{-\mathrm{i}\omega t}\right\} = \frac{\mathrm{i}}{\hbar}\mu\left(\frac{\hbar}{\mu}\Omega_{12}^{r}e^{-\mathrm{i}\omega t} + \frac{\hbar}{\mu}\Omega_{12}^{r*}e^{\mathrm{i}\omega t}\right)\Delta - \mathrm{i}\omega_{\mathrm{qd}}\tilde{\rho}_{21}e^{-\mathrm{i}\omega t} - \frac{\tilde{\rho}_{21}e^{-\mathrm{i}\omega t}}{T(\omega)}$$

$$\dot{\tilde{\rho}}_{21}e^{-\mathrm{i}\omega t} - \mathrm{i}\omega\tilde{\rho}_{21}e^{-\mathrm{i}\omega t} = \mathrm{i}\left(\Omega_{12}^{r}e^{-\mathrm{i}\omega t} + \Omega_{12}^{r*}e^{\mathrm{i}\omega t}\right)\Delta - i\omega_{\mathrm{qd}}\tilde{\rho}_{21}e^{-i\omega t} - \frac{\tilde{\rho}_{21}e^{-\mathrm{i}\omega t}}{T(\omega)}$$

$$\dot{\tilde{\rho}}_{21} = \left\{\mathrm{i}\Delta\Omega_{12}^{r}e^{-\mathrm{i}\omega t} + \mathrm{i}\Delta\Omega_{12}^{r*}e^{\mathrm{i}\omega t} - \left[\mathrm{i}(\omega_{\mathrm{qd}} - \omega) + \frac{1}{T(\omega)}\right]\tilde{\rho}_{21}e^{-\mathrm{i}\omega t}\right\}e^{\mathrm{i}\omega t}$$

Eliminating the term oscillating as $e^{2i\omega t}$ using the rotating wave approximation,

$$\dot{\tilde{\rho}}_{21} \approx \mathrm{i}\Delta\Omega_{12}^{r} - \left[\mathrm{i}(\omega_{\mathrm{qd}} - \omega) + \frac{1}{T(\omega)}\right]\tilde{\rho}_{21}.$$

D.3 Root selection for Population Difference

For $q^3 + r^2 < 0$, $\mathcal{P}_1$ and $\mathcal{P}_2$ from (5.27) will be complex conjugates such that,

$$\mathcal{P}_1 = r + \sqrt{q^3 + r^2} = |\mathcal{P}_1|\underline{/\theta_1},$$
$$\mathcal{P}_2 = r - \sqrt{q^3 + r^2} = |\mathcal{P}_1|\underline{/-\theta_1}.$$

Equation (5.26) mandates p_1 and p_2 to be complex conjugates of each other for at least one cubic root of (5.25) to be real. Using De Moivre's nth root theorem [209] and trignometric identities, it can be shown that for $j = 0, 1, 2$,

$$\mathcal{P}_1^{\frac{1}{3}}(j) = |\mathcal{P}_1|^{\frac{1}{3}}\left[\cos\left(\frac{\theta_1}{3} + \frac{2j\pi}{3}\right) + \mathrm{i}\sin\left(\frac{\theta_1}{3} + \frac{2j\pi}{3}\right)\right],$$

$$= |\mathcal{P}_2|^{\frac{1}{3}} \left[\cos\left(\frac{\theta_1}{3} + \frac{2(-j)\pi}{3}\right) - \mathrm{i}\sin\left(\frac{\theta_1}{3} + \frac{2(-j)\pi}{3}\right)\right],$$
$$= \left[\mathcal{P}_2^{\frac{1}{3}}(-j)\right]^*,$$

Comparison of all possibilities of the roots of (5.25) against its steady state numerical solution over the large parameter space used in this work reveals that the valid root for $-1 \leq \Delta \leq 1$ when $q^3 + r^2 < 0$ is given by,

$$\Delta = p_1 + p_2 - \tilde{w}_2/3, \qquad \text{where,}$$
$$p_1 = \mathcal{P}_1^{\frac{1}{3}}(j=0) = |\mathcal{P}_1|^{\frac{1}{3}} \left[\cos\left(\frac{\theta_1}{3}\right) + \mathrm{i}\sin\left(\frac{\theta_1}{3}\right)\right],$$
$$p_2 = p_1^*.$$

D.4 Normalized Exciton Energy and Dephasing

From (5.21c),

$$\dot{\tilde{\rho}}_{21} \approx -\left[\mathrm{i}(\omega_{\mathrm{qd}} - \omega) + 1/T(\omega)\right]\tilde{\rho}_{21} + \mathrm{i}\Omega_{12}^r\Delta. \tag{D.10}$$

Substituting from (5.9) in (5.21c),

$$\Omega_{12}^r = \Omega_{12}^{\mathrm{eff}} + \eta\tilde{\rho}_{21} = \Omega_{12}^{\mathrm{eff}} + (\eta_{\mathrm{re}} + \mathrm{i}\eta_{\mathrm{im}})\tilde{\rho}_{21}, \tag{D.11}$$

and rearranging,

$$\dot{\tilde{\rho}}_{21} \approx -\left[\mathrm{i}(\omega_{\mathrm{qd}} - \eta_{\mathrm{re}}\Delta - \omega) + \left\{1/T(\omega) + \eta_{\mathrm{im}}\Delta\right\}\right]\tilde{\rho}_{21} + \mathrm{i}\Omega_{12}^{\mathrm{eff}}\Delta \tag{D.12a}$$
$$\dot{\tilde{\rho}}_{21} \approx -\left[\mathrm{i}(\Pi_{21} - \omega) + \Lambda_{21}\right]\tilde{\rho}_{21} + \mathrm{i}\Omega_{12}^{\mathrm{eff}}\Delta. \tag{D.12b}$$

where $\Pi_{21} = \omega_{\mathrm{qd}} - \eta_{\mathrm{re}}\Delta$ and $\Lambda_{21} = 1/T(\omega) + \eta_{\mathrm{im}}\Delta$ denote the normalized exciton energy and dephasing in the presence of the MNP, respectively.

D.5 Quantum State Purity Derivation

Using the matrix notation of the QD density operator, we can obtain $\hat{\rho}^2$ as,

$$\hat{\rho}^2 = \begin{bmatrix} \rho_{11} & \rho_{12} \\ \rho_{12}^* & \rho_{22} \end{bmatrix} \begin{bmatrix} \rho_{11} & \rho_{12} \\ \rho_{12}^* & \rho_{22} \end{bmatrix} = \begin{bmatrix} \left\{\rho_{11}^2 + |\rho_{12}|^2\right\} & \{\rho_{11}\rho_{12} + \rho_{12}\rho_{22}\} \\ \{\rho_{12}^*(\rho_{11} + \rho_{22})\} & \left\{|\rho_{12}|^2 + \rho_{22}^2\right\} \end{bmatrix}.$$

The trace of $\hat{\rho}^2$ can be obtained as the sum of diagonal elements,

$$\mathrm{Tr}\left(\hat{\rho}^2\right) = \rho_{11}^2 + \rho_{22}^2 + 2|\rho_{12}|^2 \tag{D.13}$$

Using $\rho_{11} + \rho_{22} = 1$ and $\Delta = \rho_{11} - \rho_{22}$ we can obtain,

$$\rho_{11} = \frac{1+\Delta}{2}, \tag{D.14a}$$

$$\rho_{22} = \frac{1-\Delta}{2} \tag{D.14b}$$

Substituting (D.14) and $\rho_{12} = \tilde{\rho}_{12}e^{\mathrm{i}\omega t} = (\mathcal{A} + i\mathcal{B})e^{\mathrm{i}\omega t}$ in (D.13) leads to,

$$\mathrm{Tr}(\hat{\rho}^2) = \frac{1+\Delta^2}{2} + 2\left(\mathcal{A}^2 + \mathcal{B}^2\right).$$

Appendix E

Cavity-QED based Characterization of Nanohybrid Scattering Spectra

E.1 Time Evolution of Plasmon Annihilation Operator

Equation (8.17) reads,

$$\frac{\partial}{\partial t}\langle \hat{a} \rangle = \mathrm{Tr}\left[\hat{a}\left(\frac{\mathrm{i}}{\hbar}[\hat{\rho}, \hat{\mathcal{H}}_{\mathrm{sys}}^{\mathrm{Int}}] + \hat{\mathcal{L}}_{\mathrm{qd}} + \hat{\mathcal{L}}_{\mathrm{m}}\right)\right]. \tag{E.1}$$

Expanding the commutator such that the corresponding terms reside close together for the ease of simplification,

$$\begin{aligned}
\frac{\partial}{\partial t}\langle \hat{a} \rangle = \frac{\mathrm{i}}{\hbar}\Big\{ & \hbar\Delta_{\mathrm{m}}\,\mathrm{Tr}\left[\hat{a}\hat{\rho}\hat{a}^{\dagger}\hat{a} - \hat{a}\hat{a}^{\dagger}\hat{a}\rho\right] + \hbar\Delta_{\mathrm{qd}}\,\mathrm{Tr}\left[\hat{a}\hat{\rho}\hat{\sigma}^{\dagger}\hat{\sigma} - \hat{a}\hat{\sigma}^{\dagger}\hat{\sigma}\hat{\rho}\right] \\
& + \mathrm{i}\hbar g\,\mathrm{Tr}\left[\hat{a}\hat{\rho}\hat{a}^{\dagger}\hat{\sigma} - \hat{a}\hat{a}^{\dagger}\hat{\sigma}\hat{\rho}\right] - \mathrm{i}\hbar g\,\mathrm{Tr}\left[\hat{a}\hat{\rho}\hat{a}\hat{\sigma}^{\dagger} - \hat{a}\hat{a}\hat{\sigma}^{\dagger}\hat{\rho}\right] \\
& - E_0\mu_{\mathrm{m}}^{*}\,\mathrm{Tr}\left[\hat{a}\hat{\rho}\hat{a} - \hat{a}\hat{a}\hat{\rho}\right] - E_0\mu_{\mathrm{m}}\,\mathrm{Tr}\left[\hat{a}\hat{\rho}\hat{a}^{\dagger} - \hat{a}\hat{a}^{\dagger}\hat{\rho}\right] \\
& - E_0\mu_{\mathrm{qd}}\,\mathrm{Tr}\left[\hat{a}\hat{\rho}\hat{\sigma} - \hat{a}\hat{\sigma}\hat{\rho}\right] - E_0\mu_{\mathrm{qd}}\,\mathrm{Tr}\left[\hat{a}\hat{\rho}\hat{\sigma^{\dagger}} - \hat{a}\hat{\sigma}^{\dagger}\hat{\rho}\right]\Big\} \\
& + \frac{\gamma_{\mathrm{qd}}}{2}\,\mathrm{Tr}\left[2\hat{a}\hat{\sigma}\hat{\rho}\hat{\sigma}^{\dagger} - \hat{a}\hat{\sigma}^{\dagger}\hat{\sigma}\hat{\rho} - \hat{a}\hat{\rho}\hat{\sigma}^{\dagger}\hat{\sigma}\right] \\
& + \frac{\gamma_{\mathrm{m}}}{2}\,\mathrm{Tr}\left[2\hat{a}\hat{a}\hat{\rho}\hat{a}^{\dagger} - \hat{a}\hat{a}^{\dagger}\hat{a}\hat{\rho} - \hat{a}\hat{\rho}\hat{a}^{\dagger}\hat{a}\right]
\end{aligned}$$

Using the cyclic property of trace and as the operators of QD and MNP commute

(hence the order operation can be changed), the above can be rearranged as,

$$\begin{aligned}\frac{\partial}{\partial t}\langle\hat{a}\rangle = \frac{\mathrm{i}}{\hbar}\Big\{&\hbar\Delta_{\mathrm{m}}\,\mathrm{Tr}\left[\left(\hat{a}^{\dagger}\hat{a}-\hat{a}\hat{a}^{\dagger}\right)\hat{a}\rho\right]+\hbar\Delta_{\mathrm{qd}}\,\mathrm{Tr}\left[\hat{\sigma}^{\dagger}\hat{\sigma}\hat{a}\hat{\rho}-\hat{\sigma}^{\dagger}\hat{\sigma}\hat{a}\hat{\rho}\right]\\&+\mathrm{i}\hbar g\,\mathrm{Tr}\left[\left(\hat{a}^{\dagger}\hat{a}-\hat{a}\hat{a}^{\dagger}\right)\hat{\sigma}\hat{\rho}\right]-\mathrm{i}\hbar g\,\mathrm{Tr}\left[\hat{a}\hat{a}\hat{\sigma}^{\dagger}\hat{\rho}-\hat{a}\hat{a}\hat{\sigma}^{\dagger}\hat{\rho}\right]\\&-E_0\mu_{\mathrm{m}}^{*}\,\mathrm{Tr}\left[\hat{a}\hat{a}\hat{\rho}-\hat{a}\hat{a}\hat{\rho}\right]-E_0\mu_{\mathrm{m}}\,\mathrm{Tr}\left[\left(\hat{a}^{\dagger}\hat{a}-\hat{a}\hat{a}^{\dagger}\right)\hat{\rho}\right]\\&-E_0\mu_{\mathrm{qd}}\,\mathrm{Tr}\left[\hat{a}\hat{\sigma}\hat{\rho}-\hat{a}\hat{\sigma}\hat{\rho}\right]-E_0\mu_{\mathrm{qd}}\,\mathrm{Tr}\left[\hat{\sigma}^{\dagger}\hat{a}\hat{\rho}-\hat{\sigma}^{\dagger}\hat{a}\hat{\rho}\right]\Big\}\\&+\frac{\gamma_{\mathrm{qd}}}{2}\,\mathrm{Tr}\left[2\hat{a}\hat{\sigma}^{\dagger}\hat{\sigma}\hat{\rho}-\hat{a}\hat{\sigma}^{\dagger}\hat{\sigma}\hat{\rho}-\hat{a}\hat{\sigma}^{\dagger}\hat{\sigma}\hat{\rho}\right]\\&+\frac{\gamma_{\mathrm{m}}}{2}\,\mathrm{Tr}\left[\left(\hat{a}^{\dagger}\hat{a}-\hat{a}\hat{a}^{\dagger}\right)\hat{a}\hat{\rho}\right]\\&=-\left(\mathrm{i}\Delta_{\mathrm{m}}+\frac{\gamma_{\mathrm{m}}}{2}\right)\langle\hat{a}\rangle+g\langle\hat{\sigma}\rangle+\frac{\mathrm{i}\mu_{\mathrm{m}}E_0}{\hbar}.\end{aligned}$$

where we have utilized the bosonic commutator relation $\hat{a}\hat{a}^{\dagger}-\hat{a}^{\dagger}\hat{a}=1$.

E.2 Time Evolution of QD Lowering Operator

Equation (8.20) reads,

$$\frac{\partial}{\partial t}\langle\hat{\sigma}\rangle=\mathrm{Tr}\left[\hat{\sigma}\left(\frac{\mathrm{i}}{\hbar}[\hat{\rho},\hat{\mathcal{H}}_{\mathrm{sys}}^{\mathrm{Int}}]+\hat{\mathcal{L}}_{\mathrm{qd}}+\hat{\mathcal{L}}_{\mathrm{m}}\right)\right].$$

Expanding the commutator as earlier,

$$\begin{aligned}\frac{\partial}{\partial t}\langle\hat{\sigma}\rangle = \frac{\mathrm{i}}{\hbar}\Big\{&\hbar\Delta_{\mathrm{m}}\,\mathrm{Tr}\left[\hat{\sigma}\hat{\rho}\hat{a}^{\dagger}\hat{a}-\hat{\sigma}\hat{a}^{\dagger}\hat{a}\rho\right]+\hbar\Delta_{\mathrm{qd}}\,\mathrm{Tr}\left[\hat{\sigma}\hat{\rho}\hat{\sigma}^{\dagger}\hat{\sigma}-\hat{\sigma}\hat{\sigma}^{\dagger}\hat{\sigma}\hat{\rho}\right]\\&+\mathrm{i}\hbar g\,\mathrm{Tr}\left[\hat{\sigma}\hat{\rho}\hat{a}^{\dagger}\hat{\sigma}-\hat{\sigma}\hat{a}^{\dagger}\hat{\sigma}\hat{\rho}\right]-\mathrm{i}\hbar g\,\mathrm{Tr}\left[\hat{\sigma}\hat{\rho}\hat{a}\hat{\sigma}^{\dagger}-\hat{\sigma}\hat{a}\hat{\sigma}^{\dagger}\hat{\rho}\right]\\&-E_0\mu_{\mathrm{m}}^{*}\,\mathrm{Tr}\left[\hat{\sigma}\hat{\rho}\hat{a}-\hat{\sigma}\hat{a}\hat{\rho}\right]-E_0\mu_{\mathrm{m}}\,\mathrm{Tr}\left[\hat{\sigma}\hat{\rho}\hat{a}^{\dagger}-\hat{\sigma}\hat{a}^{\dagger}\hat{\rho}\right]\\&-E_0\mu_{\mathrm{qd}}\,\mathrm{Tr}\left[\hat{\sigma}\hat{\rho}\hat{\sigma}-\hat{\sigma}\hat{\sigma}\hat{\rho}\right]-E_0\mu_{\mathrm{qd}}\,\mathrm{Tr}\left[\hat{\sigma}\hat{\rho}\hat{\sigma^{\dagger}}-\hat{\sigma}\hat{\sigma}^{\dagger}\hat{\rho}\right]\Big\}\\&+\frac{\gamma_{\mathrm{qd}}}{2}\,\mathrm{Tr}\left[2\hat{\sigma}\hat{\sigma}\hat{\rho}\hat{\sigma}^{\dagger}-\hat{\sigma}\hat{\sigma}^{\dagger}\hat{\sigma}\hat{\rho}-\hat{\sigma}\hat{\rho}\hat{\sigma}^{\dagger}\hat{\sigma}\right]\\&+\frac{\gamma_{\mathrm{m}}}{2}\,\mathrm{Tr}\left[2\hat{\sigma}\hat{a}\hat{\rho}\hat{a}^{\dagger}-\hat{\sigma}\hat{a}^{\dagger}\hat{a}\hat{\rho}-\hat{\sigma}\hat{\rho}\hat{a}^{\dagger}\hat{a}\right]\end{aligned}$$

Using the cyclic property of trace and commutation of QD and MNP operators,

$$\begin{aligned}
\frac{\partial}{\partial t}\langle\hat{\sigma}\rangle = \frac{\mathrm{i}}{\hbar}\Big\{&\hbar\Delta_{\mathrm{m}}\,\mathrm{Tr}\left[\hat{a}^{\dagger}\hat{a}\hat{\sigma}\hat{\rho} - \hat{a}^{\dagger}\hat{a}\hat{\sigma}\rho\right] + \hbar\Delta_{\mathrm{qd}}\,\mathrm{Tr}\left[\hat{\sigma}^{\dagger}\hat{\sigma}\hat{\sigma}\hat{\rho} - \hat{\sigma}\hat{\sigma}^{\dagger}\hat{\sigma}\hat{\rho}\right] \\
&+ \mathrm{i}\hbar g\,\mathrm{Tr}\left[\hat{a}^{\dagger}\hat{\sigma}\hat{\sigma}\hat{\rho} - \hat{a}^{\dagger}\hat{\sigma}\hat{\sigma}\hat{\rho}\right] - \mathrm{i}\hbar g\,\mathrm{Tr}\left[\hat{a}\hat{\sigma}^{\dagger}\hat{\sigma}\hat{\rho} - \hat{\sigma}\hat{\sigma}^{\dagger}\hat{a}\hat{\rho}\right] \\
&- E_0\mu_{\mathrm{m}}^{*}\,\mathrm{Tr}\left[\hat{a}\hat{\sigma}\hat{\rho} - \hat{a}\hat{\sigma}\hat{\rho}\right] - E_0\mu_{\mathrm{m}}\,\mathrm{Tr}\left[\hat{a}^{\dagger}\hat{\sigma}\hat{\rho} - \hat{a}^{\dagger}\hat{\sigma}\hat{\rho}\right] \\
&- E_0\mu_{\mathrm{qd}}\,\mathrm{Tr}\left[\hat{\sigma}\hat{\rho}\hat{\sigma} - \hat{\sigma}\hat{\rho}\hat{\sigma}\right] - E_0\mu_{\mathrm{qd}}\,\mathrm{Tr}\left[\hat{\sigma}^{\dagger}\hat{\sigma}\hat{\rho} - \hat{\sigma}\hat{\sigma}^{\dagger}\hat{\rho}\right]\Big\} \\
&+ \frac{\gamma_{\mathrm{qd}}}{2}\,\mathrm{Tr}\left[2\hat{\sigma}^{\dagger}\hat{\sigma}\hat{\sigma}\hat{\rho} - \hat{\sigma}\hat{\sigma}^{\dagger}\hat{\sigma}\hat{\rho} - \hat{\sigma}^{\dagger}\hat{\sigma}\hat{\sigma}\hat{\rho}\right] \\
&+ \frac{\gamma_{\mathrm{m}}}{2}\,\mathrm{Tr}\left[2\hat{a}^{\dagger}\hat{\sigma}\hat{a}\hat{\rho} - \hat{a}^{\dagger}\hat{\sigma}\hat{a}\hat{\rho} - \hat{a}^{\dagger}\hat{\sigma}\hat{a}\hat{\rho}\right]
\end{aligned}$$

$$\begin{aligned}
&= \frac{\mathrm{i}}{\hbar}\Big\{\hbar\Delta_{\mathrm{qd}}\,\mathrm{Tr}\left[\hat{\sigma}^{\dagger}\hat{\sigma}\hat{\sigma}\hat{\rho} - \hat{\sigma}\hat{\sigma}^{\dagger}\hat{\sigma}\hat{\rho}\right] - \mathrm{i}\hbar g\,\mathrm{Tr}\left[\hat{a}\hat{\sigma}^{\dagger}\hat{\sigma}\hat{\rho} - \hat{\sigma}\hat{\sigma}^{\dagger}\hat{a}\hat{\rho}\right] \\
&- E_0\mu_{\mathrm{qd}}\,\mathrm{Tr}\left[\hat{\sigma}^{\dagger}\hat{\sigma}\hat{\rho} - \hat{\sigma}\hat{\sigma}^{\dagger}\hat{\rho}\right]\Big\} + \frac{\gamma_{\mathrm{qd}}}{2}\,\mathrm{Tr}\left[2\hat{\sigma}^{\dagger}\hat{\sigma}\hat{\sigma}\hat{\rho} - \hat{\sigma}\hat{\sigma}^{\dagger}\hat{\sigma}\hat{\rho} - \hat{\sigma}^{\dagger}\hat{\sigma}\hat{\sigma}\hat{\rho}\right]
\end{aligned}$$

$$\begin{aligned}
&= \frac{\mathrm{i}}{\hbar}\Big\{\hbar\Delta_{\mathrm{qd}}\,\mathrm{Tr}\left[\hat{\sigma}^{\dagger}\hat{\sigma}\hat{\sigma}\hat{\rho} - \hat{\sigma}\hat{\sigma}^{\dagger}\hat{\sigma}\hat{\rho}\right] - \mathrm{i}\hbar g\,\mathrm{Tr}\left[\hat{a}\hat{\sigma}^{\dagger}\hat{\sigma}\hat{\rho} + \hat{a}\hat{\sigma}^{\dagger}\hat{\sigma}\hat{\rho} - \hat{a}\hat{\sigma}^{\dagger}\hat{\sigma}\hat{\rho} - \hat{a}\hat{\sigma}\hat{\sigma}^{\dagger}\hat{\rho}\right] \\
&- E_0\mu_{\mathrm{qd}}\,\mathrm{Tr}\left[\hat{\sigma}^{\dagger}\hat{\sigma}\hat{\rho} + \hat{\sigma}^{\dagger}\hat{\sigma}\hat{\rho} - \hat{\sigma}^{\dagger}\hat{\sigma}\hat{\rho} - \hat{\sigma}\hat{\sigma}^{\dagger}\hat{\rho}\right]\Big\} \\
&+ \frac{\gamma_{\mathrm{qd}}}{2}\,\mathrm{Tr}\left[2\hat{\sigma}^{\dagger}\hat{\sigma}\hat{\sigma}\hat{\rho} - \hat{\sigma}\hat{\sigma}^{\dagger}\hat{\sigma}\hat{\rho} - \hat{\sigma}^{\dagger}\hat{\sigma}\hat{\sigma}\hat{\rho}\right]
\end{aligned}$$

Using the fermionic operator expansions $\hat{\sigma} = |g\rangle\langle e|$ and $\hat{\sigma}^{\dagger} = |e\rangle\langle g|$,

$$\begin{aligned}
\frac{\partial}{\partial t}\langle\hat{\sigma}\rangle = \frac{\mathrm{i}}{\hbar}\Big\{&\hbar\Delta_{\mathrm{qd}}\,\mathrm{Tr}\left[\{|e\rangle\langle g|g\rangle\langle e|g\rangle\langle e| - |g\rangle\langle e|e\rangle\langle g|g\rangle\langle e|\}\,\hat{\rho}\right] \\
&- \mathrm{i}\hbar g\left(2\left\langle\hat{a}\hat{\sigma}^{\dagger}\hat{\sigma}\right\rangle - \mathrm{Tr}\left[\hat{a}\left(|e\rangle\langle g|g\rangle\langle e| + |g\rangle\langle e|e\rangle\langle g|\right)\hat{\rho}\right]\right) \\
&- E_0\mu_{\mathrm{qd}}\left(2\left\langle\hat{\sigma}^{\dagger}\hat{\sigma}\right\rangle - \mathrm{Tr}\left[|e\rangle\langle g|g\rangle\langle e|\,\hat{\rho} + |g\rangle\langle e|e\rangle\langle g|\,\hat{\rho}\right]\right)\Big\} \\
&+ \frac{\gamma_{\mathrm{qd}}}{2}\,\mathrm{Tr}\left[2\,|e\rangle\langle g|g\rangle\langle e|g\rangle\langle e|\,\hat{\rho} - |g\rangle\langle e|e\rangle\langle g|g\rangle\langle e|\,\hat{\rho} - |e\rangle\langle g|g\rangle\langle e|g\rangle\langle e|\,\hat{\rho}\right]
\end{aligned}$$

Using orthogonality relations $\langle e|g\rangle = \langle g|e\rangle = 0$ and $\langle g|g\rangle = \langle e|e\rangle = 1$,

$$\begin{aligned}\frac{\partial}{\partial t}\langle\hat{\sigma}\rangle = \frac{\mathrm{i}}{\hbar}\Big\{&\hbar\Delta_{\mathrm{qd}}\,\mathrm{Tr}\left[-|g\rangle\langle e|\,\hat{\rho}\right]\\ &-\mathrm{i}\hbar g\left(2\left\langle\hat{a}\hat{\sigma}^{\dagger}\hat{\sigma}\right\rangle - \mathrm{Tr}\left[\hat{a}\left(|e\rangle\langle e| + |g\rangle\langle g|\right)\hat{\rho}\right]\right)\\ &-E_0\mu_{\mathrm{qd}}\left(2\left\langle\hat{\sigma}^{\dagger}\hat{\sigma}\right\rangle - \mathrm{Tr}\left[|e\rangle\langle e|\,\hat{\rho} + |g\rangle\langle g|\,\hat{\rho}\right]\right)\Big\}\\ &+\frac{\gamma_{\mathrm{qd}}}{2}\,\mathrm{Tr}\left[-|g\rangle\langle e|\,\hat{\rho}\right]\end{aligned}$$

Utilizing the completeness relation of basis states, $|e\rangle\langle e| + |g\rangle\langle g| = 1$, $\mathrm{Tr}\left[\hat{\rho}\right] = 1$, and assuming the separability of operators [128], we can arrive at (8.21),

$$\frac{\partial}{\partial t}\langle\hat{\sigma}\rangle = -\left[\mathrm{i}\Delta_{\mathrm{qd}} + \frac{\gamma_{\mathrm{qd}}}{2}\right]\langle\hat{\sigma}\rangle - \left(1 - 2\langle\hat{\sigma}^{\dagger}\hat{\sigma}\rangle\right)\left(g\langle\hat{a}\rangle - \frac{\mathrm{i}\mu_{\mathrm{qd}}E_0}{\hbar}\right).$$

E.3 Classical Response Field of the MNP

Recall that in (2.9) of chapter 2, we obtained the classical dipole response field of an MNP utilizing the LRA as,

$$\vec{E}_{\mathrm{res}}(r \geq r_{\mathrm{m}}) = \frac{\beta_{\mathrm{LRA}} r_{\mathrm{m}}^3}{r^3}\left[3(\vec{E}_{\mathrm{in}}.\hat{r})\hat{r} - \vec{E}_{\mathrm{in}}\right].$$

where $\vec{E}_{\mathrm{in}}$ denotes the sum of the externally incident and QD induced fields in this context. In the quasi-static regime, the response field of the MNP takes the form of the field radiated by a point dipole [210] located at the centre of the MNP oriented along the incoming field [9]. Therefore, $\vec{E}_{\mathrm{res}}$ can be approximated by,

$$\vec{E}_{\mathrm{res}}(r \geq r_{\mathrm{m}}) \approx \frac{1}{4\pi\epsilon_0\epsilon_{\mathrm{b}} r^3}\left[\left(3\boldsymbol{d}_{\mathrm{m}}.\hat{r}\right)\hat{r} - \boldsymbol{d}_{\mathrm{m}}\right], \tag{E.8}$$

where $\vec{\boldsymbol{d}}_{\mathrm{m}}$ is the classical dipole moment of the MNP, with the magnitude d_{m}. Let the magnitude of $\vec{\boldsymbol{E}}_{\mathrm{res}}$ be denoted by E_{res}. Moreover, let E_{res} imply $E_{\mathrm{res}}(r \geq r_{\mathrm{m}})$ from here onwards.

When $\vec{\boldsymbol{d}}_{\mathrm{m}}$ lies along $\hat{r}$ (radial direction towards the QD), (E.8) leads to $E_{\mathrm{res}} \approx 2d_{\mathrm{m}}/\left(4\pi\epsilon_0\epsilon_{\mathrm{b}}r^3\right)$. It can also be observed that when d_{m} is perpendicular to $\hat{r}$, (E.8) simplifies to $E_{\mathrm{res}} \approx -d_{\mathrm{m}}/\left(4\pi\epsilon_0\epsilon_{\mathrm{b}}r^3\right)$. Using the orientation parameter s_α such that, $s_\alpha = 2$ when the external field is polarized along the axis of the hybrid molecule and $s_\alpha = -1$ when the field is polarized perpendicularly to the molecular axis, the above results can be summarized as,

$$E^{+}_{\mathrm{res}}\Big|_{r=R} \approx \frac{s_\alpha d^{+}_{\mathrm{m}}}{4\pi\epsilon_0\epsilon_{\mathrm{b}}R^3}.$$

Following a similar procedure, the response field of the QD dipole felt by the MNP can be obtained as $E^{+}_{\mathrm{qd}}\big|_{r=0} \approx s_\alpha d^{+}_{\mathrm{qd}}/\left(4\pi\epsilon_0\epsilon_{\mathrm{b}}R^3\right)$.

Comparing (2.9) with (E.8) and considering only the positive frequency coefficients, we arrive at,

$$d^{+}_{\mathrm{m}} \approx 4\pi\epsilon_0\epsilon_{\mathrm{b}}\beta_{\mathrm{LRA}}r^3_{\mathrm{m}}E^{+}_{\mathrm{in}}. \tag{E.9}$$

Substituting for $\boldsymbol{E}_{\mathrm{in}}$ in (E.9), we obtain the final classical expression for the MNP dipole moment as,

$$d^{+}_{\mathrm{m}} \approx 4\pi\epsilon_0\epsilon_{\mathrm{b}}\beta_{\mathrm{LRA}}r^3_{\mathrm{m}}\left(E_0 + \frac{s_\alpha d^{+}_{\mathrm{qd}}}{4\pi\epsilon_0\epsilon_{\mathrm{b}}R^3}\right). \tag{E.10}$$

E.4 Approximate $\mathcal{E}$ and μ_{m} in the LRA

Equation (8.26a) reads,

$$\mathcal{E} = \frac{s_\alpha}{R^3}\sqrt{\frac{\beta_{\mathrm{LRA}}r^3_{\mathrm{m}}\hbar\mathcal{D}_{\mathrm{m}}}{4i\pi\epsilon_0\epsilon_{\mathrm{b}}}}.$$

Expanding β_{LRA} and $\mathcal{D}_{\mathrm{m}}$,

$$\mathcal{E} = \frac{s_\alpha}{R^3}\sqrt{\frac{\left(\mathrm{Re}[\epsilon_{\mathrm{m}}(\omega)] + \mathrm{i}\,\mathrm{Im}\left[\epsilon_{\mathrm{m}}(\omega)\right] - \epsilon_{\mathrm{b}}\right) r_{\mathrm{m}}^3 \hbar \left(\mathrm{i}\Delta_{\mathrm{m}} + \gamma_{\mathrm{m}}/2\right)}{4i\pi\epsilon_0\epsilon_{\mathrm{b}}\left(\mathrm{Re}[\epsilon_{\mathrm{m}}(\omega)] + \mathrm{i}\,\mathrm{Im}\left[\epsilon_{\mathrm{m}}(\omega)\right] + 2\epsilon_{\mathrm{b}}\right)}}.$$

For good plasmonic materials ($\mathrm{Im}\left[\epsilon_m(\omega)\right] \ll -\mathrm{Re}\left[\epsilon_m(\omega)\right]$) near SP resonance ($\Delta_{\mathrm{m}} \approx 0$, $\mathrm{Re}\left[\epsilon_{\mathrm{m}}(\omega_{\mathrm{m}})\right] \approx -2\epsilon_{\mathrm{b}}$), substituting for γ_{m} from (8.30),

$$\mathcal{E} = \frac{s_\alpha}{R^3}\sqrt{\frac{-3\epsilon_{\mathrm{b}} r_{\mathrm{m}}^3 \hbar\eta\,\mathrm{Im}\left[\epsilon_{\mathrm{m}}(\omega)\right]}{-4\pi\epsilon_0\epsilon_{\mathrm{b}}\,\mathrm{Im}\left[\epsilon_{\mathrm{m}}(\omega)\right]}} \approx \frac{s_\alpha}{R^3}\sqrt{\frac{3r_{\mathrm{m}}^3\hbar\eta}{4\pi\epsilon_0}}.$$

Using a similar procedure, it can be shown that,

$$\mu_{\mathrm{m}} \approx -i\epsilon_b\sqrt{12\pi\epsilon_0\eta r_{\mathrm{m}}^3\hbar}.$$

Bibliography

[1] Leonhardt, U. Optical metamaterials: Invisibility cup. *Nature photonics* **1**, 207 (2007).

[2] Hapuarachchi, H. *et al.* Cavity qed analysis of an exciton-plasmon hybrid molecule via the generalized nonlocal optical response method. *Physical Review B* **95**, 245419 (2017).

[3] Huang, X. & El-Sayed, M. A. Plasmonic photo-thermal therapy (pptt). *Alexandria journal of medicine* **47** (2011).

[4] Hapuarachchi, H. P., Mallawaarachchi, S., Hattori, H. T., Zhu, W. & Premaratne, M. Optoelectronic figure of merit of a metal nanoparticle-quantum dot (mnp-qd) hybrid molecule for assessing its suitability for sensing applications. *J. Phys.: Condens. Matter* (2017).

[5] Artuso, R. D. *The Optical Response of Strongly Coupled Quantum Dot-Metal Nanoparticle Hybrid Systems* (University of Maryland, College Park, 2012).

[6] Pillai, S., & Green, M. Plasmonics for photovoltaic applications. *Solar Energy Materials and Solar Cells* **94**, 1481–1486 (2010).

[7] Kamat, P. V. Quantum dot solar cells. semiconductor nanocrystals as light harvesters. *The Journal of Physical Chemistry C* **112**, 18737–18753 (2008).

[8] Stockman, M. I. Spasers explained. *Nat. Photon .* **2**, 327–329 (2008).

[9] Maier, S. A. *Plasmonics: fundamentals and applications* (Springer Science & Business Media, 2007).

[10] Giljohann, D. A. *et al.* Gold nanoparticles for biology and medicine. *Angewandte Chemie International Edition* **49**, 3280–3294 (2010).

[11] Raza, S., Bozhevolnyi, S. I., Wubs, M. & Mortensen, N. A. Nonlocal optical response in metallic nanostructures. *J. Phys. Condens. Matter* **27**, 183204 (2015).

[12] Griffiths, D. J. *Introduction to electrodynamics* (Prentice Hall New Jersey, 1962).

[13] Hapuarachchi, H., Gunapala, S. D., Bao, Q., Stockman, M. I. & Premaratne, M. Exciton behavior under the influence of metal nanoparticle near fields: Significance of nonlocal effects. *Physical Review B* **98**, 115430 (2018).

[14] Aizpurua, J. *et al.* Optical properties of gold nanorings. *Physical review letters* **90**, 057401 (2003).

[15] Ergin, T., Stenger, N., Brenner, P., Pendry, J. B. & Wegener, M. Three-dimensional invisibility cloak at optical wavelengths. *Science* 1186351 (2010).

[16] Ritchie, R. H. Plasma losses by fast electrons in thin films. *Physical review* **106**, 874 (1957).

[17] Schaffer, B., Hohenester, U., Trügler, A. & Hofer, F. High-resolution surface plasmon imaging of gold nanoparticles by energy-filtered transmission electron microscopy. *Physical Review B* **79**, 041401 (2009).

[18] Hofmann, C. E. *et al.* Plasmonic modes of annular nanoresonators imaged by spectrally resolved cathodoluminescence. *Nano letters* **7**, 3612–3617 (2007).

[19] De Abajo, F. G. Optical excitations in electron microscopy. *Reviews of modern physics* **82**, 209 (2010).

[20] Schnell, M. *et al.* Controlling the near-field oscillations of loaded plasmonic nanoantennas. *Nature Photonics* **3**, 287 (2009).

[21] Duan, H., Fernández-Domínguez, A. I., Bosman, M., Maier, S. A. & Yang, J. K. Nanoplasmonics: classical down to the nanometer scale. *Nano letters* **12**, 1683–1689 (2012).

[22] Chen, J. *et al.* Optical nano-imaging of gate-tunable graphene plasmons. *Nature* **487**, 77 (2012).

[23] Artuso, R. D. & Bryant, G. W. Optical response of strongly coupled quantum dot- metal nanoparticle systems: Double peaked fano structure and bistability. *Nano Lett* **8**, 2106–2111 (2008).

[24] Artuso, R. D. & Bryant, G. W. Strongly coupled quantum dot-metal nanoparticle systems: Exciton-induced transparency, discontinuous response, and suppression as driven quantum oscillator effects. *Phys. Rev. B* **82**, 195419 (2010).

[25] Zhang, W., Govorov, A. O. & Bryant, G. W. Semiconductor-metal nanoparticle molecules: Hybrid excitons and the nonlinear fano effect. *Phys. Rev. Lett.* **97**, 146804 (2006).

[26] Sadeghi, S. The inhibition of optical excitations and enhancement of rabi flopping in hybrid quantum dot–metallic nanoparticle systems. *Nanotechnology* **20**, 225401 (2009).

[27] Sadeghi, S. Quantum bio-nanosensors based on quantum dot-metallic nanoparticle systems. In *Frontiers in Biological Detection: From Nanosensors to*

Systems V, vol. 8570, 85700J (International Society for Optics and Photonics, 2013).

[28] Bryant, G. W., Artuso, R. D., Garcia-Etxarri, A. & Aizpurua, J. Using local fields to tailor hybrid quantum dot-metal nanoparticle systems: Connecting the dots. In *Quantum Electronics and Laser Science Conference*, QThL3 (Optical Society of America, 2011).

[29] Sadeghi, S. Prospect of detection and recognition of single biological molecules using ultrafast coherent dynamics in quantum dot-metallic nanoparticle systems. In *Plasmonics: Metallic Nanostructures and Their Optical Properties XIII*, vol. 9547, 95473D (International Society for Optics and Photonics, 2015).

[30] Hatef, A., Sadeghi, S. M., Fortin-Deschênes, S., Boulais, E. & Meunier, M. Coherently-enabled environmental control of optics and energy transfer pathways of hybrid quantum dot-metallic nanoparticle systems. *Opt. Express* **21**, 5643–5653 (2013).

[31] Kreibig, U. & Genzel, L. Optical absorption of small metallic particles. *Surface Science* **156**, 678–700 (1985).

[32] Kreibig, U. & Vollmer, M. Theoretical considerations. In *Optical properties of metal clusters*, 13–201 (Springer, 1995).

[33] Baida, H. *et al.* Quantitative determination of the size dependence of surface plasmon resonance damping in single ag@ sio2 nanoparticles. *Nano letters* **9**, 3463–3469 (2009).

[34] Tiggesbäumker, J., Köller, L., Meiwes-Broer, K.-H. & Liebsch, A. Blue shift of the mie plasma frequency in ag clusters and particles. *Phys. Rev. A* **48**, R1749 (1993).

[35] Charlé, K.-P., König, L., Nepijko, S., Rabin, I. & Schulze, W. The surface plasmon resonance of free and embedded ag-clusters in the size range 1, 5 nm¡ d¡ 30 nm. *Crystal Research and Technology: Journal of Experimental and Industrial Crystallography* **33**, 1085–1096 (1998).

[36] Raza, S., Yan, W., Stenger, N., Wubs, M. & Mortensen, N. A. Blueshift of the surface plasmon resonance in silver nanoparticles: substrate effects. *Opt. Express* **21**, 27344–27355 (2013).

[37] Tsuei, K.-D., Plummer, E., Liebsch, A., Kempa, K. & Bakshi, P. Multipole plasmon modes at a metal surface. *Physical review letters* **64**, 44 (1990).

[38] Lindau, I. & Nilsson, P. Experimental evidence for excitation of longitudinal plasmons by photons. *Physics Letters A* **31**, 352–353 (1970).

[39] Anderegg, M., Feuerbacher, B. & Fitton, B. Optically excited longitudinal plasmons in potassium. *Physical Review Letters* **27**, 1565 (1971).

[40] Kern, J. *et al.* Atomic-scale confinement of resonant optical fields. *Nano letters* **12**, 5504–5509 (2012).

[41] Cha, H., Yoon, J. H. & Yoon, S. Probing quantum plasmon coupling using gold nanoparticle dimers with tunable interparticle distances down to the subnanometer range. *ACS nano* **8**, 8554–8563 (2014).

[42] Kravtsov, V., Berweger, S., Atkin, J. M. & Raschke, M. B. Control of plasmon emission and dynamics at the transition from classical to quantum coupling. *Nano letters* **14**, 5270–5275 (2014).

[43] Hajisalem, G., Nezami, M. S. & Gordon, R. Probing the quantum tunneling limit of plasmonic enhancement by third harmonic generation. *Nano letters* **14**, 6651–6654 (2014).

[44] Wubs, M. & Mortensen, N. A. *Nonlocal Response in Plasmonic Nanostructures* (Springer, 2017).

[45] Raza, S. *et al.* Blueshift of the surface plasmon resonance in silver nanoparticles studied with eels. *Nanophotonics* **2**, 131–138 (2013).

[46] Kumarasinghe, C., Premaratne, M. & Agrawal, G. P. Dielectric function of spherical dome shells with quantum size effects. *Opt. Express* **22**, 11966–11984 (2014).

[47] Kumarasinghe, C. S., Premaratne, M., Gunapala, S. D. & Agrawal, G. P. Theoretical analysis of hot electron injection from metallic nanotubes into a semiconductor interface. *Phys. Chem. Chem. Phys.* **18**, 18227–18236 (2016).

[48] Brázdová, V. & Bowler, D. R. *Atomistic computer simulations: a practical guide* (John Wiley & Sons, 2013).

[49] Zuloaga, J., Prodan, E. & Nordlander, P. Quantum description of the plasmon resonances of a nanoparticle dimer. *Nano Lett.* **9**, 887–891 (2009).

[50] Esteban, R., Borisov, A. G., Nordlander, P. & Aizpurua, J. Bridging quantum and classical plasmonics with a quantum-corrected model. *Nature communications* **3**, 825 (2012).

[51] Teperik, T. V., Nordlander, P., Aizpurua, J. & Borisov, A. G. Robust subnanometric plasmon ruler by rescaling of the nonlocal optical response. *Physical review letters* **110**, 263901 (2013).

[52] Mortensen, N. A., Raza, S., Wubs, M., Søndergaard, T. & Bozhevolnyi, S. I. A generalized non-local optical response theory for plasmonic nanostructures. *Nature communications* **5**, 3809 (2014).

[53] Ciracì, C. *et al.* Probing the ultimate limits of plasmonic enhancement. *Science* **337**, 1072–1074 (2012).

[54] Boardman, A. D. *Electromagnetic surface modes* (John Wiley & Sons, 1982).

[55] Eguiluz, A. & Quinn, J. Hydrodynamic model for surface plasmons in metals and degenerate semiconductors. *Physical Review B* **14**, 1347 (1976).

[56] Pitarke, J., Silkin, V., Chulkov, E. & Echenique, P. Theory of surface plasmons and surface-plasmon polaritons. *Reports on progress in physics* **70**, 1 (2006).

[57] Boardman, A. & Ruppin, R. The boundary conditions between spatially dispersive media. *Surface Science* **112**, 153–167 (1981).

[58] Toscano, G., Raza, S., Jauho, A.-P., Mortensen, N. A. & Wubs, M. Modified field enhancement and extinction by plasmonic nanowire dimers due to nonlocal response. *Optics express* **20**, 4176–4188 (2012).

[59] Raza, S., Toscano, G., Jauho, A.-P., Wubs, M. & Mortensen, N. A. Unusual resonances in nanoplasmonic structures due to nonlocal response. *Physical Review B* **84**, 121412 (2011).

[60] Johnson, P. B. & Christy, R.-W. Optical constants of the noble metals. *Phys. Rev. B* **6**, 4370 (1972).

[61] Toscano, G. *et al.* Nonlocal response in plasmonic waveguiding with extreme light confinement. *Nanophotonics* **2**, 161–166 (2013).

[62] Villo-Perez, I., Mišković, Z. & Arista, N. Plasmon spectra of nanostructures: A hydrodynamic model. In *Trends in Nanophysics*, 217–254 (Springer, 2010).

[63] Scholl, J. A., Koh, A. L. & Dionne, J. A. Quantum plasmon resonances of individual metallic nanoparticles. *Nature* **483**, 421 (2012).

[64] Savage, K. J. *et al.* Revealing the quantum regime in tunnelling plasmonics. *Nature* **491**, 574 (2012).

[65] Scholl, J. A., García-Etxarri, A., Koh, A. L. & Dionne, J. A. Observation of quantum tunneling between two plasmonic nanoparticles. *Nano letters* **13**, 564–569 (2013).

[66] Green, M. *Semiconductor quantum dots: organometallic and inorganic synthesis* (Royal Society of Chemistry, 2014).

[67] Woggon, U. *Optical properties of semiconductor quantum dots* (Springer, 1997).

[68] Rosenthal, S. J. & McBride, J. R. Quantum dots: Putting the squeeze on nanocrystals. *Nature nanotechnology* **4**, 16 (2009).

[69] Gammon, D. & Steel, D. G. Optical studies of single quantum dots. Tech. Rep., NAVAL RESEARCH LAB WASHINGTON DC (2002).

[70] Bimberg, D., Grundmann, M. & Ledentsov, N. N. *Quantum dot heterostructures* (John Wiley & Sons, 1999).

[71] Bonadeo, N. H. *et al.* Coherent optical control of the quantum state of a single quantum dot. *Science* **282**, 1473–1476 (1998).

[72] Stievater, T. & Li, X. Th stievater, x. li, dg steel, d. gammon, ds katzer, d. park, c. piermarocchi, and lj sham, phys. rev. lett. 87, 133603 (2001). *Phys. Rev. Lett.* **87**, 133603 (2001).

[73] Masumoto, Y. & Takagahara, T. *Semiconductor quantum dots: physics, spectroscopy and applications* (Springer Science & Business Media, 2013).

[74] Glutsch, S. *Excitons in low-dimensional semiconductors: theory numerical methods applications*, vol. 141 (Springer Science & Business Media, 2013).

[75] Griffiths, D. J. & Schroeter, D. F. *Introduction to quantum mechanics* (Cambridge University Press, 2018).

[76] Salasnich, L. *Quantum Physics of Light and Matter* (Springer, 2014).

[77] Yariv, A. Quantum electronics, 3rd. *Edn.(John WieLy & Sons, New York, 1988) p* **389** (1989).

[78] Lancaster, T. & Blundell, S. J. *Quantum field theory for the gifted amateur* (OUP Oxford, 2014).

[79] Schlosshauer, M. A. *Decoherence: and the quantum-to-classical transition* (Springer Science & Business Media, 2007).

[80] Bettles, R. *Cooperative interactions in lattices of atomic dipoles* (Springer, 2017).

[81] McMahon, D. *Quantum mechanics demystified* (McGraw-Hill, 2013).

[82] Gerry, C., Knight, P. & Knight, P. L. *Introductory quantum optics* (Cambridge university press, 2005).

[83] Shore, B. W. & Cook, R. J. Coherent dynamics of n-level atoms and molecules. iv. two-and three-level behavior. *Physical Review A* **20**, 1958 (1979).

[84] Tsukakoshi, M. Coherent excitation of multilevel atomic systems. *Japanese Journal of Applied Physics* **20**, 1849 (1981).

[85] Dorfman, K. E. *et al.* Quantum-coherence-enhanced surface plasmon amplification by stimulated emission of radiation. *Physical review letters* **111**, 043601 (2013).

[86] Blum, K. *Density matrix theory and applications*, vol. 64 (Springer Science & Business Media, 2012).

[87] Breuer, H.-P. & Petruccione, F. *The theory of open quantum systems* (Oxford University Press on Demand, 2002).

[88] Lindblad, G. On the generators of quantum dynamical semigroups. *Communications in Mathematical Physics* **48**, 119–130 (1976).

[89] Brasil, C. A., Fanchini, F. F. & Napolitano, R. d. J. A simple derivation of the lindblad equation. *Revista Brasileira de Ensino de Física* **35**, 01–09 (2013).

[90] Jeske, J. & Cole, J. H. Derivation of markovian master equations for spatially correlated decoherence. *Physical Review A* **87**, 052138 (2013).

[91] Kamiya, N. Quantum-to-classical reduction of quantum master equations. *Progress of Theoretical and Experimental Physics* **2015** (2015).

[92] Kosionis, S. G., Terzis, A. F., Yannopapas, V. & Paspalakis, E. Nonlocal effects in energy absorption of coupled quantum dot–metal nanoparticle systems. *J. Phys. Chem. C* **116**, 23663–23670 (2012).

[93] Mallawaarachchi, S., Premaratne, M., Gunapala, S. D. & Maini, P. K. Tuneable superradiant thermal emitter assembly. *Physical Review B* **95**, 155443 (2017).

[94] Mallawaarachchi, S., Gunapala, S. D., Stockman, M. I. & Premaratne, M. Generalized superradiant assembly for nanophotonic thermal emitters. *Phys. Rev. B* **97**, 125406 (2018).

[95] Davydov, A. *Theory of molecular excitons* (Springer, 2013).

[96] Flagg, E. *et al.* Resonantly driven coherent oscillations in a solid-state quantum emitter. *Nature Phys.* **5**, 203–207 (2009).

[97] Ridolfo, A., Di Stefano, O., Fina, N., Saija, R. & Savasta, S. Quantum plasmonics with quantum dot-metal nanoparticle molecules: influence of the fano effect on photon statistics. *Phys. Rev. Lett.* **105**, 263601 (2010).

[98] Weeraddana, D., Premaratne, M. & Andrews, D. L. Quantum electrodynamics of resonance energy transfer in nanowire systems. *Phys. Rev. B* **93**, 075151 (2016).

[99] Weeraddana, D., Premaratne, M., Gunapala, S. D. & Andrews, D. L. Controlling resonance energy transfer in nanostructure emitters by positioning near a mirror. *J. Chem. Phys.* **147**, 074117 (2017).

[100] Weeraddana, D., Premaratne, M., Gunapala, S. D. & Andrews, D. L. Quantum electrodynamical theory of high-efficiency excitation energy transfer in laser-driven nanostructure systems. *Phys. Rev. B* **94**, 085133 (2016).

[101] Yariv, A. *Quantum electronics* (Wiley, 1989).

[102] Hatef, A., Sadeghi, S. & Singh, M. R. Coherent molecular resonances in quantum dot–metallic nanoparticle systems: coherent self-renormalization and structural effects. *Nanotechnology* **23**, 205203 (2012).

[103] Premaratne, M. & Agrawal, G. P. *Light propagation in gain media: optical amplifiers* (Cambridge University Press, 2011).

[104] Meystre, P. & Sargent, M. *Elements of quantum optics* (Springer Science & Business Media, 2013).

[105] Sadeghi, S. Tunable nanoswitches based on nanoparticle meta-molecules. *Nanotechnology* **21**, 355501 (2010).

[106] Artuso, R. & Bryant, G. Hybrid quantum dot-metal nanoparticle systems: Connecting the dots. *Acta Phys. Pol. A* **122** (2012).

[107] Vielma, J. & Leung, P. Nonlocal optical effects on the fluorescence and decay rates for admolecules at a metallic nanoparticle. *J. Chem. Phys.* **126**, 194704 (2007).

[108] Leung, P. Decay of molecules at spherical surfaces: nonlocal effects. *Phys. Rev. B* **42**, 7622 (1990).

[109] Grant, H. & Kleiner, I. *Turning points in the history of mathematics* (Birkhäuser, 2016).

[110] Thorgrimsson, B. *et al.* Extending the coherence of a quantum dot hybrid qubit. *npj Quantum Inf.* **3**, 32 (2017).

[111] Loss, D. & DiVincenzo, D. P. Quantum computation with quantum dots. *Phys. Rev. A* **57**, 120 (1998).

[112] Jaeger, G. *Quantum information* (Springer, 2007).

[113] Demchenko, D. O. & Wang, L.-W. Optical transitions and nature of stokes shift in spherical cds quantum dots. *Phys. Rev. B* **73**, 155326 (2006).

[114] Nonlocal study of ultimate plasmon hybridization .

[115] Sadeghi, S. Plasmonic metaresonances: Molecular resonances in quantum dot–metallic nanoparticle conjugates. *Physical Review B* **79**, 233309 (2009).

[116] Sadeghi, S. Plasmonic metaresonance nanosensors: Ultrasensitive tunable optical sensors based on nanoparticle molecules. *IEEE Trans. Nanotechnol.* **10**, 566–571 (2011).

[117] Malyshev, A. & Malyshev, V. Optical bistability and hysteresis of a hybrid metal-semiconductor nanodimer. *Phys. Rev. B* **84**, 035314 (2011).

[118] Premaratne, M. & Stockman, M. I. Theory and technology of spasers. *Adv. Opt. Photonics* **9**, 79–128 (2017).

[119] Sarid, D. & Challener, W. *Modern introduction to surface plasmons: theory, Mathematica modeling, and applications* (Cambridge University Press, 2010).

[120] Salasnich, L. *QUANTUM PHYSICS OF LIGHT AND MATTER*. (Springer, 2017).

[121] Glauber, R. J. The quantum theory of optical coherence. *Phys. Rev.* **130**, 2529 (1963).

[122] Gulfam, Q.-u.-A., Ficek, Z. & Evers, J. Effect of retardation on the dynamics of entanglement between atoms. *Phys. Rev. A* **86**, 022325 (2012). URL `http://link.aps.org/doi/10.1103/PhysRevA.86.022325`.

[123] Carmichael, H. Quantum fluctuations in absorptive bistability without adiabatic elimination. *Phys. Rev. A* **33**, 32–62 (1986).

[124] Hohenester, U. & Trugler, A. Interaction of single molecules with metallic nanoparticles. *IEEE J. Sel. Top. Quantum Electron.* **14**, 1430–1440 (2008).

[125] Wiseman, H. M. & Milburn, G. J. *Quantum measurement and control* (Cambridge University Press, 2009).

[126] Scully, M. O. & Zubairy, M. S. *Quantum optics* (Cambridge university press, 1997), 6 edn.

[127] He, Y. & Zhu, K.-D. Strong coupling among semiconductor quantum dots induced by a metal nanoparticle. *Nanoscale Res. Lett.* **7**, 1–6 (2012).

[128] Waks, E. & Sridharan, D. Cavity qed treatment of interactions between a metal nanoparticle and a dipole emitter. *Phys. Rev. A* **82**, 043845 (2010).

[129] Sakoda, K. *Optical properties of photonic crystals*, vol. 80 (Springer Science & Business Media, 2004), 2 edn.

[130] Jayasekara, C., Premaratne, M., Gunapala, S. D. & Stockman, M. I. Mos2 spaser. *J. Appl. Phys.* **119**, 133101 (2016).

[131] Stockman, M. I. Nanoplasmonics: past, present, and glimpse into future. *Opt. Express* **19**, 22029–22106 (2011).

[132] Landau, L. D. *et al. Electrodynamics of continuous media*, vol. 8 (elsevier, 2013).

[133] Jain, P. K., Huang, X., El-Sayed, I. H. & El-Sayed, M. A. Review of some interesting surface plasmon resonance-enhanced properties of noble metal nanoparticles and their applications to biosystems. *Plasmonics* **2**, 107–118 (2007).

[134] West, P. R. *et al.* Searching for better plasmonic materials. *Laser Photon. Rev.* **4**, 795–808 (2010).

[135] Ohring, M. *Engineering materials science* (Academic press, 1995).

[136] Barchiesi, D. & Grosges, T. Fitting the optical constants of gold, silver, chromium, titanium, and aluminum in the visible bandwidth. *J. Nanophotonics* **8**, 083097–083097 (2014).

[137] Huang, X., Jain, P. K., El-Sayed, I. H. & El-Sayed, M. A. Gold nanoparticles: interesting optical properties and recent applications in cancer diagnostics and therapy. *Nanomedicine* **2**, 681–693 (2007).

[138] Jain, P. K., Lee, K. S., El-Sayed, I. H. & El-Sayed, M. A. Calculated absorption and scattering properties of gold nanoparticles of different size, shape, and composition: applications in biological imaging and biomedicine. *The journal of physical chemistry B* **110**, 7238–7248 (2006).

[139] McFarland, A. D. & Van Duyne, R. P. Single silver nanoparticles as real-time optical sensors with zeptomole sensitivity. *Nano Lett.* **3**, 1057–1062 (2003).

[140] Kinkhabwala, A. *et al.* Large single-molecule fluorescence enhancements produced by a bowtie nanoantenna. *Nat. Photon* **3**, 654–657 (2009).

[141] Atwater, H. A. & Polman, A. Plasmonics for improved photovoltaic devices. *Nature materials* **9**, 205–213 (2010).

[142] Rai, M., Yadav, A. & Gade, A. Silver nanoparticles as a new generation of antimicrobials. *Biotechnology advances* **27**, 76–83 (2009).

[143] Murray, W. A., Suckling, J. R. & Barnes, W. L. Overlayers on silver nanotriangles: field confinement and spectral position of localized surface plasmon resonances. *Nano lett.* **6**, 1772–1777 (2006).

[144] Nehl, C. L., Liao, H. & Hafner, J. H. Optical properties of star-shaped gold nanoparticles. *Nano lett.* **6**, 683–688 (2006).

[145] Chan, G. H., Zhao, J., Hicks, E. M., Schatz, G. C. & Van Duyne, R. P. Plasmonic properties of copper nanoparticles fabricated by nanosphere lithography. *Nano Lett.* **7**, 1947–1952 (2007).

[146] Blaber, M. G., Arnold, M. D. & Ford, M. Search for the ideal plasmonic nanoshell: the effects of surface scattering and alternatives to gold and silver. *Journal of Physical Chemistry C* (2009).

[147] Kolobkova, E. & Nikonorov, N. Metal sodium nanoparticles in fluorophosphate glasses. *Journal of Alloys and Compounds* **637**, 545–551 (2015).

[148] Lee, K.-H. & Chang, K. First-principles study of the optical properties and the dielectric response of al. *Phys. Rev. B* **49**, 2362 (1994).

[149] Langhammer, C., Schwind, M., Kasemo, B. & Zoric, I. Localized surface plasmon resonances in aluminum nanodisks. *Nano lett.* **8**, 1461–1471 (2008).

[150] Palmer, R. E. & Schnatterly, S. E. Observation of surface plasmons and measurement of the optical constants for sodium and potassium. *Phys. Rev. B* **4**, 2329 (1971).

[151] Blaber, M., Arnold, M., Harris, N., Ford, M. & Cortie, M. Plasmon absorption in nanospheres: A comparison of sodium, potassium, aluminium, silver and gold. *Physica B Condens. Matter* **394**, 184–187 (2007).

[152] Palik, E. D. *Handbook of optical constants of solids*, vol. 3 (Academic press, 1998).

[153] Thornton, S. T. & Rex, A. *Modern physics for scientists and engineers* (Cengage Learning, 2012).

[154] Rakić, A. D. Algorithm for the determination of intrinsic optical constants of metal films: application to aluminum. *Appl. Opt.* **34**, 4755–4767 (1995).

[155] Inagaki, T., Emerson, L., Arakawa, E. T. & Williams, M. Optical properties of solid na and li between 0.6 and 3.8 ev. *Phys. Rev. B* **13**, 2305 (1976).

[156] Foster, K. & Schepps, J. Dielectric properties of tumor and normal tissues at radio through microwave frequencies. *Journal of Microwave Power* **16**, 107–119 (1981).

[157] Tobing, L. Y. *et al.* Polarization invariant plasmonic nanostructures for sensing applications. *Scientific Reports* **7** (2017).

[158] Costa-Fernández, J. M., Pereiro, R. & Sanz-Medel, A. The use of luminescent quantum dots for optical sensing. *TrAC Trends in Analytical Chemistry* **25**, 207–218 (2006).

[159] Hartsfield, T. *et al.* Single quantum dot controls a plasmonic cavitys scattering and anisotropy. *Proceedings of the National Academy of Sciences* **112**, 12288–12292 (2015).

[160] Park, K. *et al.* New generation of multifunctional nanoparticles for cancer imaging and therapy. *Advanced functional materials* **19**, 1553–1566 (2009).

[161] Chan, W. C. & Nie, S. Quantum dot bioconjugates for ultrasensitive nonisotopic detection. *Science* **281**, 2016–2018 (1998).

[162] Howes, P. D., Chandrawati, R. & Stevens, M. M. Colloidal nanoparticles as advanced biological sensors. *Science* **346**, 1247390 (2014).

[163] Cai, W., Gao, T., Hong, H. & Sun, J. Applications of gold nanoparticles in cancer nanotechnology. *Nanotechnology, science and applications* **1**, 17 (2008).

[164] Medintz, I. L., Uyeda, H. T., Goldman, E. R. & Mattoussi, H. Quantum dot bioconjugates for imaging, labelling and sensing. *Nature materials* **4**, 435 (2005).

[165] Pons, T. *et al.* On the quenching of semiconductor quantum dot photoluminescence by proximal gold nanoparticles. *Nano letters* **7**, 3157–3164 (2007).

[166] Zhou, G. *et al.* Aptamers: A promising chemical antibody for cancer therapy. *Oncotarget* **7**, 13446 (2016).

[167] Forier, C. *et al.* Dna aptamer affinity ligands for highly selective purification of human plasma-related proteins from multiple sources. *Journal of Chromatography A* **1489**, 39–50 (2017).

[168] Javier, D. J., Nitin, N., Levy, M., Ellington, A. & Richards-Kortum, R. Aptamer-targeted gold nanoparticles as molecular-specific contrast agents for reflectance imaging. *Bioconjugate chemistry* **19**, 1309–1312 (2008).

[169] Zhang, Z. *et al.* Three biomarkers identified from serum proteomic analysis for the detection of early stage ovarian cancer. *Cancer research* **64**, 5882–5890 (2004).

[170] Mitchell, P. S. *et al.* Circulating micrornas as stable blood-based markers for cancer detection. *Proceedings of the National Academy of Sciences* **105**, 10513–10518 (2008).

[171] Choy, T. C. *Effective medium theory: principles and applications*, vol. 165 (Oxford University Press, 2015).

[172] Aminzadeh, R., Saviz, M. & Shishegar, A. A. Dielectric properties estimation of normal and malignant skin tissues at millimeter-wave frequencies using effective medium theory. In *Electrical Engineering (ICEE), 2014 22nd Iranian Conference on*, 1657–1661 (IEEE, 2014).

[173] Greish, K. Enhanced permeability and retention (epr) effect for anticancer nanomedicine drug targeting. In *Cancer Nanotechnology*, 25–37 (Springer, 2010).

[174] Dickerson, E. B. *et al.* Gold nanorod assisted near-infrared plasmonic photothermal therapy (pptt) of squamous cell carcinoma in mice. *Cancer letters* **269**, 57–66 (2008).

[175] Huang, X., Jain, P. K., El-Sayed, I. H. & El-Sayed, M. A. Plasmonic photothermal therapy (pptt) using gold nanoparticles. *Lasers in medical science* **23**, 217 (2008).

[176] Zhang, W. *et al.* Novel nanoparticles with cr 3+ substituted ferrite for self-regulating temperature hyperthermia. *Nanoscale* **9**, 13929–13937 (2017).

[177] Hoogenboom, R. *et al.* Tuning the lcst of poly (2-oxazoline) s by varying composition and molecular weight: alternatives to poly (n-isopropylacrylamide)? *Chemical communications* 5758–5760 (2008).

[178] Meyer, D. E., Shin, B., Kong, G., Dewhirst, M. & Chilkoti, A. Drug targeting using thermally responsive polymers and local hyperthermia. *Journal of controlled release* **74**, 213–224 (2001).

[179] Liu, Y. *et al.* Poly (n-isopropylacrylamide) capped plasmonic nanoparticles as resonance intensity-based temperature sensors with linear correlation. *J. Mater. Chem. C* **5**, 10926–10932 (2017).

[180] Singh, N. & Lyon, L. A. Au nanoparticle templated synthesis of pnipam nanogels. *Chemistry of Materials* **19**, 719–726 (2007).

[181] Schepps, J. L. & Foster, K. R. The uhf and microwave dielectric properties of normal and tumour tissues: variation in dielectric properties with tissue water content. *Physics in Medicine & Biology* **25**, 1149 (1980).

[182] Ross, K. & Gordon, R. Water in malignant tissue, measured by cell refractometry and nuclear magnetic resonance. *Journal of microscopy* **128**, 7–21 (1982).

[183] Naves, L. B. *et al.* Nanotechnology for the treatment of melanoma skin cancer. *Progress in biomaterials* **6**, 13–26 (2017).

[184] Maeda, H. Vascular permeability in cancer and infection as related to macromolecular drug delivery, with emphasis on the epr effect for tumor-selective drug targeting. *Proceedings of the Japan Academy, Series B* **88**, 53–71 (2012).

[185] Tiwari, P. M., Vig, K., Dennis, V. A. & Singh, S. R. Functionalized gold nanoparticles and their biomedical applications. *Nanomaterials* **1**, 31–63 (2011).

[186] Veith, G. M. *et al.* Thermal stability and catalytic activity of gold nanoparticles supported on silica. *Journal of Catalysis* **262**, 92–101 (2009).

[187] Resch-Genger, U., Grabolle, M., Cavaliere-Jaricot, S., Nitschke, R. & Nann, T. Quantum dots versus organic dyes as fluorescent labels. *Nature methods* **5**, 763 (2008).

[188] Choi, H. S. *et al.* Renal clearance of quantum dots. *Nature biotechnology* **25**, 1165 (2007).

[189] Patenaude, M. & Hoare, T. Injectable, degradable thermoresponsive poly (n-isopropylacrylamide) hydrogels. *ACS Macro Letters* **1**, 409–413 (2012).

[190] Alkilany, A. M. & Murphy, C. J. Toxicity and cellular uptake of gold nanoparticles: what we have learned so far? *Journal of nanoparticle research* **12**, 2313–2333 (2010).

[191] Veronese, F. M. & Mero, A. The impact of pegylation on biological therapies. *BioDrugs* **22**, 315–329 (2008).

[192] Link, S., Mohamed, M. & El-Sayed, M. Simulation of the optical absorption spectra of gold nanorods as a function of their aspect ratio and the effect of the medium dielectric constant. *The Journal of Physical Chemistry B* **103**, 3073–3077 (1999).

[193] Bao, H., Hao, N., Yang, Y. & Zhao, D. Biosynthesis of biocompatible cadmium telluride quantum dots using yeast cells. *Nano Research* **3**, 481–489 (2010).

[194] Kumar, A. & Biradar, A. Effect of cadmium telluride quantum dots on the dielectric and electro-optical properties of ferroelectric liquid crystals. *Physical Review E* **83**, 041708 (2011).

[195] de Mello Donega, C. & Koole, R. Size dependence of the spontaneous emission rate and absorption cross section of cdse and cdte quantum dots. *The Journal of Physical Chemistry C* **113**, 6511–6520 (2009).

[196] Christensen, T. *et al.* Nonlocal response of metallic nanospheres probed by light, electrons, and atoms. *ACS nano* **8**, 1745–1758 (2014).

[197] Garcia de Abajo, F. J. Nonlocal effects in the plasmons of strongly interacting nanoparticles, dimers, and waveguides. *The Journal of Physical Chemistry C* **112**, 17983–17987 (2008).

[198] Hatef, A., Sadeghi, S. M., Boulais, É. & Meunier, M. Quantum dot–metallic nanorod sensors via exciton–plasmon interaction. *Nanotechnology* **24**, 015502 (2012).

[199] Singh, M. R., Schindel, D. G. & Hatef, A. Dipole-dipole interaction in a quantum dot and metallic nanorod hybrid system. *Applied Physics Letters* **99**, 181106 (2011).

[200] Hatef, A. & Singh, M. R. Plasmonic effect on quantum coherence and interference in metallic photonic crystals doped with quantum dots. *Physical Review A* **81**, 063816 (2010).

[201] Reed, M. *et al.* Observation of discrete electronic states in a zero-dimensional semiconductor nanostructure. *Physical Review Letters* **60**, 535 (1988).

[202] Spataru, C. D., Ismail-Beigi, S., Capaz, R. B. & Louie, S. G. Theory and ab initio calculation of radiative lifetime of excitons in semiconducting carbon nanotubes. *Physical review letters* **95**, 247402 (2005).

[203] Jayasekara, C., Premaratne, M., Stockman, M. I. & Gunapala, S. D. Multimode analysis of highly tunable, quantum cascade powered, circular graphene spaser. *J. Appl. Phys.* **118**, 173101 (2015).

[204] Senevirathne, V. *et al.* Scattering characteristics of an exciton-plasmon nanohybrid made by coupling a monolayer graphene nanoflake to a carbon nanotube. *Journal of Physics: Condensed Matter* **31**, 085302 (2019).

[205] McEnery, K., Tame, M., Maier, S. & Kim, M. Tunable negative permeability in a quantum plasmonic metamaterial. *Physical Review A* **89**, 013822 (2014).

[206] Nordlander, P. & Prodan, E. Plasmon hybridization in nanoparticles near metallic surfaces. *Nano Letters* **4**, 2209–2213 (2004).

[207] Fujimoto, M. *Physics of classical electromagnetism*, vol. 240 (Springer Science & Business Media, 2007).

[208] El Attar, R. *Special functions and orthogonal polynomials*, vol. 3 (Lulu. com, 2006).

[209] Young, C. Y. *Trigonometry* (John Wiley & Sons, 2011).

[210] Griffiths, D. J. & College, R. *Introduction to electrodynamics*, vol. 3 (prentice Hall Upper Saddle River, NJ, 1999).